

Draft Task Report

Task 3 Passive Force Displacement Relationships for Pile Cap Without Wing Walls

Prepared For:

Utah Department of Transportation/
Research Division

Submitted By:

Brigham Young University
Department of Civil and Environmental Engineering

Authored By:

Kyle M. Rollins and Aaron K. Marsh

Task 3 Report

ABSTRACT

Accounting for seismic forces and thermal expansion in bridge design requires an accurate passive force versus backwall deflection relationship. Current design codes make no allowances for skew effects on the development of the passive force. However, small-scale experimental results and available numerical models indicate that there is a significant reduction in peak passive force as skew angle increases for plane-strain cases. To further explore this issue large-scale field tests were conducted at skew angles of 0°, 15°, and 30° with unconfined backfill geometry. The abutment backwall was 11-feet (3.35-m) wide by 5.5-feet (1.68-m) high and backfill material consisted of dense compacted sand. The peak passive force for the 15° and 30° skew tests was found to be 73% and 58%, respectively of the peak passive force for the 0° skew test which is in good agreement with the small-scale and numerical model results. However, the small differences may suggest that backfill properties (e.g. geometry and density) may have some second order effect on the reduction in peak passive force with respect to skew angle. Longitudinal displacement necessary to develop the peak passive force was found to be decrease somewhat as skew angle increased. However, this displacement was still approximately 3% of the backfill height for all field tests and is consistent with previously reported values for large-scale passive force-deflection tests. As skew angle increases, the backfill failure mechanism appears to transition from a log spiral failure mechanism on the obtuse side to a more linear failure mechanism at the acute corner in which the backwall cuts into the backfill materials.

Keywords: passive force, bridge abutment, large scale, skew, pile caps, lateral resistance

DISCLAIMER

The authors alone are responsible for the preparation and accuracy of the information, data, analysis, discussions, recommendations, and conclusions presented herein. The contents do not necessarily reflect the views, opinions, endorsements, or policies of the Utah Department of Transportation, the US Department of Transportation or other agencies that provided funding for the project. The Utah Department of Transportation makes no representation or warranty of any kind, and assumes no liability therefore.

ACKNOWLEDGEMENTS

Funding for this study was provided by FHWA pooled fund TPF-5(264) supported by the Departments of Transportation from the states of California, Minnesota, Montana, New York, Oregon, and Utah. Utah served as the lead agency with David Stevens as the project manager. This support is gratefully acknowledged. We also express appreciation to the Salt Lake City Airport Department for providing access to the test site used for this study. BYU Department Technicians David Anderson and Rodney Mayo provided invaluable service in performing these tests which is much appreciated.

TABLE OF CONTENTS

LIST OF TABLES	ix
LIST OF FIGURES	xi
1 Introduction.....	1
1.1 Background	2
1.2 Research Objectives.....	3
1.3 Order of Presentation	3
2 Literature Review.....	5
2.1 Passive Earth Pressure Theories.....	5
2.1.1 Coulomb and Rankine Earth Pressure Theories	6
2.1.2 Log Spiral Theory	8
2.1.3 Factors Governing Passive Earth Pressures	11
2.1.4 Methods for Determining the Passive Force-Deflection Relationship	17
2.2 Passive Force-Displacement Tests for Non-Skewed Abutment Walls	20
2.2.1 Duncan and Mokwa (2001).....	20
2.2.2 Rollins and Sparks (2002).....	21
2.2.3 Rollins and Cole (2006)	21
2.2.4 Lemnitzer et al. (2009).....	22
2.3 Movements and Forces for Skewed Bridges.....	23
2.4 Behavior/Performance of Skew Walls.....	26
2.4.1 Rollins and Jessee (2012) – Lab Results.....	26
2.4.2 Shamsabadi et al. (2006) – 3D Numerical Modeling Results	27
2.4.3 Sandford and Elgaaly (1993) – Skew Effects on Backfill Pressures at Frame Bridge Abutments	30
2.4.4 Steinberg et al. (2004) – Forces in Wingwalls of Skewed Semi-Integral Bridges	31

2.4.5	Elnashai et al. (2010a) – The Maule (Chile) Earthquake of February 27, 2010	32
2.5	Current Design Methods	32
2.5.1	Caltrans Seismic Bridge Design	32
2.5.2	AASHTO LRFD Bridge Design Specifications	34
2.6	Nasr and Rollins (2010)	35
3	Field Test Layout and Properties.....	39
3.1	Site Location	39
3.2	Geotechnical Site Characterization	40
3.3	Test Layout.....	43
3.3.1	Reaction Foundation	43
3.3.2	Pile Cap and Piles	45
3.3.3	Concrete Wedges	46
3.3.4	Loading Apparatus.....	55
3.3.5	Backfill Zone	56
3.3.6	General Instrumentation and Measurements	57
3.4	Geotechnical Backfill Properties	68
3.4.1	Backfill Gradation and Relative Density	68
3.4.2	Backfill Shear Strength	76
4	General Test Procedures	81
4.1	Test Order	81
4.2	Backfill Placement and Test Preparation	82
4.3	Pile Cap Displacement Procedures.....	83
4.4	Final Measurement Procedures	83
4.5	Baseline Curves	84
4.5.1	0° Baseline Test	86

4.5.2	30° Baseline Test	87
4.5.3	15° Baseline Test	88
4.5.4	Baseline Selection.....	89
5	Load versus Displacement Results.....	91
5.1	Baseline Tests: Actuator and Reaction Foundation Behavior.....	91
5.2	Backfill Tests: Actuator and Reaction Foundation Behavior	93
5.3	Backfill Load Displacement Results	96
5.4	Differential Actuator Loading.....	105
5.5	Actuator Load Reduction with Respect to Time after Peak	110
6	Backwall Movement	117
6.1	Longitudinal and Transverse Backwall Movement.....	117
6.1.1	Longitudinal Pile Cap Movement.....	119
6.1.2	Transverse Pile Deflection	123
6.2	Backwall Rotation	125
6.2.1	Pile Cap Rotation about a Vertical Axis	126
6.2.2	Pile Cap Rotation about a Transverse Axis.....	130
7	Backfill Displacement, Strain, and Failure.....	133
7.1	Backfill Heave and Surface Cracking.....	133
7.2	Internal Failure Surfaces	139
7.3	Backfill Displacement.....	145
7.4	Backfill Strain	153
7.5	Governing Backfill Failure Mechanisms	159
8	Comparison of Test Results to Design Code and Analytical Results.....	165
8.1	AASHTO and Caltrans Passive Force versus Backwall Deflection Design Curves...	165
8.2	PYCAP and ABUTMENT Passive Force versus Backwall Deflection Curves	168

8.3 Comparison of Calculated Passive Force and Failure Geometry According to the
Coulomb, Rankine, and Log Spiral Methods with Test Results171

9 Conclusion and Recommendations for Future Testing.....177

References.....181

Appendix A. Procedures for Correcting Shape Array Data.....187

LIST OF TABLES

Table 2-1: K_p Values as Calculated by Rankine, Coulomb, and Log Spiral Theories	9
Table 2-2: Movement Necessary for Development of Maximum Passive Earth Pressures [Reproduced from Cole and Rollins (2006)]	13
Table 2-3: Proposed Minimum Coefficients of Skin Friction between Soil and Construction Material [reproduced from Potyondy (1961)].....	16
Table 2-4: E_i Values for Soils at Shallow Depths (2-5 ft) for Sands and Gravels [reproduced from Duncan et al. (1980)].....	19
Table 2-5: Shamsabadi et al. (2006) Soil Finite Element parameters.....	27
Table 2-6: Input Parameters for Hardening Soil Model as Used by Nasr and Rollins (2010)	36
Table 3-1: String Potentiometer Distances from Wedge Face Measured Parallel to the Direction of Pile Cap Movement	64
Table 3-2: Soil Gradation Characteristics, Pre- and Post-Testing	69
Table 3-3: Summary of Backfill Dry Unit Weight Characteristics as Obtained from the Nuclear Density Tests.....	72
Table 3-4: Backfill Relative Compaction and Relative Densities for All Tests.....	73
Table 3-5: Backfill Strength Parameters	79
Table 4-1: 2012 Testing Summary	82
Table 5-1: Reduction in Reaction Force with Respect to Time for All Tests	115
Table 8-1: Soil and Wall Parameters used for Calculating AASHTO Passive Force versus Deflection Design Curve	167
Table 8-2: Soil and Wall Parameters used for Calculating Caltrans Passive Force versus Deflection Design Curve	168
Table 8-3: PYCAP Soil Strength Parameters	169
Table 8-4: ABUTMENT Soil Strength Parameters	170
Table 8-5: Comparison of Measured Total Passive Force to Values Predicted by Log Spiral, Coulomb, and Rankine Methods.....	172

LIST OF FIGURES

Figure 2-1: Rankine failure geometry	8
Figure 2-2: Normalized failure surface geometries predicted by Rankine, Coulomb, and Log Spiral theories	9
Figure 2-3: Log spiral failure geometry	11
Figure 2-4: Shape of typical stress-strain or load-displacement curve	20
Figure 2-5: Resolution of longitudinal force exerted by bridge abutment onto soil backfill into components normal to, and transverse to abutment backwall [adapted from Burke Jr. (1994)].....	24
Figure 2-6: Pressure distribution.....	28
Figure 2-7: Passive force-deflection curves for bridge abutments at various skew angles (Shamsabadi et al. 2006)	29
Figure 2-8: Bridge model used to determine global behavior of bridge subjected to earthquake loading (Shamsabadi et al. 2006)	30
Figure 2-9: Proposed design soil pressure envelope (Sandford and Elgaaly 1993)	31
Figure 2-10: Observed shear planes obtained from (a) Plaxis 2D finite element models for (b) homogeneous sand backfill, and (c) homogeneous gravel backfill (Nasr and Rollins 2010)	37
Figure 3-1: Aerial photograph of Salt Lake City airport control tower and test site (adapted from Google Earth)	40
Figure 3-2: Idealized soil profile constructed from laboratory and in-situ test data (Christensen 2006)	42
Figure 3-3: Plan view and cross section of general testing layout.....	44
Figure 3-4: Simultaneous casting of 15° and 30° wedges.....	47
Figure 3-5: Reinforcing grid for 30° wedge	48
Figure 3-6: Reinforcing grid for 15° wedge	49
Figure 3-7: Interface connection details (a) plan view detail of individual split connection, (b) plan view detail with bars extended out of pipe, and (c) plan view layout of the entire assembly with five split bar connections across width of pile cap.....	51

Figure 3-8: Plate interface connections	52
Figure 3-9: Railroad tie foundation for 15° and 30° wedges.....	53
Figure 3-10: Railroad tie foundation for 15° and 30° wedges with sand compacted between ties.....	53
Figure 3-11: Roller foundation for 15° and 30° wedges	54
Figure 3-12: Removal of 30° wedge	55
Figure 3-13: MTS hydraulic actuators	56
Figure 3-14: String potentiometer locations on south end of pile cap	58
Figure 3-15: LVDTs for measuring transverse cap movement (north end)	59
Figure 3-16: LVDTs for measuring transverse cap movement (south end).....	60
Figure 3-17: Corrected versus uncorrected south shape array readings (from final displacement increment of 0° test).....	62
Figure 3-18: Offset in red sand columns showing upper failure surface of the 0° test (inset more clearly shows column offset at test completion)	66
Figure 3-19: Photograph of embedded pressure plates in 30° wedge face	67
Figure 3-20: Drawing of embedded pressure plates in 30° wedge face.....	68
Figure 3-21: Particle size distribution of backfill soil pre- and post-test.....	69
Figure 3-22: Backfill dry unit weight histogram for 0° test	70
Figure 3-23: Backfill dry unit weight histogram for 15° test	71
Figure 3-24: Backfill dry unit weight histogram for 30° test	71
Figure 3-25: Backfill dry unit weight histogram for all tests	72
Figure 3-26: Moisture content with respect to depth for all tests	74
Figure 3-27: Dry unit weight with respect to depth for all tests	74
Figure 3-28: Moist unit weight with respect to depth for all tests.....	75
Figure 3-29: Relative compaction with respect to depth for all tests	75
Figure 3-30: Horizontal load-deflection plots for dry direct shear tests	77

Figure 3-31: Horizontal load-deflection plots for submerged direct shear tests	77
Figure 3-32: Normal stress versus shear stress plots for dry tests	78
Figure 3-33: Normal stress versus shear stress plots for submerged tests	78
Figure 4-1: Baseline curves for 0° test.....	85
Figure 4-2: Baseline curves for 15° and 30° tests.....	85
Figure 4-3: Baseline Curves for all tests	86
Figure 4-4: Comparison between first 0° skew baseline and 30° skew baseline tests.....	88
Figure 5-1: Actuator load versus pile cap displacement curves for 0° and 30° baseline tests.....	92
Figure 5-2: Actuator load versus reaction foundation displacement for 0° and 30° baseline tests	93
Figure 5-3: Actuator load versus pile cap displacement curves for the 0°, 15°, and 30° tests.....	95
Figure 5-4: Actuator load versus reaction foundation displacement for 0°, 15°, and 30° backfill tests	96
Figure 5-5: Illustration of calculation of longitudinal soil resistance from total load and baseline load versus deflection curves	97
Figure 5-6: Load-deflection curves for the 0° test	98
Figure 5-7: Load-deflection curves for the 15° test	99
Figure 5-8: Load-deflection curves for the 30° test	99
Figure 5-9: Passive force-deflection curves for the 0°, 15°, and 30° skew tests.....	101
Figure 5-10: Lab test passive force versus backwall displacement results (Rollins and Jessee 2012)	101
Figure 5-11: Normalized peak passive force with respect to skew angle as obtained from field tests, lab tests, and numerical analyses.....	103
Figure 5-12: Reduction factor trend lines plotted versus skew angle for field tests, lab tests, numerical analysis, and all tests	104
Figure 5-13: Total and individual actuator contribution to the passive force versus pile cap deflection curve for the 0° test.....	106

Figure 5-14: Total and individual actuator contributions to the passive force versus pile cap deflection curve for the 15° test.....	107
Figure 5-15: Total and individual actuator contribution to the passive force versus pile cap deflection curve for the 30° test.....	107
Figure 5-16: Percentage of total load resisted by west and east actuators for 15° and 30° skew tests.....	108
Figure 5-17: Actuator applied counterclockwise for 0°, 15°, and 30° tests.....	110
Figure 5-18: Reduction in reaction force with respect to time for 0° skew baseline test.....	112
Figure 5-19: Reduction in reaction force with respect to time for 30° skew baseline test.....	112
Figure 5-20: Reduction in reaction force with respect to time for the 0° test.....	113
Figure 5-21: Reduction in reaction force with respect to time for the 15° test.....	113
Figure 5-22: Reduction in reaction force with respect to time for the 30° test.....	114
Figure 5-23: Average reduction in reaction force with respect to time for the 0° and 30° baseline tests, and for the 0°, 15°, and 30° backfill tests.....	115
Figure 6-1: Relative north and south shape array measurement directions where the top of the cap represents the north end of the pile cap.....	118
Figure 6-2: Longitudinal pile deflection as measured by the north and south shape arrays, inclinometers, and string pots for 0° test.....	120
Figure 6-3: Longitudinal pile deflection at selected pile cap displacement intervals as measured by the north and south shape arrays for the 0° test.....	120
Figure 6-4: Longitudinal pile deflection as measured by north and south shape arrays, inclinometers, and string pots for 15° test.....	121
Figure 6-5: Longitudinal pile deflection at selected pile cap displacement intervals as measured by the north and south shape arrays for the 15° test.....	121
Figure 6-6: Longitudinal pile cap deflection as measured by shape arrays, inclinometers, and string pots for 30° test.....	122
Figure 6-7: Longitudinal pile deflection at selected pile cap displacement intervals as measured by the south shape arrays for the 30° test.....	122
Figure 6-8: Transverse pile deflection as measured by the shape arrays and inclinometers for the 0° test.....	123

Figure 6-9: Transverse pile deflection as measured by the shape arrays, inclinometers, and LVDTs for the 15° test.....	124
Figure 6-10: Transverse pile deflection as measured by the shape arrays and inclinometers for the 30° test.....	124
Figure 6-11: Transverse movement of the pile cap as measured by the shape arrays for the 0° test	127
Figure 6-12: Transverse movement of the pile cap at selected displacement intervals as measured by the shape arrays and inclinometer for the 15° test.....	127
Figure 6-13: Transverse movement of pile cap at test completion as measured by the inclinometer for the 30° test.....	128
Figure 6-14: Counterclockwise rotation of the pile cap about a vertical axis with respect to total actuator load for the 0°, 15°, and 30° tests.....	130
Figure 6-15: Forward rotation of the pile cap about a transverse axis as measured by the string pots for the 0°, 15°, and 30° test.....	131
Figure 7-1: Backfill heave contours, final surface cracks, and string pot locations on a 2-ft (0.61-m) grid for the 0° test	134
Figure 7-2: Backfill heave contours, final surface cracks, and string pot locations on a skewed 2-ft (0.61-m) grid for the 15° test	135
Figure 7-3: Backfill heave contours, final surface cracks, and string pot locations on a skewed 2-ft (0.61-m) grid for the 30° test	136
Figure 7-4: Maximum heave with respect to maximum pile cap displacement	139
Figure 7-5: Internal failure surfaces for the 0° test	140
Figure 7-6: Internal failure surfaces for the 15° test (inset shows locations sand columns)	141
Figure 7-7: Offsets in columns located 6 and 9 feet (1.83 and 2.74 m) back from the backwall face on the east side of the backfill	142
Figure 7-8: Internal failure surfaces for the 30° test (inset shows location of sand columns)	143
Figure 7-9: Backfill string pot displacement with respect to pile cap displacement for the 0° test.....	147
Figure 7-10: Transverse compression cracks at test completion	147
Figure 7-11: Backfill string pot displacement with respect to pile cap deflection for the 15° test.....	148

Figure 7-12: Corrected and uncorrected backfill string pot displacement with respect to pile cap displacement for the 30° test.....	149
Figure 7-13: Completely developed failure wedge for the 30° test	150
Figure 7-14: Total backfill displacement versus distance from backwall face at selected cap displacement intervals for the 0° test	152
Figure 7-15: Total backfill displacement versus distance from backwall face at selected cap displacement intervals for the 15° test	152
Figure 7-16: Total backfill displacement versus distance from backwall face at selected cap displacement intervals for the 30° test	153
Figure 7-17: Backfill compressive strain versus original distance from backwall face at selected displacement intervals for the 0° test	154
Figure 7-18: Backfill compressive strain versus original distance from backwall face at selected displacement intervals for the 15° test	155
Figure 7-19: Backfill compressive strain versus original distance from backwall face at selected displacement intervals for the 30° test	156
Figure 7-20: Total backfill displacement versus distance from backwall face at test completion for 0°, 15°, and 30° tests.....	157
Figure 7-21: Backfill strain with respect to initial distance from the backwall face for the 0°, 15°, and 30° tests at test completion	158
Figure 7-22: Average backfill strain with respect to pile cap deflection for all tests	159
Figure 7-23: Comparison of peak passive force, longitudinal force, shear strength, and applied shear force with respect to skew angle.....	161
Figure 7-24: Comparison of internal shear planes for 0°, 15°, and 30° tests	163
Figure 8-1: Comparison of Caltrans and AASHTO design curves with the passive force versus backwall deflection curve for the 0° skew 5.5-ft (1.68-m) unconfined backfill test.....	166
Figure 8-2: Comparison of low bound, best fit, and high bound PYCAP passive force versus backwall deflection curves with the 0° test curve	169
Figure 8-3: Comparison of low bound, best fit, and high bound ABUTMENT passive force versus backwall deflection curves with the 0° test curve	170
Figure 8-4: Actual and predicted failure surface geometry for the 0° test	173
Figure 8-5: Actual and predicted failure surface geometry for the 15° test	174

Figure 8-6: Actual and predicted failure surface geometry for the 30° test 175

1 INTRODUCTION

The purpose of this research is to determine the effect that bridge skew angle has on the passive force versus backwall deflection relationship. In the past, numerous large-scale tests have been conducted with the intent of determining the passive force versus backwall deflection relationship for dense, compacted backfill behind non-skewed walls (Mokwa and Duncan 2001; Rollins and Cole 2006; Rollins et al. 2010b; Rollins and Sparks 2002). Much of this research indicates that the peak passive force can be accurately predicted using the Log Spiral method, and that the peak passive force is achieved at longitudinal deflections between 3% and 5% of the backwall height (Rollins and Cole 2006). Furthermore, researchers have found that the complete passive force versus longitudinal deflection relationship can be described using a hyperbola (Duncan and Mokwa 2001; Shamsabadi et al. 2005). However, for simplicity in design, most bridge design specifications recommend a bi-linear passive force versus longitudinal deflection relationship (AASHTO 2011; Caltrans 2010)

Current bridge design practices assume that the peak passive force is the same for skewed bridges as for non-skewed bridges (AASHTO 2011) despite the fact that field evidence clearly indicates that skewed bridges do not perform as well as non-skewed bridges when subjected to seismic forces (Apirakyorapinit et al. 2012; Elnashai et al. 2010b; Shamsabadi et al. 2006; Unjoh 2012) or thermal expansion (Steinberg and Sargand 2010).

1.1 Background

Until recently, only small-scale lab tests (Rollins and Jessee 2012) and numerical models (Shamsabadi et al. 2006) have been conducted with the intent of determining the effect that skew angle has on the passive force versus backwall deflection relationship. Both of these studies found that there is a significant reduction in the peak passive force at high skew angles. Using their data, Rollins and Jessee (2012) proposed the correction factor, R_{skew} , given by Equation (1-1), which defines the relationship between the peak passive force for a skewed abutment (P_{P-skew}) and a non-skewed abutment ($P_{P-no skew}$) as a function of skew angle, θ .

$$R_{skew} = \frac{P_{P-skew}}{P_{P-no skew}} = 8.0 * 10^{-5}\theta - 0.018\theta + 1.0 \quad (1-1)$$

Rollins and Jessee (2012) performed lab-scale tests on a 2-foot (0.6 m) high wall that was used to determine the passive force versus backwall deflection curves for bridge abutments at 0°, 15°, 30°, and 45° skew angles. Concrete “wingwalls” constrained the failure surface to develop in a plane strain or 2D geometry. Although these tests produced high quality results, the authors recommended that additional large-scale tests and calibrated numerical models be created to validate their results and to provide designers with additional guidance for situations requiring different abutment geometries and/or backfill properties.

Therefore, large scale tests using dense, clean sand were performed at skew angles of 0°, 15°, and 30° degrees without any wingwalls to confine the backfill and with backfill heights of 3 and 5.5 feet (0.91 and 1.68 m). In contrast to the lab tests, the shear surfaces were allowed to develop beyond the edges of the pile cap and create a more 3D family geometry. These tests were designed to determine whether the increase in fill height and the unconfined geometry would alter the reduction factor described in Equation 1-1. This thesis will only describe the

results obtained for the 5.5-foot (1.68-m) unconfined backfill tests, while results for the 3.0-foot (0.90-m) backfill will be described by Palmer (2013). An additional set of companion tests conducted with MSE wingwalls and a backfill height of 5.5 feet (1.68 m) is described by Franke (2013).

Tests performed for this study employed an existing 11-foot (3.35-m) wide by 5.5-foot (1.68-m) high by 15-foot (4.57-m) long pile cap which has been used for a number of previously conducted lateral load and passive force versus lateral deflection tests. The 0° skew test was conducted in a similar fashion to previous tests. However, for the 15° and 30° tests, concrete wedges were attached to the face of this pile cap

1.2 Research Objectives

The objectives of this research investigation are:

1. Determine reduction in peak passive force as a function of skew angle
2. Evaluate changes in the passive force-deflection curve as a function of skew angle.
3. Identify the effect of skew angle on backwall movement, backfill heave and failure surface geometry
4. Identify the governing failure mechanism associated with different skew angles

1.3 Order of Presentation

This thesis will begin with a literature review that will describe the current state of knowledge and the need for new research pertaining to the effects that bridge skew has on the passive force versus lateral deflection relationship. Next, the field site layout and test setup will be described in detail. Field test results will then be presented in the following order: load versus displacement results (including baseline tests and reaction foundation behavior), backwall

movement, and backfill displacement failure mechanisms. Next, test results will be compared with available methods for predicting the passive force versus lateral deflection relationship. Following that, the field test results will be compared with the numerical model results. Finally, applicable conclusions will be drawn and recommendations made using all the available data.

2 LITERATURE REVIEW

This chapter describes the current state of knowledge pertaining to the passive force-deflection relationship for skewed bridge abutments. To begin, passive earth pressure theories will be outlined and the various theories' advantages and limitations will be discussed. Next, the currently available research results will be presented and their application to the current study will be addressed. Forces arising from bridge movement will then be addressed, followed by an analysis of the behavior and performance of skewed bridges subjected to thermal expansion and seismic loading. Current design methods will then be discussed. Finally, finite element methods for predicting the passive force-deflection relationship for skewed abutments will be introduced in conjunction with applicable soil constitutive models.

2.1 Passive Earth Pressure Theories

Several theories have been developed over the years that attempt to describe passive soil pressures and backfill failure mechanisms. The most prominent are the Coulomb (1776), Rankine (1857), and Log-Spiral theories (Terzaghi 1943). However, additional methods for calculating passive earth pressures have been developed in recent years by various researchers including Chen and Su (1994), Kumar and Subba Rao (1997), Soubra (2000), and Zhu and Qian (2000) which essentially confirm the accuracy of the log-spiral method. This section will only discuss the Rankine, Coulomb, and Log Spiral theories.

When calculating the passive pressure, σ'_p , all three theories reduce to the general form shown in Equation (2-1).

$$\sigma'_p = \frac{1}{2}K_p\gamma H^2 + 2 \overline{K_p}c'H \quad (2-1)$$

where

$$K_p = \frac{\sigma'_p}{\sigma'_0} = \text{passive earth pressure coefficient}$$

γ = moist unit weight of the soil

H = backfill height

c' = soil cohesion

Methods for calculating K_p according to the Rankine, Coulomb, and Log Spiral theories will be described below.

Following the discussion of the various passive pressure theories, those factors that have the largest effect on passive earth pressures will be discussed: namely structure movement, soil strength parameters, and soil-structure interaction parameters (Duncan and Mokwa 2001).

2.1.1 Coulomb and Rankine Earth Pressure Theories

Using the Mohr-Coulomb failure criterion Rankine (1857) developed and published equations for passive and active earth pressures. Though his equations do not account for wall friction the error associated with assuming no wall friction is usually on the conservative side as wall roughness typically increases passive and decreases active pressures (Terzaghi et al. 1996). However, this assumption may, in many cases provide a result that is very uneconomical to implement. Much prior to Rankine developing his theories, Coulomb (1776) published what was probably the first method for determining passive earth pressures on a retaining wall (Kramer

1996). After modification by other researchers, Coulomb's equations can be used to account for both wall friction and non-horizontal backfill conditions. Equation (2-2) and (2-3) define the passive earth pressure coefficient, as defined by Coulomb and Rankine, respectively.

$$K_p = \sin^2 \frac{\sin^2(\beta - \phi')}{\sin^2 \beta \sin \beta + \delta' \left[1 - \frac{\sin \phi' + \delta' \sin \phi' + \alpha}{\sin \beta + \delta' \sin \beta + \alpha} \right]^2} \quad (2-2)$$

$$K_p = \tan^2 \left(45 + \frac{\phi'}{2} \right) \quad (2-3)$$

where

β = angle of backwall from horizontal

ϕ' = effective soil friction angle

δ' = wall friction angle

α = angle of the backfill from horizontal

Both the Rankine and Coulomb earth pressure theories assume a linear failure surface that begins at the bottom of the wall and progresses up to the backfill surface. For passive pressures, Rankine's method assumes the failure plane rises from the bottom of the wall to the surface at an angle of inclination equal to $45^\circ - \phi / 2$ with the horizontal, where ϕ = angle of internal friction for the soil (see Figure 2-1). For the Coulomb theory the angle of inclination of the linear failure plane is determined iteratively, and though this was originally accomplished graphically (Culmann 1875), the problem can now be easily solved with a computer (Das 2010).

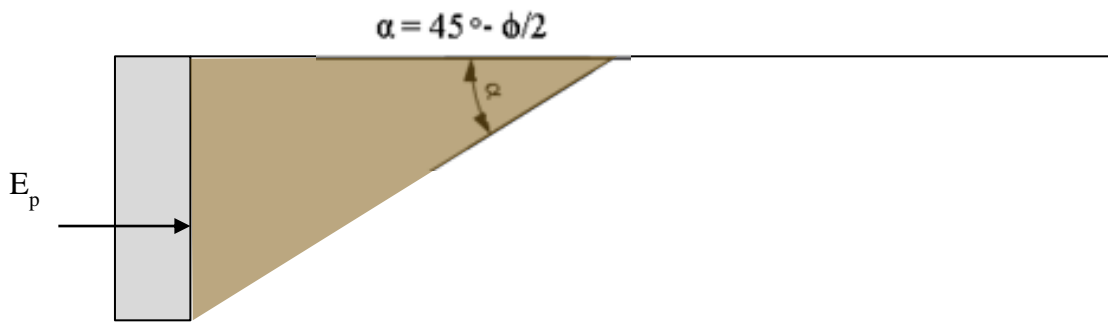


Figure 2-1: Rankine failure geometry

As both theories assume a linear sliding surface, these methods will not produce accurate results for situations where the wall friction is greater than approximately 40% of the soil friction angle (Duncan and Mokwa 2001).

2.1.2 Log Spiral Theory

In comparison to the Rankine and Coulomb earth pressure theories, the log spiral method, as described by Terzaghi (1943) and Terzaghi et al. (1996), is widely considered to be the most accurate method for determining the passive earth pressure coefficient (K_p) when large wall friction angles are present (AASHTO 2011; Duncan and Mokwa 2001). However, in instances where the ratio between the wall friction angle, δ , and the soil friction angle, ϕ , is less than 0.4, the Coulomb and Log Spiral theories produce nearly identical values of K_p and very similar failure geometries, though the Coulomb theory predicts a slightly lower angle of inclination of the failure plane. However, when $\delta/\phi \geq 0.4$ the Coulomb theory tends to produce unrealistically large values of K_p , and unrealistically long failure wedges (Duncan and Mokwa 2001). Figure 2-2 compares the different failure surfaces predicted by each of the three theories at δ/ϕ ratios of 0.2, 0.4, and 0.8 (Rankine theory assumes zero wall friction and matches curves from Coulomb

and Log-Spiral theories at $\delta = 0$). All curves shown assume 0 cohesion, and $\phi=30^\circ$. Table 2-1 shows the K_p values as calculated by each of the three methods for different δ/ϕ ratios.

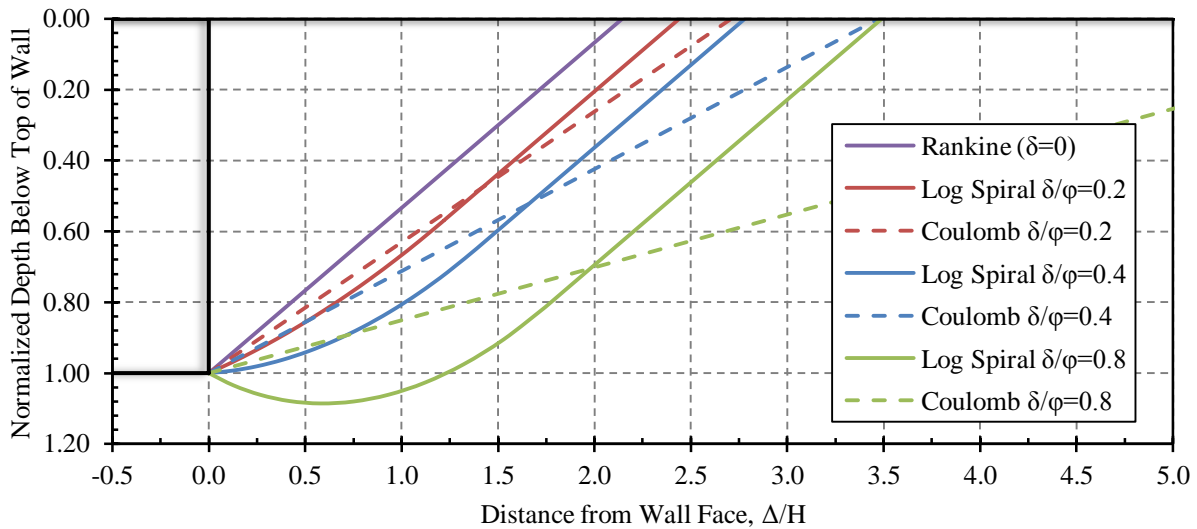


Figure 2-2: Normalized failure surface geometries predicted by Rankine, Coulomb, and Log Spiral theories

Table 2-1: K_p Values as Calculated by Rankine, Coulomb, and Log Spiral Theories

	$\delta/\phi=0$	$\delta/\phi=0.2$	$\delta/\phi=0.4$	$\delta/\phi=0.9$
Rankine	4.60	N/A	N/A	N/A
Coulomb	4.60	6.35	9.36	30.36
Log Spiral	4.60	6.21	8.35	14.63

There are three common methods used to compute passive force using the Log Spiral method. The first, and most common, is to use table or charts of passive earth pressure coefficients that are based on various properties of *cohesionless* soil [can be found in Caquot and Kerisel (1948)]. This method, however, does not account for cohesion and cannot account for complex soil geometries. The second, and most robust method, requires the use of the graphical

solution described by Terzaghi (1943) and Terzaghi et al. (1996) which can account for cohesion and complex geometries, though this procedure requires considerable time and effort to perform. The third option is numerical analysis and though the currently available numerical methods do account for cohesion and a uniform surcharge, they do not allow for non-level backfill (Duncan and Mokwa 2001).

The Log Spiral method makes the following assumptions, in addition to other less significant assumptions that won't be listed or discussed (see Figure 2-3 for failure geometry):

1. The failure surface consists of a curved portion that can be represented with reasonable accuracy by either the arc of a circle or a portion of a logarithmic spiral, and a linear portion. However, the mathematical properties of the spiral are such that there is no break between the curved and linear portion of the failure surface; therefore the log spiral is more commonly used.
2. The failure zone can be broken into two distinct regions, namely a Prandtl zone and a Rankine zone. The Prandtl zone is bounded by the wall and a line descending from the top of the wall down to intersect the rising failure surface. This line descends at an angle of $45^\circ - \phi/2$ from the horizontal. The Rankine zone is bounded by this same line and a second line ascending up to the ground surface from the aforementioned intersection at an angle of $45^\circ - \phi/2$ to the horizontal.
3. The component of passive force due to the weight of the soil mass and the friction due to the weight acts $1/3$ of the way up the wall.
4. The component of the passive force due to cohesion and adhesion acts at the vertical midpoint of the wall.

parameters (Duncan and Mokwa 2001). This section will briefly outline the effect that these parameters have on the development of passive earth pressures.

2.1.3.1 Structure Movement

All of the passive earth pressure theories presented in Sections 2.1.1 and 2.1.2 calculate the ultimate passive force independently of structure movement. In order to identify the force-deflection relationship numerous researchers have performed lab tests, field tests, and numerical analyses and found that the relationship between developed passive force and lateral structure movement is—not surprisingly—nonlinear (Shamsabadi et al. 2007). Furthermore, many of the currently available models that approximate the relationship between passive force and lateral deflection are based upon observations first made by Kondner (1963), and expanded upon by Duncan and Chang (1970), that this relationship can be approximated with a hyperbola. These hyperbolic relationships will be described in Section 2.1.4.

Though many researchers agree that the passive force versus backwall deflection relationship can be approximated with a hyperbola, the backwall deflection necessary to develop this peak passive force is still debated. Table 2-2 shows estimates of wall deflection (Δ_{\max}) normalized against wall height (H) as stated by three different sources. However, Cole and Rollins (2006) performed several large-scale field tests and found that for dense sand the peak passive force occurred at normalized deflections between 3% and 5.2% of the backwall height.

Table 2-2: Movement Necessary for Development of Maximum Passive Earth Pressures [Reproduced from Cole and Rollins (2006)]

<i>Type of Backfill</i>	<i>Values of Δ_{max}/H</i>		
	<i>Sowers and Sowers (1961)</i>	<i>Canadian Geotechnical Society (1992)</i>	<i>Clough and Duncan (1991)</i>
Dense Sand	0.002	0.02	0.01
Medium-dense sand	-	-	0.02
Loose sand	0.006	0.06	0.04
Stiff cohesive	-	0.02	-
Compacted silt	-	0.04	-
Compacted lean clay	-	-	0.02
Compacted fat clay	-	-	0.05

In addition to lateral movement, vertical movement of the structure can also play a significant role in the development of the peak passive force. As a wall is pushed laterally into a soil mass, the resulting movement of the soil up the inclined failure surface exerts an upward shear force on the face of the structure that is proportional to the friction between the soil and structure, and the force acting normal to the backwall. If the structure is sufficiently massive and/or vertically restrained enough to resist this upward shear force, the opposite downward force applied to the soil by the structure will increase the normal force acting at the internal soil failure surface thereby increasing the developed passive force. However, if the structure weight is small relative to the upward shear force applied by the soil wedge then the developed passive force will not be as high as the previously described condition.

2.1.3.2 Structure Shape

All of the methods for calculating the peak passive force described in Sections 2.1.1 and 2.1.2 assume plane-strain soil boundary conditions. However, the boundary conditions at the ends of a structure are obviously significantly different than the conditions at the center of the

structure, and only in situations where a structure is very long with respect to height can earth pressures be accurately calculated if plane-strain boundary conditions are assumed. Ovesen (1964) conducted a number of tests in which he found that for short structures the measured passive pressures were significantly higher than those predicted by the conventional passive pressure theories. Using the data obtained by Ovesen (1964), Brinch Hansen (1966) developed a method by which the 3D effects of short structures could be accounted for (Duncan and Mokwa 2001). Brinch Hansen (1966) developed a method for approximating the ultimate capacity, T_{ult} , of embedded anchor blocks. This method accounts for 3D end effects by multiplying the width of the structure by a width correction factor, M , in order to get the effective structure width. The peak passive force is then calculated according Equation (2-4).

$$T_{ult} = M K_p - K_a p'_0 b h \quad (2-4)$$

where

$$M = 1 + K_p - K_a^{0.67} \frac{1.1E4}{1 + 5 \frac{b}{h}} + \frac{0.4 K_p - K_a E^3 B^2}{1 + 0.05 \frac{b}{h}}$$

K_p = coefficient of passive earth pressure

K_a = coefficient of active earth pressure

p'_0 = effective overburden pressure at midheight of anchor block

$$B = 1 - \frac{b^2}{s}$$

$$E = 1 - \frac{h}{z + h}$$

b = width of anchor block

s = center to center spacing of anchor blocks for only 1 block $s = 0$

h = height of anchor block

z = depth of top of anchor block below ground surface

2.1.3.3 Soil Structure Interaction Parameters

Within the context of this thesis, the only soil-structure interaction parameters of interest are the interface friction angle, δ , and adhesion between the soil and the concrete wall; therefore, only those two parameters will be discussed.

Section 2.1.3.1 stated that the relative vertical movement of the structure plays a particularly significant role in the mobilization of the soil-wall interface friction force and in instances where the soil moves vertically relative to the wall face the resulting passive force will be inclined at an angle δ to the normal to the wall face. A more accurate statement would be to

say that the passive force acts at an angle δ_{mob} to the normal to the wall face where δ_{mob} is a percentage less than or equal to 100% of the total interface friction angle. When the backwall is vertically restrained δ_{mob} will be very close to δ_{max} , but for instances where the backwall is not vertically restrained or is light relative to the upward shear force, δ_{mob} will approach 0° . For instances where the soil moves up relative to the wall, δ_{mob} will be measured upward from the normal to the wall face; whereas if the soil moves down relative to the wall face, δ_{mob} will be measured downward from the normal to the wall face. Past researchers have found that relative shear displacement values of 0.10 inches to 0.25 inches (2.5 mm to 6 mm) between the soil and wall can mobilize all of the interface friction (Duncan and Mokwa 2001). Of course, peak interface friction values vary from material to material, and in order to determine this value for different materials Potyondy (1961) performed numerous direct shear tests between soil and various construction materials and recommended the minimum design values of δ/ϕ shown in Table 2-3.

Table 2-3: Proposed Minimum Coefficients of Skin Friction between Soil and Construction Material [reproduced from Potyondy (1961)]

Construction Material		<i>Dense Sand</i>		<i>Cohesive granular soil</i>
		<i>Dry</i> δ/ϕ	<i>Sat.</i> δ/ϕ	δ/ϕ
Steel	Smooth: Polished	0.54	0.64	0.40
	Rough: Rusted	0.76	0.80	0.65
Wood	Parallel to grain	0.76	0.85	0.80
	At right angles to grain	0.88	0.89	0.90
Concrete	Smooth: Made in iron form	0.76	0.80	0.84
	Grained: Made in wood form	0.88	0.88	0.90
	Rough: Made in adjusted ground	0.98	0.90	0.95

Adhesion between the backfill and backwall interface can also increase the shear forces extant at the soil-structure interface, thereby increasing or decreasing the ultimate passive force depending on the relative vertical movement of the soil with respect to the wall. For this study, backwall adhesion is assumed to be equal to soil cohesion.

2.1.4 Methods for Determining the Passive Force-Deflection Relationship

As mentioned in Section 2.1.3.1, structure movement plays a very significant role in the development of the peak passive force; and the relationship between structure movement and the developed passive force can be approximated with good accuracy using a hyperbola of the form shown in Equation (2-5). The failure ratio, R_f , shown below, represents the ratio between the hypothesized failure stress and the hyperbolic asymptote (Shamsabadi et al. 2007). Shamsabadi et al. (2007) suggest that R_f should be between 0.94 to 0.98 if soil capacity data is available, but if no capacity data is available R_f should be taken as 0.97. However, Duncan and Mokwa (2001) recommend R_f values ranging from 0.75 to 0.95, and for their research they used an R_f value of 0.85. The discrepancies between these two models suggest the use of varying assumptions with respect to the application of the failure ratio, R_f .

$$\sigma_1 - \sigma_3 \text{ }_i = \frac{\varepsilon_i}{\frac{1}{E_0} + \frac{R_f \varepsilon_i}{\sigma_1 - \sigma_3 \text{ }_f}} \quad (2-5)$$

where

$\sigma_1 - \sigma_3 \text{ }_i$ = intermediate deviatoric stress

$\sigma_1 - \sigma_3 \text{ }_f$ = deviatoric stress at failure

ε_i = intermediate strain level

E_0 = initial tangent modulus of the stress-strain curve

$$R_f = \frac{\sigma_1 - \sigma_3 \text{ }_f}{\sigma_1 - \sigma_3 \text{ }_{ult}} = \text{failure ratio}$$

With the exception of the method for calculating passive force as presented by Shamsabadi et al. (2007) and some soil stress-strain relationships many of the methods for approximating the passive force-deflection curve operate on the macro-, rather than the micro-scale. As such, the equation for passive force with respect to wall displacement takes the form shown in Equation (2-6).

$$P = \frac{y}{\frac{1}{K_{max}} + R_f \frac{y}{P_{ult}}} \quad (2-6)$$

where

P = passive resistance

P_{ult} = ultimate passive resistance as calculated by the log-spiral method

y = wall deflection

K_{max} = initial slope of the load-deflection curve

$$R_f = \frac{P_{ult}}{\text{hyperbolic asymptote}} \text{ (dimensionless)}$$

Duncan and Mokwa (2001) recommend that the elastic solution for horizontal displacements of a uniformly loaded vertical rectangular area in an elastic half space, as outlined by Douglas and Davis (1964), be used to determine K_{max} (assuming Young's modulus, E , and Poisson's ratio, ν). Duncan and Mokwa (2001) note that because the elastic solution is used to calculate the initial slope of the load-deflection plot, the initial tangent modulus of the stress-strain curve should be used for the calculations (see Table 2-4 for suggested initial tangent moduli values).

Table 2-4: E_i Values for Soils at Shallow Depths (2-5 ft) for Sands and Gravels [reproduced from Duncan et al. (1980)]

<i>Density</i>	D_r	N_{60}	<i>Normally Loaded</i>	<i>Preloaded or Compacted</i>
Loose	40%	3	$E_i = 200 - 400$ ksf	$E_i = 400 - 800$ ksf
Medium	60%	7	$E_i = 300 - 500$ ksf	$E_i = 500 - 1000$ ksf
Dense	80%	15	$E_i = 400 - 600$ ksf	$E_i = 600 - 1200$ ksf

Both Equation (2-5) and (2-6) produce a stress-strain or load-displacement curve similar to the one shown in Figure 2-4. Once the failure strain or displacement (ϵ_f or y_f , respectively) is reached, stress or load, respectively, is assumed to remain constant for higher strains or displacements.

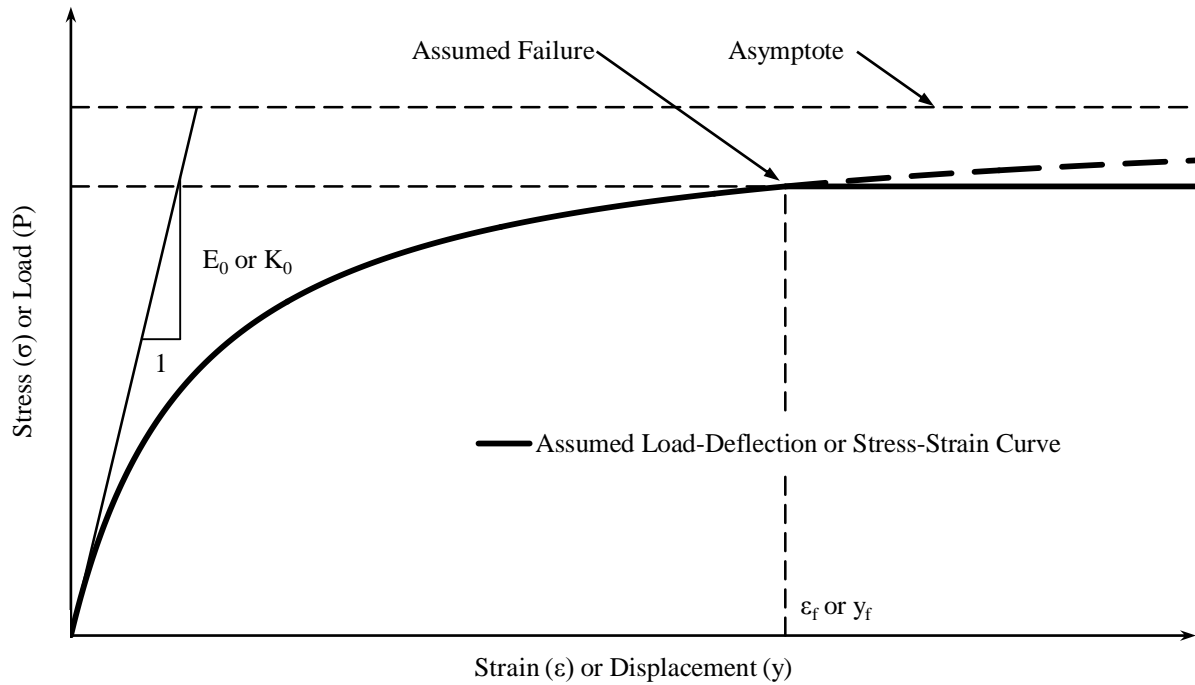


Figure 2-4: Shape of typical stress-strain or load-displacement curve

2.2 Passive Force-Displacement Tests for Non-Skewed Abutment Walls

As previously noted, numerous researchers have performed laboratory and field tests in an effort to determine the passive force-deflection relationship for a longitudinally displaced pile cap or abutment backwall. This section of the paper will describe and summarize the results of Maroney (1995), Duncan and Mokwa (2001), Rollins and Sparks (2002), Rollins and Cole (2006), and Lemnitzer et al. (2009).

2.2.1 Duncan and Mokwa (2001)

These authors performed two passive pressure load tests, one in a stiff sandy silt, and the other in a well-graded gravel, and compared the resulting passive force versus deflection curves to the curves obtained using their method for calculating the passive force versus deflection

relationship, also described in the same paper. They found that their method agreed reasonably well with the measured results (this method was briefly described in Section 2.1.4). Furthermore, they also found that the most accurate method for predicting the ultimate passive pressure was the Log Spiral method corrected for 3D effects using the Ovesen-Brinch Hansen correction factor.

2.2.2 Rollins and Sparks (2002)

Rollins and Sparks performed a full-scale lateral load test on a 3x3 pile group with a 4.0-ft (1.22-m) high by 9.0-ft (2.74-m) square pile cap installed in saturated low-plasticity silts and clays. Compacted sandy gravel backfill was placed on one side of the pile cap and the cap was pushed into this backfill. Their results showed that the Log Spiral method proved to be the best method for predicting the ultimate passive resistance and the Coulomb method significantly overestimated the measured passive resistance due to the high interface friction angle. Longitudinal deflection necessary to mobilize the ultimate passive force was found to be 6% of the wall height. Though this value is slightly higher than most of the values reported in literature, Rollins and Sparks suggest that the soft clay layer underlying the pile cap may have increased the lateral displacement necessary to develop the ultimate passive force. This assumption is consistent with AASHTO design code recommendations (2011).

2.2.3 Rollins and Cole (2006)

Rollins and Cole performed a series of static and cyclic load tests on a full-scale 4x3 pile group with a 3.67 ft (1.12 m) high by 17.0 ft (5.18 m) wide by 10.0 ft (3.05 m) long pile cap installed in cohesive soils. Backfill materials consisted of clean sand, silty sand, fine gravel, and course gravel with measured friction angles of 39°, 27°, 34°, and 40°, respectively. Their test

results indicated that the Log Spiral method can be used with reasonable accuracy to predict the length of the failure surface beyond the pile cap face. Furthermore, the authors found that when sand and gravel backfill materials were used peak passive force was developed between 3.0 and 5.2% of the wall height which is consistent with findings from other large-scale tests.

2.2.4 Lemnitzer et al. (2009)

Lemnitzer et al. performed a full-scale lateral load test on a simulated bridge abutment designed to be representative of typical California bridge design practices. Backfill materials consisted of well-graded sand with silt (SW-SM) according to the Unified Soil Classification System. Triaxial tests of the backfill materials showed that the soil friction angle, ϕ , was between 39 and 40°, and soil cohesion between 300 psf (14 kPa) and 500 psf (24 kPa). Soil unit weight was 126 pcf (2.02 g/cm³). Their test setup allowed for the measurement of both horizontal and vertical passive resistance. They found that the maximum passive pressure developed at a wall deflection equal to 3% of the wall height. Using the horizontal and vertical components of the resulting passive force, the authors found that the mobilized wall friction angle was approximately 0.35 ϕ . However, mechanical errors that occurred during testing likely significantly reduced the reliability of test results. That being said, backfill secant stiffness at 50% of the ultimate load was found to be 50 kip/in per foot of wall width (290 kN/cm per meter of wall width), and is in good agreement with the values reported by Shamsabadi et al. (2007). The most effective method for calculating the ultimate passive force proved to be the Log Spiral-Modified Hyperbolic model proposed by Shamsabadi et al. (2005) and Shamsabadi et al. (2007).

2.3 Movements and Forces for Skewed Bridges

Considering the previously described theories for predicting the ultimate passive force and the passive force versus lateral deflection relationship, this section will describe the forces that develop when a bridge abutment is pushed laterally into the backfill, either due to seismic forces or thermal expansion.

As outlined by Burke Jr. (1994), and shown in Figure 2-5, the interaction of forces at the interface between the bridge abutment backwall and soil backfill may be expressed in terms of the total longitudinal force, P_L , and its components normal to, and transverse to the abutment. The normal force is resisted by the passive force, P_p [see Equation (2-7)]; and the transverse, or shear force, P_T [see Equation (2-8)], is resisted by the shear resistance, P_R [see Equation (2-9)]. To prevent instability of the bridge caused by sliding of the abutment against the soil backfill the inequality shown in Equation (2-10) must be satisfied. Additionally, rotation of the entire bridge can occur if the inequality in Equation (2-11) is not satisfied.

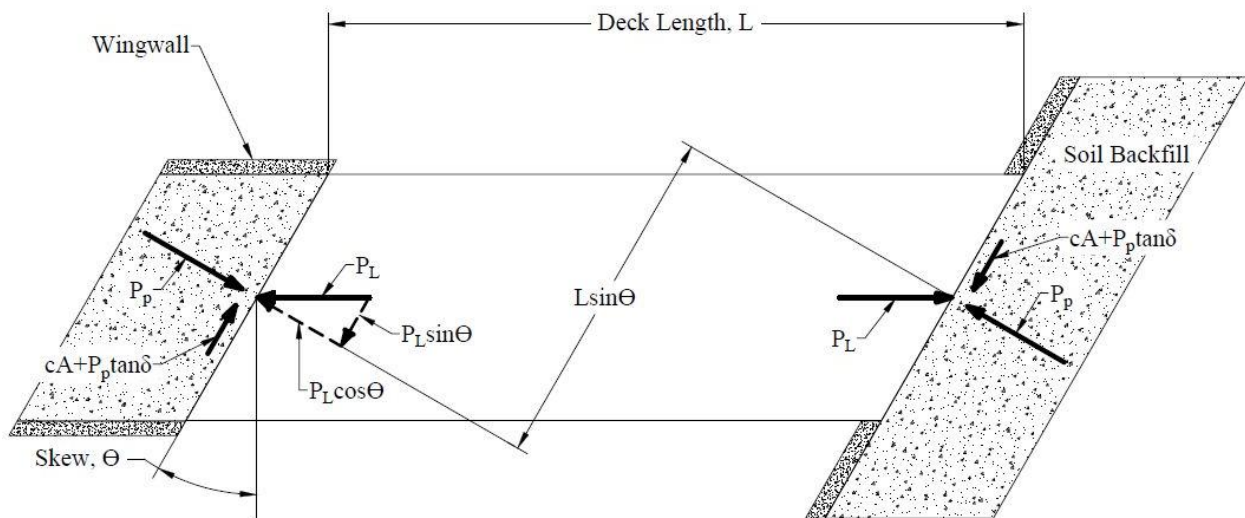


Figure 2-5: Resolution of longitudinal force exerted by bridge abutment onto soil backfill into components normal to, and transverse to abutment backwall [adapted from Burke Jr. (1994)]

As can be seen from Figure 2-5, the longitudinal force applied to the soil by the bridge abutment is resisted by the resultant passive force and the interface friction. As such, for instances where the bridge skew and longitudinal forces are sufficiently high, the developed interface friction may not provide adequate rotational restraint and the force couple applied by the transverse component of the longitudinal force will cause the bridge to rotate about a vertical axis. The resultant passive force (P_p), transverse shear force (P_T), transverse shear resistance (P_R), factor of safety against rotation about a vertical axis (FS_R), and factor of safety against the abutment sliding along the soil-abutment interface (FS_T) can all be expressed in terms of the applied longitudinal force (P_L), bridge skew angle (θ), soil cohesion (c), backwall area (A), and interface friction angle (δ) as shown in Equations (2-7) through (2-11), respectively.

$$P_p = P_L \cos \theta \quad (2-7)$$

$$P_T = P_L \sin(\theta) \quad (2-8)$$

$$P_R = cA + P_p \tan(\delta) \quad (2-9)$$

$$\frac{cA + P_p \tan \delta \quad L \cos \theta}{P_p L \sin \theta} = FS_R \quad (2-10)$$

$$\frac{cA + P_p \tan \delta}{P_L \sin \theta} = FS_T \quad (2-11)$$

where

θ = skew angle of backwall

c = soil cohesion

A = backwall area

δ = angle of friction between backfill soil and abutment wall

F_s = factor of safety

L = length of bridge

These equations are only valid if the bridge remains stable; however, if the bridge rotates, the distribution of forces on the abutment backwall will change, rendering these equations inaccurate. Based on Equation (2-10), Burke Jr. (1994) noted that if cohesion is ignored the potential for bridge rotation is independent of passive force and bridge length such that at a typical design interface friction angle of 22° the factor of safety against rotation decreases to below 1.5 if bridge skew exceeds 15°. However, this distribution of forces described by Burke does not account for the lateral restraint applied to an abutment by the foundation system.

In addition to the forces described above, which only deal with the longitudinal movement of the bridge deck, additional rotational forces can be induced on the bridge structure

when the bridge moves transversely and impacts the abutment. However, this force-deflection relationship for the bridge abutment is not discussed herein.

2.4 Behavior/Performance of Skew Walls

With the recent exception of some research conducted by Rollins and Jessee (2012), no physical testing has been performed with the intent of determining the passive force versus backwall deflection relationship for skewed bridge abutments. However, data obtained from instrumented bridges, as well as results from some finite element models created by Shamsabadi et al. (2006) have shown that skewed bridges do not perform as well as non-skewed bridges when subjected to thermal expansion or seismic loading. This section will discuss the lab results obtained by Rollins and Jessee (2012), available numerical results, and finally results obtained by researchers who instrumented skewed bridges.

2.4.1 Rollins and Jessee (2012) – Lab Results

Rollins and Jessee (2012) conducted a number of laboratory tests to determine the passive force versus backwall deflection curve for bridge abutments at skew angles of 0°, 15°, 30°, and 45°. They used a backwall 4 feet (1.22 m) wide and 2 feet (0.61 m) high. Backfill consisted of a poorly graded washed concrete sand (SP classification according to the Unified Soil Classification System, and ASTM C33) with a C_u of 3.7, and a C_c of 0.7 compacted to a relative compaction 96% of the modified proctor maximum (ASTM D1557 and AASHTO T180). Using the data obtained from their load deflection tests Rollins and Jessee (2012) proposed the correction factor R_{skew} , given by Equation (2-12) which describes the relationship between the peak passive force for a skewed abutment (P_{P-skew}) and the peak passive force for a non-skewed abutment ($P_{P-no skew}$) as a function of skew angle, θ .

$$R_{skew} = \frac{P_{p-skew}}{P_{p-no skew}} = 8.0 * 10^{-5} \theta^2 - 0.018\theta + 1.0 \quad (2-12)$$

Their proposed relationship predicts an approximate reduction in the peak passive force for a bridge abutment on a 30° skew with respect to a 0° skew bridge of 50%.

These authors also found that the peak passive force was obtained at longitudinal deflections between 2% and 3% of the backwall height, which is consistent with values reported in literature and shows that skew angle does not have a significant effect on the displacement at which peak passive force is obtained.

2.4.2 Shamsabadi et al. (2006) – 3D Numerical Modeling Results

Shamsabadi et al. (2006) created a number of 3D finite element models using Plaxis 3D Tunnel (Brinkgreve 2006) and compared the passive force deflection curves for bridge abutments at skew angles of 0°, 30°, 45°, and 60°. Their models were based on a 74.80 ft (22.8 m) wide by 5.5 ft (1.68 m) high abutment backwall. The high width to height ratio (13.6) enabled the authors to assume plane-strain conditions for their models. Input model soil parameters were obtained by calibrating their models to the test results obtained by Rollins and Cole (2006) which used a silty-sand typical of the materials used for structural backfill in California. The soil parameters used in the authors' Plaxis models are summarized in Table 2-5.

Table 2-5: Shamsabadi et al. (2006) Soil Finite Element parameters

<i>Soil Type</i>	γ <i>kN/m³ (lbf/ft³)</i>	ϕ	χ <i>kN/m² (lbf/ft²)</i>	δ	E_{50}^{ref} <i>MN/m² (kip/ft²)</i>	E_{ur}^{ref} <i>MN/m² (kip/ft²)</i>	ν
Silty Sand	18.8 (119.7)	34°	24 (52.2)	23°	100 (2,089)	200 (4,177)	0.35

When modeling the pressure distribution on the face of the abutment the authors assumed a pressure distribution on a 0° skew abutment offset at an angle equal to the skew angle where the pressure decreased linearly from a maximum at the obtuse corner of the bridge deck to zero at the acute corner of the bridge deck, as shown in Figure 2-6.

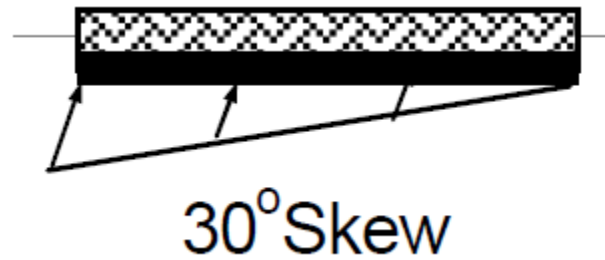


Figure 2-6: Pressure distribution

Using the aforementioned soil data and soil pressure distribution, the authors obtained the passive force-deflection curves for abutments skewed at 0° , 30° , 45° , and 60° shown in Figure 2-7.

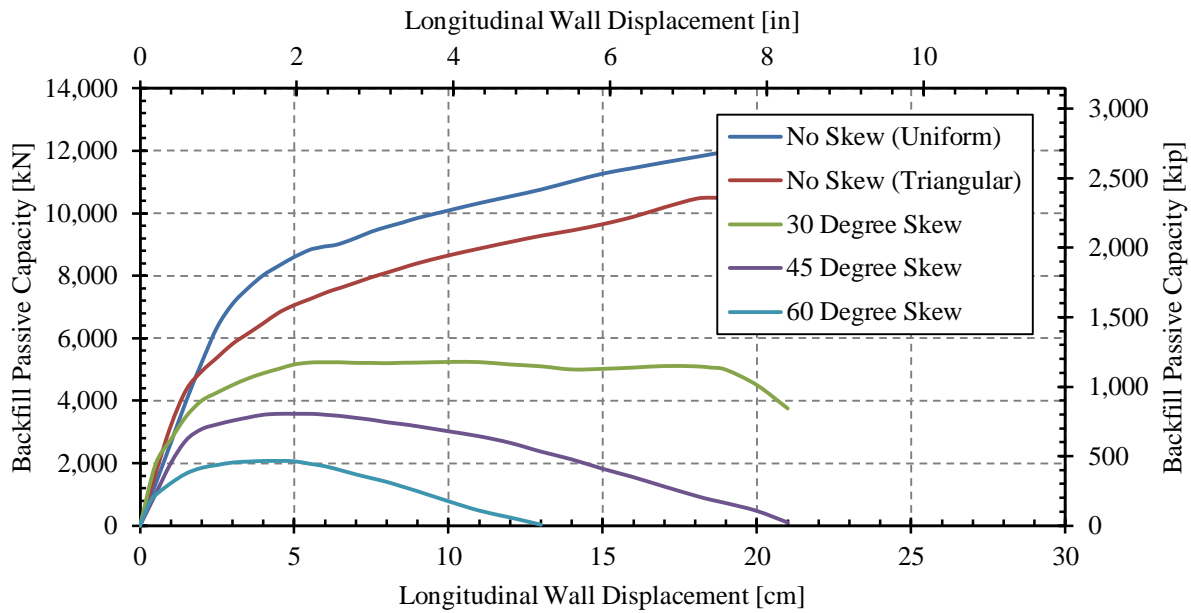


Figure 2-7: Passive force-deflection curves for bridge abutments at various skew angles (Shamsabadi et al. 2006)

These results clearly show that at high skew angles there is a very significant reduction in the developed peak and ultimate passive force, and in cases of extreme skew the passive capacity reduces to zero as a result of the disintegration of the failure wedge.

These authors also performed a global finite element model on a two-span box-girder bridge with nonlinear soil springs as shown in Figure 2-8. The results confirmed their initial assumption that the pressure distribution on the face of the abutment was indeed nonlinear with the highest pressures occurring at the obtuse corner of the bridge deck. They also found that the bridge underwent significant and permanent rotation about a vertical axis.

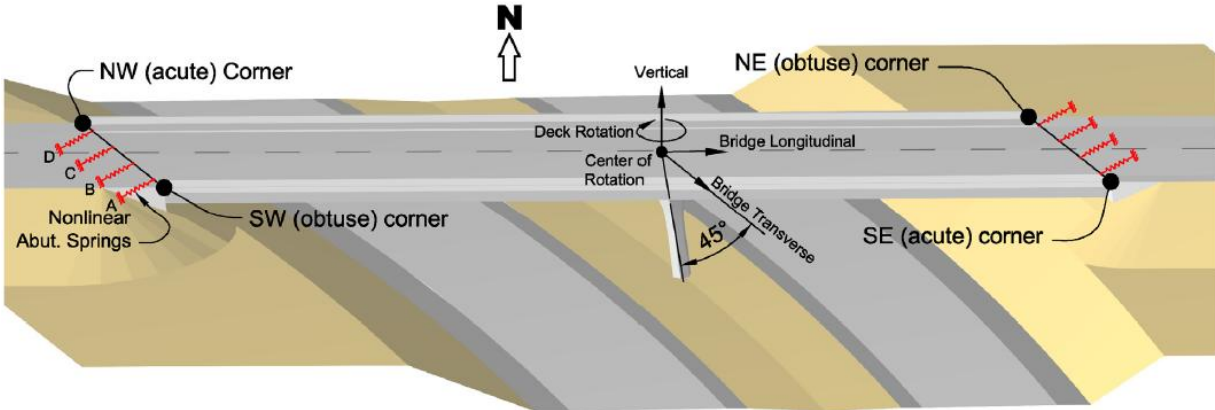


Figure 2-8: Bridge model used to determine global behavior of bridge subjected to earthquake loading (Shamsabadi et al. 2006)

2.4.3 Sandford and Elgaaly (1993) – Skew Effects on Backfill

Pressures at Frame Bridge Abutments

These authors conducted a study in which a new 20° skewed integral abutment bridge in Maine was instrumented with a number of pressure cells and temperature indicators and monitored four times a day for 33 months. The data showed that at peak thermal expansion soil pressures were significantly higher than active pressures on the upper part of the abutment wall, and that skew effects caused considerably higher pressures to develop on the obtuse corner of the bridge abutment in comparison to the acute corner. Also, higher pressures developed on the upper third of the wall than on the lower part of the wall as the bottom of the wall was laterally restrained by the foundation.

The authors also found that the difference in measured soil pressures between the acute and obtuse corners of the bridge abutment reduced as time went on which suggested that greater permanent soil deformation occurred at the obtuse corner of the bridge abutment than at the acute corner.

Finally, the authors recommended that for design the horizontal pressure distribution be approximated such that pressures decrease from Rankine passive pressures on the obtuse corner to Rankine active pressures on the acute corner of the abutment, as shown in Figure 2-9.

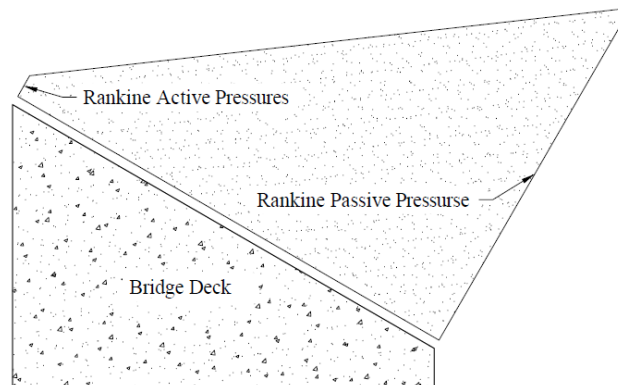


Figure 2-9: Proposed design soil pressure envelope (Sandford and Elgaaly 1993)

2.4.4 Steinberg et al. (2004) – Forces in Wingwalls of Skewed Semi-Integral Bridges

This article describes the results obtained from monitoring two bridges in Ohio, one 87 ft (26.5 m) long with a skew angle of 65° , and the other a four-span bridge 314 ft (95.7 m) long with a skew angle of 25° . The study was conducted to determine the effect that skew angle has on the transfer of rotational forces due to thermal expansion from the bridge abutment to the wingwalls. Additionally, these authors included results that were obtained from SAP 2000 finite element models created for bridges 100 ft, 200 ft, and 400 ft (30.5 m, 61 m, and 122 m) long with skew angles of 25° , 35° , and 45° . These models were designed to further investigate the effect that skew angle has on the aforementioned forces. They concluded that the rotational forces exerted on wingwalls by the rotating of the bridge deck are significant and should be accounted for in design.

2.4.5 Elnashai et al. (2010a) – The Maule (Chile) Earthquake of February 27, 2010

This report created by Elnashai et al. (2010b) details, among other things, the failure modes of the nearly 50 highway bridges that were damaged by the 8.8 magnitude 2010 Maule, Chile earthquake. The authors concluded that the most common bridge damage occurred due to unseating of the bridge from its foundations or excessive displacement of the bridge structure. This was particularly common for skewed bridges which tended to rotate about a vertical axis and fail the shear keys. In particular, the newer bridges tended to fare worse than the older bridges as recent code modifications allowed for smaller shear keys and transverse restraint systems in an effort to simplify construction and design requirements.

2.5 Current Design Methods

Current bridge design methods [e.g. Caltrans (2010) and AASHTO (2011)] do not take bridge skew angle into account when calculating the passive forces acting on an abutment wall. This section will briefly describe the procedures these design specifications use for calculating the passive force versus backwall deflection relationship for non-skewed bridge abutments. Both the Caltrans and AASHTO bridge design methods assume that passive force increases linearly with respect to displacement until failure and thereafter remains constant.

2.5.1 Caltrans Seismic Bridge Design

Caltrans seismic bridge design requires that the passive force versus backwall displacement relationship for a bridge abutment be modeled either as a bilinear relationship, or by using the closed form hyperbolic force-deformation relationship described by Shamsabadi (2007).

The bilinear force-deflection relationship described by Caltrans utilizes an initial abutment stiffness that accounts for both the expansion gaps and a realistic backfill response. For backfills meeting the Caltrans Standard Specification requirements (2010), the initial stiffness, K_i , shown in Equation (2-13) can be used. Soils meeting these requirements typically have the following properties:

- Standard penetration, upper layer [0 to 10 ft (0 to 3 m)] $N = 20$ (Granular soils)
- Standard penetration, lower layer [10 to 30 ft (3 to 9 m)] $N = 30$ (Granular soils)
- Undrained shear strength, $s_u > 1500\text{psf}$ 72KPa (Cohesive soils)
- Shear wave velocity, $v_s > 600\text{ft/sec}$ (180 m/sec)
- Low potential for liquefaction, lateral spreading, or scour

NOTE: N = The uncorrected blow count from the Standard Penetration Test (SPT)

However, if the backfill material does not meet the aforementioned specifications, the initial backfill stiffness shown in Equation (2-14) must be used.

$$K_i \approx \frac{50\text{kip/in}}{\text{ft}} \text{ or } \frac{28.70\text{kN/mm}}{\text{m}} \quad (2-13)$$

$$K_i \approx \frac{25\text{kip/in}}{\text{ft}} \text{ or } \frac{14.35\text{kN/mm}}{\text{m}} \quad (2-14)$$

As these stiffness values were obtained from large-scale testing performed at UC Davis (Maroney 1995) and UCLA (Stewart et al. 2007) and idealized by Shamsabadi et al. (2007), they should be adjusted to account for the height, h , of the actual bridge abutment as shown in Equation (2-15)

$$K_{\text{abut}} = \begin{matrix} K_i \times w \times \frac{h}{5.5 \text{ ft}} & \text{US units} \\ K_i \times w \times \frac{h}{1.7 \text{ m}} & \text{SI units} \end{matrix} \quad (2-15)$$

where w is the projected width of the abutment. The maximum passive force, P_p , is then calculated according to Equation (2-16)

$$P_p = \begin{matrix} A_e \times 5.0 \text{ ksf} \times \frac{h}{5.5\text{ft}} & (\text{ft, kip}) \\ A_e \times 239 \text{ kPa} \times \frac{h}{1.7\text{m}} & (\text{m, kN}) \end{matrix} \quad (2-16)$$

where the ultimate passive force of 5.0 ksf (239 kPa) is based on the ultimate static force developed in the full-scale abutment tests (Maroney 1995; Stewart et al. 2007), h is the height of the bridge abutment, and the projected area of the abutment, A_e , is calculated according to Equation (2-17).

$$A_e = h \times w_{\text{eff}} \quad (2-17)$$

where

$$w_{\text{eff}} = \text{effective abutment width corrected for skew}$$

Using the initial abutment stiffness as calculated according to Equation (2-15) and the maximum passive pressure as calculated according to Equation (2-16), the complete bilinear relationship can be obtained such that the initial part of the curve increases from zero up to the peak passive force and thereafter remains constant with respect to deflection

2.5.2 AASHTO LRFD Bridge Design Specifications

The AASHTO LRFD Bridge Design Specifications (2011) require the passive pressure coefficient, K_p , be obtained either from Figure 3.11.5.4-1 or Figure 3.5.11.4-2 in section 3.11.5.4 of the 2011 specifications; or by using the graphical method for calculating passive pressures described by Terzaghi et al. (1996) where the soil/structure interface friction angle, δ , cannot be greater than half of the soil friction angle, ϕ . Using this K_p value the total passive pressure acting on an abutment wall can be calculated according to Equation (2-18).

$$P_p = \frac{1}{2} K_p \gamma_s H w_1 + 2c \overline{K_p} w_2 H \cos \delta \quad (2-18)$$

where

P_p = horizontal component of the passive lateral earth pressure ksf

γ_s = unit weight of soil (kcf)

w_1 = effective width of failure wedge [see Ovesen (1964)]

w_2 = abutment width (ft)

c = soil cohesion (ksf)

H = abutment height (ft)

K_p = coefficient of passive earth pressure calculated as specified above

Regarding the force-deflection relationship, the AASHTO specifications note that, on average, the abutment wall must be displaced 5% of the wall height into the soil mass in order to mobilize all of the passive resistance. For dense soils somewhat less lateral movement is required to mobilize all of the passive resistance, and for loose soils somewhat more movement is required. Though these displacement estimates are not consistent with those values reported by Clough and Duncan (1991), they are fairly consistent with more recently reported values as discussed in Section 2.1.3.1.

As mentioned above, passive pressures are assumed to develop linearly with respect to wall displacement until failure, and thereafter remain constant.

2.6 Nasr and Rollins (2010)

Nasr and Rollins (2010) created a 2D finite element model using the computer software PLAXIS 2D Version-8 (2004) with the intent of modeling plane-strain passive force-deflection behavior of limited width dense gravel backfills. The model was initially calibrated using

analytical results obtained from PYCAP (Mokwa and Duncan 2001) and ABUTMENT (Shamsabadi et al. 2007) and then compared against large-scale test data obtained by Rollins et al. (2010c) and Gerber et al. (2010). Model input parameters used by Nasr and Rollins (2010) are shown in Table 2-6. The authors found that model results were most sensitive to changes in the friction angle, cohesion, dilation angle, and the interface strength reduction factor as defined by Equation (2-19). Using these parameters, agreement between the field tests, analytical results, and numerical models was within 10% at the peak passive force.

$$R_{inter} = \frac{\tan\delta}{\tan\phi} \quad (2-19)$$

Table 2-6: Input Parameters for Hardening Soil Model as Used by Nasr and Rollins (2010)

<i>Parameter</i>	<i>Loose Sand</i>	<i>Dense Gravel</i>	<i>Unit</i>
Friction Angle, ϕ	27.7	42.0	Degrees
Cohesion, c_{ref}	0.5 (10.44)	1.9 (39.68)	kPa (lb/ft ²)
Dilation Angle, ψ	0	12	Degrees
Soil Unit Weight	17.3 (110.1)	22.1 (140.7)	kN/m ³ (lb/ft ³)
Secant Stiffness Modulus E_{50}^{ref}	15.8 (330)	81.4 (1,700)	MPa (kip/ft ²)
Reference Stress, P_{ref}	100 (2089)	100 (2089)	kPa (lb/ft ²)
Poisson's Ratio, ν_{ur}	0.2	0.2	—
Interface Friction Angle, δ	0.75 ϕ	0.75 ϕ	Degrees
Interface Strength Reduction Factor, R_{inter}	0.7	0.7	—

Figure 2-10 shows the developed finite element model and incremental strain contours for the homogeneous sand and gravel backfill model runs. The apparent failure surface that descends from the top of the backwall to intersect the rising failure surface is consistent with the shear surface anticipated by the Prandtl zone and Rankine zone that occur in the log spiral failure geometry (see Figure 2-3).

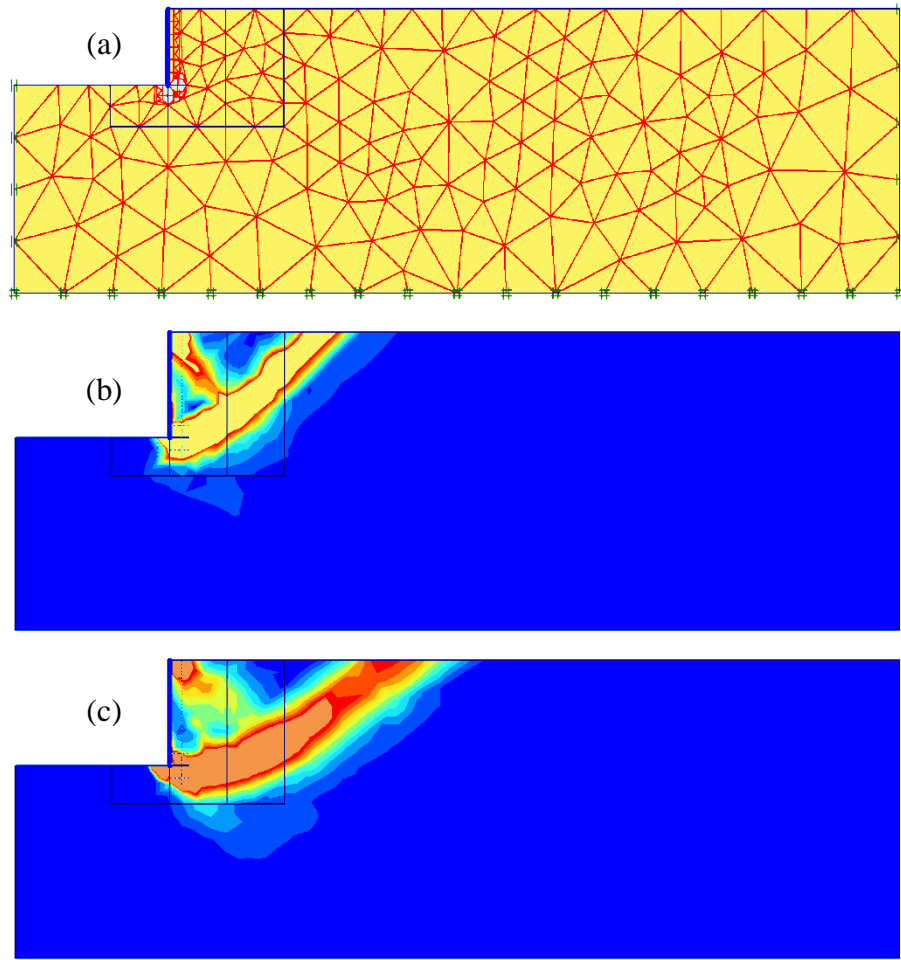


Figure 2-10: Observed shear planes obtained from (a) Plaxis 2D finite element models for (b) homogeneous sand backfill, and (c) homogeneous gravel backfill (Nasr and Rollins 2010)

3 FIELD TEST LAYOUT AND PROPERTIES

This chapter will describe the test location, geotechnical characteristics of the test site, layout of the test setup, and geotechnical properties of the backfill material.

3.1 Site Location

This series of tests was conducted at a test site located approximately 900 ft (275 m) north of the control tower at the Salt Lake International Airport. An aerial photo of the site and adjacent airport control tower is shown in Figure 3-1. The site has been used for several series of tests, including those conducted by Johnson (2003), Rollins et al. (2005a; 2005b), Taylor (2006), and Rollins et al. (2010a; 2010b). Conditions at the site are ideal for conducting long-term field tests for several reasons, including the absence of overhead obstructions, site security, available soil stratigraphic information, and the ease of maneuvering heavy equipment in and around the test site.



Figure 3-1: Aerial photograph of Salt Lake City airport control tower and test site (adapted from Google Earth)

3.2 Geotechnical Site Characterization

As much of the previously conducted tests focused on the capacity of piles or drilled shafts, significant information is available that describes the site's subsurface conditions. As no subsurface investigations were conducted for this series of tests, subsurface conditions as described herein have primarily been derived from those given by Christensen (2006) and Rollins et al. (2010b).

Extensive subsurface investigation has been conducted at or around this test site over the past 17 years, beginning with the construction of the air traffic control tower in 1995. Tests conducted primarily for research purposes were first performed by Peterson (1996). Overall, in-situ tests, as well as undisturbed and disturbed sampling, were conducted in order to fully investigate soil conditions at the test site; however, the majority of the available information will not be discussed herein as this material has little relevance to this study.

In summary, the original soil profile consisted of 5 feet (1.5 m) of dense compacted sandy gravel fill overlaying alternating layers of silty clay and sand to a depth of 100 feet (30 m). In 2002 the upper 5 feet (1.5 m) of compacted fill was removed to enable the testing of pile groups in the native sandy clay. In 2004, another 3 feet (0.91 m) of clay was removed from the test site and backfilled with washed concrete sand. An idealized soil profile constructed using the aforementioned data is presented below in Figure 3-2.

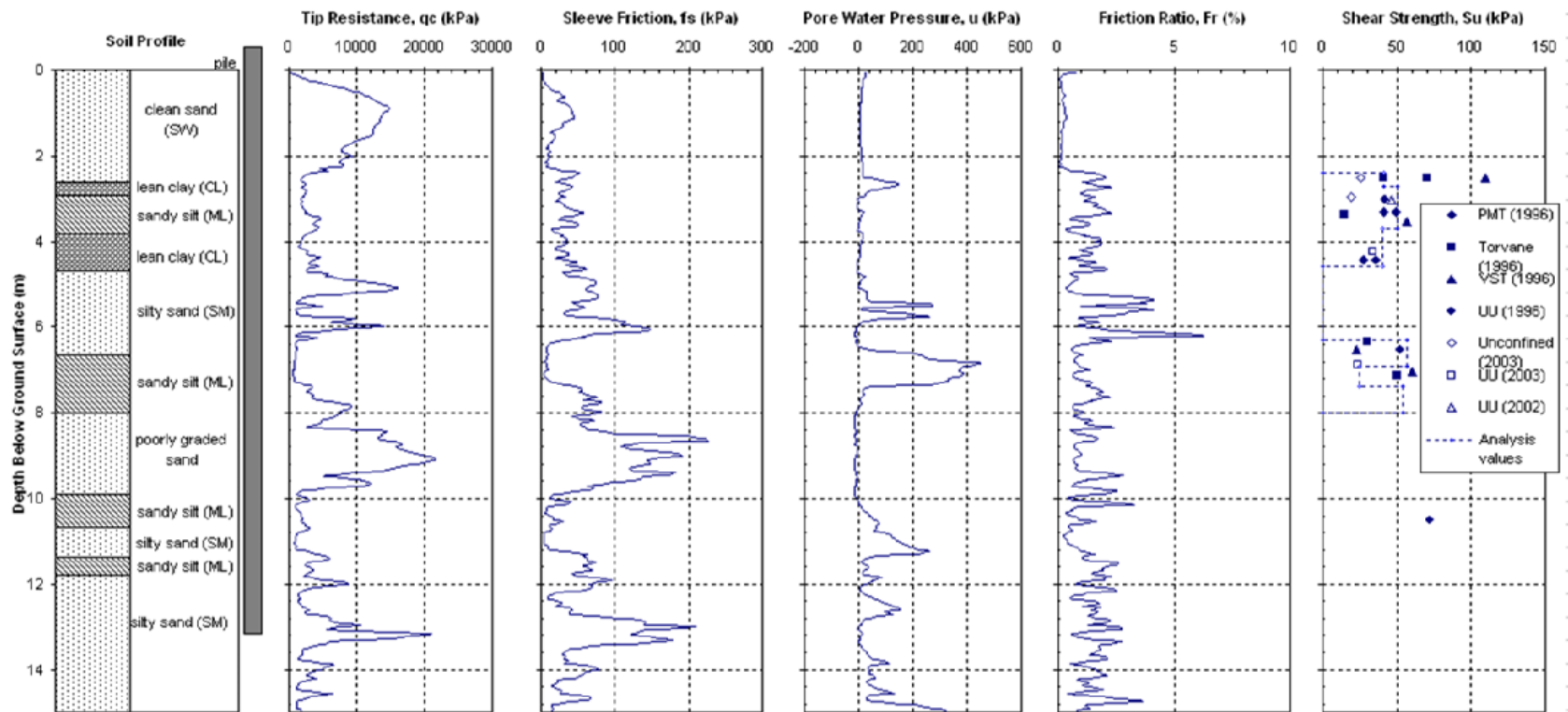


Figure 3-2: Idealized soil profile constructed from laboratory and in-situ test data (Christensen 2006)

3.3 Test Layout

The layout for each of the tests conducted for this study consisted of four primary components: the reaction foundation, the pile cap with attached 15° and 30° wedges (when applicable), the loading apparatus, and the backfill zone. With the exception of the 15° and 30° wedges, all other components of the test setup had been designed and used for previous tests. Plan and elevation views of the complete test setup are shown in Figure 3-3.

3.3.1 Reaction Foundation

The reaction foundation consisted of two 4-foot (1.22-m) diameter drilled shafts spaced 12 feet (3.66 m) apart center to center on an east-west line with a sheet-pile wall spanning the north side of the drilled shafts. Additionally, two large steel I-beams with the strong axis oriented in the north-south direction spanned both the north and south sides of the drilled-shaft/sheet-pile wall group to provide the foundation with additional lateral rigidity.

The east and west drilled shafts extend to depths of 70.0 feet (21.35 m) and 55.2 feet (16.82 m), respectively. Four-foot square by two-foot thick caps were installed at the top of each drilled shaft. Reinforcement of the top 35 feet (10.67 m) of each drilled shaft consisted of 18 #11 (#36) vertical bars with a #5 (#16) bar spiral at a pitch of 3 inches (75 mm). Below 35 feet, vertical reinforcement consisted of 9 #11 (#36) vertical bars with spiral reinforcement at a pitch of 12 inches (300 mm). Concrete cover throughout the length of the shaft was approximately 4.75 inches (120 mm). The compressive strength of the concrete in the drilled shafts was 6,000 psi (41 MPa).

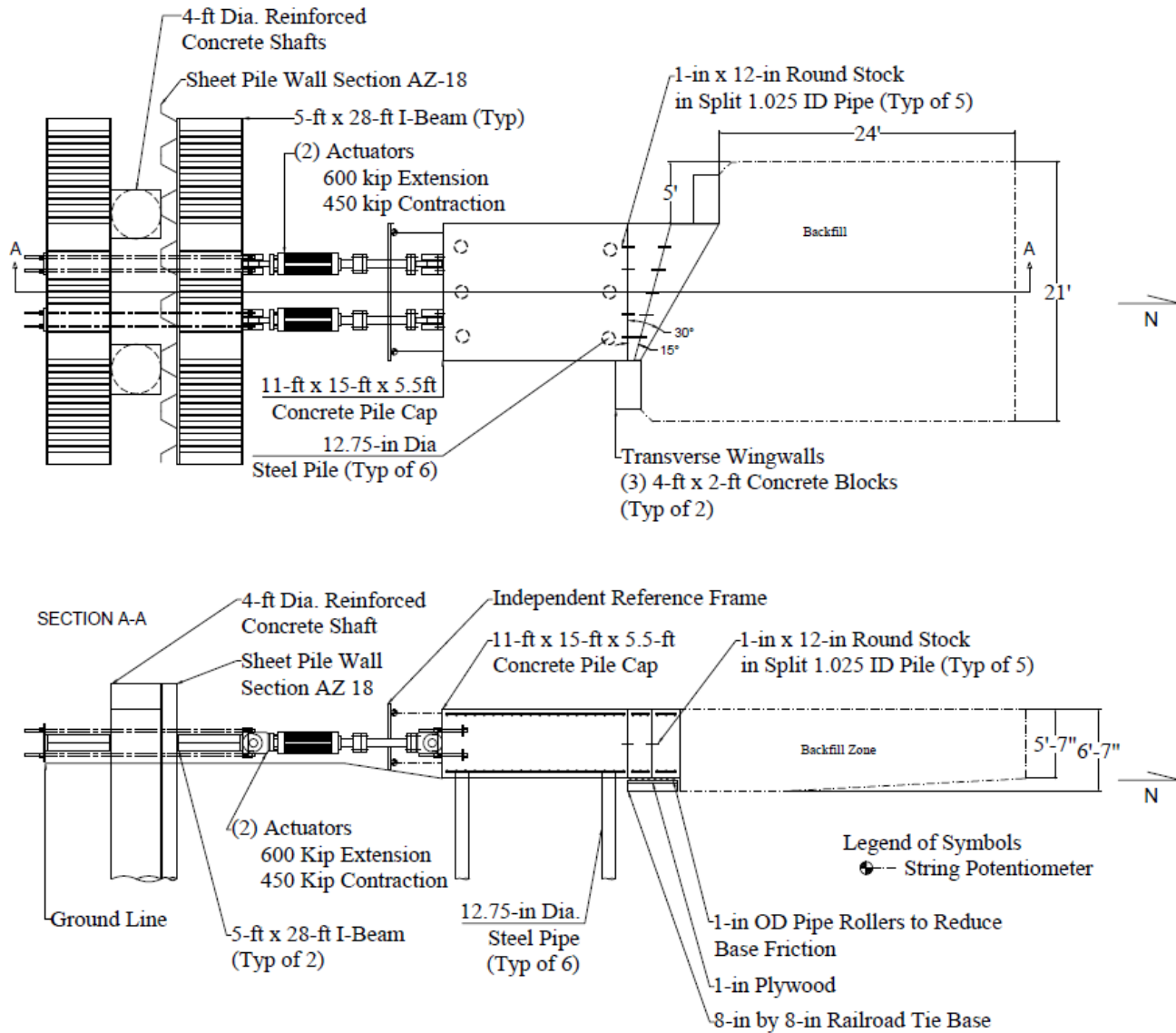


Figure 3-3: Plan view and cross section of general testing layout

AZ-18 sheet piling made of ASTM A-572 Grade 50 steel was used for the sheet pile wall on the north side of the two drilled shafts. A vibratory hammer was used to install the wall as close to the drilled shafts as possible and to depths ranging from 33.6 feet to 35.6 feet (10.24 m to 10.85 m) below the excavated ground surface.

The steel I-beams were 28 feet (8.53 m) long and 64 inches (1,626 mm) high by 16 inches (406 mm) wide. Numerous additional stiffeners were installed between the flanges to prevent the beams from buckling during loading.

Eight 1.75 inch (44 mm) DYWIDAGs with minimal post-tensioning were used to tie the I-beams, drilled shafts, and sheet pile wall together. Only minimal post-tensioning of the DYWIDAGs was used as the reaction foundation was not subjected to dynamic loading for any of the tests conducted summer 2012.

3.3.2 Pile Cap and Piles

The south edge of the pile cap was located 16.4 feet (5.0 m) to the north of the reaction foundation and was constructed on a six-pile group with two rows of three piles oriented in the east-west direction. Prior to the construction of the pile cap, the pile group contained nine piles but the middle row was removed to reduce the lateral resistance of the pile group itself so that the actuators would have adequate capacity to fail the pile cap with backfill in place. Each pile had an outside diameter of 12.75 inches (324 mm), a wall thickness of 0.75 inches (9.5 mm) and was constructed with ASTM A252 Grade 3 steel pipe with an average yield strength of 57 ksi (393 MPa). All piles were driven closed-ended to a depth of approximately 43 feet (13.1 m) below the ground surface.

The top of each of the piles was embedded a minimum of 6 inches (150 mm) into the base of the pile cap. To provide sufficient connection strength between the piles and the pile cap,

18-foot long (5.49 m) rebar cages consisting of 6 #8 (#25) vertical bars and a #4 (#13) spiral at a pitch of 6 inches (152 mm) were lowered 13.2 feet (4.02 m) into the steel piles with the remaining 4.8 feet (1.47 m) extending into the pile cap and supporting the upper horizontal reinforcing grid. The upper and lower reinforcing mats consisted of #5 (#19) bars in the longitudinal and transverse direction at 8 inches (203 mm) on center. Concrete with a compressive strength of 6,000 psi (41.37 MPa) was used to fill the steel piles and to construct the pile cap. The final pile cap dimensions were 15 feet (4.57 m) long (north-south direction), 11 feet (3.35 m) wide, and 5.72 feet (1.74 m) high. Inclinometer and shape array tubes were also cast into the center pile of each row. Finally, eight DYWIDAGs with plate anchors were cast horizontally into the pile cap to provide a connection point for the loading apparatus. The placement of these DYWIDAGS positioned the two actuators on the vertical center of the pile cap but offset 2.25 feet (0.69 m) on either side of the horizontal centerline.

3.3.3 Concrete Wedges

To test the effect that bridge skew angle has on the passive force versus backwall deflection relationship, concrete wedges were constructed and attached to the face of the existing pile cap. Following the completion of the 0° skew test, both the 15° and 30° wedges were cast simultaneously against the face of the pile cap using 6,000 psi (41.4 MPa), high early strength concrete. The casting process is shown in Figure 3-4. A double layer of ¾-in (1.90 cm) plywood was used as the interface between the 15° and 30° wedges. Also, a double layer of plastic sheeting was placed between the 15° wedge and the face of the pile cap to prevent bonding of the new concrete to the old concrete. After the concrete reached sufficient compressive strength the 30° tests were conducted, then the outer 30° wedge was removed prior to performing the 15° tests.



Figure 3-4: Simultaneous casting of 15° and 30° wedges

Reinforcement requirements for each wedge were calculated assuming worst-case load assumptions: namely a vertical and horizontal triangular pressure distribution with the maximum force occurring at the bottom acute corner of the wedge. For the 30° wedge, top and bottom reinforcing grids consisted of #5 (#16) bars placed approximately 11 inches (280 mm) on center oriented perpendicular and parallel to the face of the wedge. Horizontal reinforcement was placed in the face of the wedge to prevent tensile cracking at the acute corner of the wedge. Bar sizes were selected according to the calculated tensile forces in the face of the wedge given the aforementioned pressure distribution. Three #6 (#19) bars were located at 3, 9, and 15 inches (76, 230, and 380 mm) from the bottom, acute corner of the wedge and extended 56 inches (1.42 m) along the face of the wedge towards the obtuse corner. At 21, 27, 37, 49, and 63 inches (0.53,

0.69, 0.94, 1.24, and 1.60 m) up from the base #5 (#16) bars extending 50 inches (1.27 m) along the face towards the obtuse corner were used. In all cases #5 (#16) bars were used to span the remaining distance to the obtuse corner. Limited horizontal reinforcement was used on the backside of the wedge. Vertical reinforcement on the front and back of the wedge was limited to what was necessary to hold the horizontal elements in place. Figure 3-5 shows a 3D Google Sketchup[®] model of the 30° wedge reinforcement.

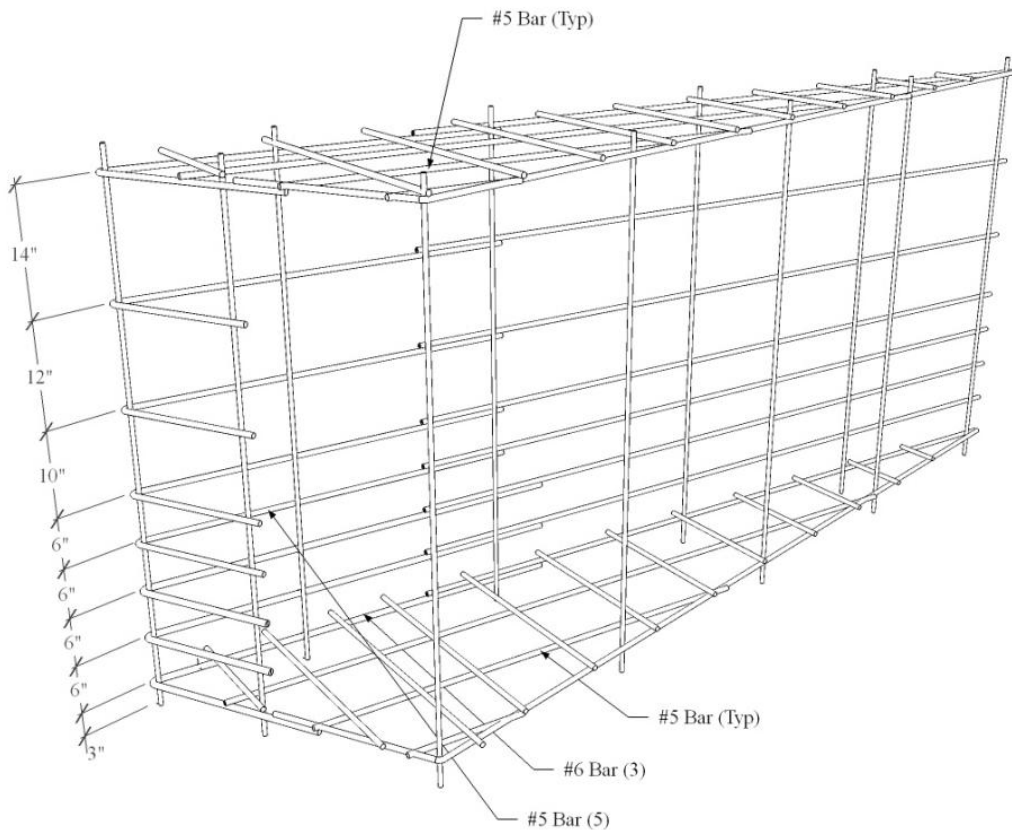


Figure 3-5: Reinforcing grid for 30° wedge

For the 15° degree wedge, top and bottom reinforcing grids consisted of #4 (#13) bars oriented perpendicular and parallel to the face of the wedge spaced at approximately 11 inches (280 mm) on center. All other reinforcing bars for the 15° wedge consisted of #4 (#13) bar.

Horizontal reinforcement was located in the wedge face 3, 15, 27, 45, and 64 inches (0.08, 0.38, 0.69, 1.14, and 1.63 m) up from the base of the wedge. Limited horizontal reinforcing was used on the back face of the wedge. Vertical reinforcement in the front and back face was limited to what was necessary to hold the horizontal elements in place. Figure 3-6 shows a 3D Google Sketchup® model of the 15° wedge reinforcement grid.

Though not shown in either Figure 3-5 or Figure 3-6, reinforcing cages were placed in the ends of each wedge to insure that the embedded concrete anchors used to tie the wedges to each other and to the pile cap did not pull or spall out.

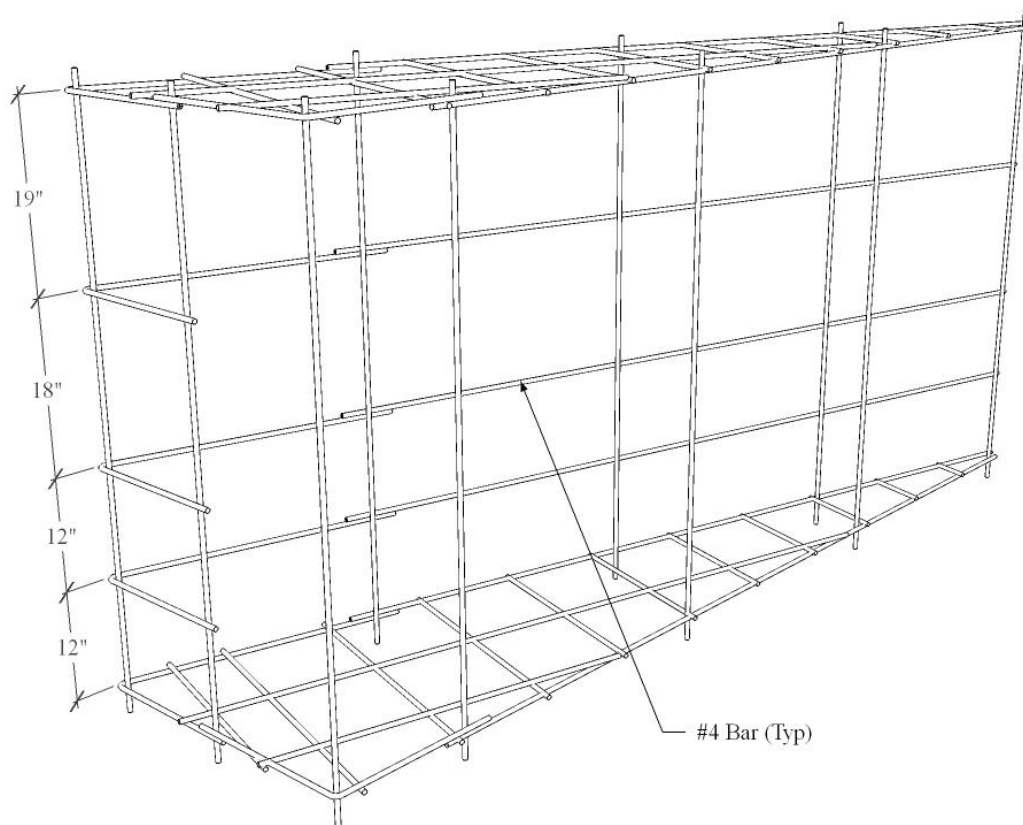


Figure 3-6: Reinforcing grid for 15° wedge

To eliminate the potential for lateral or vertical movement of either wedge relative to each other or the existing pile cap, interface connections were designed that provided transverse and vertical rigidity but also provided means for removing the 30° wedge without damaging the 15° wedge. For this purpose a slip connection was used in which a 1-inch (25.40 mm) diameter by 11-inch (279 mm) long piece of round stock was inserted into 1.0625-inch (26.987 mm) inside-diameter pipe as shown in Figure 3-7(a). The slip connections come apart as shown in Figure 3-7(b). Approximately 6 inches of this pipe was tied into the rebar cage at the wedge-wedge interface in each wedge and the round stock was placed in the pile as shown in Figure 3-7(a) prior to casting the concrete. A similar setup was used for the connection between the existing pile cap and the 15° wedge except the round stock was placed in 1-1/8-inch (28.58 mm) diameter, 6-inch (152 mm) deep holes that were drilled into the face of the existing pile cap. Five such connection elements were used for both the pile cap-wedge interface and the wedge-wedge interface. To ensure that the entire connection acted as a unit, 3/4-in (1.90 cm) angle iron stiffeners were welded to the ends of the pipes as shown in Figure 3-7(c).

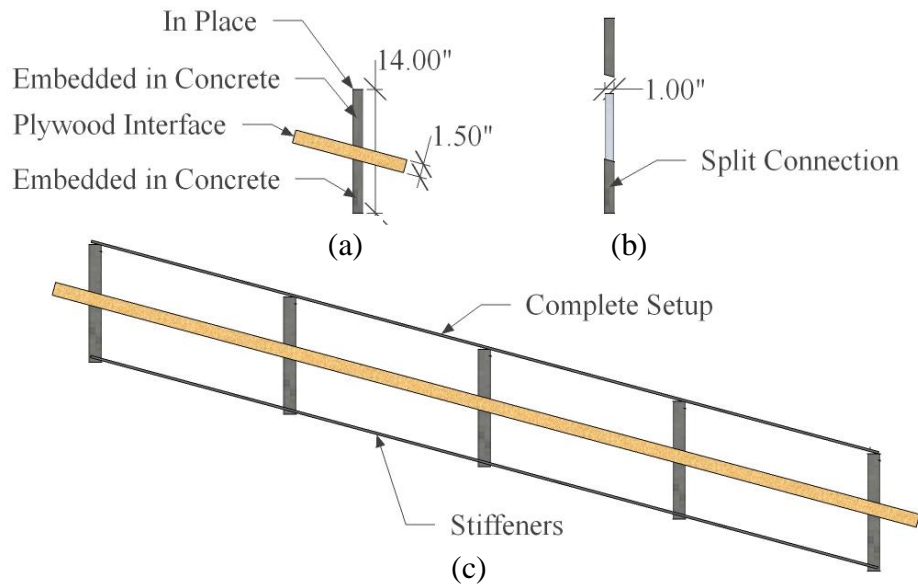


Figure 3-7: Interface connection details (a) plan view detail of individual split connection, (b) plan view detail with bars extended out of pipe, and (c) plan view layout of the entire assembly with five split bar connections across width of pile cap

In addition to the internal connection elements, side and top plates, as shown in Figure 3-8, were used to further ensure that the wedges did not move relative to the existing pile cap. These connections were also designed to support the entire weight of the concrete wedges, even in the absence of a base support.

1-inch (25.4 mm) diameter, 8-inch (203 mm) long cast-in-place anchors were used for all newly poured concrete; otherwise 1-inch (25.4 mm) diameter, 7-inch (177.8 mm) long wedge-type anchors (Redheads[®]) were set in place within holes drilled into the in-place concrete.

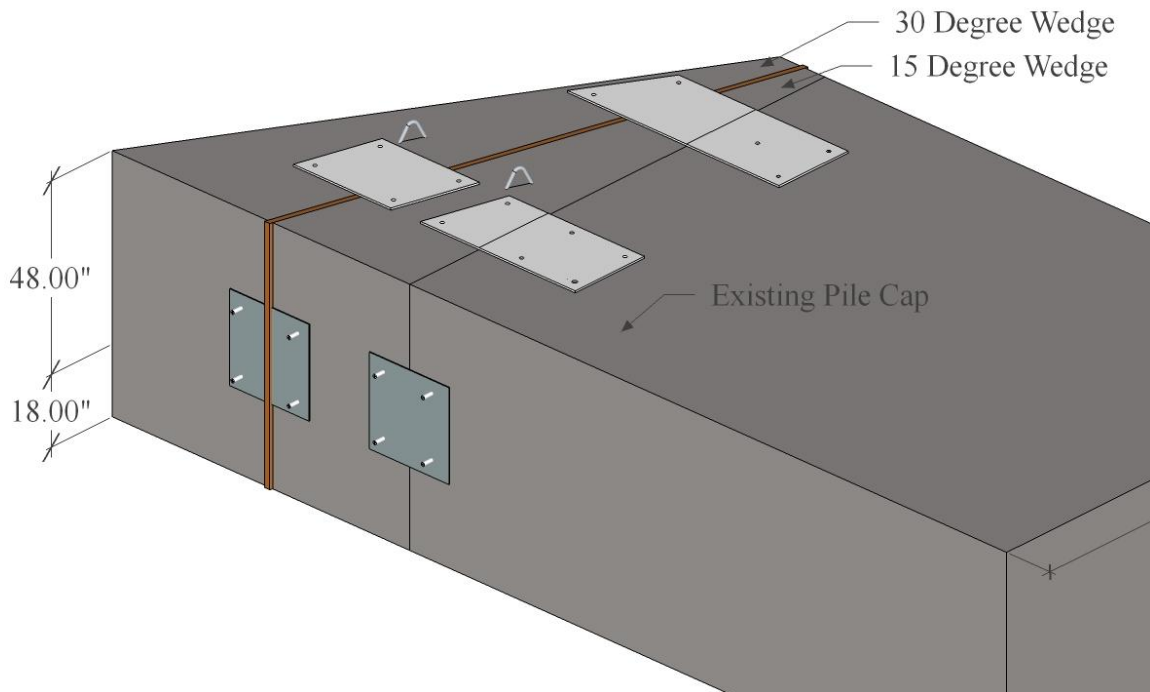


Figure 3-8: Plate interface connections

To prevent excessive friction from developing at the base of the attached wedges, the concrete forms were placed on rollers as illustrated in Figure 3-9, Figure 3-10, and Figure 3-11. After completing the 30° tests and removing the 30° wedge several of the rollers were cut with a cutting torch so that they did not stick out into the backfill at the base of the 15° wedge. Finally, to insure that too much sand did not become embedded under the wedges filter fabric was taped around the base and sides of the wedges before backfill placement. In addition to minimizing base friction, this setup also reduced the potential for forward rotation of the pile cap.



Figure 3-9: Railroad tie foundation for 15° and 30° wedges



Figure 3-10: Railroad tie foundation for 15° and 30° wedges with sand compacted between ties



Figure 3-11: Roller foundation for 15° and 30° wedges

As mentioned previously, the 0° skew tests were conducted first, followed by the 30° skew tests, then the 15° skew tests. Following the completion of the 30° skew tests, the outer wedge was removed by first removing the appropriate side and top plates, and then lifting the 30° wedge with a crane until no weight was supported by the foundation. The backhoe was then used to provide sufficient longitudinal force to split the wedges apart as shown in Figure 3-12. The interface connection worked exactly as designed.



Figure 3-12: Removal of 30° wedge

3.3.4 Loading Apparatus

Loading of the pile cap was accomplished through the use of two MTS actuators placed between the reaction foundation and the pile cap in a north-south direction as shown in Figure 3-13. The DYWIDAGs tying the reaction foundation together (see Section 3.3.1) were used as the connection point between the actuators and the reaction system. The eight DYWIDAGs embedded in the pile cap, in addition to the two 4-foot (1.22 m) long extensions shown in Figure 3-13, provided the connection point between the actuators and the pile cap.

Each actuator had an extensional capacity of 600 kips (2.67 MN) (north direction) and a contractive capacity of 450 kips (2.00 MN) (south direction). Swivel heads were located at both the north and south ends of the actuators to provide a zero-moment connection between the

actuators and pile cap. The actuators were installed level and were centered 2.75 feet (0.84 m) above the base of the pile cap.



Figure 3-13: MTS hydraulic actuators

3.3.5 Backfill Zone

The backfill zone was located on the north end of the pile cap and was approximately 24 feet (7.32 m) wide and 24 feet (7.32 m) long. The first 8 feet (2.44 m) of backfill to the north of the pile cap extended approximately 1 foot (0.30 to 0.61 m) below the base of the pile cap to allow a potential log-spiral failure surface to be fully contained in the backfill soil. Further out, the bottom of the backfill zone was approximately level with the bottom of the pile cap. To ensure proper compaction and to determine the soil unit weight and moisture content, two nuclear density measurements were taken for each lift.

As the natural ground water level was located approximately at the base of the pile cap two submersible pumps were installed on the east and west sides of the pile cap and were used to maintain the water level 1 to 2 feet (0.30 m to 0.60 m) below the base of the pile cap.

3.3.6 General Instrumentation and Measurements

3.3.6.1 Instruments for Monitoring Longitudinal Pile Cap Movement

In order to accurately determine pile cap displacement, an independent reference frame was established between the reaction foundation and the pile cap. Six string potentiometers (string pots) were attached to this reference frame. Four of the string pots were attached to the pile cap 3 inches and 51 inches (7.6 cm and 129.5 cm) from the top of the pile cap, and 3 inches and 129 inches (7.6 cm and 328 cm) from the west side of the pile cap, as shown in Figure 3-14. Displacement data obtained by these four string pots was considered to be the most accurate and as such all other data will be compared to the values recorded by these string pots. The two remaining string pots were attached to the large I-beam on the north side of the drilled shafts at positions that placed them in line with the approximate center of the drilled shafts and at the same level as the line of action of the actuators. These two string pots measured the north/south displacement of the reaction foundation during testing.

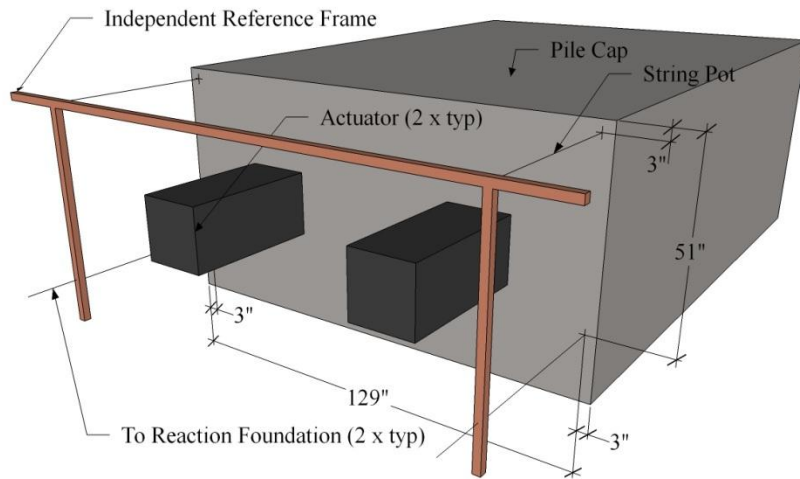


Figure 3-14: String potentiometer locations on south end of pile cap

3.3.6.2 Instruments for Monitoring Transverse Pile Cap Movement

For the 15° and 30° tests, Linear Variable Differential Transformers (LVDTs) and string pots were used to measure the transverse movement of the pile cap. LVDTs were located on the west side of the pile cap as shown in Figure 3-15 and Figure 3-16. These instruments were mounted to the vertical stakes shown in the figure such that the tip of the LVDT slid against a metal plate that had been attached to the side of the pile cap. However, as the sides of the pile cap may not have been exactly parallel with the direction of push the LVDTs likely measured transverse movement due more to the shape of the cap than to the actual movement of the cap. Furthermore, though the 4x4s in the figures were used to restrict transverse movement of the top of the stakes they did not prevent the bottom of the stakes from moving as the pile moved

through and displaced the surrounding materials. Thus, the data obtained by these LVDTs is considered less reliable. So though the LVDT data will be presented, the reader should keep in mind that these instruments can only be used to show a trend and do not necessarily show actual pile cap movement.



Figure 3-15: LVDTs for measuring transverse cap movement (north end)

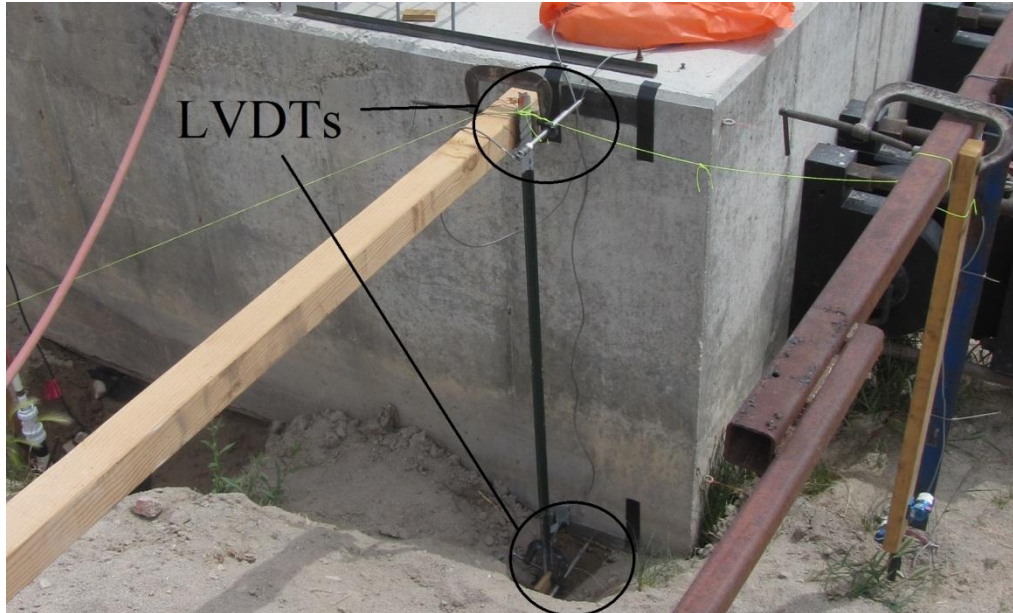


Figure 3-16: LVDTs for measuring transverse cap movement (south end)

3.3.6.3 Instruments for Monitoring Pile Movement

As mentioned in Section 3.3.2, inclinometer and shape array tubes were installed in the center pile in each pile row of the pile group. These tubes were installed to a depth of about 43 feet (13.1 m). The slotted inclinometer tubes had an outside diameter of 2.75 inches (70 mm) and an inside diameter of 2.32 in (60 mm).

Inclinometer readings were taken by lowering the instrument all the way to the bottom of the inclinometer tube and then raising the instrument in 2-foot (0.30-m) intervals and taking readings at each interval. In order to reduce instrument error, two passes were taken in each inclinometer tube with the instrument “pointed” north for the first reading, and south for the second. Reported displacement data was taken as the normalized averages of these two passes.

The two shape arrays (Danisch et al. 2005; Measurand Inc. 2009) were installed parallel with the inclinometer tubes on the north and south end of the pile cap to depths of 38.75 feet and 23.08 feet (11.81 m and 7.03 m), respectively. Measurand Geotechnical recommends that the shape array be installed such that the bottom end of the instrument is forced against the bottom of the shape array tube with 50 pounds (222 N) of force. As the south shape array was not long enough to reach the bottom of the pile cap, a sufficient quantity of electrician's tape was wrapped around the bottom end of the shape array in order to provide adequate side friction to resist the required downward force. However, the taped end of the shape array may have slipped over time thereby reducing the accuracy of the instrument.

The aforementioned installation technique and the fact that the south shape array was not long enough to reach the bottom of the pile (which was assumed to be stationary) resulted in some slight variation in the measured deflection in comparison to the north shape array. The assumption that the bottom of the piles did not translate is verified by the fact that the longitudinal deflection measured by the north shape array agreed quite well with the longitudinal deflection as measured by the string pots. To prevent pure translation of the shape array, the instrument must be long enough to reach a point outside the zone that will experience movement. This error in the south shape array data was corrected by shifting the entire data curve such that the displacement measured by the top viable node of the shape array lined up with the displacement at the top of the inclinometer tube.

A second possible explanation for the discrepancy in readings between the north and south shape arrays is that one of the nodes in the south shape array was not functioning and produced a discontinuity in the measured deflections as shown in Figure 3-17. This discrepancy was corrected in the raw x-y displacement data by adding half the differential displacement

between the node above and below the two offending nodes that recorded nearly identical displacement values.

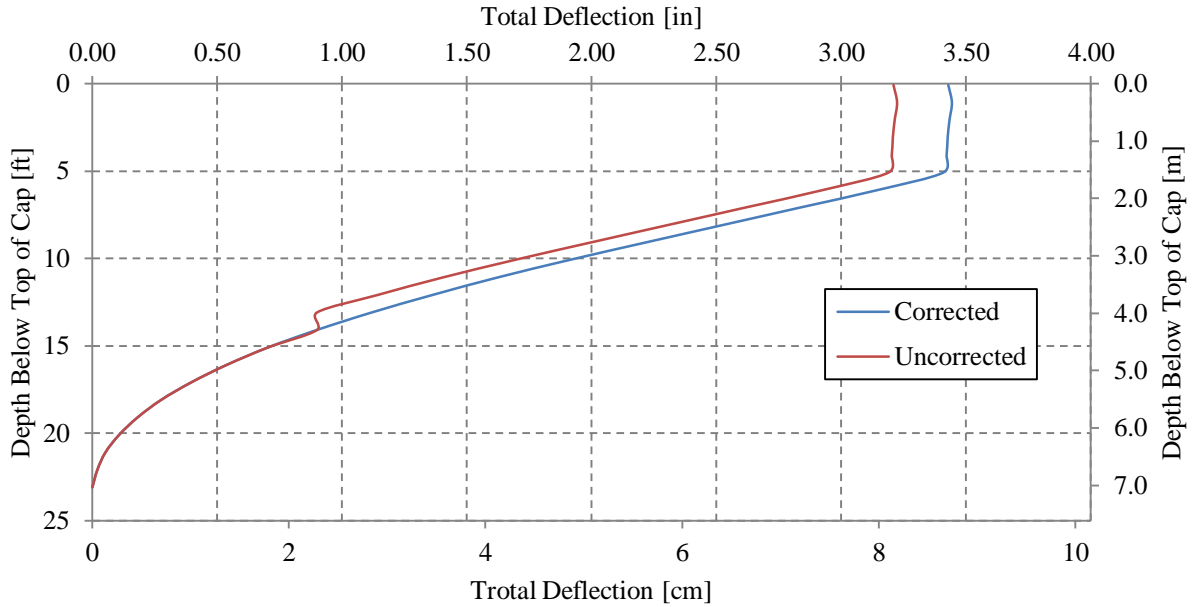


Figure 3-17: Corrected versus uncorrected south shape array readings (from final displacement increment of 0° test)

Shape arrays determine displacement by measuring the relative slope of instrument segments using accelerometers located 1 foot (0.30 m) apart at the ends of these segments. These accelerometers measure the tilt angle (θ_x and θ_y) of the individual segments in the x- and y-planes according to Equation (2-3) and Equation (2-3), respectively. This method of determining instrument tilt is known as “gravity-referenced” tilt and is very similar to the method conventional inclinometers use for determining instrument slope.

$$\theta_x = \sin^{-1} kv_x \quad (3-1)$$

$$\theta_y = \sin^{-1} kv_y \quad (3-2)$$

where

k = accelerometer constant

v_x = output voltage of accelerometer measuring movement in x-plane

v_y = output voltage of accelerometer measuring movement in y-plane

kv_x = acceleration relative to gravity in x-plane (range +1 to -1)

kv_y = acceleration relative to gravity in y-plane (range +1 to -1)

By using measured slope of the instrument in the x- and y- planes the azimuth of the shape array could be resolved by performing 3D joint-angle calculations using the joint construction (which allows bending but no twisting) as a constraint (Measurand Inc. 2011).

Relative displacement of the instrument was determined by comparing the initial and final slope of the instrument segments over the total length of the instrument and using basic trigonometry to calculate displacement of individual segments and then finding the total. For these calculations the bottom node was considered deeper than any expected lateral movement and was set as a zero movement reference point.

3.3.6.4 Instruments for Monitoring Backfill Movement and Strain

To measure backfill deformation, seven additional string pots were mounted to the top of the pile cap near the north end of the cap. For the 0° skew tests the seven string pots were located 10 inches (254 mm) from the north face of the cap while for the 15° and 30° skew tests, the string pots were located on the 15° degree wedge 10 inches (254 mm) to the north of the original

pile cap face. These string pots were attached to stakes in the backfill at the distances from the wedge face and backfill centerline shown in Table 3-1. Ideally, all of the string pots would have been installed along the backfill centerline; however this was not possible due to instrument width.

Table 3-1: String Potentiometer Distances from Wedge Face Measured Parallel to the Direction of Pile Cap Movement

<i>String Pot ID</i>	<i>0° Skew</i>		<i>String Pot ID</i>	<i>15° Skew</i>		<i>String Pot ID</i>	<i>30° Skew</i>	
	<i>Dist. from Face ft (m)</i>	<i>Dist. from Center ft (m)</i>		<i>Dist. from Face ft (m)</i>	<i>Dist. from Center ft (m)</i>		<i>Dist. from Face ft (m)</i>	<i>Dist. from Center ft (m)</i>
SP25	2.00 (0.61)	0.58 (0.18)	SP968	2.00 (0.61)	0	SP968	2.00 (0.61)	0
SP968	4.00 (1.22)	-0.25 (-0.08)	SP10	4.04 (1.23)	-0.58 (-0.18)	SP10	3.96 (1.21)	-0.58 (-0.18)
SP18	6.00 (1.83)	1.42 (0.43)	SP25	6.08 (1.85)	0.33 (0.10)	SP25	5.88 (1.79)	0.33 (0.10)
SP10	10.00 (3.05)	-1.08 (-0.33)	SP969	10.13 (3.09)	-0.92 (-0.28)	SP969	9.96 (3.04)	-0.92 (-0.28)
SP11	14.00 (4.27)	2.25 (0.69)	SP2	14.13 (4.31)	-1.58 (-0.48)	SP18	13.88 (4.23)	0.75 (0.22)
SP969	18.00 (5.49)	-1.75 (-0.53)	SP11	18.08 (5.51)	0.75 (0.23)	SP2	18.17 (5.54)	-1.58 (-0.48)
SP2	22.00 (6.71)	-2.50 (-0.76)	SP18	22.17 (6.76)	1.33 (0.41)	SP11	21.96 (6.69)	1.33 (0.41)

NOTE: Negative distances from center of pile cap indicates the string pot is located to west of backfill centerline

Using the backfill movement data obtained from the aforementioned string pots, the backfill compressive strain was calculated using Equation (3-3).

$$\varepsilon = \Delta L / L \tag{3-3}$$

where

ε = compressive strain

ΔL = change in distance between stringpots

L = original north – south distance between adjacent stakes

3.3.6.5 Methods for Monitoring Backfill Heave

For each test a 2 x 2 foot (0.61 x 0.61 m) grid was painted on the backfill surface for purposes of crack mapping and heave measurements. Gridlines were painted parallel to the direction of pile cap displacement and parallel to the backwall face. For the 15° and 30° skew tests, the grid lines parallel to the cap/wedge face were refined to 1-foot (0.30 m) intervals within 8 feet (2.44 m) of the cap/wedge face so that more precise heave data could be obtained. Prior to testing, a survey level was used to measure the relative elevation of each grid intersection point. Once the maximum longitudinal displacement of the pile cap had been achieved elevation measurements were again taken at the grid intersection points and the difference in elevation was used to create contour plots of the vertical displacement of the backfill. Additionally, surface cracks visible at test completion were marked with paint and their locations recorded. These cracks will be shown on the corresponding heave contour plots.

3.3.6.6 Mechanism Used to Determine the Location of the Internal Failure Surface

In order to determine the location of the internal failure surface a 2-inch (51 mm) diameter hand auger was used to core holes in the backfill at various locations to depths below the expected failure surface. These holes were then refilled and compacted with red-dyed soil. Following the final pile cap displacement, a trench was excavated adjacent to these holes and the offset in the sand columns identified the location of the failure plane as shown in Figure 3-18. For the 0° skew test, sand columns were located on the longitudinal centerline at 2, 4, 6, and 8 feet (0.61, 1.22, 1.83, and 2.44 m) from the backwall face. For the 15° test, two rows of soil cores were located at a transverse offset of 1.94 feet (0.59 m) from a line running perpendicular to the face of the wedge at distances of 2, 6, 9, 12, and 15 feet (0.61, 1.83, 2.74, 3.66, and 4.57 m) from the face of the wedge. For the 30° test, soil columns were located 2 feet (0.61 m) on

each side of the longitudinal center line at distances of 2, 6, 10, 14, and 18 feet (0.61, 1.83, 3.05, 4.27, and 5.49 m) from the backwall face.



Figure 3-18: Offset in red sand columns showing upper failure surface of the 0° test (inset more clearly shows column offset at test completion)

3.3.6.7 Instruments for Determining the Pressure Distribution on the 30° Wedge

Six “Fat Back” Pressure cells manufactured by Geokon were installed in the face of the 30° wedge in order to determine the backfill pressure against the wedge face relative to the horizontal position on the wedge face. The pressure plate configuration is shown in Figure 3-19 and Figure 3-20. The pressure plates were located approximately 22 inches (0.559 m) up from the base of the wedge, and 21.5 inches (0.546 m) center to center along a horizontal line, with the first plate 17.75 inches (0.451 m) in from the west edge. The three eastern pressure plates were “Geokon Model 3510-2-600” 600 kPA pressure plates, and the three west plates were “Geokon

Model 3510-2-1" 1 MPa pressure plates. These were hydraulic type pressure plates with a semiconductor pressure transducer that was capable of measuring dynamic pressures.

To ensure that the plates were flush with the concrete surface, each plate was mounted to the inside of the concrete form prior to placing the concrete. Steel 2 x 1 inch (50.8 x 25.4 mm) channels were used to protect the pressure plate wiring from the poured concrete and backfill materials and enable the retrieval of the pressure plate after testing.

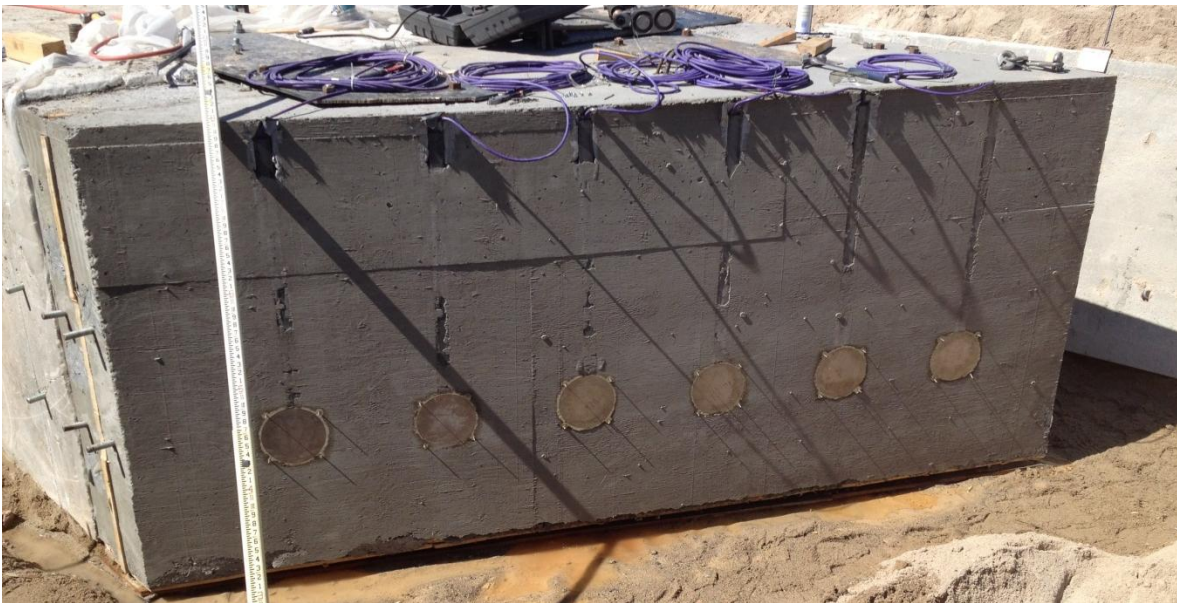


Figure 3-19: Photograph of embedded pressure plates in 30° wedge face

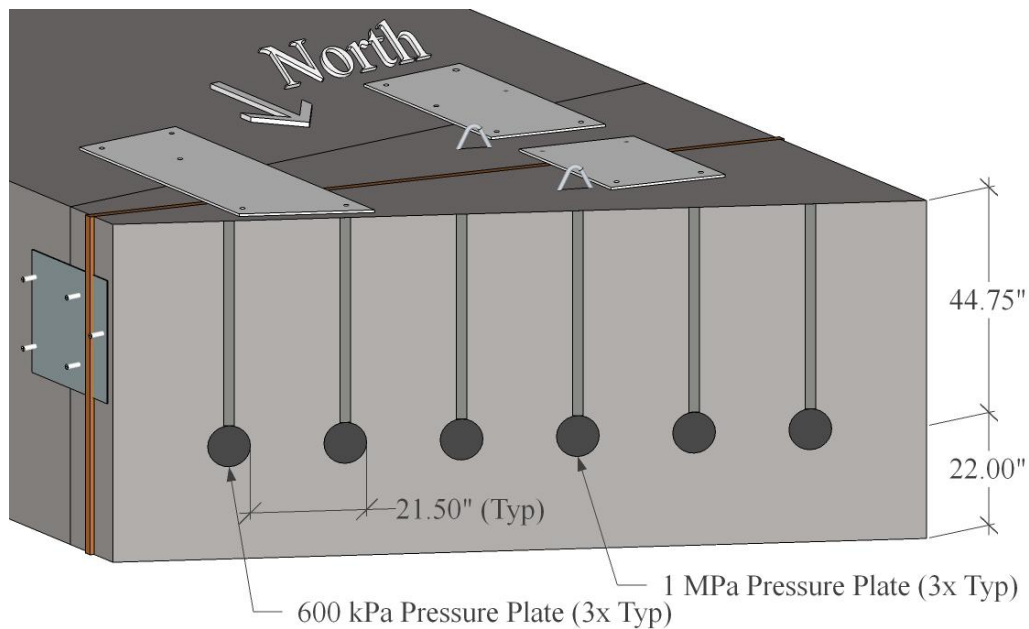


Figure 3-20: Drawing of embedded pressure plates in 30° wedge face

3.4 Geotechnical Backfill Properties

This section describes the geotechnical properties of the backfill material used for this series of tests. Soil gradation, unit weights, relative compaction, relative density, and strength parameters are outlined herein.

3.4.1 Backfill Gradation and Relative Density

Soil for this series of tests consisted of approximately 250 tons (227 metric tons) at 7% moisture content of poorly graded sand classifying as SP type soil according to the Unified Soil Classification System or an A-1-b type soil according to the AASHTO Classification System. Pre- and post-testing gradation plots are shown in Figure 3-21. The small difference between the

pre- and post-test gradation plots was likely the result of natural variations in the backfill material. The measured grain size distribution curves generally fall within the gradation limits of washed concrete sand (ASTM C33) although the fines content is a little above the limit for the gradation at the end of testing. Table 3-2 provides the soil gradation parameters for the soil particle size analyses conducted before and after the abutment skew tests.

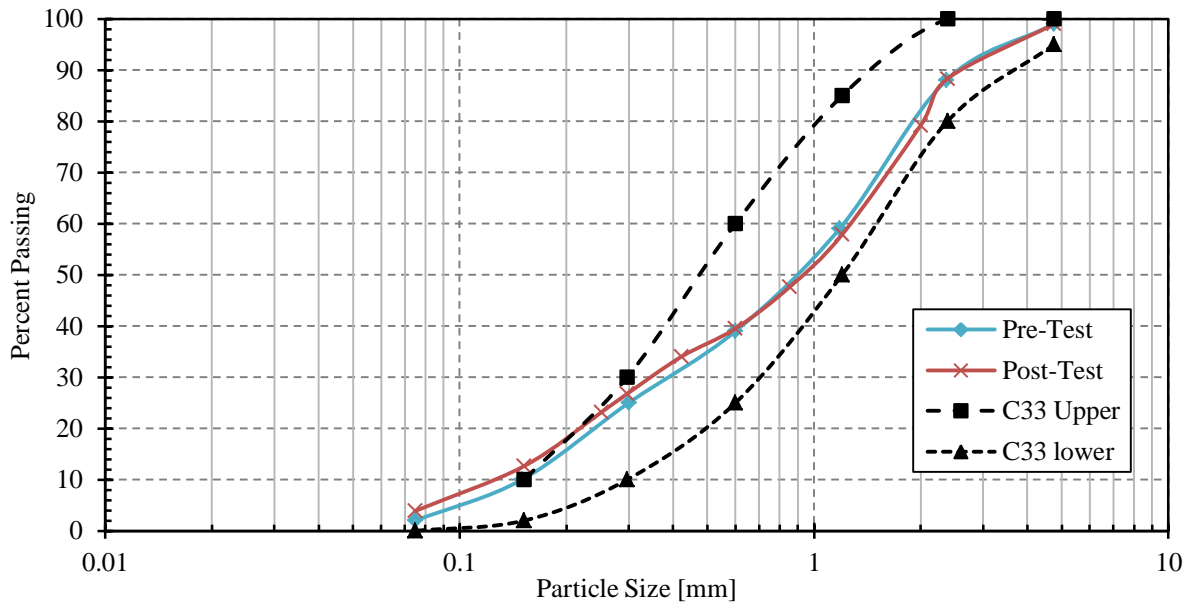


Figure 3-21: Particle size distribution of backfill soil pre- and post-test

Table 3-2: Soil Gradation Characteristics, Pre- and Post-Testing

	<i>Sand</i>	<i>Fines</i>	D_{60}		D_{50}		D_{30}		D_{10}		C_u	C_c
	[%]	[%]	[in]	[mm]	[in]	[mm]	[in]	[mm]	[in]	[mm]		
Pre-Test	98.0	2.0	1.22	(31.0)	0.9	(22.9)	0.4	(10.2)	0.16	(4.1)	7.6	0.8
Post-Test	96.1	3.9	1.26	(32.0)	0.92	(23.4)	0.34	(8.6)	0.13	(3.3)	9.7	0.7

The maximum dry unit weight according to the modified Proctor compaction test (ASTM D1557) was 111.5 lbf/ft³ (17.52 kN/m³) and the optimum moisture content was 7.1%. The target

on-site compaction level was 95% of the modified proctor maximum, though average relative compaction for all tests considered herein was 96.7% of the modified proctor maximum.

Histograms showing the frequency of backfill dry unit weight occurrences for the 0° skew test [$\gamma_d=107.0$ pcf (16.81 kN/m³)], the 15° skew test [$\gamma_d=108.3$ pcf (17.01 kN/m³)], and the 30° skew test [$\gamma_d=108.3$ pcf (17.02 kN/m³)] are shown in Figure 3-22, Figure 3-23, and Figure 3-24, respectively. Figure 3-25 and Table 3-3 summarize the dry unit weight characteristics of all three tests. The mean dry unit weights are within 1.30 lbf/ft³ (0.20 kN/m³) of one another with the skewed values at the higher unit weight. Furthermore, the histograms are generally quite tight about the mean with 80% to 90% of the measurements falling within ± 1.5 lbf/ft³ (0.24 kN/m³) of the mean.

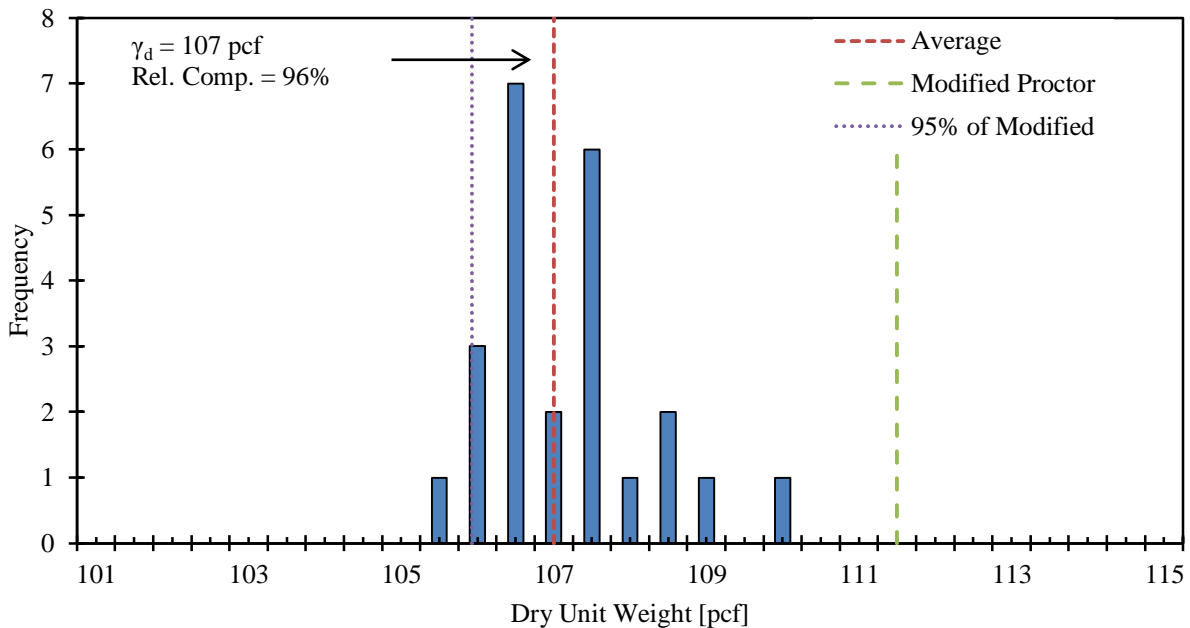


Figure 3-22: Backfill dry unit weight histogram for 0° test

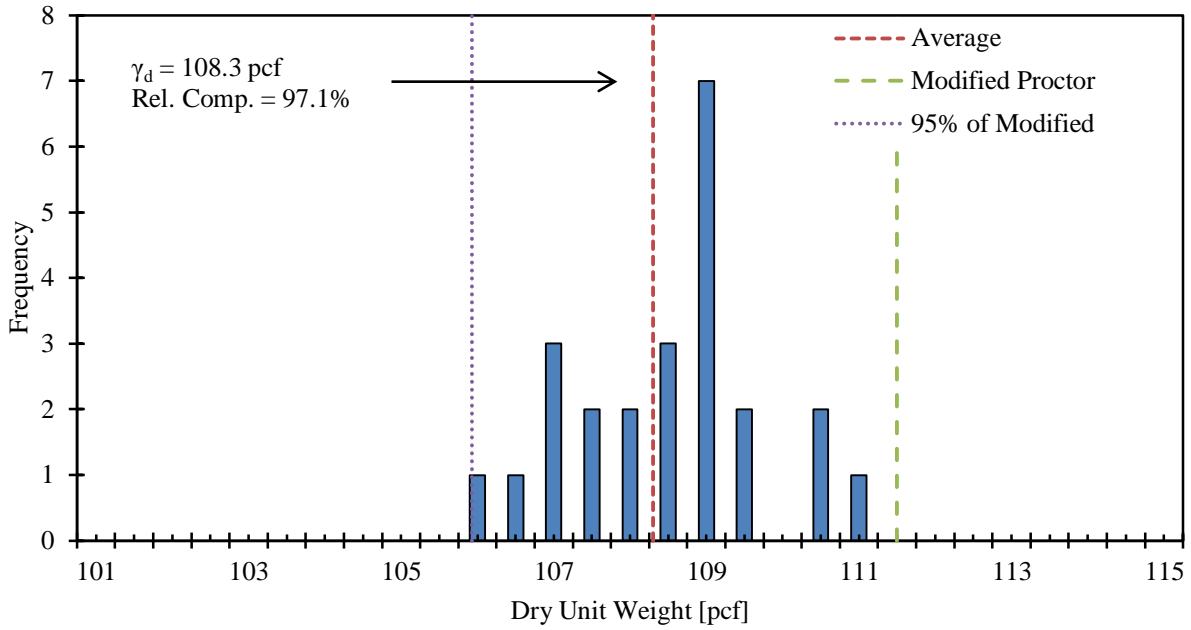


Figure 3-23: Backfill dry unit weight histogram for 15° test

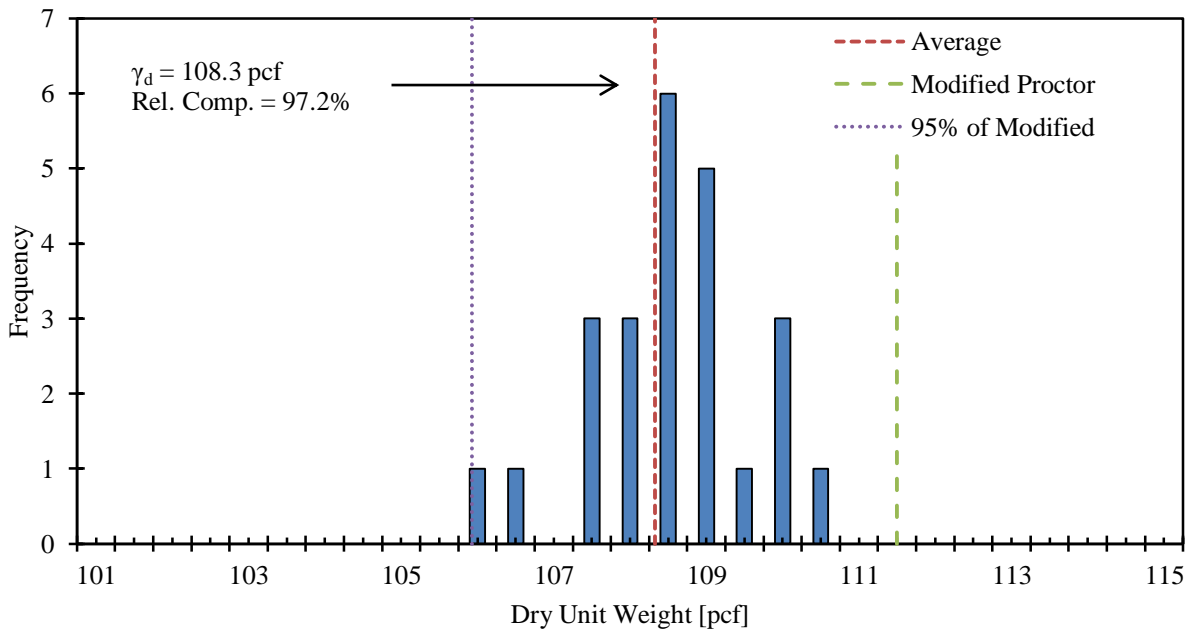


Figure 3-24: Backfill dry unit weight histogram for 30° test

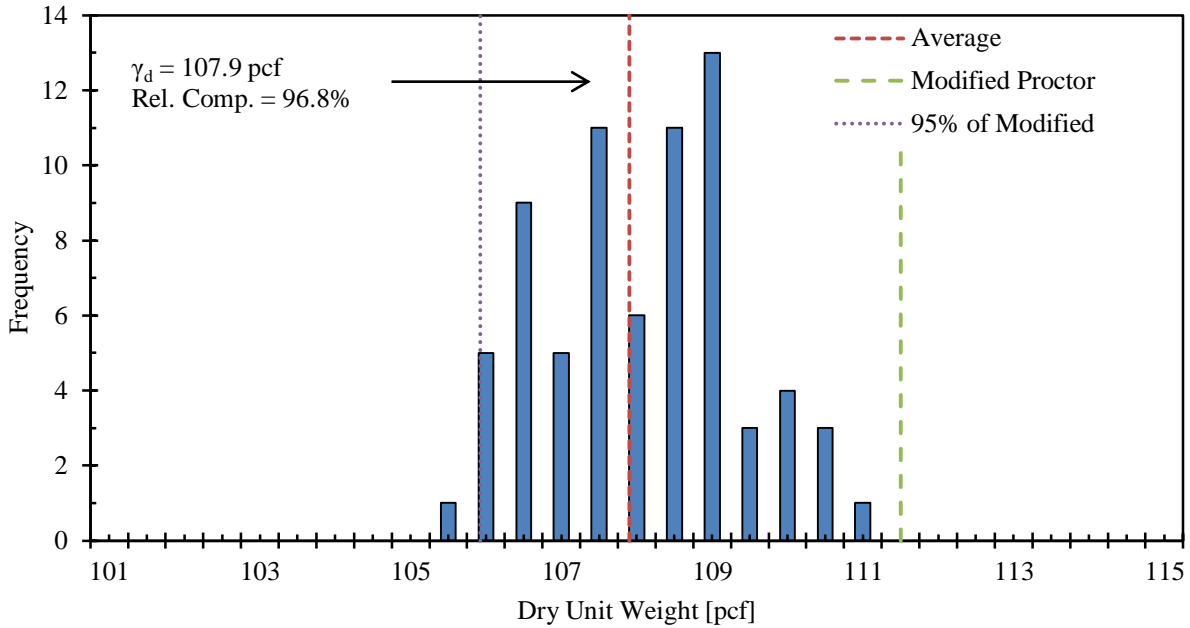


Figure 3-25: Backfill dry unit weight histogram for all tests

Table 3-3: Summary of Backfill Dry Unit Weight Characteristics as Obtained from the Nuclear Density Tests

	<i>0° Skew Test</i>		<i>15° Skew Test</i>		<i>30° Skew Test</i>	
	[pcf]	[kN/m ³]	[pcf]	[kN/m ³]	[pcf]	[kN/m ³]
Minimum Dry Unit Weight	105.4	16.56	105.6	16.59	105.6	16.59
Maximum Dry Unit Weight	109.9	17.26	110.6	17.37	110.1	17.30
Average Dry Unit Weight	107.0	16.81	108.3	17.01	108.3	17.02
Median Dry Unit Weight	106.9	16.79	108.6	17.05	108.5	17.04
Standard Deviation	1.04	0.163	1.24	0.194	1.09	0.172

Relative density was calculated using the correlation between relative density (D_r) and relative compaction (R) of granular soils developed by Lee and Singh (1971). This correlation is shown as Equation (3-4) and the relative densities and relative compaction values from each test are summarized in Table 3-4.

$$R = 80 + 0.2D_r \tag{3-4}$$

Table 3-4: Backfill Relative Compaction and Relative Densities for All Tests

	<i>0° Skew Test</i>	<i>15° Skew Test</i>	<i>30° Skew Test</i>
Relative Compaction	96%	97%	97%
Relative Density	80%	86%	86%

Plots showing moisture content, dry unit weight, and moist unit weight, and relative compaction with respect to elevation above the base of the pile cap for all three tests are shown in Figure 3-26, Figure 3-27, Figure 3-28, and Figure 3-29, respectively.

As would be expected for backfill materials placed near the water table, the moisture content, and thus the moist unit weight, of the backfill material increased slightly with depth. However, the overall variation in moisture content was typically within plus or minus 2 to 3%, which is typical of what can be accomplished in practice. The only significant exception was for the materials placed at the bottom of the test pit for the 30° test where the moisture content was over 13% in comparison to the average moisture content of approximately 8.3%. However, this higher moisture content did not significantly affect the dry unit weight of the material at this layer, though obviously the moist unit weight was proportionally higher.

In general, the dry unit weight for the 15° and 30° test was somewhat higher than the dry unit weight for the 0° test, though for the most part the difference was between 1% and 3%.

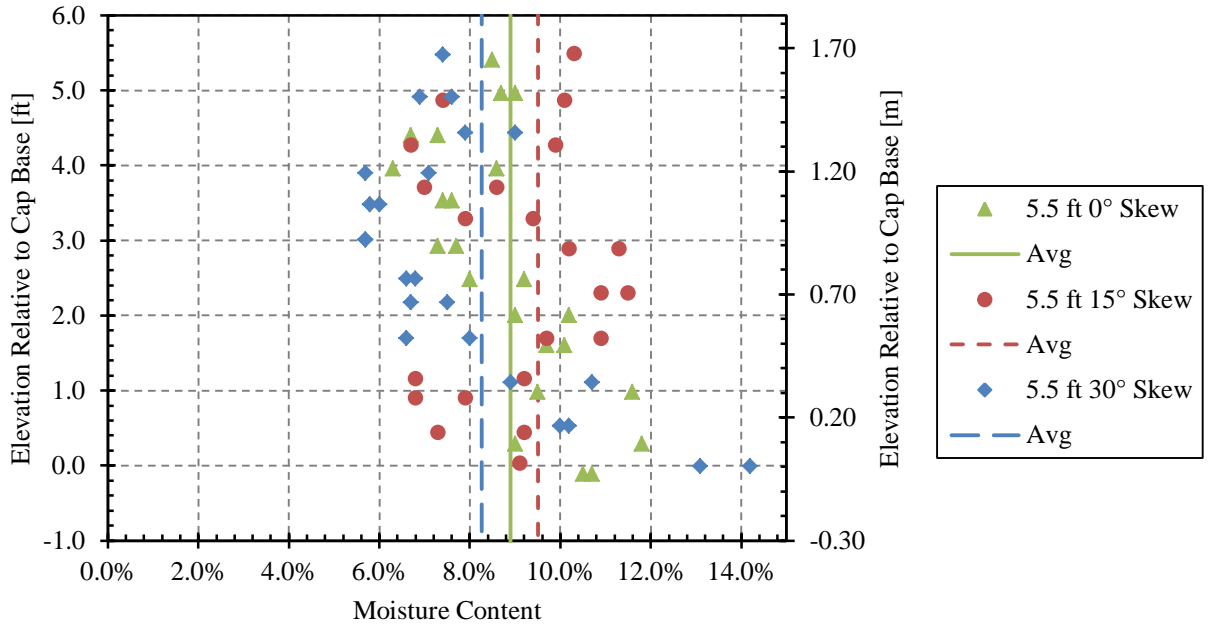


Figure 3-26: Moisture content with respect to depth for all tests

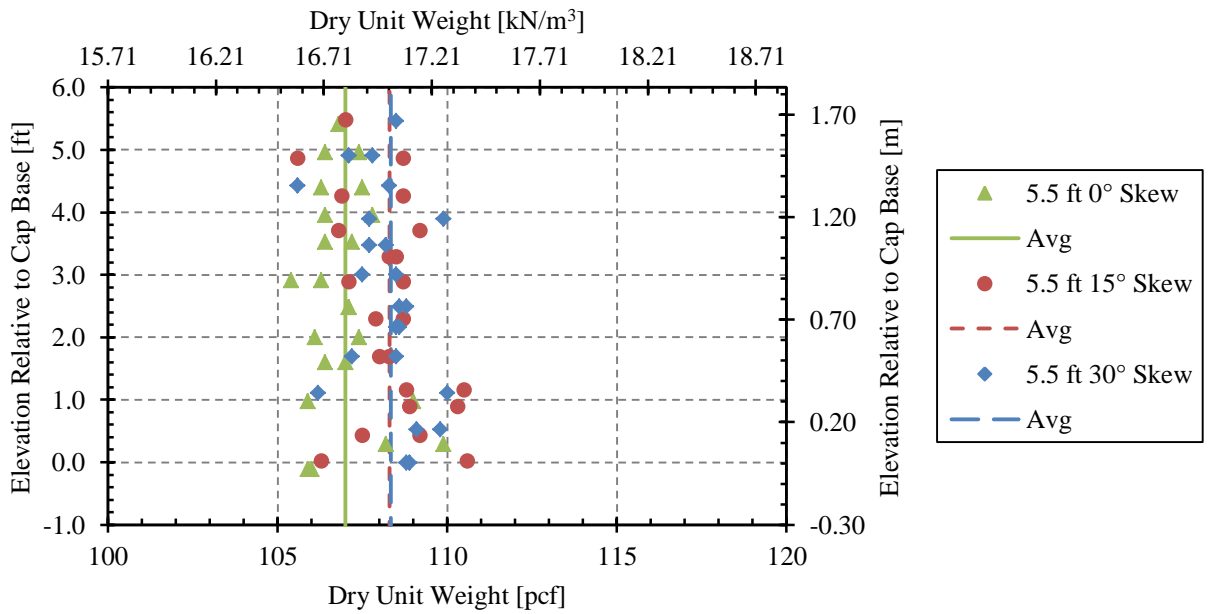


Figure 3-27: Dry unit weight with respect to depth for all tests

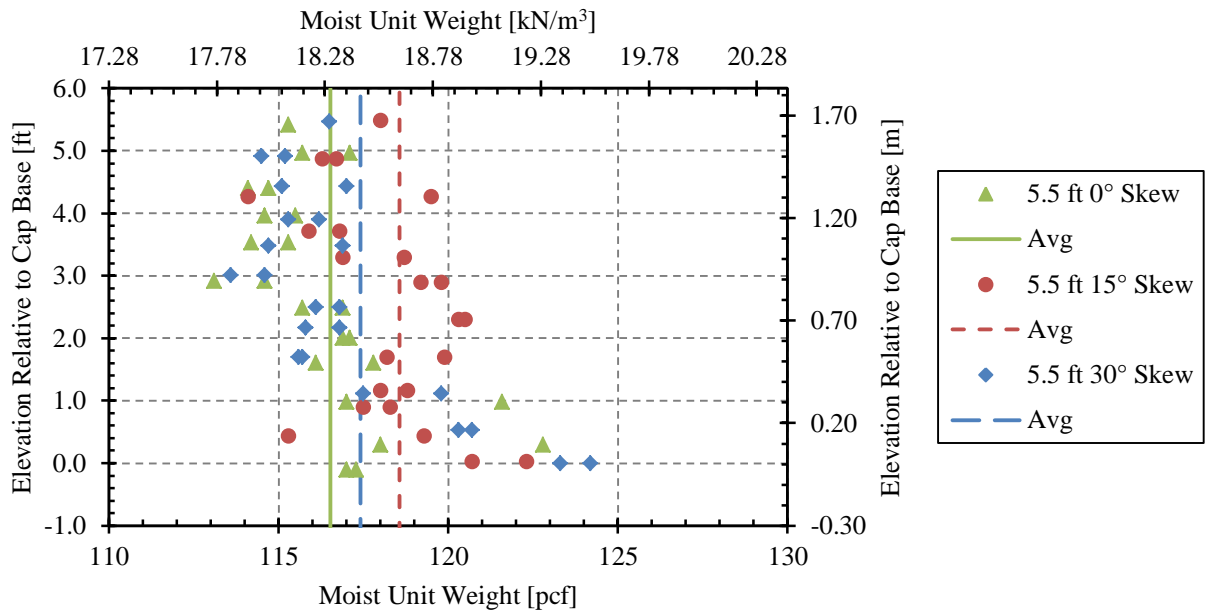


Figure 3-28: Moist unit weight with respect to depth for all tests.

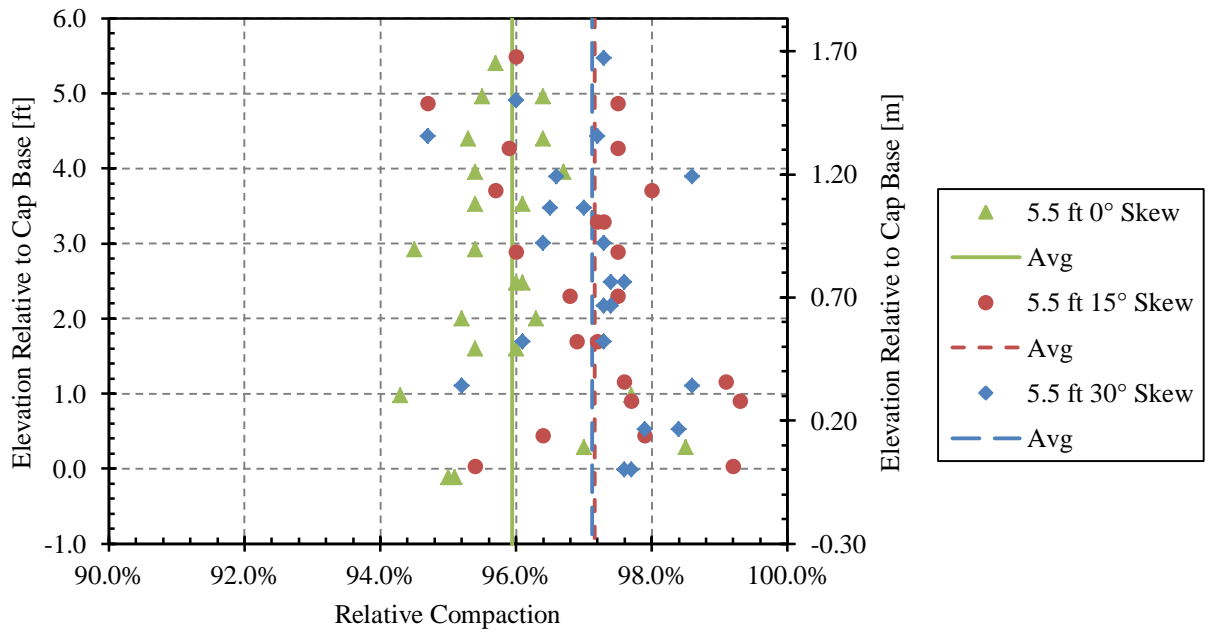


Figure 3-29: Relative compaction with respect to depth for all tests

3.4.2 Backfill Shear Strength

Backfill friction angle (ϕ) and cohesion (c) were determined by conducting direct shear tests (ASTM D 3080) in the BYU soils laboratory in order to verify previously obtained values (Cummins 2009).

For the direct shear tests normal stresses of 4.1, 8.2, 16.3, and 24.5 psi (28.1, 56.3, 112.5, and 168.8 kPa) were selected as those values encompassed the range of vertical stresses the backfill material experienced during testing. Test materials were compacted at the average field moisture content, and tests were conducted in submerged and un-submerged conditions. Horizontal load-deflection plots for the moist and submerged tests are shown in Figure 3-30 and Figure 3-31, respectively. Using this data, the normal stress versus shear stress plots for the dry and submerged direct shear tests were developed and the results are shown in Figure 3-32 and Figure 3-33, respectively. Backfill strength properties are summarized in Table 3-5.

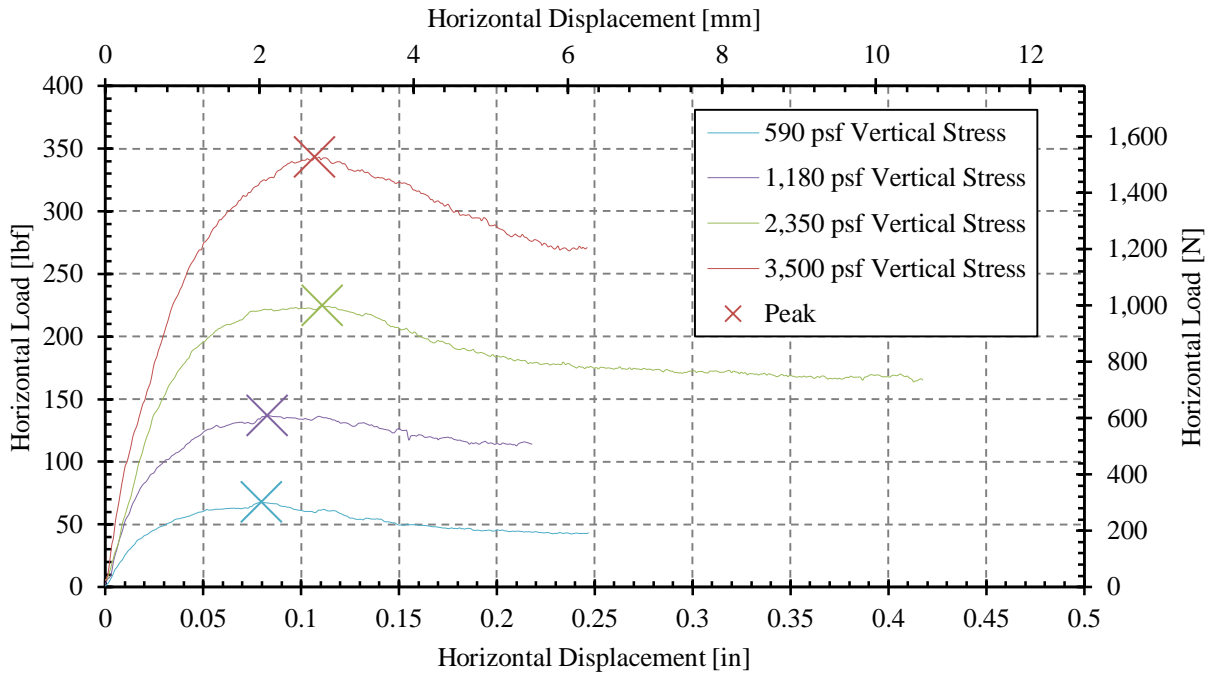


Figure 3-30: Horizontal load-deflection plots for dry direct shear tests

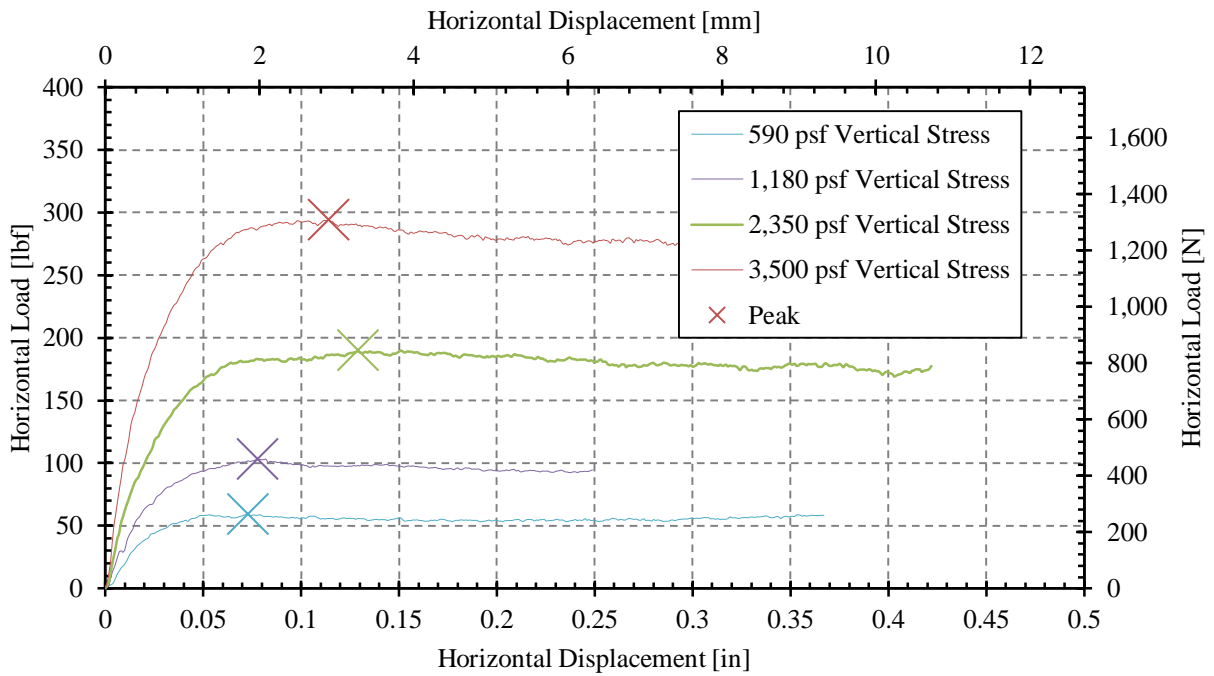


Figure 3-31: Horizontal load-deflection plots for submerged direct shear tests

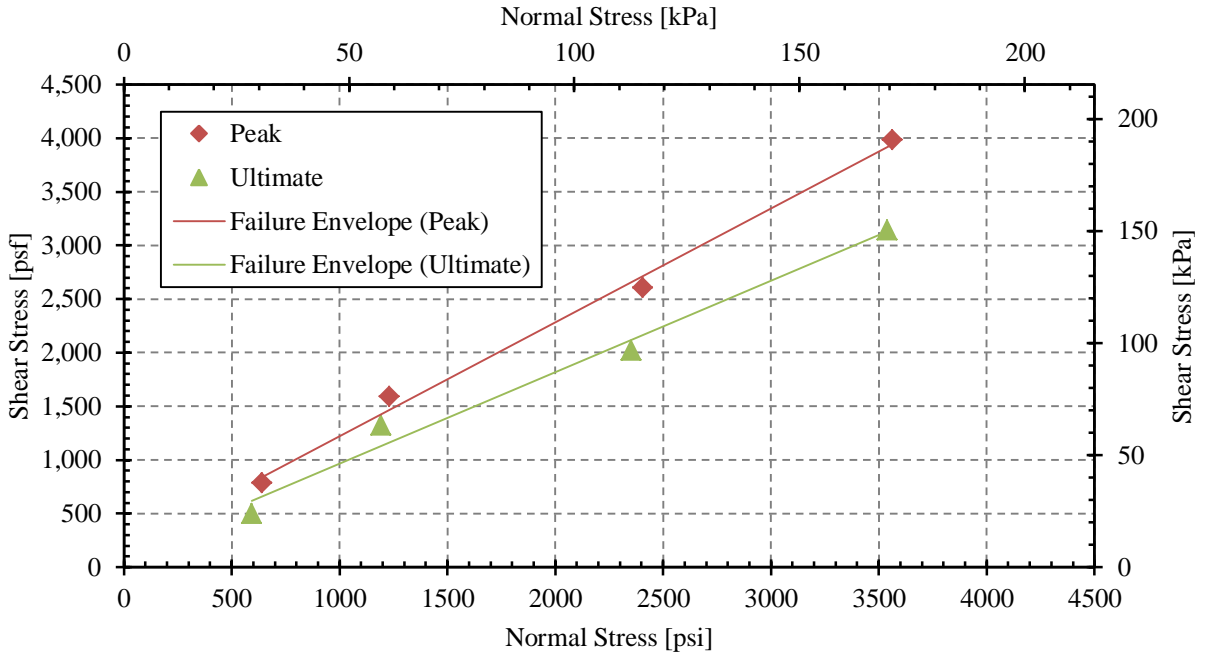


Figure 3-32: Normal stress versus shear stress plots for dry tests

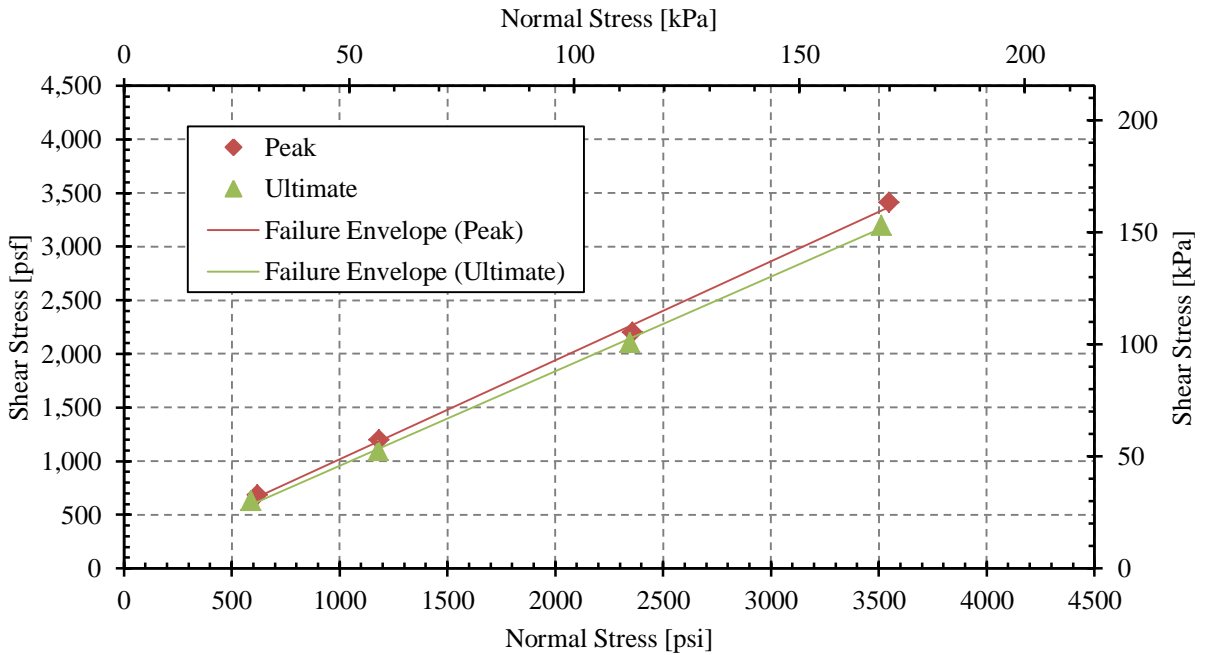


Figure 3-33: Normal stress versus shear stress plots for submerged tests

Table 3-5: Backfill Strength Parameters

<i>Source of Test Result</i>	<i>Peak</i>		<i>Ultimate</i>	
	ϕ (deg)	<i>c</i> (psf)	ϕ (deg)	<i>c</i> (psf)
Direct Shear (full range, dry)	46.7	161.6	40.4	113.8
Direct Shear (full range, dry, zero cohesion)	48.3	0	41.8	0
Direct Shear (full range, submerged)	42.7	92.9	41.4	78.8
Direct Shear (full range, submerged, zero cohesion)	43.8	0	42.3	0

4 GENERAL TEST PROCEDURES

This chapter will outline the order of the tests, backfill placement and test preparation, pile cap displacement procedures, and final measurement procedures. Also, each baseline test will be addressed and the selection of the appropriate baseline curve for a given test will be addressed.

4.1 Test Order

A total of 16 tests were conducted during the summer 2012 at the Salt Lake City Airport: ten backfilled tests and six baseline tests without backfill. The test order is shown in Table 4-1. However, as has been mentioned previously, this thesis will only discuss in detail the no-backfill tests, the 0° Skew, 15° skew, and 30° skew 5.5-foot (1.68 m) unconfined backfill tests.

Table 4-1: 2012 Testing Summary

<i>Test Number</i>	<i>Test Date</i>	<i>Test Description</i>
1*	4/25/2012	0° Skew, No Backfill (Baseline)
2*	4/25/2012	0° Skew, No Backfill (Baseline Retest)
3	4/30/2012	0° Skew, 3.0 ft (0.91 m) Backfill
4*	5/3/2012	0° Skew, 5.5 ft (1.68 m) Backfill
5*	5/3/2012	0° Skew, No Backfill (Baseline)
6	5/8/2012	0° Skew, MSE, 5.5 ft (1.68 m) Backfill
7*	5/14/2012	30° Skew, No Backfill (Baseline)
8*	5/15/2012	30° Skew, No Backfill (Baseline Retest 2)
9	5/18/2012	30° Skew, MSE, 5.5 ft (1.68 m) Backfill
10*	5/24/2012	30° Skew, 5.5 ft (1.68 m) Backfill
11	5/30/2012	30° Skew, 3.0 ft (0.91 m) Backfill
12*	5/31/2012	15° Skew, No Backfill (Baseline)
13*	6/4/2012	15° Skew, 5.5 ft (1.68 m) Backfill
14	6/6/2012	15° Skew, 3.0 ft (0.91 m) Backfill
15	6/8/2012	15° Skew, 3.0 ft Backfill Retest
16	6/13/2012	15° Skew, MSE, 5.5 ft (1.68 m) Backfill
*Only tests so marked are considered in this thesis		

4.2 Backfill Placement and Test Preparation

Backfilling was accomplished by laying lifts of soil approximately 6 inches to 8 inches (15 cm to 20 cm) thick and then compacting with a vibratory drum roller and walk-behind vibratory plate compactor to a density greater than or equal to 95% of the modified proctor value [111.5 pcf (17.52 kN/m³)]. Water was added to the material during placement to aid in compaction. Following backfill completion the aforementioned 2-foot (0.61 m) grid was painted on the surface of the backfill and relative elevations of each grid point were measured using a survey level, and the red-dyed sand columns were installed. Additionally, initial shape array and inclinometer readings were taken.

4.3 Pile Cap Displacement Procedures

After backfill placement and elevation measurements had been obtained, the two hydraulic actuators were used to displace the pile cap into the backfill zone at a velocity of approximately 0.25 inches per minute (6.4 mm/min) to target displacement intervals of approximately 0.25 inch (6.4 mm). At the end of each displacement interval a shape array reading was taken to measure pile displacement versus depth, and the actuators were held in place for approximately 2 minutes to observe the reduction in actuator load as a function of time. This process was repeated until the cap had been displaced approximately 3.25 inches to 3.75 inches (8.26 cm to 9.53 cm) into the backfill zone (larger displacements were not used to prevent failure of the piles supporting the pile cap).

Due to variations in subsurface soil properties, the reaction frame did not respond in a uniform manner, but for all cases the drilled shaft on the west side of the reaction frame had a stiffer response than the one on the east side. Therefore, in order to prevent the pile cap from rotating, the east actuator had to be displaced further than the west. Also, in order to keep the pile cap square for the skewed tests a significantly higher load had to be applied to the pile cap by the west actuator than the east actuator.

4.4 Final Measurement Procedures

After the pile cap had reached maximum displacement final inclinometer readings were taken, cracks in the backfill surface were mapped, and the relative elevations of each grid point were again recorded.

4.5 Baseline Curves

Baseline tests were performed in order to determine the lateral resistance of the pile group without backfill materials. Using this data, the longitudinal resistance supplied by just the soil could be determined by comparing the lateral resistance with soil to the lateral resistance without soil. A baseline test was conducted in the same fashion as a backfill test; however, no backfill was placed prior to displacing the pile cap.

For the tests conducted in the summer of 2012, six baseline tests were performed. A longitudinal force versus pile cap deflection plot showing the test results for the 0° skew tests, the 15° and 30° skew baseline tests, and all other baseline tests, adjusted to a common starting point, are shown in Figure 4-1, Figure 4-2, and Figure 4-3, respectively. For these plots displacements are zeroed relative to the initial pile cap position. In this section characteristics of each baseline curve will be discussed and the logic for selecting a given baseline for a given backfill test will be presented.

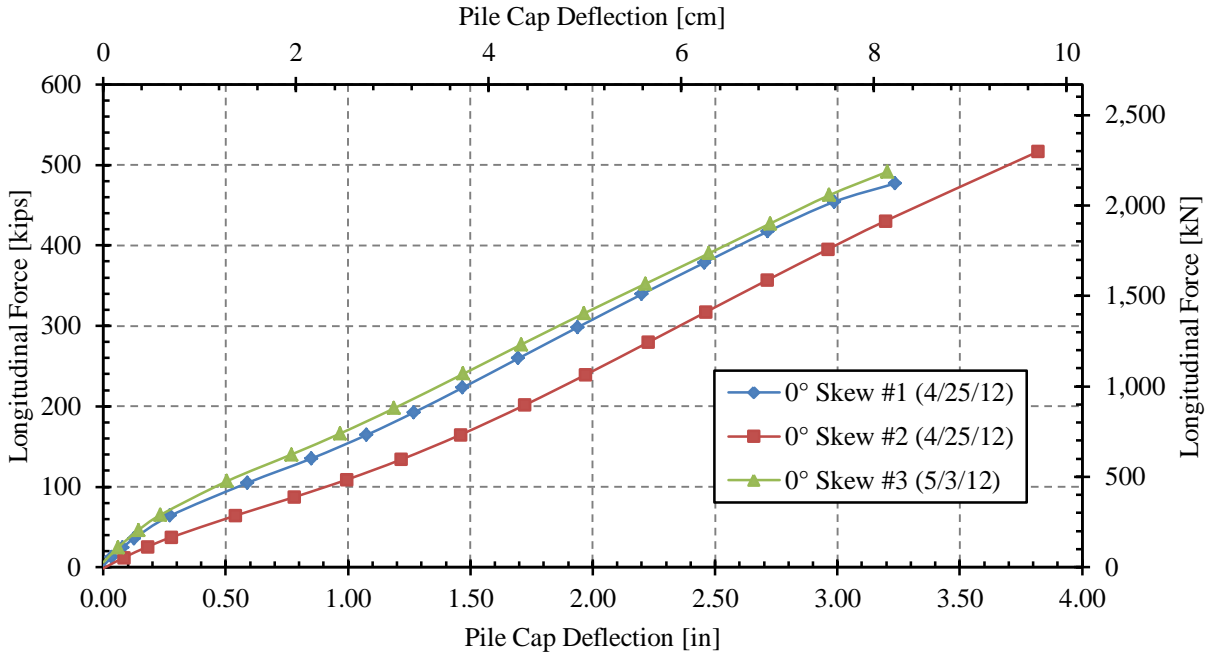


Figure 4-1: Baseline curves for 0° test

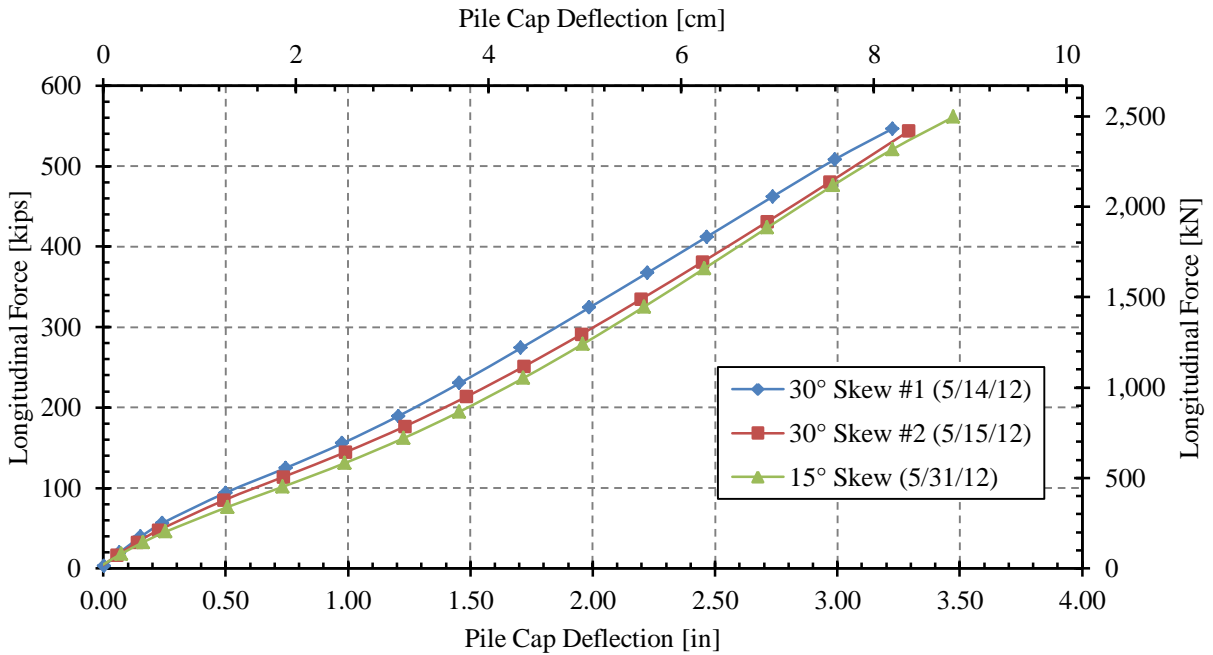


Figure 4-2: Baseline curves for 15° and 30° tests

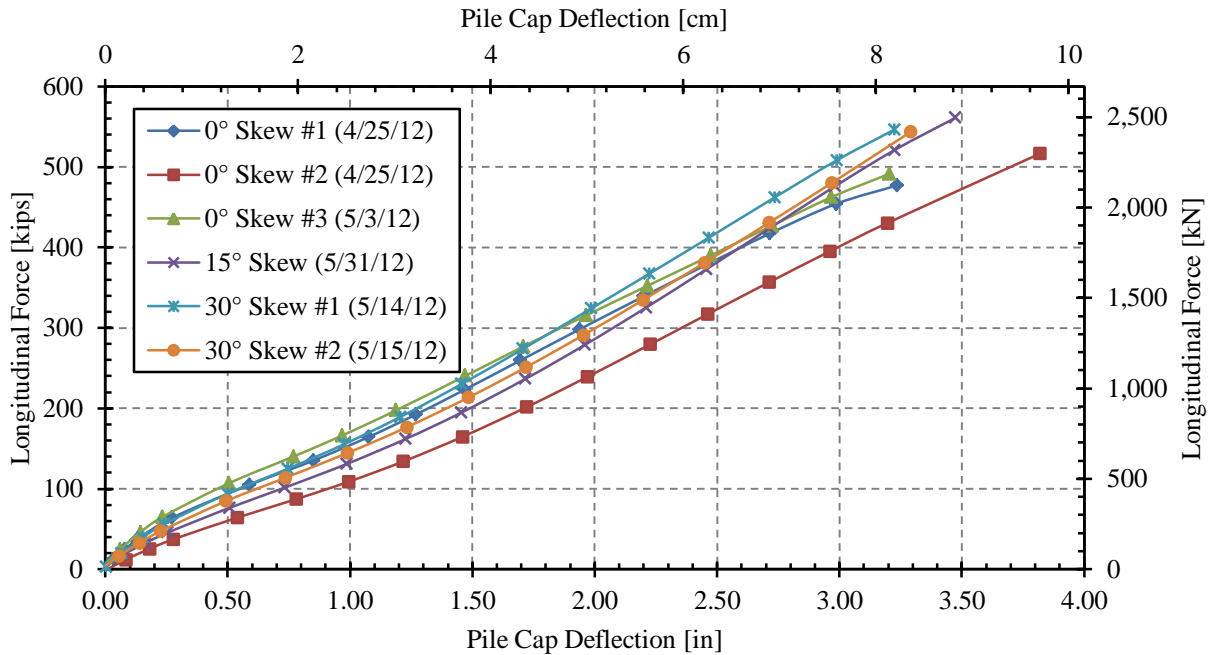


Figure 4-3: Baseline Curves for all tests

4.5.1 0° Baseline Test

The first 0° skew baseline test was the very first test conducted after completing the initial test setup and as such, the pile cap had not been displaced in over a year. Therefore, the soil around the piles had likely filled in all gaps created from previous lateral load tests. The second 0° skew baseline test, however, was run immediately after the first baseline test; and as such, the soil around the piles did not have sufficient time to reform around the piles. This significantly reduced the lateral resistance of the pile cap as can be seen in Figure 4-1. The third 0° baseline test was performed immediately after completing the 0° skew 5.5 ft (1.68 m) backfill no MSE wall test. As can be seen in the figure, the load-deflection curve for this test was *higher* than the curve for the first baseline test. At first, this phenomenon seemed to violate the assumption that the longer the pile cap sat, the more the soil had an opportunity to reform around

the piles. A likely explanation, however, is that the excavation process forced a large amount of soil under the pile cap and into the gaps between piles and surrounding soil that were created during pile cap displacement. Typically, excavation was performed from the north end of the backfill zone with the loader end of the backhoe; however, in order to facilitate immediate baseline testing following the completion of the 5.5 ft (1.68 m) backfill 0° skew no MSE wall test, excavation was performed from the west side of the test pit with the hoe-end of the backhoe. According to a professional excavator, this method of excavation had the potential to force significantly more soil under the pile cap than when excavating from the north using the loader end of the backhoe (John Cazier, personal communication, July 27, 2012). As the second and third 0° baseline tests were conducted immediately after a previous test the first 0° baseline was used when calculating the 0° backfill resistance. In order to avoid this problem in the future, all baseline tests should be conducted after a sufficient amount of time has passed since a previous test. A good time frame is probably between 2 and 6 days, though more time should probably not be allowed to elapse before conducting another test in order to prevent the soil from settling in too much around the piles. Furthermore, care should be taken to ensure that all tests are conducted on as regular a schedule as possible.

4.5.2 30° Baseline Test

Two baselines for the 30° geometry were performed. The first baseline test was performed on May 14, 2012, six days after completing the 0° skew MSE wall test. This extended period of time between tests likely allowed the soil to reform around the piles, thereby increasing the lateral stiffness of the pile cap. Note the similarities and differences between the first 0° skew baseline test, and the first and second 30° skew baseline test shown in Figure 4-4: up until 1 inch (2.54 cm) of displacement the two curves are nearly identical. On the other hand, the second 30°

baseline test was performed only one day following the first 30° baseline test. The decreased initial lateral stiffness for this test is obvious in comparison to the first 0° and first 30° baseline tests. The higher final loads achieved during the 30° baseline tests in comparison to the 0° tests is likely due to the additional 40-kip (178 kN) concrete wedge attached to the front face of the pile cap.

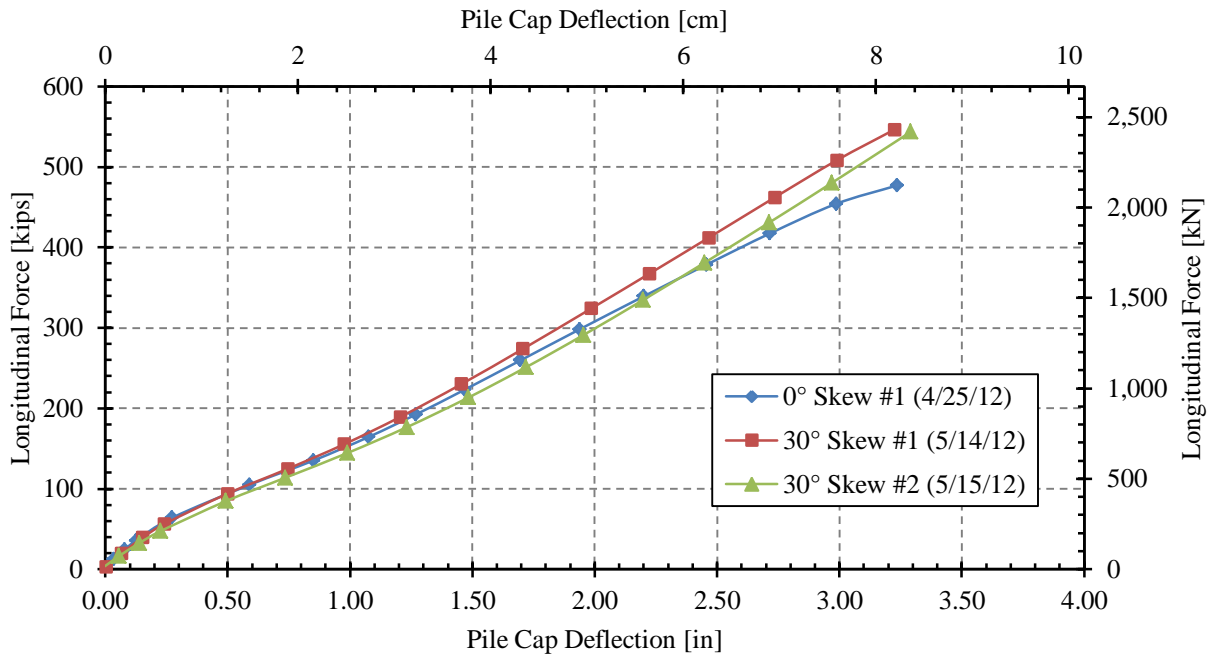


Figure 4-4: Comparison between first 0° skew baseline and 30° skew baseline tests

4.5.3 15° Baseline Test

Only one 15° baseline test was performed. This test was performed on May 31, 2012, one day after completing the 30° skew, 3 ft (0.91 m) backfill test. This baseline test is compared to the two 30° baseline tests in Figure 4-2 above. The reduced lateral resistance of the pile cap for the 15° test in comparison to the second 30° baseline test is likely due to the removal of the 20-kip (89 kN) 30° wedge. More importantly, however, is that the lower initial stiffness of the 15°

baseline test in comparison to the first 30° baseline test can probably be explained because the 15° test was run only one day after a previous test.

4.5.4 Baseline Selection

Because the 0° skew, 5.5 ft (1.68 m), unconfined test was conducted three days after a previous test; the 15° skew, 5.5 ft (1.68 m), unconfined test was conducted four days after a previous test; and the 30° skew, 5.5 ft (1.68 m), unconfined test was conducted six days after a previous test, those baselines that represented conditions in which the soil had been allowed to settle in around the piles were used. Therefore, the first 0° skew baseline and the first 30° skew baseline will be used for the 0° and 30° backfill test, respectively. However, because the 15° backfill test was conducted four days after a previous test and the 15° baseline test was conducted only one day after a previous test, and given the similarities in curve shape for the 15° and 30° baseline tests, the first 30° baseline test will be used for the 15° backfill test instead of the 15° baseline test.

5 LOAD VERSUS DISPLACEMENT RESULTS

This chapter will present pile cap, backfill, and reaction foundation load displacement results for each of the tests. Similar data will be presented together when appropriate. Because load-deflection results were obtained for peak load values associated with each displacement interval, the reduction in actuator load with respect to time after the peak will also be discussed.

The purpose for discussing the behavior of the reaction foundation is so that future tests can be conducted in such a way as to minimize test variability and corresponding recommendations will be made at the end of this chapter.

5.1 Baseline Tests: Actuator and Reaction Foundation Behavior

Due to the anisotropic nature of the materials in which the reaction foundation was located, actuator displacements had to be closely monitored in order to ensure that the pile cap was displaced evenly into the backfill for all tests (baseline and backfill). Figure 5-1 shows east and west actuator load plotted against pile cap displacement as measured by the east and west string pots, respectively, for the 0° and 30° baseline tests. Unsurprisingly, the east and west actuators for the 0° test resisted nearly identical loads throughout the test; however, this was not true for the 30° test. The increase in lateral load applied to the west actuator during the 30° baseline test was likely caused by the upward force applied primarily to the acute corner of the wedge by the roller foundation described in Section 3.3.3. This upward force would have

increased the moment applied to the west piles as the cap was displaced laterally and thereby the lateral resistance applied to the west actuator, particularly at high deflections.

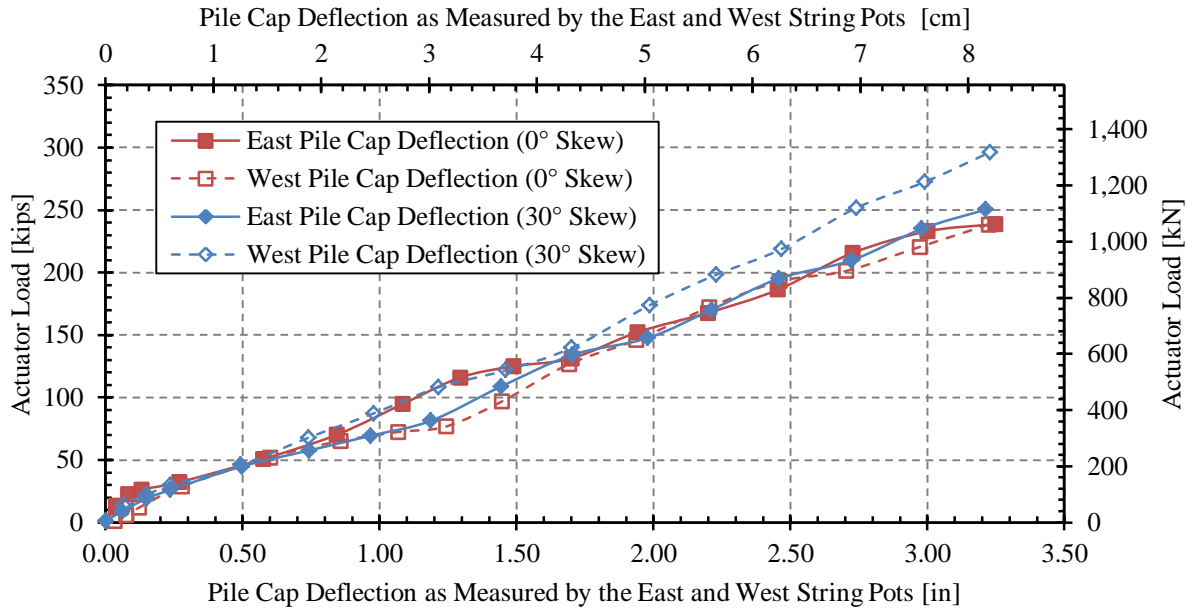


Figure 5-1: Actuator load versus pile cap displacement curves for 0° and 30° baseline tests

Figure 5-2 shows actuator load plotted against the displacement of the reaction foundation as measured by string pots mounted on the east and west ends of the reaction foundation for the 0° and 30° baseline tests. This plot shows that the west side of the reaction foundation was significantly stronger than the east side. Though in general, the reaction foundation behaved much more linearly for the 30° baseline test than for the 0° baseline test. This was likely the result of having loaded the foundation several times prior to conducting the 30° baseline test and the materials around the drilled shafts and sheet pile wall had reached a semi-stable condition. This is not to say that the pile cap load-deflection response was less stiff for the 30° test than for the 0° test as Figure 5-1 shows that this is clearly not the case.

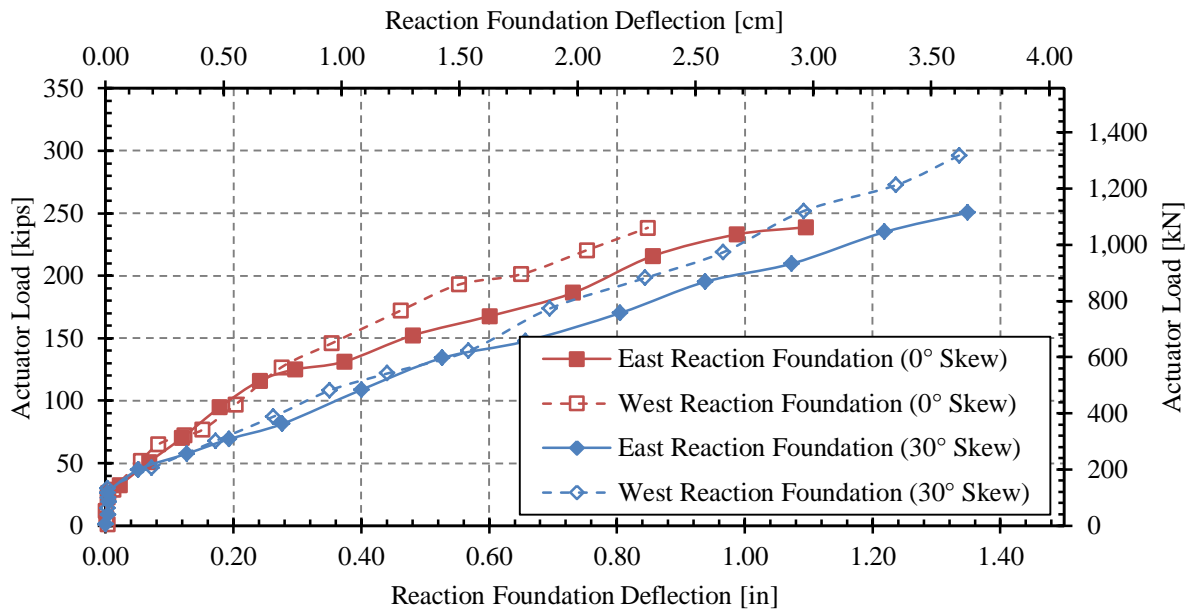


Figure 5-2: Actuator load versus reaction foundation displacement for 0° and 30° baseline tests

5.2 Backfill Tests: Actuator and Reaction Foundation Behavior

The reaction foundation behavior for the backfill tests was very similar to the behavior for the baseline tests, though obviously the reaction foundation was subjected to significantly higher loading, and thus higher displacement, for the backfill tests. Figure 5-3 shows actuator load plotted against pile cap displacement as measured by the string pots mounted on the east and west corners of the pile cap for the 0°, 15°, and 30° backfill tests. Figure 5-4 shows actuator load plotted against the displacement of the reaction foundation as measured by string pots mounted on the east and west ends of the reaction foundation for the 0°, 15°, and 30° backfill tests.

As was the case for the 0° baseline test, the loads recorded by the east and west actuators were relatively similar throughout the test for the 0° backfill test. However, as shown in Figure

5-3, the slope of the east actuator load-deflection curve for the 0° skew test changed significantly once approximately 300 kips (1,330 kN) was applied to the foundation by each actuator, or as shown in Figure 5-4, when the reaction foundation had been pushed further than approximately 1.7 inches (4.3 cm). Though not discussed in this thesis, the 3-ft (0.91-m) test (conducted just prior to the 5.5-ft (1.68-m) unconfined backfill test) did not require that the reaction foundation be pushed further than 1.7 inches (4.3 cm). As such, a likely explanation for the significant change in slope of the east actuator load versus pile cap deflection curve for the 0° test is because the 5.5-ft (1.68-m) backfill test was the first time the reaction foundation had been pushed to those high deflections. Also, the change in the shape of the baseline curves between the 0° and 30° baseline tests shown in Figure 5-2 seems to suggest that the load-deflection behavior of the reaction foundation was heavily dependent on previous loadings. This is important to know so that for future tests the anomalies associated with the reaction foundation movement can be adequately addressed and/or resolved prior to beginning the backfill testing routine.

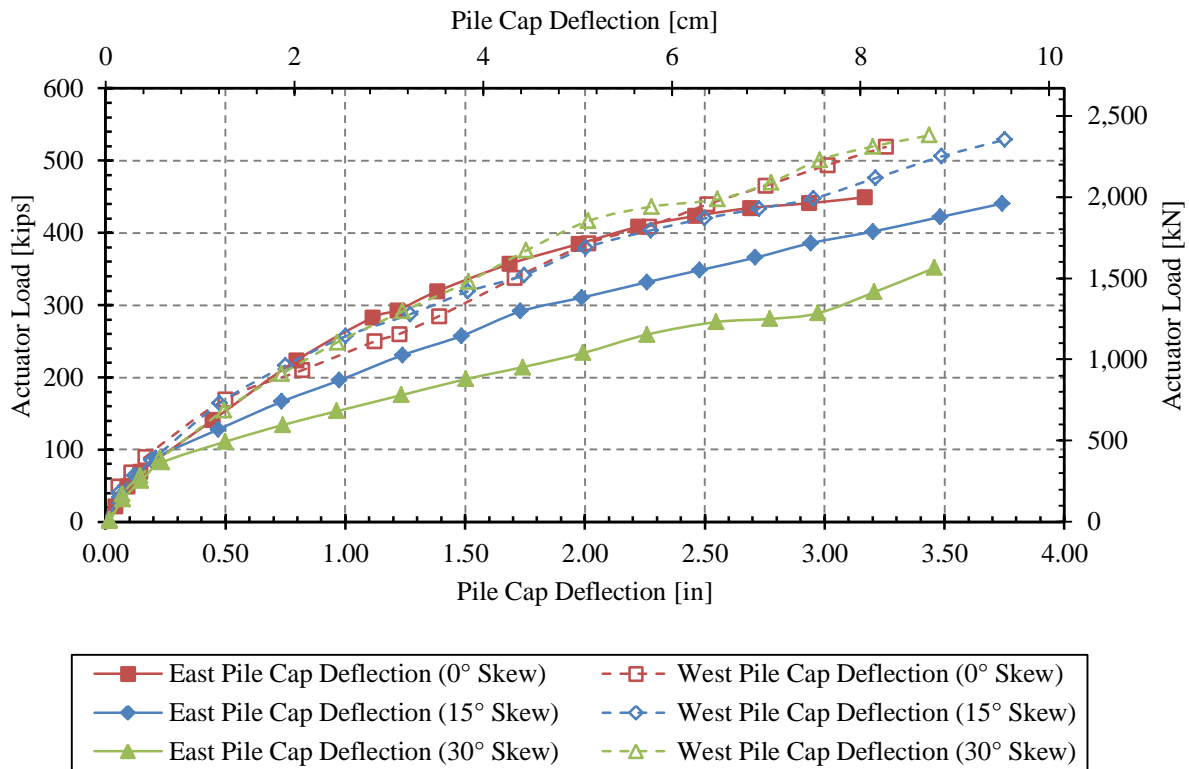


Figure 5-3: Actuator load versus pile cap displacement curves for the 0°, 15°, and 30° tests

If future tests are conducted with this test setup, in order to prevent this non-linear behavior of the reaction foundation the pile cap should be loaded such that the reaction foundation is displaced at least as far as is expected for any subsequent backfill tests. This should probably be done before the existing backfill material is excavated. Then, by the time the material has been excavated and the rest of the site prepared for testing, sufficient time should have passed so as to avoid the baseline test problems described in Section 4.5.

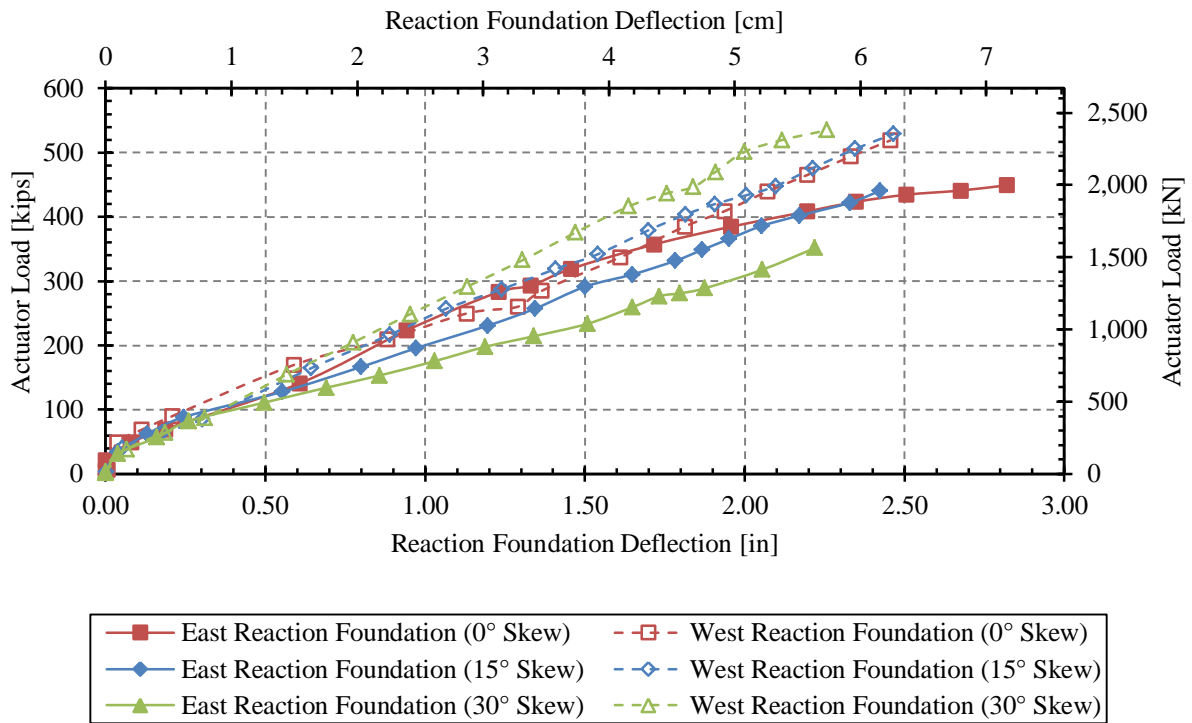


Figure 5-4: Actuator load versus reaction foundation displacement for 0°, 15°, and 30° backfill tests

As would be expected for the skew tests, the west actuator resisted significantly higher loads for the 15° and 30° backfill tests, likely for the reasons described in Section 2.3. This differential loading applied to the pile cap prevented the pile cap from rotating significantly about a vertical axis. Though, as will be described in Section 6.2.1 some very minor rotation about a vertical axis of the pile cap still occurred.

5.3 Backfill Load Displacement Results

In order to calculate the contribution of the lateral resistance of backfill to the total load, the appropriate baseline load versus deflection curve identified in Section 4.5.4 was subtracted from the corresponding total load versus deflection curve as shown in Figure 5-5. However, because displacement increments for the backfill and baseline tests didn't line up exactly, an

automated process was developed that created a sixth-order polynomial regression equation corresponding to the baseline resistance curve (applicable VBA code is available in the Appendix¹). As high order polynomials can usually only be used effectively for interpolation purposes, in instances where the baseline curve didn't extend to the required displacement a *linear* regression equation was fitted to the tail of the baseline curve when extrapolation was required. This composite equation, not the measured baseline curve points, was used for performing the lateral soil resistance calculations. Though the high-order polynomial does imply more precision in the recorded data than was actually obtained, this method essentially eliminated calculation errors associated with not accurately representing the baseline curve and thereby reduced controllable error.

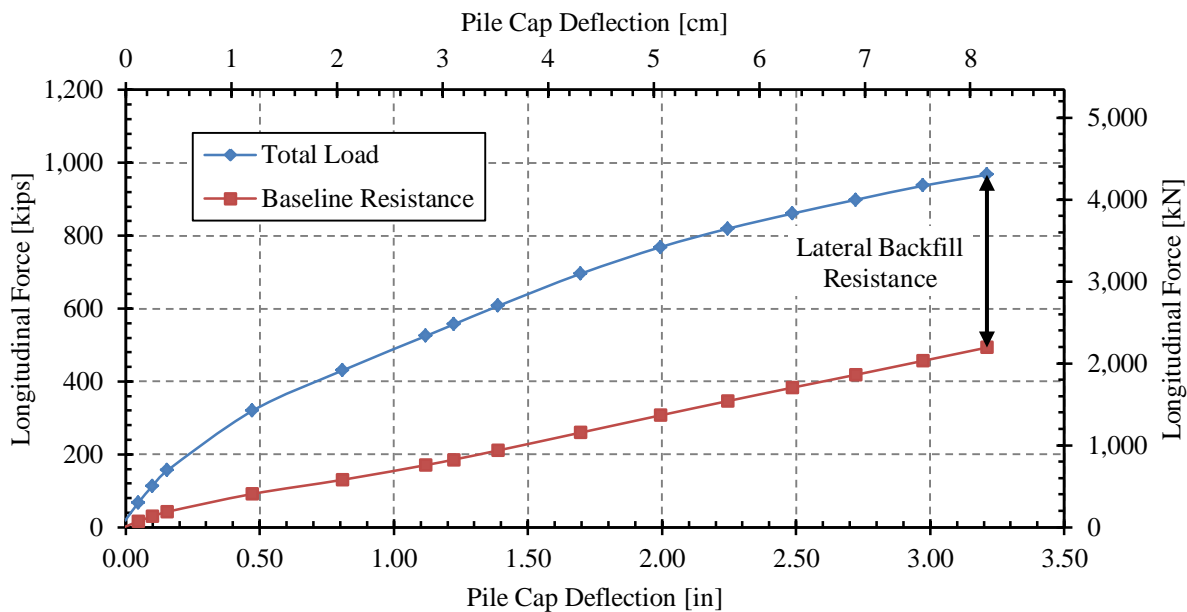


Figure 5-5: Illustration of calculation of longitudinal soil resistance from total load and baseline load versus deflection curves

¹ I have not included this VBA code in an Appendix for time reasons. If you think it's worth including, please let me know and I will make sure to include it before submitting the ETD.

Figure 5-6, Figure 5-7, and Figure 5-8 show the total load-deflection curve, the baseline load-deflection curve, and the longitudinal load-deflection curve for the 0°, 15°, and 30° 5.5-ft (1.68-m) unconfined backfill tests, respectively. Maximum actuator load for each of the three tests was 967 kips (4,303 kN) at 3.21 inches (8.16 cm) of deflection, 969 kips (4,311 kN) at 3.75 inches (9.52 cm) of deflection, and 887 kips (3,947 kN) at 3.43 inches (8.72 cm) of deflection for the 0°, 15°, and 30° tests, respectively. Maximum longitudinal load for each of the three tests was 481 kips (2,138 kN) at 3.21 inches of deflection, 363 kips (1,614 kN) at 1.99 inches of deflection, and 322 kips (1,431 kN) at 1.99 inches of deflection for the 0°, 15°, and 30° tests, respectively.

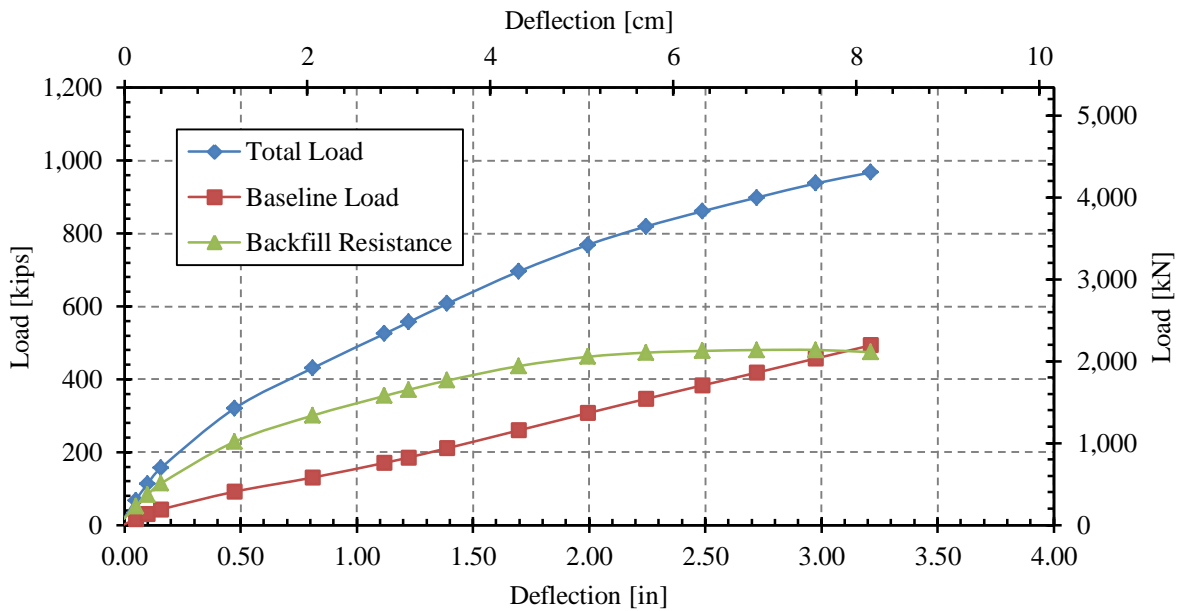


Figure 5-6: Load-deflection curves for the 0° test

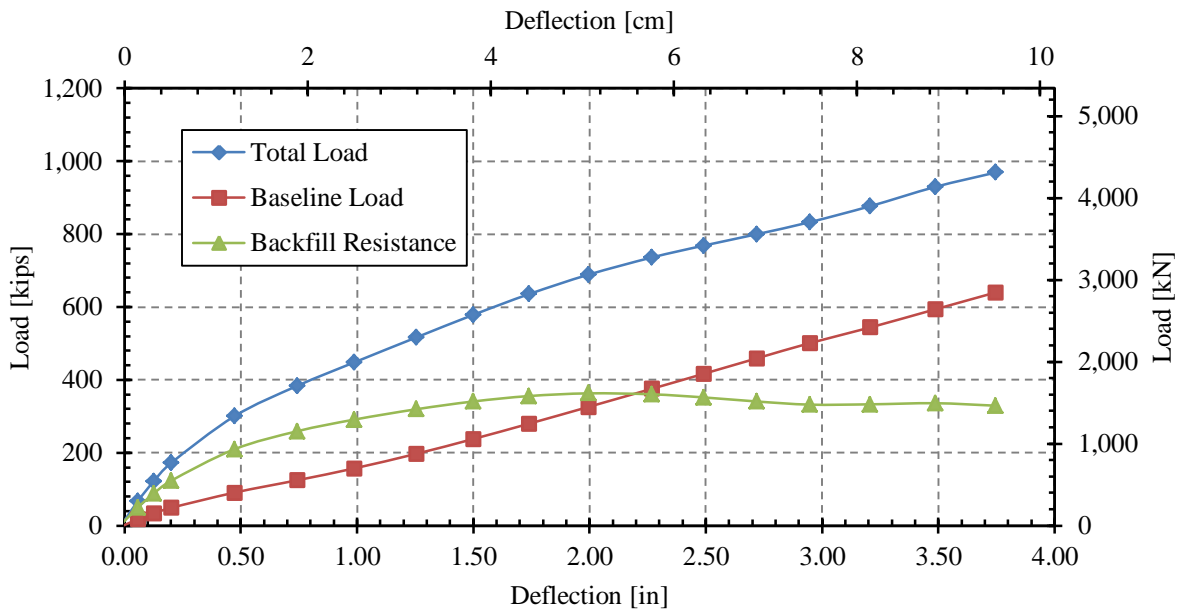


Figure 5-7: Load-deflection curves for the 15° test

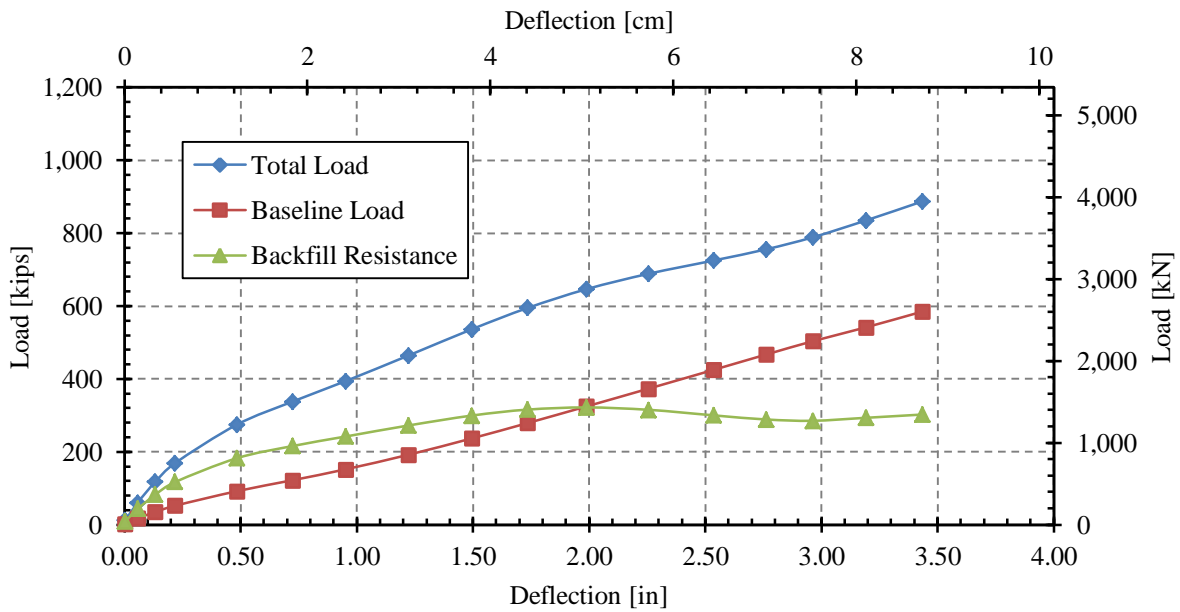


Figure 5-8: Load-deflection curves for the 30° test

Using the developed longitudinal force versus backwall deflection curves the passive force versus backwall deflection curves were obtained by multiplying the individual load points of each curve by the cosine of the appropriate skew angle. Figure 5-9 shows the resulting passive force versus longitudinal deflection curves for the 0°, 15°, and 30° skew tests. The peak passive force, as calculated using the procedure described at the beginning of this section, for the 0°, 15°, and 30° tests was 481 kips (2,138 kN) at 2.97 inches (7.54 cm) of deflection, 351 kips (1,559 kN) at 1.99 inches (5.05 cm) of deflection, and 279 kips (1,240 kN) at 1.99 inches (5.05 cm) of deflection, respectively. Peak passive force for each test occurred at 0.041H, 0.03H, and 0.03H, for the 0°, 15°, and 30° backfill tests, respectively, where H is the height of the backwall. The fact that the peak passive force was obtained at normalized backwall deflections between 0.03H and 0.05H is in good agreement with previous full-scale lateral load tests conducted with dense sand [see Rollins and Cole (2006)].

As can be seen in Figure 5-9, the passive force-deflection curve for the 0° skew test remained essentially constant past failure, while the passive force decreased about 8% below the peak passive force for the 15° test, and 11% for the 30° test. The lack of an apparent drop after failure for the 0° skew test may have resulted from not being able to push the pile cap far enough for the complete failure wedge to develop.

Field tests seem to indicate that the initial backfill stiffness is slightly dependent on skew angle. On the other hand lab tests do not indicate a significant decrease in initial backfill stiffness associated with high skew angles as shown in Figure 5-10. This may indicate that the 3D failure patterns extant for the field tests have some effect on the initial stiffness of the backfill materials. Additional lab and/or field tests should be conducted to more fully understand the effect that skew angle has on the initial stiffness of the backfill materials.

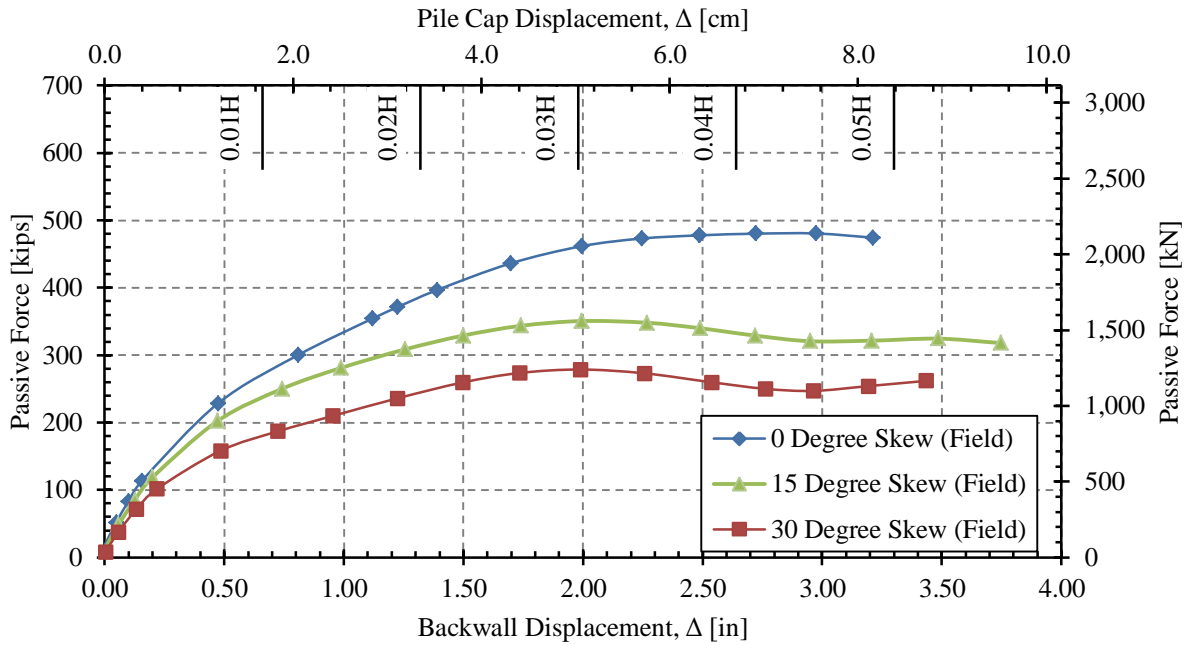


Figure 5-9: Passive force-deflection curves for the 0°, 15°, and 30° skew tests

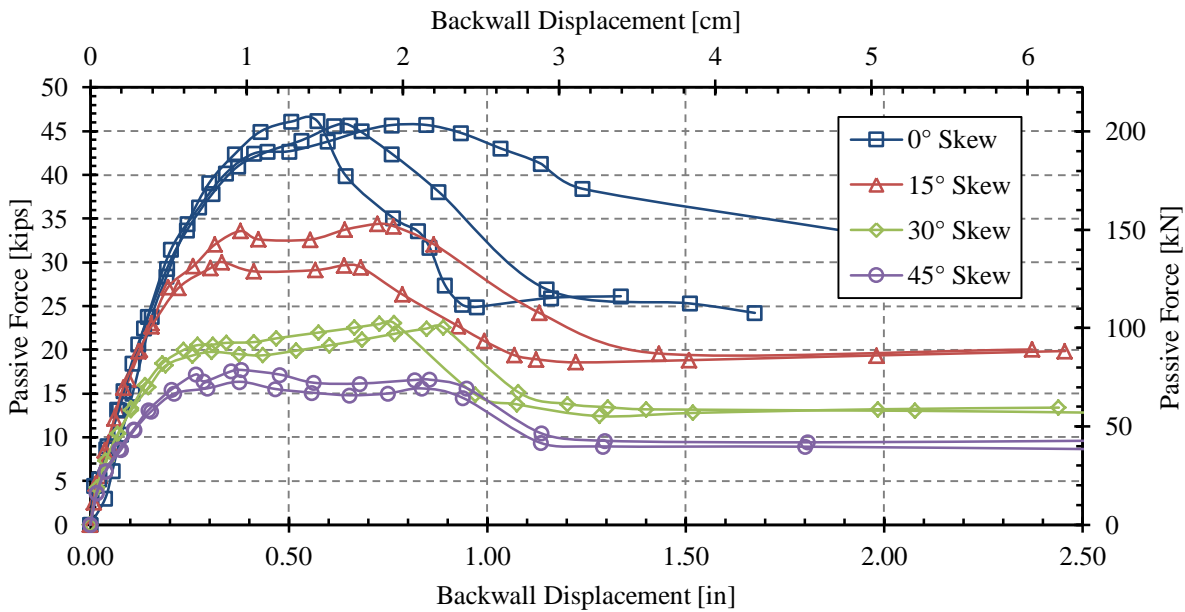


Figure 5-10: Lab test passive force versus backwall displacement results (Rollins and Jessee 2012)

Judging by the shape of the 0° passive force-deflection curve, a drop in passive force was likely eminent as the ultimate passive force appears to have been achieved at a lower normalized deflections for the 30° test than for the 15° test. Therefore, the ultimate passive force may have been achieved at a slightly higher normalized deflection than the 15° test. This apparent reduction in the normalized deflection necessary to develop the ultimate passive force may be caused by a type of progressive failure in which the material at the acute corner of the backwall strains more and fails earlier than material at the obtuse corner.

To determine the relationship between peak passive force and bridge skew angle, the peak passive force for a given skew test was normalized against the peak passive force for the 0° skew test. The results, plotted against skew angle, are shown in Figure 5-11 which also shows the reduction factors and corresponding equation for R_{skew} obtained using the data published by Rollins and Jessee (2012). Numerical model results obtained by Shamsabadi et al. (2007) are also shown in this figure. The equation for R_{skew} shown in this figure was derived using the lab test results. For the 15° and 30° field-tests the peak passive force was found to be 73% and 58%, respectively, of the peak passive force for the 0° skew test.

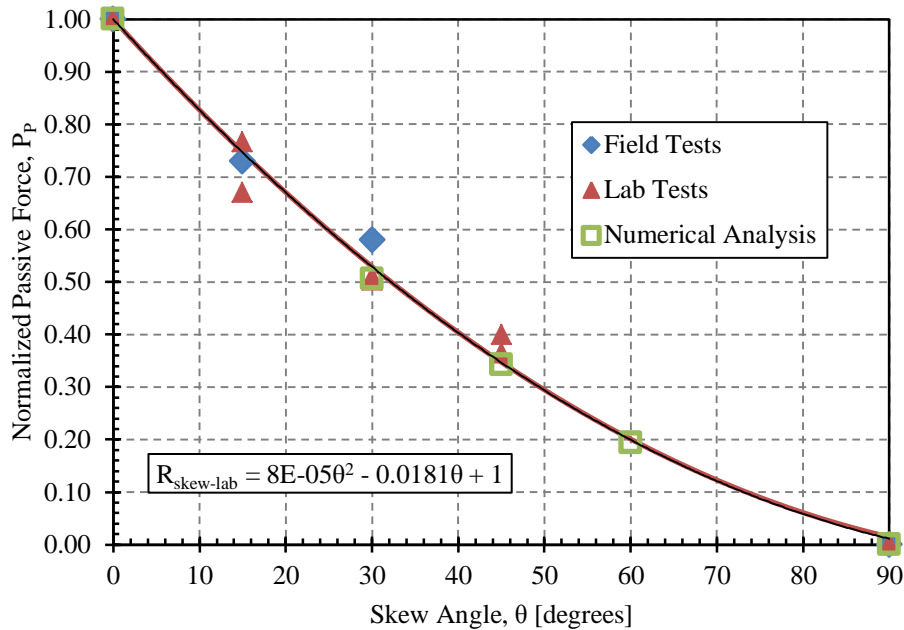


Figure 5-11: Normalized peak passive force with respect to skew angle as obtained from field tests, lab tests, and numerical analyses

Figure 5-12 shows the second order trend regression lines calculated using the field test data (this study), lab test data (Rollins and Jessee 2012), numerical analysis results (Shamsabadi et al. 2007), and combined results from all tests. In summary, all three approaches for determining the affect that skew angle has on the reduction in the peak passive force produce very similar results which appear to be fairly independent of skew angle.

Equation (5-1) shows the equations that define the reduction factor, R_{skew} , as a function of skew angle, θ , that correspond to the regression lines for the field test data points, lab test data points, numerical analysis data points, and all data points. These curves predict that at skew angles of 15° , 30° , and 45° one should expect that the peak passive force for the skew case be approximately 75%, 55%, and 35% of the non-skewed passive force, respectively. All curves were generated assuming that R_{skew} is equal to 1 and 0 at skew angles of 0° and 90° , respectively,

which is consistent with the breakdown of forces described in Section 2.3. Additional tests should be conducted at high skew angles to verify the numerical model results and insure that the aforementioned trend holds true.

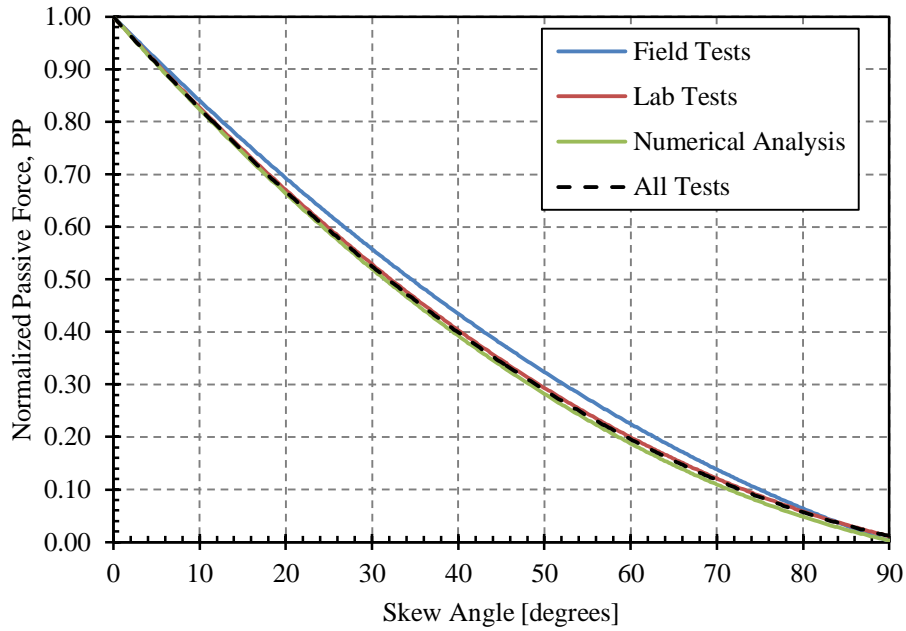


Figure 5-12: Reduction factor trend lines plotted versus skew angle for field tests, lab tests, numerical analysis, and all tests

$$R_{skew} = 6 * 10^{-5}\theta^2 - 0.0166\theta + 1.0 \text{ (field tests)} \quad (5-1)$$

$$R_{skew} = 8 * 10^{-5}\theta^2 - 0.0181\theta + 1.0 \text{ (lab tests)}$$

$$R_{skew} = 8 * 10^{-5}\theta^2 - 0.0185\theta + 1.0 \text{ (numerical analysis)}$$

$$R_{skew} = 8 * 10^{-5}\theta^2 - 0.0183\theta + 1.0 \text{ (all data points)}$$

where

$$R_{skew} = \frac{P_{P-skew}}{P_{P-no skew}}$$

This information can be applied in bridge design practice by estimating the peak passive force for a given non-skewed bridge abutment using an appropriate method (see Section 2.1.4 or Section 2.5), and then multiplying that peak passive force by the reduction factor, R_{skew} [can be obtained either from Figure 5-12, or Equation (5-1)], to get the estimated peak passive force for a skewed bridge abutment.

As mentioned previously, additional tests would need to be conducted in order to determine if the initial backfill stiffness parameters used in the Caltrans method (see Section 2.5.1) can be directly applied for skewed bridge abutments, or if the backfill stiffness should be reduced for higher skew angles.

5.4 Differential Actuator Loading

Figure 5-13, Figure 5-14, and Figure 5-15 show the individual passive force versus pile cap deflection curves for the 0°, 15°, and 30° skew 5.5-ft (1.68-m) unconfined backfill tests, respectively. The plots also show the contributions of the east and west actuators to the total passive force versus deflection curve.

For the 0° test Figure 5-13 shows that the actuators acted roughly uniformly during the entirety of the test; though as was discussed in Sections 5.1 and 5.2, the east actuator began losing ground relative to the west actuator after about 1.7 inches (4.32 cm) of pile cap deflection. In addition to the conditions described in Sections 5.1 and 5.2, there is a very slight possibility that the higher deflections on the west side of the pile cap may have influenced the development of the total passive force deflection curve. However, the relatively minor differential movement of the east and west side of the pile cap likely had very little effect on the total passive force against a backwall 11 feet (3.35 m) wide and 5.5 feet (1.68 m) high.

While for all tests, both actuators achieved peak loads at approximately the same deflection [about 2 inches (5.0 cm)], the load measured by the east actuator tended to remain relatively constant beyond this point, whereas the load applied by the west actuator tended to decrease slightly and then remain constant as deflection increased. This may indicate that the soil at the acute corner of the backwall failed before the soil at the obtuse corner, and thereafter the passive failure wedge began to break down beginning at the acute corner of the backwall and then progressing to the obtuse corner.

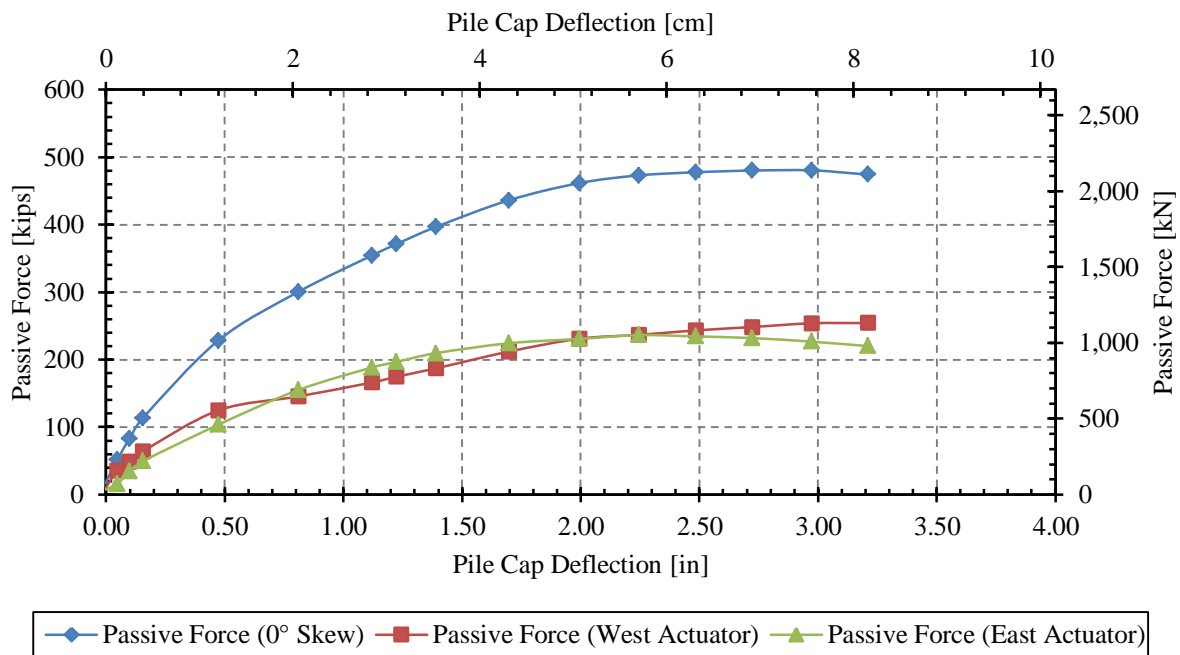


Figure 5-13: Total and individual actuator contribution to the passive force versus pile cap deflection curve for the 0° test

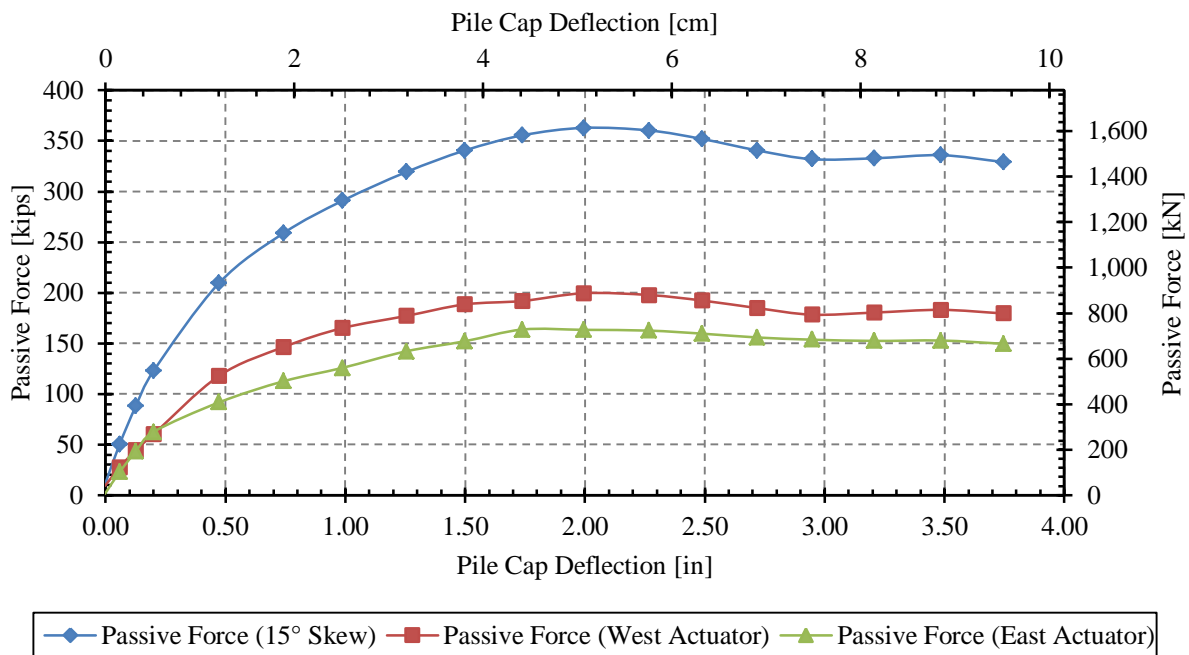


Figure 5-14: Total and individual actuator contributions to the passive force versus pile cap deflection curve for the 15° test

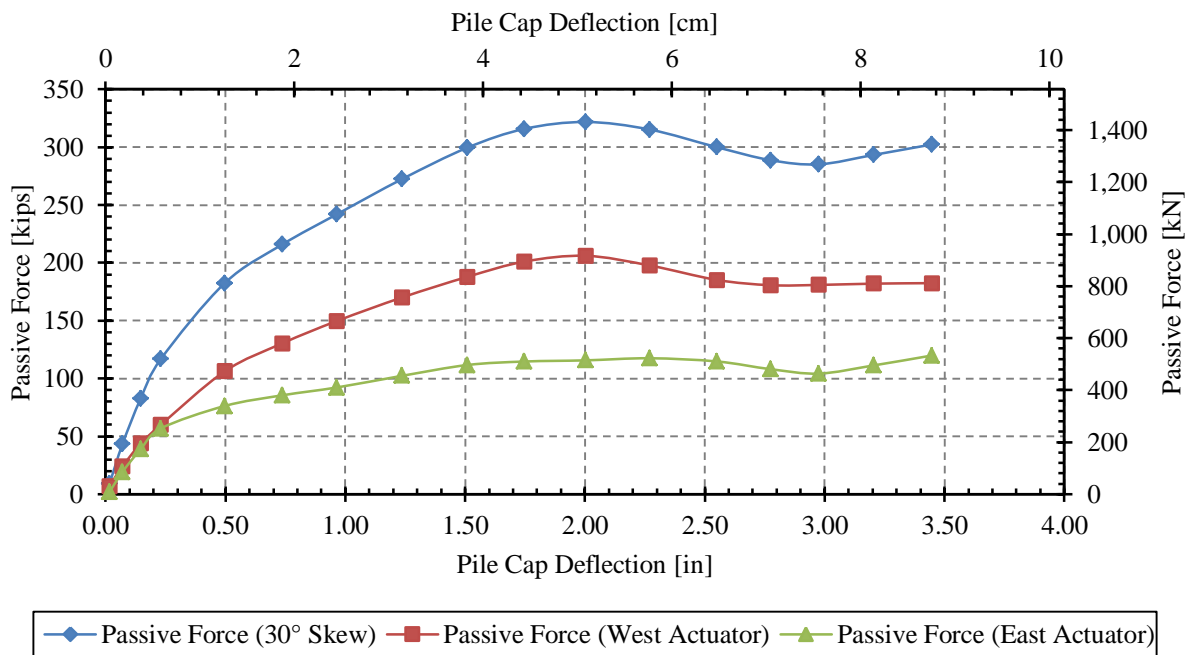


Figure 5-15: Total and individual actuator contribution to the passive force versus pile cap deflection curve for the 30° test

As can be seen in Figure 5-14 and Figure 5-15 the significant differential actuator loading began at a deflections equal to about 0.5 inch (1.27 cm) and remained fairly constant for the remainder of the test. Specifically, for the 15° test the west and east actuators held approximately 55% and 45% of the total load, respectively; and for the 30° test the west and east actuators held approximately 62% and 38% of the total load, respectively as shown in Figure 5-16.

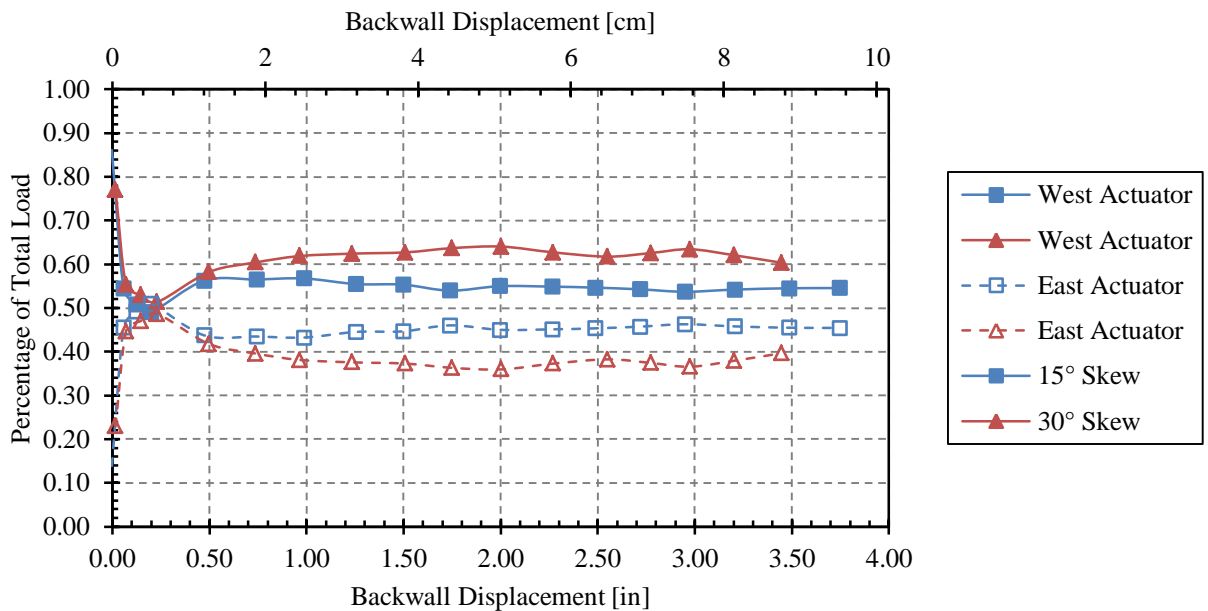


Figure 5-16: Percentage of total load resisted by west and east actuators for 15° and 30° skew tests

The data presented in the previous figures can be further summarized and broken down by converting the differential loading of the two actuators into an applied moment. Figure 5-17 shows the applied counterclockwise moment for each of the three tests with respect to pile cap deflection. As would be expected for the 15° and 30° tests, a fairly significant clockwise moment was applied to the pile cap in order to keep cap rotation to a minimum. However, likely due to the reaction foundation issues described in Sections 5.1 and 5.2, the moment applied to the pile cap for the 0° test varied from a maximum counterclockwise moment of 51 kip-ft (69 kN-m) at a

deflection of 1.39 inches (3.53 cm) to a maximum clockwise moment of 77 kip-ft (104 kN-m) at a deflection of 3.21 inches (8.15 cm). The minimum and maximum applied moment do not appear to correspond to any particular behavior of either the backfill or pile cap for the 0° test.

For the 15° test the applied moment varied from a maximum counterclockwise moment of 5 kip-ft (7 kN-m) at 0.2 inches (0.51 cm) of deflection to a maximum clockwise moment of 88 kip-ft (120 kN-m) at 0.99 inches (2.51 cm) of deflection. For the 30° test the applied moment varied from a minimum clockwise moment of 7 kip-ft (10 kN-m) at a deflection of 0.23 inches (0.58 cm) of deflection to a maximum clockwise moment of 203 kip-ft (276 kN-m) at a deflection of 2.0 inches (5.08 cm) of deflection. For the 30° test the maximum applied moment corresponded exactly with the peak passive force; however, for the 15° test the applied moment remains essentially constant beyond the maximum moment at 0.99 inch (2.51 cm) but then begins to decrease after the peak passive force is obtained at 2 inches (5.07 cm) of deflection. A similar decrease in applied moment occurred for the 30° test as well.

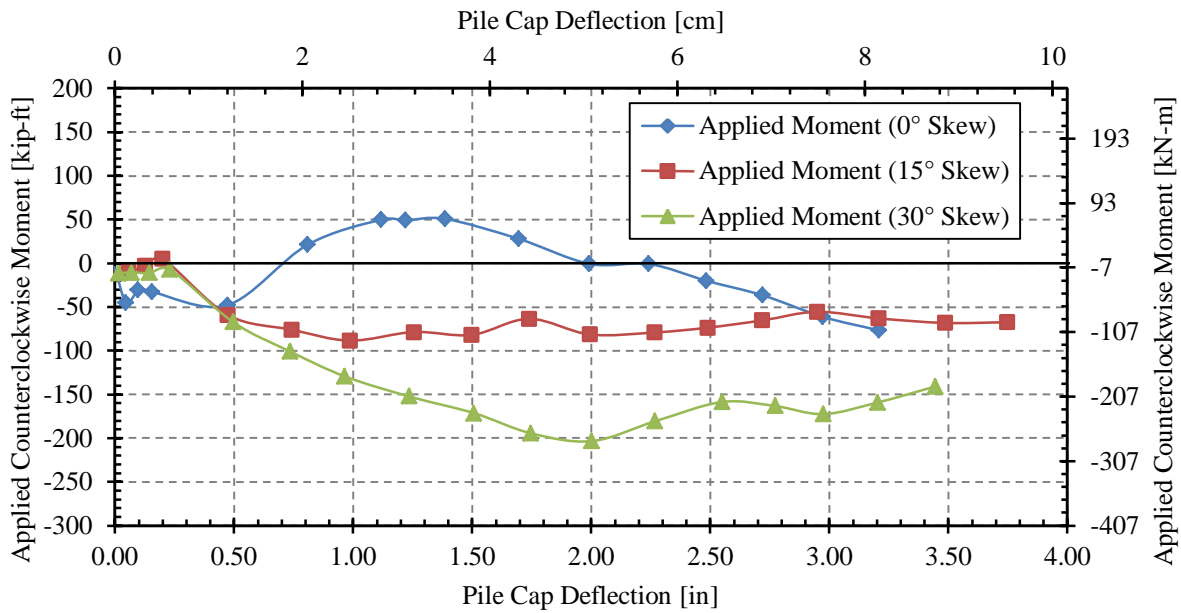


Figure 5-17: Actuator applied counterclockwise for 0°, 15°, and 30° tests

5.5 Actuator Load Reduction with Respect to Time after Peak

As noted in Section 4.3, the pile cap was displaced into the backfill zone at an approximate velocity of 0.25 inches per minute (6.4 mm/min) to target displacement intervals of 0.25 inches (6.4 mm). At each displacement interval the pile cap position was held constant for approximately 2 minutes in order to observe the reduction in actuator load with respect to time. So that individual load intervals could be compared, the actuator load at a given time interval after the peak load was normalized against the peak load for that displacement interval. Data will be presented as figures showing P/P_{max} plotted against the time after the peak, where P/P_{max} is the load at a given time after the peak normalized against the peak load for that displacement interval.

Due to the inherent variability in the normalized load-time plots, the load-time response for the backfill alone could not be analyzed; therefore in order to estimate the load-time response

for the backfill alone the appropriate baseline load-time response will be compared with the total load-time response, and conclusions will be drawn using that information.

This section will first present the normalized 0° and 30° baseline load-time plots, and then the normalized backfill load-time plots for the 0° , 15° , 30° backfill tests will be addressed.

Figure 5-18 and Figure 5-19 show the reduction in reaction force, P/P_{\max} , with respect to time for the 0° and 30° baseline tests, respectively for selected displacement intervals. These figures show that the reduction in force with respect to time is significantly higher and more variable for low load values. At higher load values the curves are more consistent from one increment to the next and less variable. For the 0° and 30° baseline tests, the average reduction in reaction force for all displacement intervals after two minutes is approximately 10.2% and 9%, respectively; however, the reduction in force after two minutes for the last 5 displacement intervals is about 8%, and 7%, for the 0° and 30° tests, respectively rather than 10.2% and 9%. The reduction in resistance is not linear with time but does tend to become more gradual with time. This behavior can be modeled with a log-linear relationship. Equations showing the best-fit relationship for the average of all displacement increments are shown in each figure. The correlation coefficients associated with these equations are very high in all cases. Creep strength loss as a log of time relationship is well documented in the technical literature (Mitchell and Soga 2005).

Figure 5-20, Figure 5-21, and Figure 5-22 shows the reduction in reaction force with respect to time for the 0° , 15° , and 30° skew backfill tests, respectively. These plots show that there is an obvious similarity between the reduction plots for the baseline and backfill tests. Namely, the reduction in reaction force appears to decrease in a log-linear fashion with similar reduction values after 2 minutes.

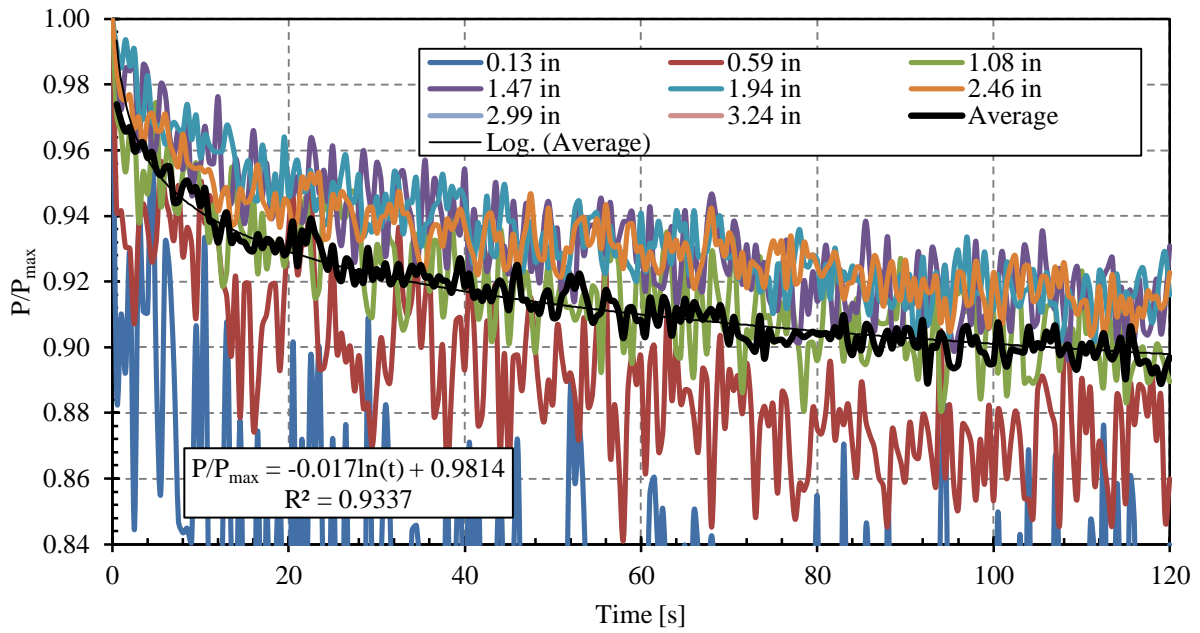


Figure 5-18: Reduction in reaction force with respect to time for 0° skew baseline test

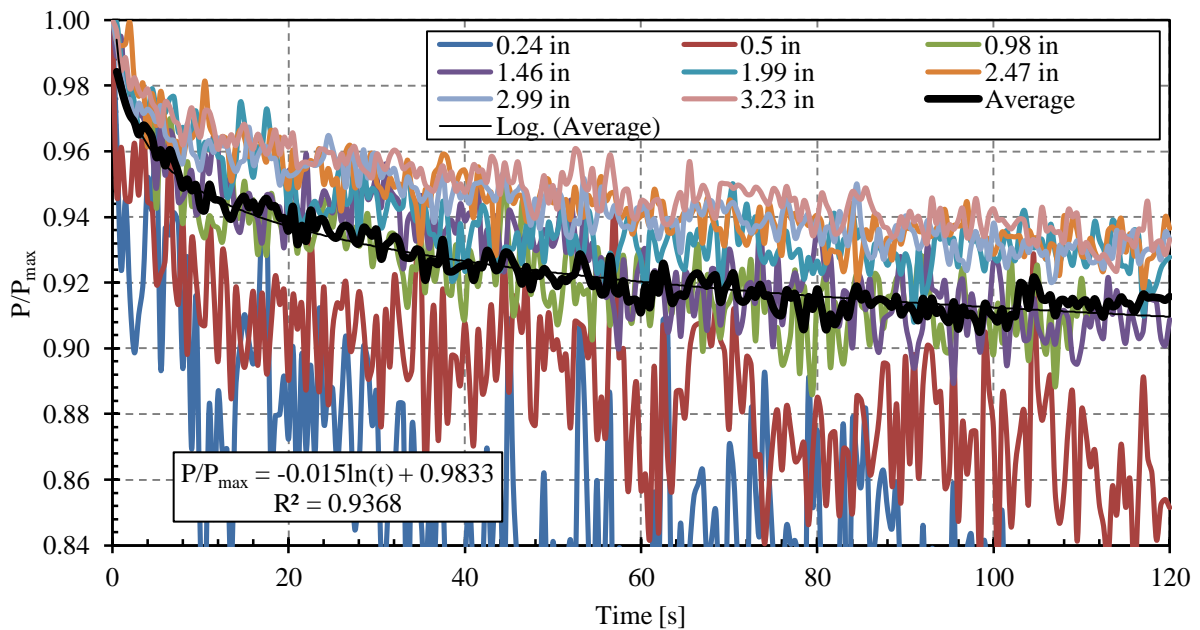


Figure 5-19: Reduction in reaction force with respect to time for 30° skew baseline test

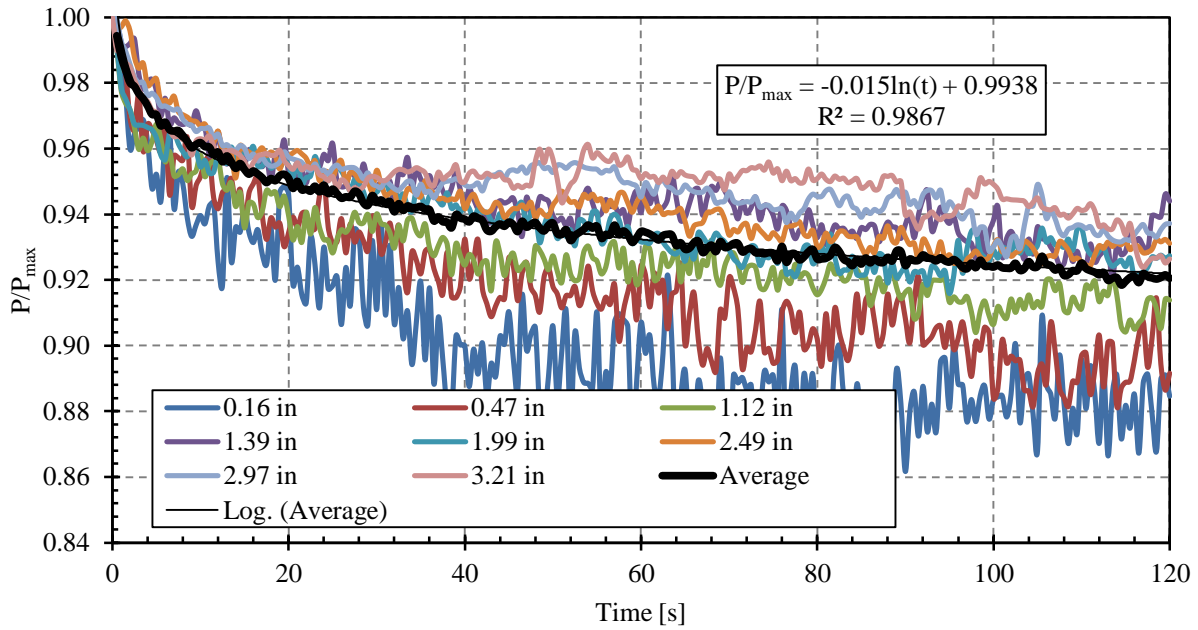


Figure 5-20: Reduction in reaction force with respect to time for the 0° test

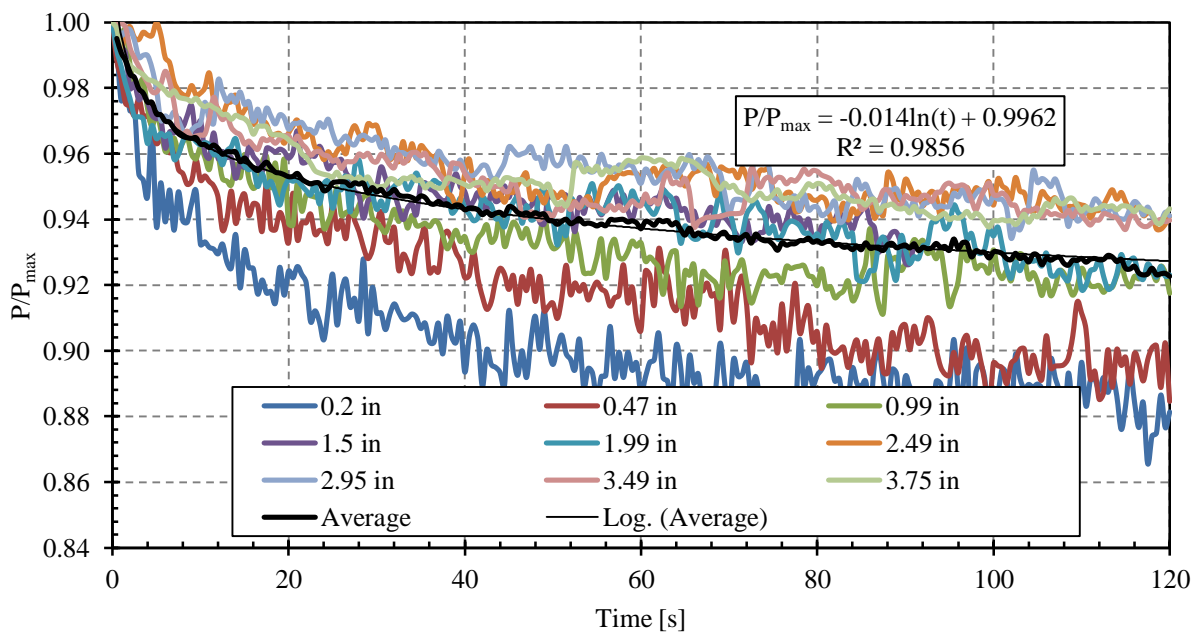


Figure 5-21: Reduction in reaction force with respect to time for the 15° test

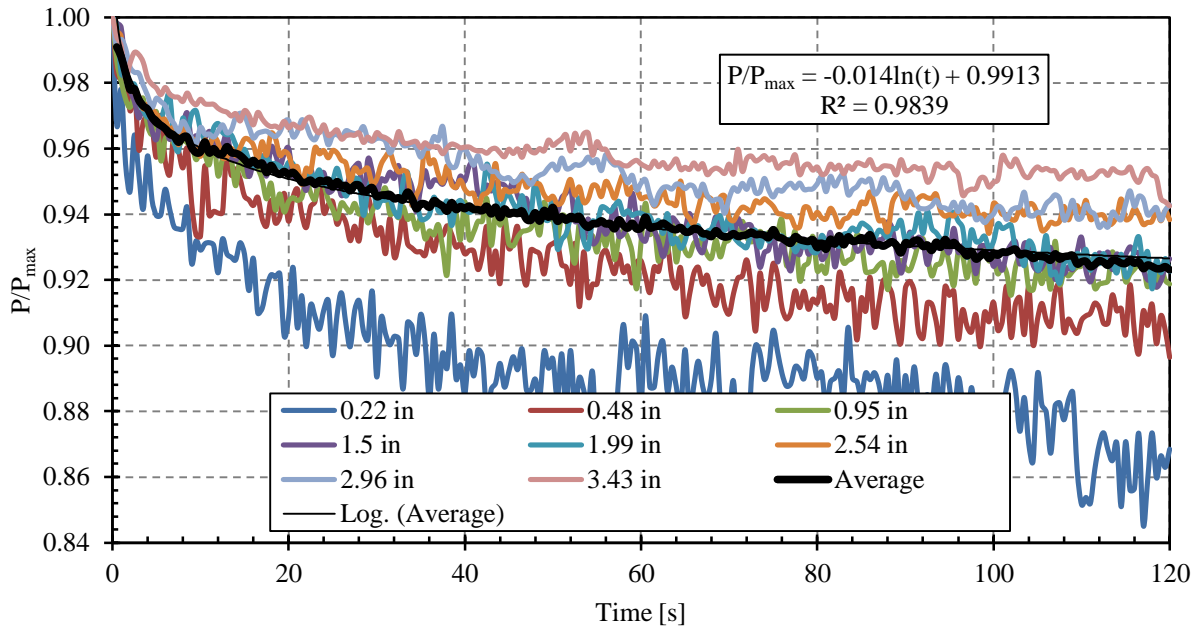


Figure 5-22: Reduction in reaction force with respect to time for the 30° test

Table 5-1 compares the reduction in reaction force for the baseline and backfill tests for all displacement intervals, and for the last five displacement intervals, and shows the average reduction lines for each of the aforementioned tests. A review of the three plots, the values in Table 5-1, and the reduction lines shown in Figure 5-23 indicates that there is much more variability in the load versus time relationship for the first two displacement increments than for the subsequent increments. Furthermore, the reduction in reaction force appears to be less significant for higher loads. Additionally, skew angle appears to reduce the reduction in reaction force with respect to time in comparison to the 0° test. However, additional tests would need to be carried out at higher skew angles and higher displacement levels to verify that this is indeed the case.

Table 5-1: Reduction in Reaction Force with Respect to Time for All Tests

	<i>Reduction after 2 Minutes for All Intervals</i>	<i>Reduction after 2 Minutes for Last 5 Displacement Intervals</i>
0° Baseline Test	10.2%	8.0%
30° Baseline Test	9.0%	7.0%
0° Backfill Test	7.8%	6.5%
15° Backfill Test	7.1%	5.8%
30° Backfill Test	7.3%	5.7%

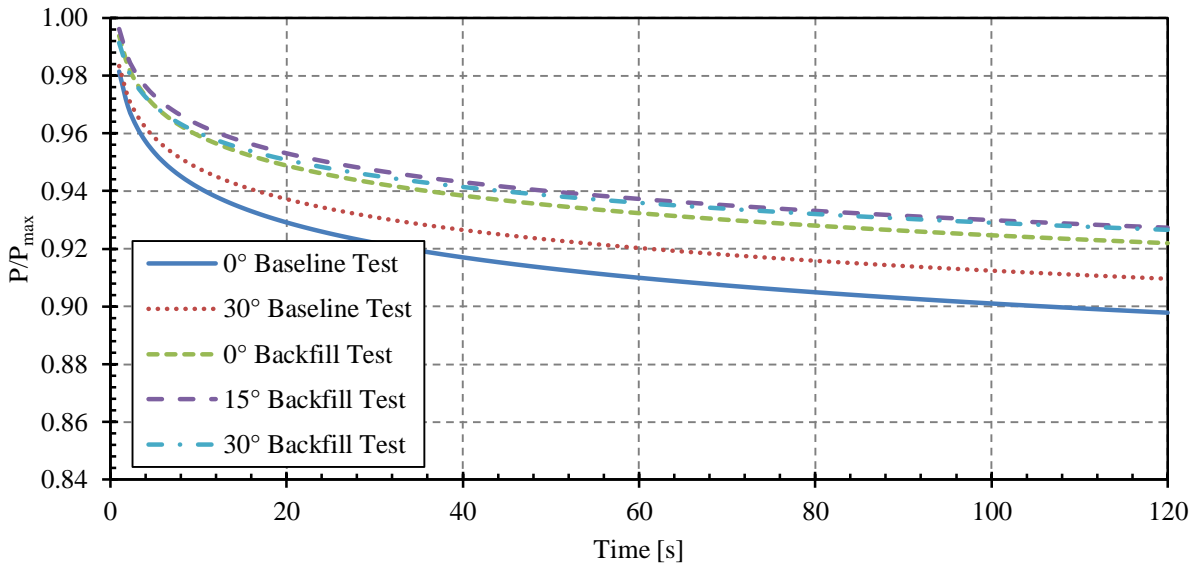


Figure 5-23: Average reduction in reaction force with respect to time for the 0° and 30° baseline tests, and for the 0°, 15°, and 30° backfill tests

Considering all of the information presented above the backfill material alone likely behaves in a very similar fashion to either the piles alone or the piles and backfill together, which means that the reduction in passive force after two minutes would be between 7% and 10% of the peak passive force if only the passive force were measured.

6 BACKWALL MOVEMENT

This chapter will present relevant backwall and pile movement data as obtained by the, shape arrays, inclinometers, and string pots for the 0°, 15°, and 30° skew 5.5-ft (1.68-m) unconfined backfill tests. Pile deflection data over the length of the piles, as obtained by the shape arrays and inclinometers, will be presented in this chapter. Pile deflection at the top of the piles will also be compared with the pile cap deflection data as obtained by the string pots.

6.1 Longitudinal and Transverse Backwall Movement

The shape arrays and inclinometers were used to measure the deflection versus depth profiles of the pile cap and piles over their entire length, through in two different fashions. The inclinometer measured the slope in the x- and y-direction of the pile over the entire length of the piles at 2-ft (0.61-m) intervals. By comparing the data obtained at the beginning and end of the test the differential pile displacement could be obtained. However, as two inclinometer passes were required per reading, and readings were taken in the north and south inclinometer tubes (15 to 20 minutes required for these readings), the time requirements precluded data collection for intermediate pile cap displacement intervals.

As the shape arrays measured movement in both the x- and y-direction, they, like the inclinometer, provided data pertaining to both the longitudinal and transverse movement of the piles. By comparing transverse displacement readings from the north and south shape

arrays/inclinometers, pile cap rotation about the vertical axis could also be obtained. Rollins et al. (2009) provide a detailed description of the type and quality of data that can be obtained using shape arrays.

Unfortunately, the shape arrays were not installed with their primary axes aligned with the primary axes of the pile cap, but rather the instruments were aligned as shown in Figure 6-1 with the top of the figure representing the north end of the pile cap. As primary pile cap movement occurred in the north direction the north shape array was installed such that the y-axis of the instrument was approximately 180° off, and the south shape array was installed with the y-axis approximately 220° off in the clockwise direction. Therefore, in order to obtain relevant pile cap deflection data, the shape array direction vector had to be aligned with the inclinometer direction vector; therefore, *any* deviations in the reduced inclinometer data from reality would similarly be reflected in the reduced shape array data. Information pertaining to the procedures for aligning the shape array vector with the inclinometer vector can be found in Appendix A.

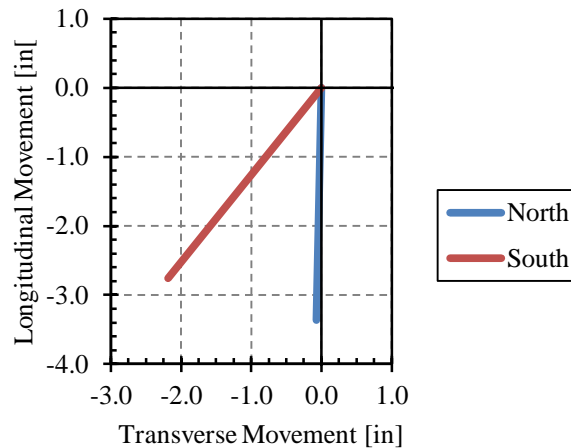


Figure 6-1: Relative north and south shape array measurement directions where the top of the cap represents the north end of the pile cap

6.1.1 Longitudinal Pile Cap Movement

Figure 6-2, Figure 6-4, and Figure 6-6 show longitudinal pile displacement versus depth profiles for the 0°, 15°, and 30° tests at test completion as measured by the north and south shape arrays, inclinometers, and string pots (only the south shape arrays was used for the 30° test as the north shape array was not functioning).

As can be seen in these figures, all three instruments recorded very similar data, with the north shape array and inclinometer readings generally agreeing quite closely with the data recorded by the string pots. The discrepancy in the data recorded by the north and south shape arrays likely occurred for the reasons described in Section 3.3.6.3.

Figure 6-3, Figure 6-5, and Figure 6-7 show longitudinal pile displacement versus depth profiles for the 0°, 15°, and 30° tests at selected pile cap displacement intervals as measured by the north and south shape arrays. As would be expected for all tests, the piles behaved in a very similar fashion with the top 20 feet (6.10 m), or approximately 19 pile diameters, being the only part of the pile that experienced significant lateral deflection. This point, 19 pile diameters below the surface, would be considered the point of fixity in a simplified analysis. The forward rotation of the pile cap itself (top 5.5 ft) is generally quite small but it does occur despite the fact that the pile cap is relatively massive. Furthermore, these three figures that the depth to fixity is fairly independent of load.

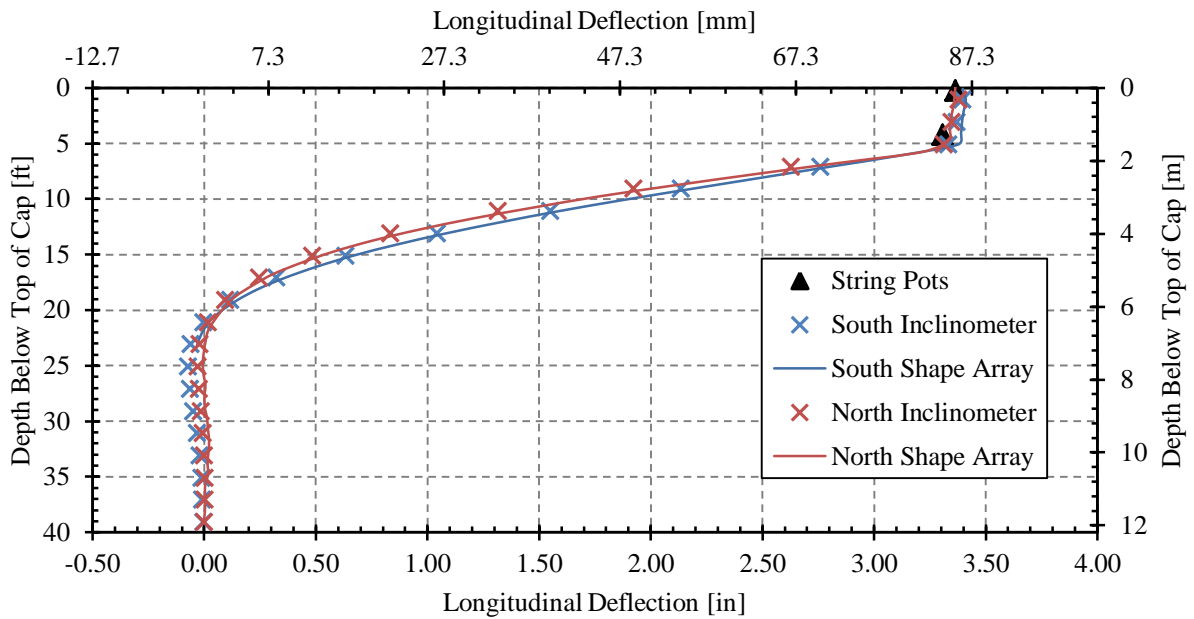


Figure 6-2: Longitudinal pile deflection as measured by the north and south shape arrays, inclinometers, and string pots for 0° test

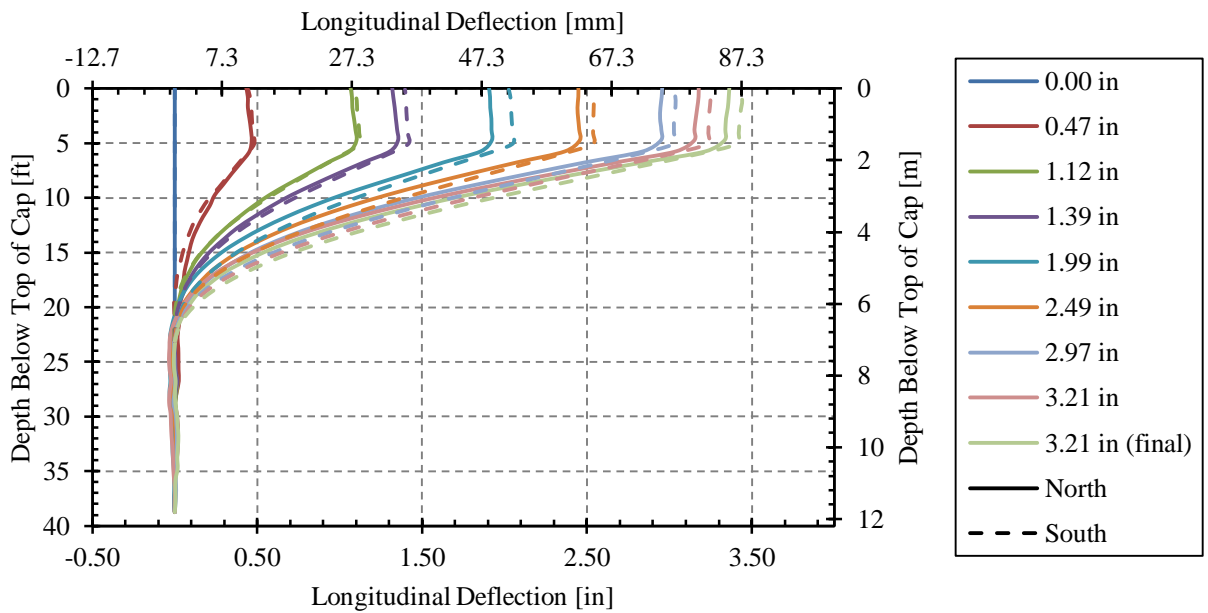


Figure 6-3: Longitudinal pile deflection at selected pile cap displacement intervals as measured by the north and south shape arrays for the 0° test

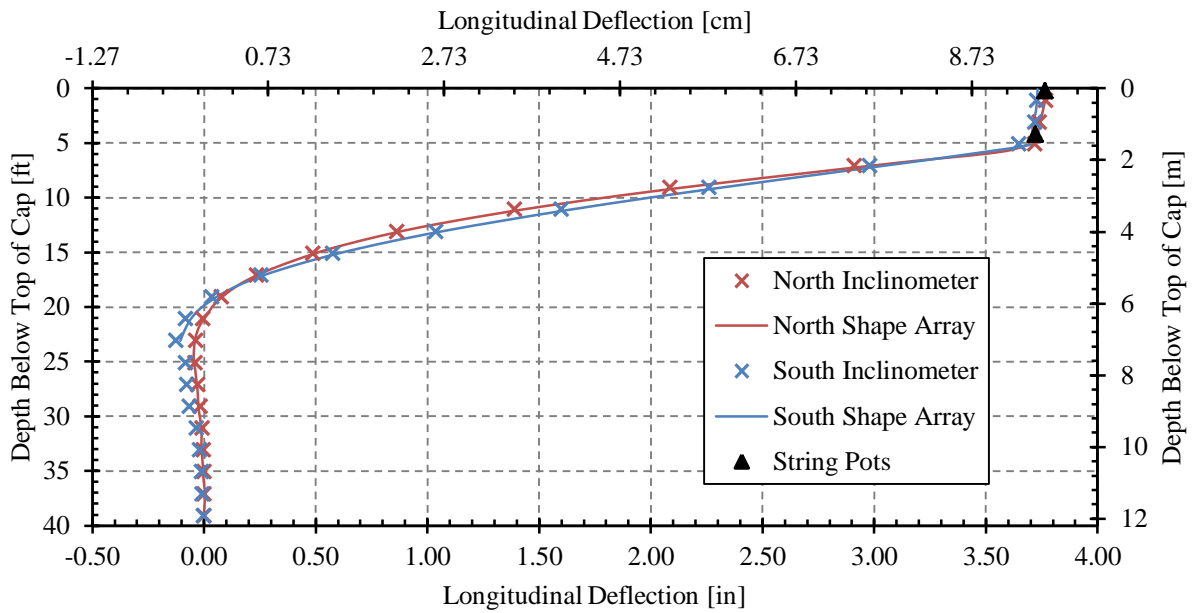


Figure 6-4: Longitudinal pile deflection as measured by north and south shape arrays, inclinometers, and string pots for 15° test

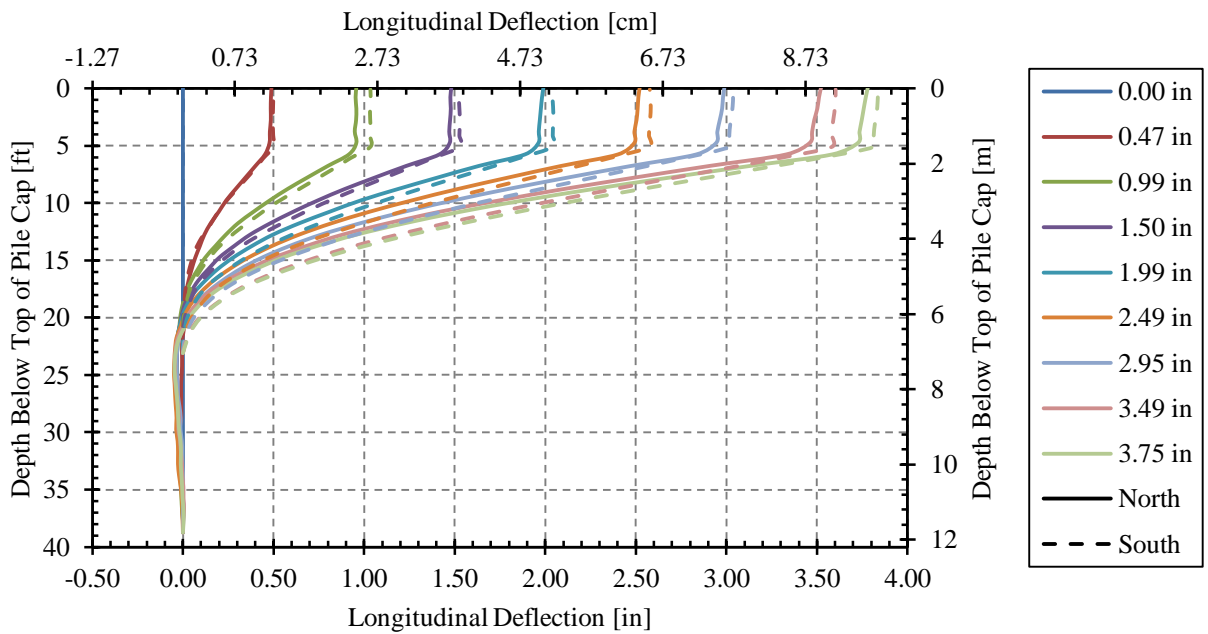


Figure 6-5: Longitudinal pile deflection at selected pile cap displacement intervals as measured by the north and south shape arrays for the 15° test

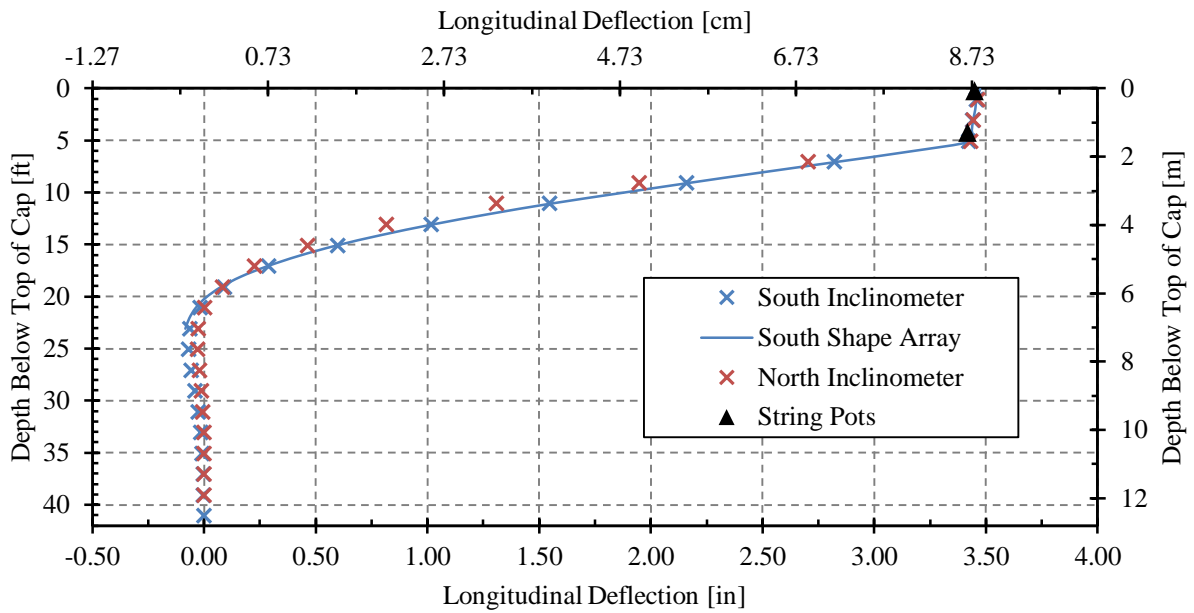


Figure 6-6: Longitudinal pile cap deflection as measured by shape arrays, inclinometers, and string pots for 30° test

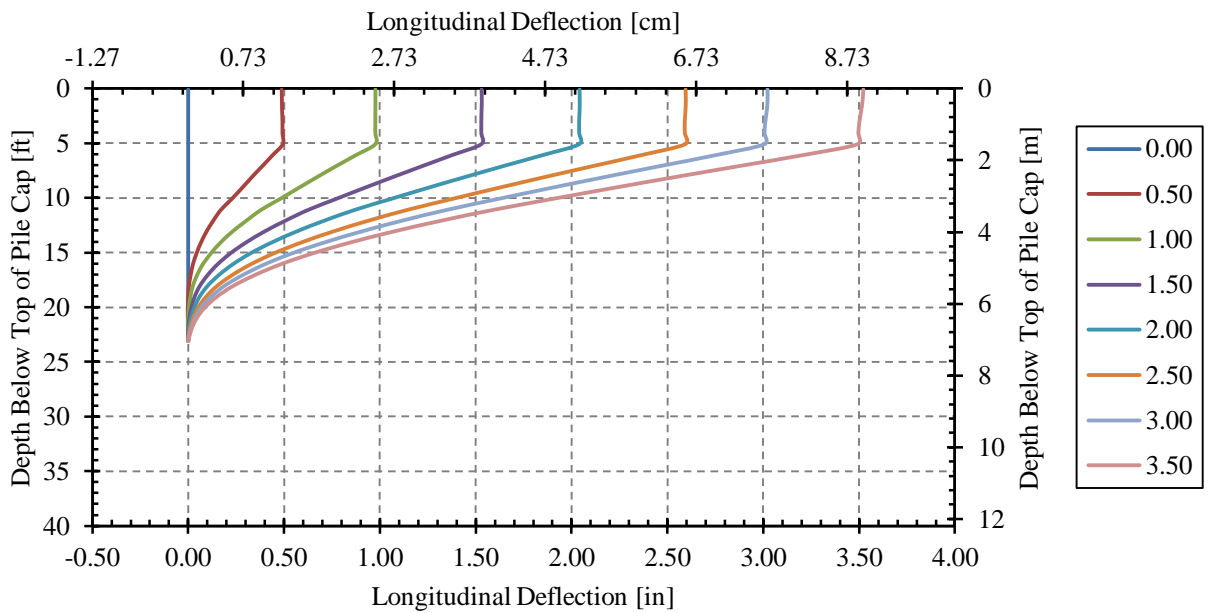


Figure 6-7: Longitudinal pile deflection at selected pile cap displacement intervals as measured by the south shape arrays for the 30° test

6.1.2 Transverse Pile Deflection

Figure 6-8, Figure 6-9, and Figure 6-10 show transverse pile deflection for the 0°, 15°, and 30° skew 5.5-foot (1.68-m) unconfined backfill tests at test completion as measured by the shape arrays and inclinometers for the 0° and 30° test. For 15° test, LVDTs were installed on the side of the pile cap in an attempt to measure transverse pile cap deflection; however, as can be seen in Figure 6-9, the LVDT data did not agree very well with either the shape array or inclinometer data – likely due to the less-than-ideal instrument setup described in Section 3.3.6.2.

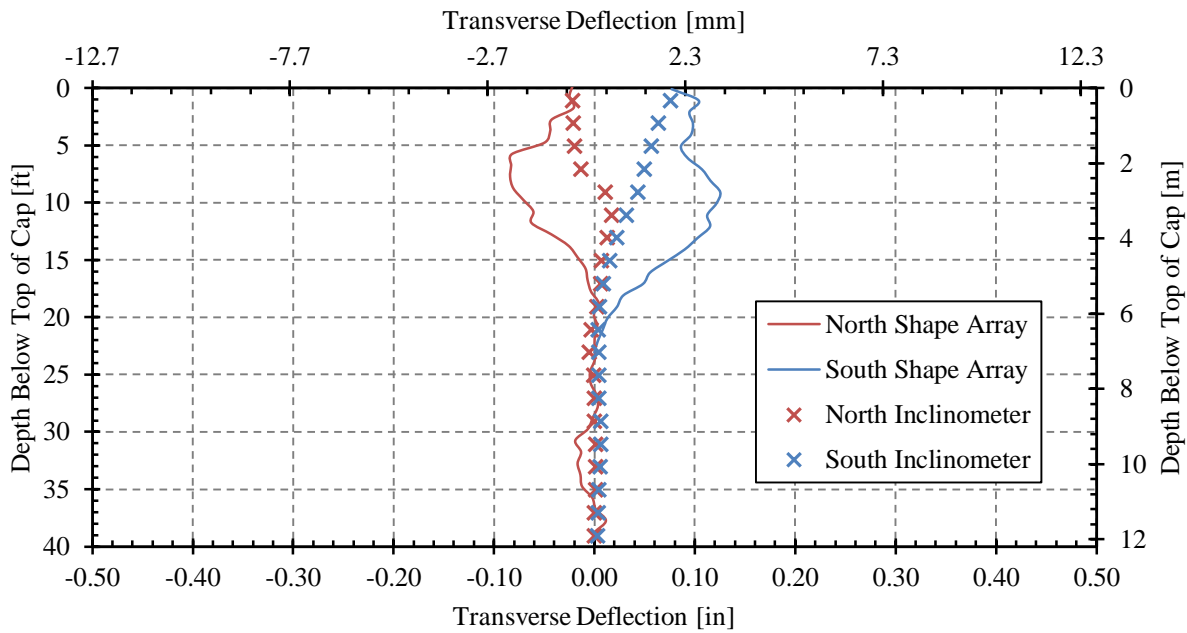


Figure 6-8: Transverse pile deflection as measured by the shape arrays and inclinometers for the 0° test

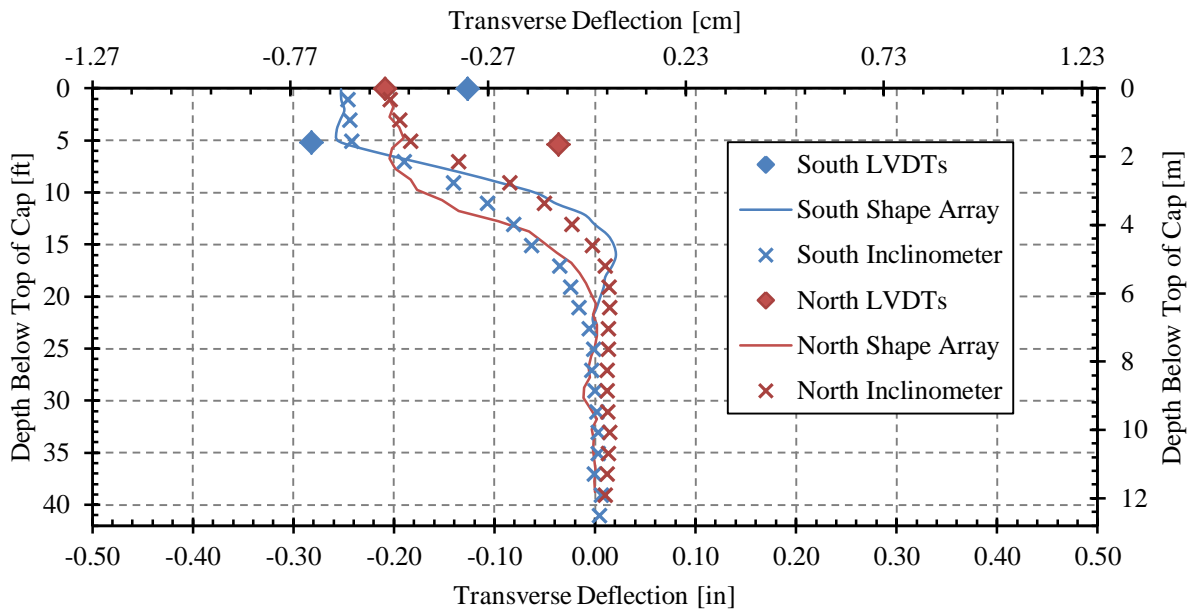


Figure 6-9: Transverse pile deflection as measured by the shape arrays, inclinometers, and LVDTs for the 15° test

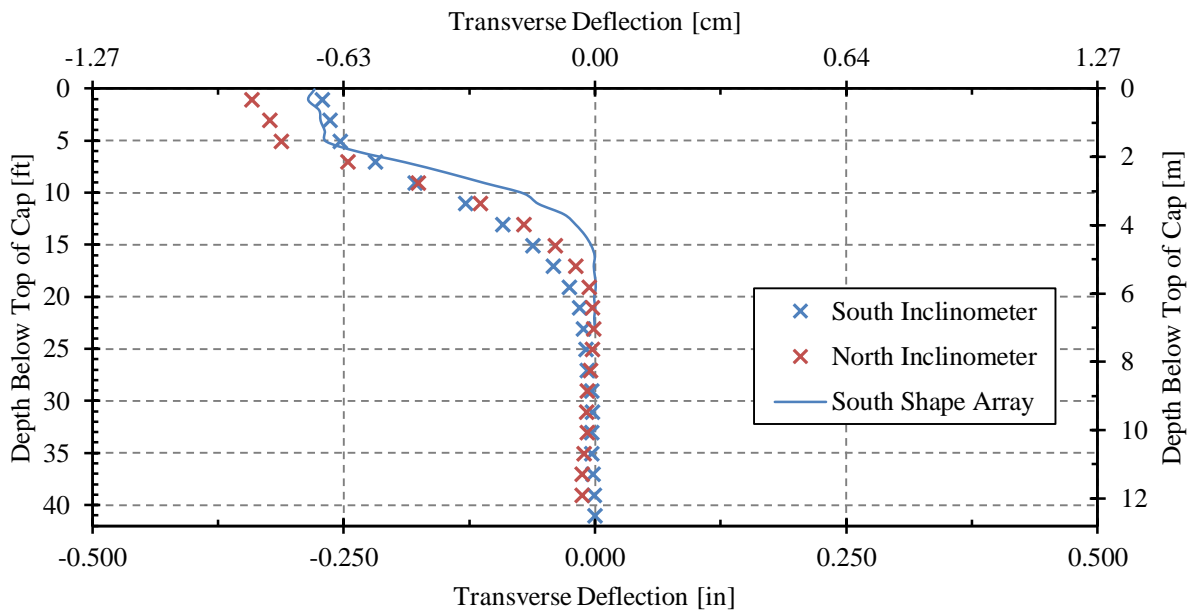


Figure 6-10: Transverse pile deflection as measured by the shape arrays and inclinometers for the 30° test

From the three curves shown above, the relative inaccuracy of the shape array at low displacement values is readily apparent. Despite this inaccuracy, the general behavior of the piles is clearly visible. Specifically, Figure 6-8 (0° skew test) indicates that the north pile moved to the west and the south to the east. Figure 6-9 (15° skew test) indicates that both the north and south piles moved to the west, though in this instance the south pile moved further than the north. Figure 6-10 (30° skew test) shows that, like the 15° test, the piles also moved to the west during the 30° test. This is not surprising considering component of the longitudinal force normal to the face of the wall (i.e. the passive force) was inclined towards the west.

As is readily apparent in Figure 6-8 the transverse pile displacement with depth profile as recorded by the shape array is rather unrealistic. However, the instrument manufacturer suggests that the shape array cannot accurately measure displacements less than 2 mm (Measurand Inc. 2009). That being said, the total instrument displacement for this test was nearly 3.5 inches (8.90 cm) which is more than enough displacement for the instrument to accurately measure. But, as described in Section 3.3.6.3 shape array movement in the x and y direction is measured independently through the use of an accelerometer that measures tilt in the x and y planes. Therefore, if only very small deflections (less than 2 mm) occurred in either the x or y direction (as was the case for the north shape array for the 0° test), then the measured shape array displacement data is not going to be precise relative to the actual instrument movement.

6.2 Backwall Rotation

Using the pile cap displacement data obtained from both the string pots and shape arrays/inclinometer readings, pile cap rotation about a vertical axis could be calculated. Also, using the data obtained from the string pots, pile cap rotation about a transverse axis could also be calculated. This section will describe pile cap rotation information as obtained from these

instruments. However, as was expressed above, shape arrays cannot be used with any real degree of accuracy to measure small displacements; therefore, the plots that will be presented below should be understood as showing general trends only. Furthermore, though the shape array/inclinometer data could technically be used to monitor cap rotation about longitudinal and transverse axes, the incredibly small differential displacements preclude using the shape array/inclinometer data for this purpose. On the other hand, string pots do accurately measure small deflections; therefore, the data describing cap rotation about vertical and transverse axes, as obtained by these instruments, should be considered accurate.

6.2.1 Pile Cap Rotation about a Vertical Axis

Using the transverse cap displacement data obtained by both the shape arrays and the inclinometer readings, rotation of the pile cap about a vertical axis was also calculated and for the 0° and 15° tests, pile cap rotation data at selected longitudinal cap displacement intervals is shown in Figure 6-11 and Figure 6-12, respectively. As mentioned previously, the north shape array for the 30° test was not functioning, and as such only the final relative position of the pile cap at the end of the 30° test, as measured by the inclinometer, is shown in Figure 6-13.

However, as is shown in Figure 6-14, the shape arrays and string pots did not record identical—or even comparative pile cap rotation values (with the exception of the 15° test)—and therefore the pile cap transverse displacement plots shown below should be viewed with much skepticism.

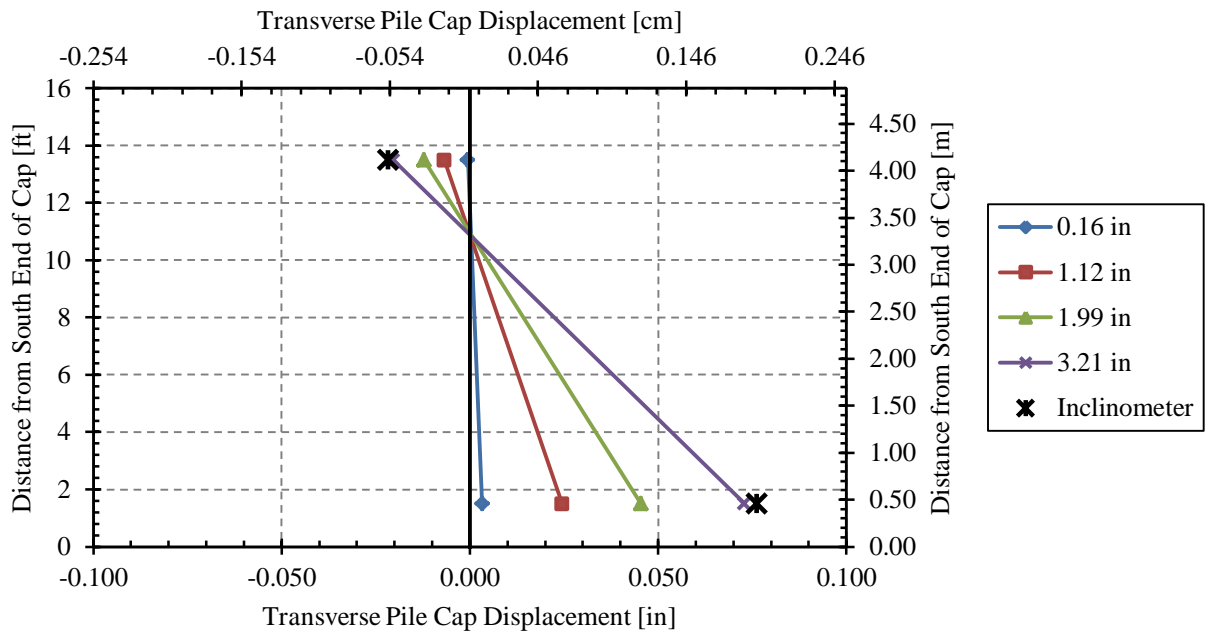


Figure 6-11: Transverse movement of the pile cap as measured by the shape arrays for the 0° test

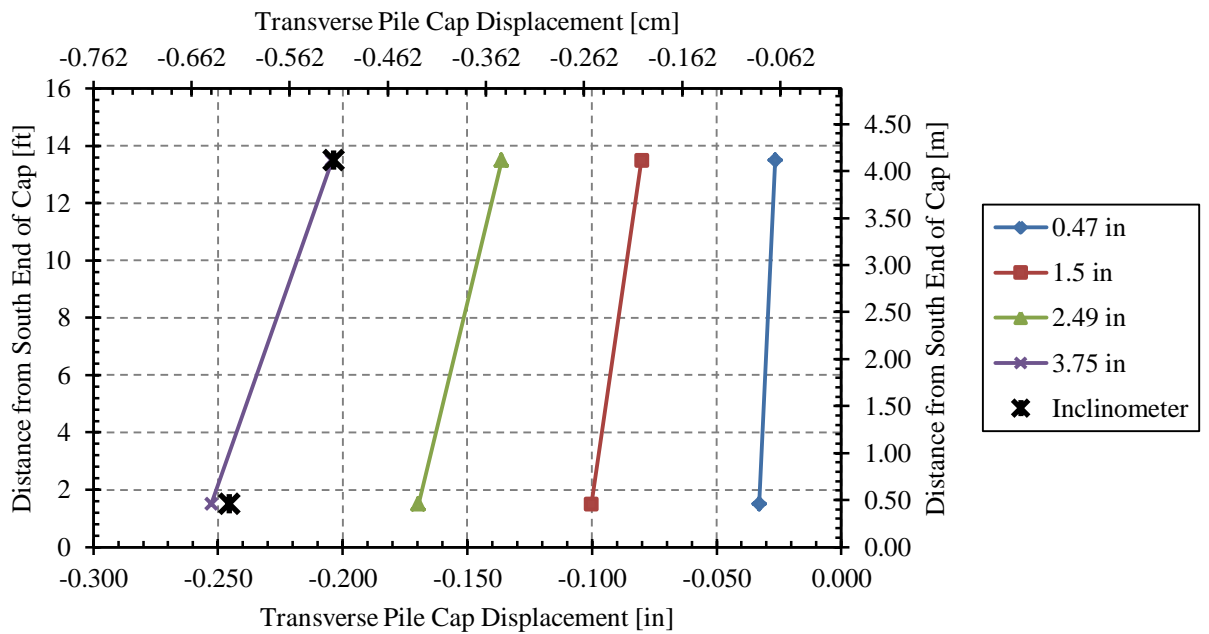


Figure 6-12: Transverse movement of the pile cap at selected displacement intervals as measured by the shape arrays and inclinometer for the 15° test

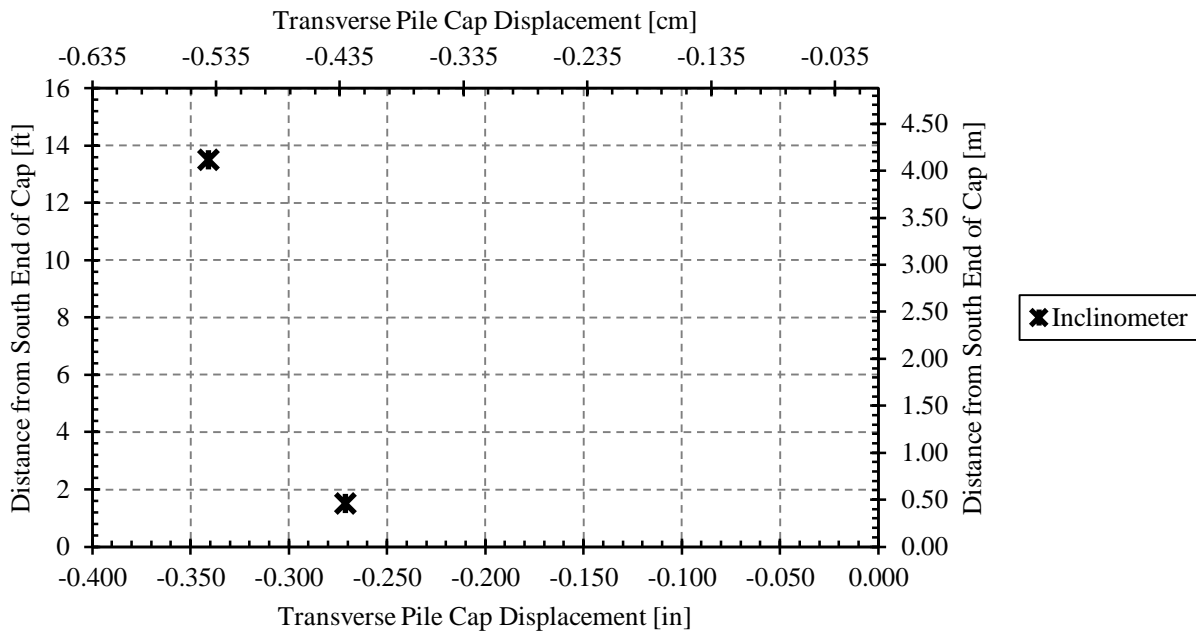


Figure 6-13: Transverse movement of pile cap at test completion as measured by the inclinometer for the 30° test

Figure 6-14 shows calculated counterclockwise pile cap rotation about a vertical axis for the 0°, 15°, and 30° tests as measured by the shape arrays and string pots. As shape array data was not available for the 30° test rotation data was based on the inclinometer data obtained at test completion. As is immediately apparent, with the exception of the 15° test (and to some extent the 30° test) the string pot and shape array/inclinometer data did not agree well at all. This discrepancy could certainly be due to inaccuracies in the way the shape array measured deflection; available evidence, however suggests that this discrepancy was likely caused due to the inclinometer readings being performed incorrectly for several of the tests. This is particularly apparent when one considers that for the 0° test, the final cap rotation values as calculated from the shape array and string pot data are nearly identical but with opposite signs.

Another potential explanation is that the inclinometer tubes were not installed with the x- and y-axes in line with the x- and y-axes of the pile cap. Therefore when the shape array

displacement vectors were rotated to match the direction of the inclinometer displacement vector the corrected shape array data showed erroneous (in direction, not magnitude) displacement data. In addition to the discrepancy associated with the direction of pile cap rotation, the shape arrays also recorded a much more smooth pile cap rotation versus deflection relationship than the string pots. However, these smooth curves can possibly be explained as the shape array cannot be used to accurately measure very small deflections.

Despite these discrepancies, the very small rotation values do indicate that in general, the pile cap did not experience significant rotation. When comparing all tests, the pile cap experienced significantly greater rotation than either the 15° or 30° test, likely for the reasons discussed in Section 5.2. As such, the force couple applied by the actuators (see Section 5.4) undoubtedly had a much more significant effect on how the pile cap rotated about a vertical axis than did the component of the passive force acting in the transverse direction.

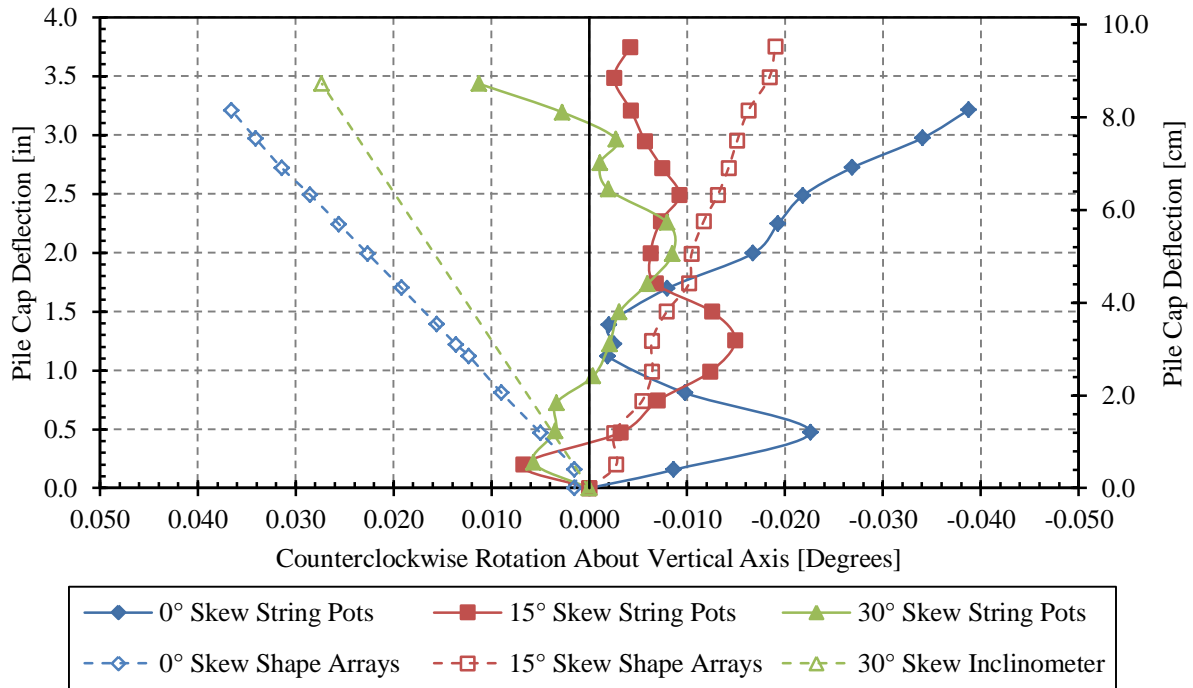


Figure 6-14: Counterclockwise rotation of the pile cap about a vertical axis with respect to total actuator load for the 0°, 15°, and 30° tests

6.2.2 Pile Cap Rotation about a Transverse Axis

For each of the tests the pile cap underwent a very minor forward rotation about a transverse axis, as shown in Figure 6-15. Though this plot shows forward rotation of the pile cap as measured by the string pots, the shape array data shows similar trends; however, this information will not be shown herein. This rotation of the pile cap about a transverse axis should be expected considering the force couple created by the forward force applied by the actuators at the vertical midpoint of the pile cap and the backward resistance applied by the piles to the base of the pile cap. Nevertheless, the actual rotation values are all relatively small and tend to increase progressively as the pile cap deflection increases.

The maximum pile cap rotations at the end of the test for the 0°, 15° and 30° skew test were 0.075°, 0.047°, and 0.042°, respectively. The sizable reduction in forward rotation between the 0° test to the 15°, and 30° tests was likely due to vertical restraint applied to the bottom edge of the 15° and 30° wedges by the rollers that were not present for the 0° test, rather than due to skew angle.

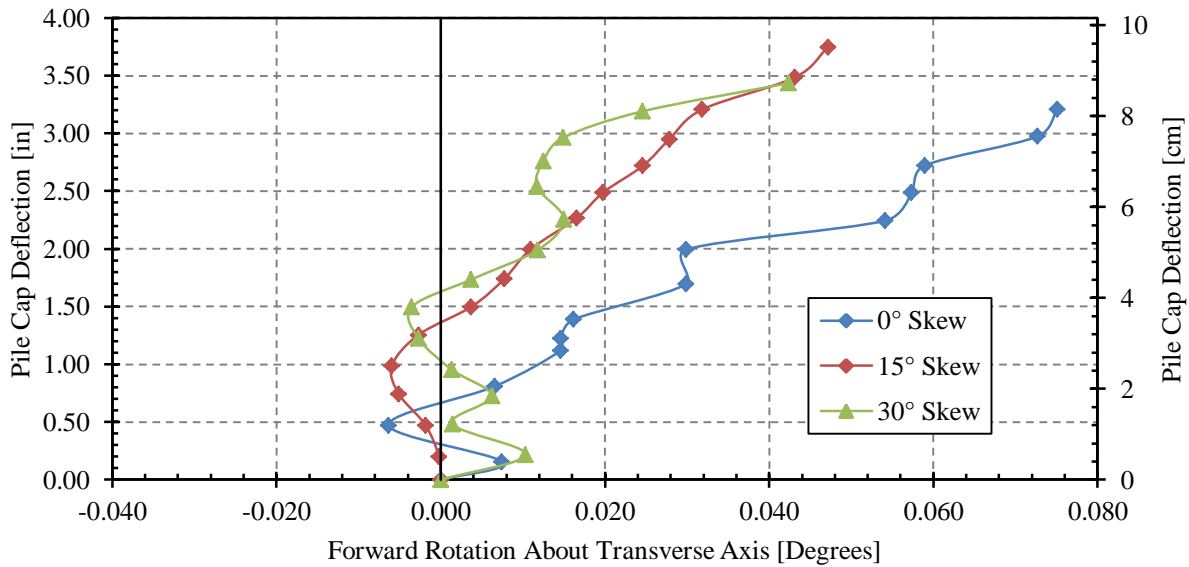


Figure 6-15: Forward rotation of the pile cap about a transverse axis as measured by the string pots for the 0°, 15°, and 30° test

7 BACKFILL DISPLACEMENT, STRAIN, AND FAILURE

This chapter will describe the observed backfill failure mechanisms by considering backfill lateral and vertical movement, lateral strain, and internal and external failure patterns. In order to most effectively describe the governing failure mechanisms the test data will be presented in the following order: 1) heave and crack data, 2) internal shear patterns, and 3) backfill movement and strain.

7.1 Backfill Heave and Surface Cracking

Figure 7-1, Figure 7-2, and Figure 7-3 show backfill heave contours, surface cracks, and string pot locations extant at test completion for the 0°, 15°, and 30° tests, respectively. Backfill heave for the 0° and 15° tests exhibited very similar characteristics with maximum heave occurring immediately adjacent to, and at the corners of the backwall. For the 0° test maximum backfill heave occurred in a half-elliptical strip approximately 4 feet (1.20 m) wide as shown by the dashed lines in the figure. For the 15° test the highest heave values also existed in a roughly elliptical strip centered at the backwall face. However, unlike the 0° test, the internal half-ellipse bounding this zone of maximum heave appeared to have shifted towards the acute corner of the backwall such that the western end of this strip was only about 2.5 feet (0.75 m) wide and the eastern end was just over 6 feet (1.80 m) wide, as shown by the dashed lines in the figure.

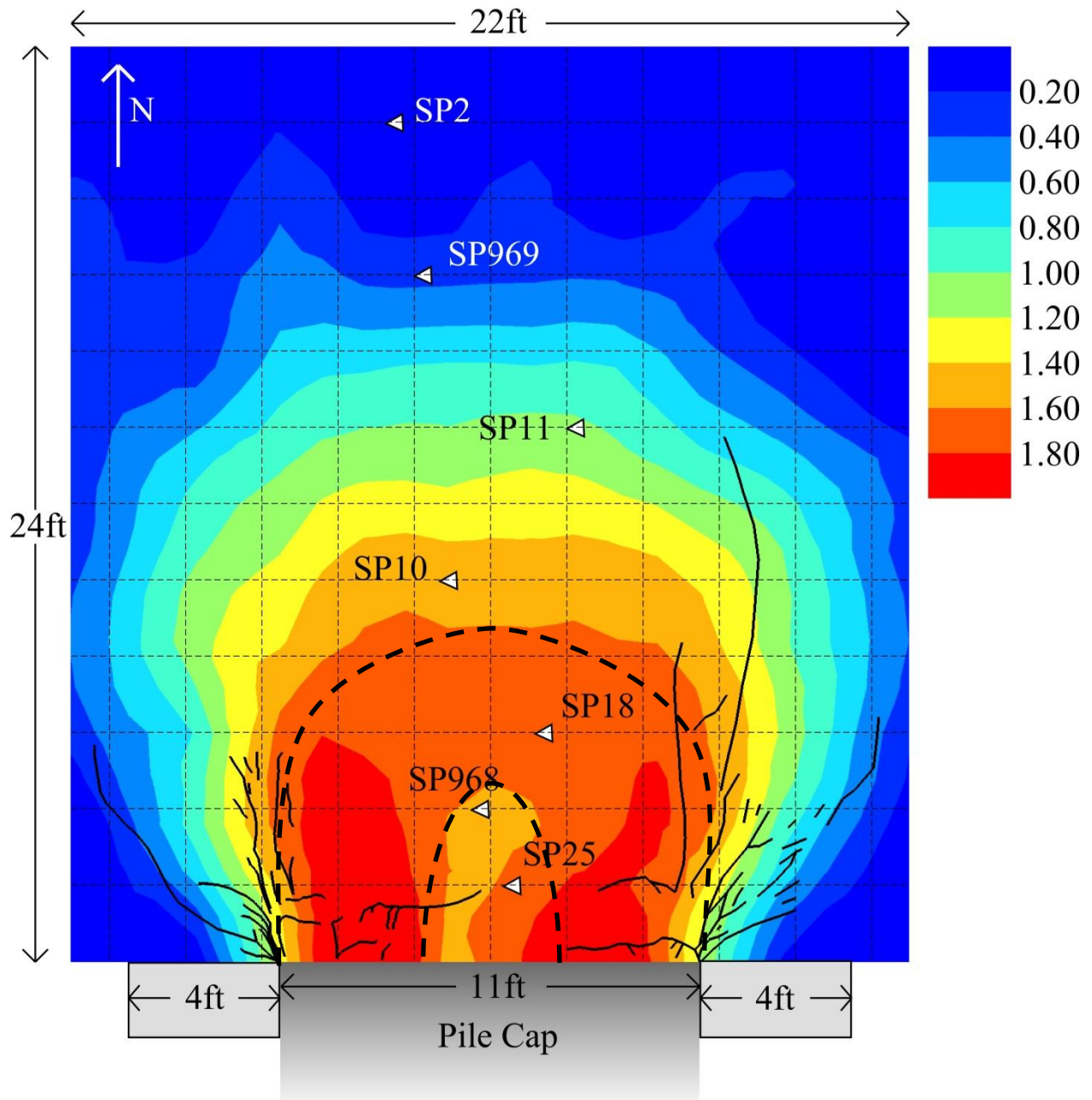


Figure 7-1: Backfill heave contours, final surface cracks, and string pot locations on a 2-ft (0.61-m) grid for the 0° test

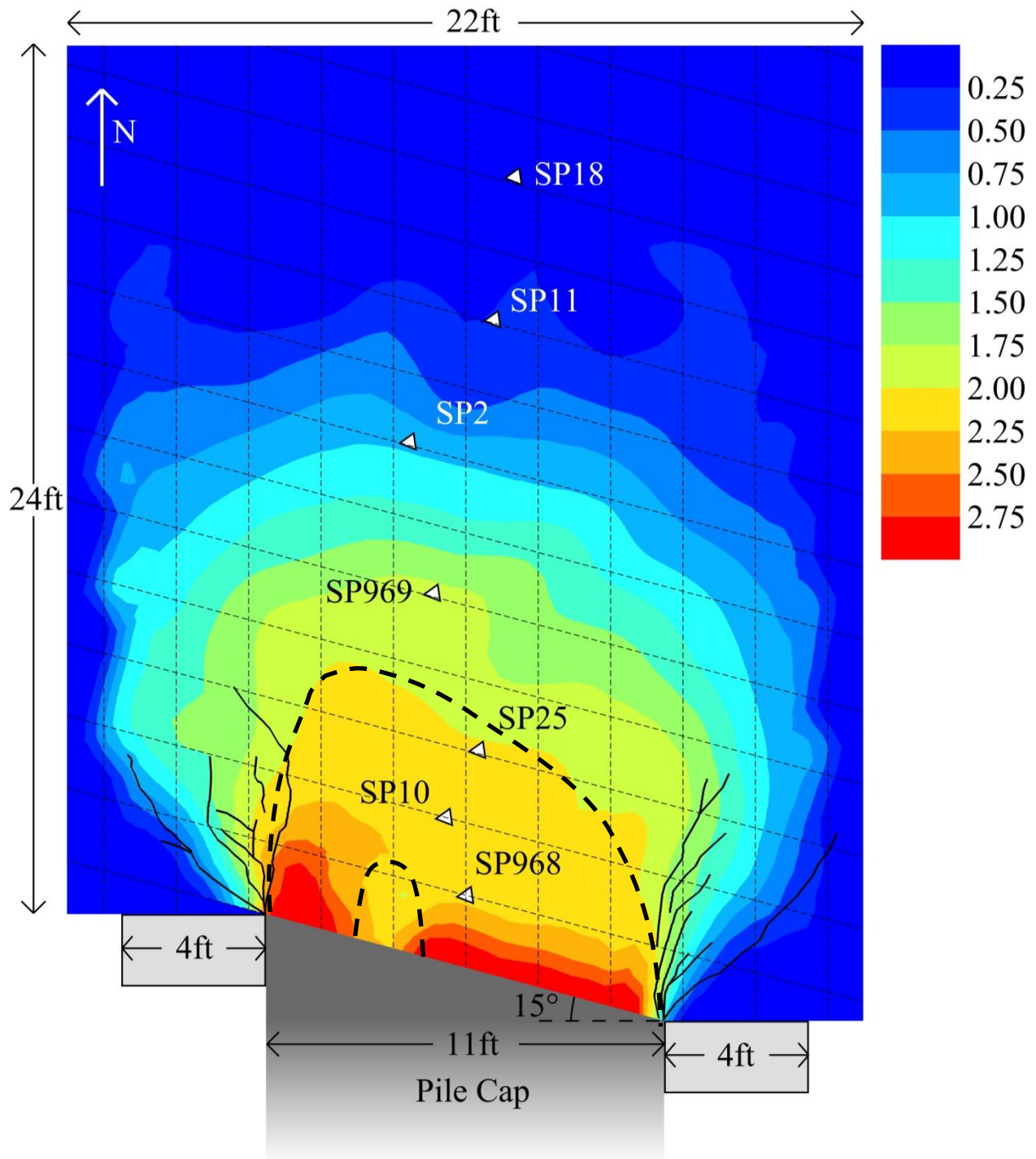


Figure 7-2: Backfill heave contours, final surface cracks, and string pot locations on a skewed 2-ft (0.61-m) grid for the 15° test

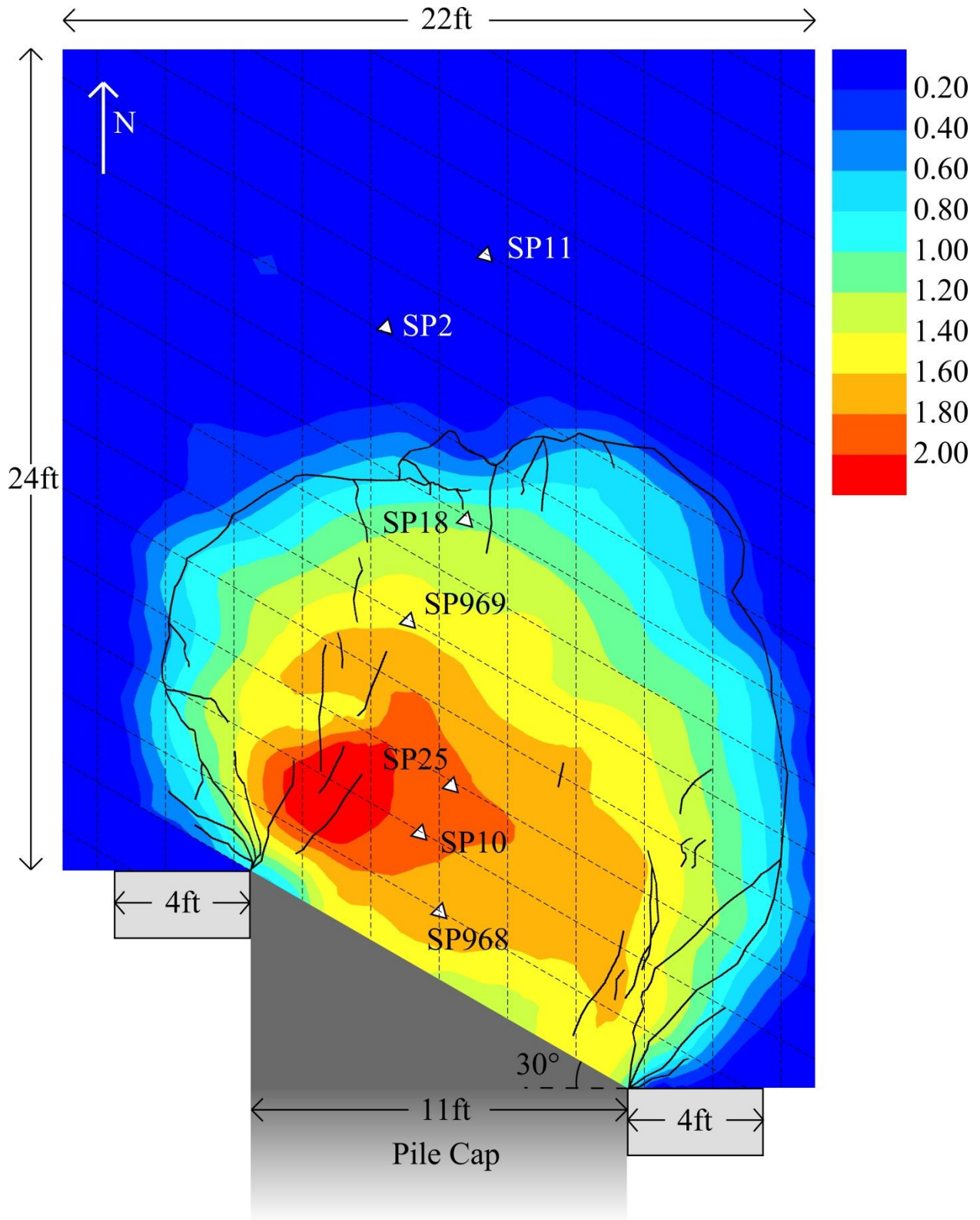


Figure 7-3: Backfill heave contours, final surface cracks, and string pot locations on a skewed 2-ft (0.61-m) grid for the 30° test

For both the 0° and 15° tests, absolute maximum heave occurred at the edges of the pile cap, which is consistent with previously conducted research that indicates that the highest passive pressures on a wall face occur at the edges of the wall (Borowicka 1938; Cummins 2009). Unlike either the 0° or 15° test maximum heave for the 30° test did not occur immediately adjacent to the face of the pile cap, but rather occurred in a small zone approximately 4 feet (1.22 m) to the north of the acute corner of the backwall, as shown in Figure 7-3. This change in the location of maximum heave suggests that a failure mechanism different than the governing failure mechanism for either the 0° or 15° test was operative for the 30° test.

Unfortunately, test limitations prevented the pile cap from being displaced far enough for the entire failure wedge to daylight for either the 0° or 15° tests. However, as is particularly evident for the 30° test (see Figure 7-3), the surface cracks that developed at the boundaries of the failure wedge occurred where backfill heave was between 0.30 inches and 0.50 inches (0.76 cm and 1.27 cm). Though not quite as evident, this phenomenon was also observed for the 0° and 15° tests (see Figure 7-1 and Figure 7-2) when considering those surface cracks that propagated outward from the corners of the backwall at an angle of approximately 45° with the direction of backwall movement.

Considering this information, all three tests appeared to exhibit similar surface crack patterns with a developed failure bulb approximately 20 feet (6.10 m) wide when measured parallel to the face of the backwall, and 17 feet (5.2 m) long when measured perpendicular to the backwall face. This suggests that skew angle, and likely the governing failure mechanism, has little effect on the overall size of the developed failure wedge if all other factors remain the same. However, as the failure wedge appeared to develop perpendicular to the wall face more so than parallel to the direction of pile cap movement the effective width of the failure wedge [see

Brinch Hansen (1966)] *decreases* as skew angle increases. Specifically, when measured perpendicular to the direction of backwall movement, the effective width of the failure wedge decreased from about 21 feet (6.40 m) for the 0° test, to 20 feet (6.10 m) for the 15° test, and to 18 feet (5.50 m) for the 30° test. This reduced effective width for the 15° and 30° failure wedges is approximately equal to the effective width of the 0° test multiplied by the cosine of the skew angle.

In addition to the boundary surface cracks extending out from the sides of the backfill extant for all three tests, cracks developed in the backfill that were roughly parallel to the direction of backwall movement. These cracks were particularly evident at the acute corner of the 30° backwall. This phenomenon may suggest that at high backwall deflections the sides of the failure wedge may shear off thereby leading to a very significant reduction in the passive resistance of the backfill.

Maximum heave for the 0°, 15°, and 30° tests was approximately 1.80 inches, 2.75 inches, and 2.20 inches (4.6 cm, 7.0 cm, and 5.6 cm), respectively, and appears to be directly proportional to pile cap displacement as shown in Figure 7-4. These heave values are equal to 2.7%, 4.2%, and 3.3% of the backfill height for the 0°, 15°, and 30° tests, respectively. Despite the data shown in Figure 7-4, the governing failure mechanism may certainly have some effect on the relationship between backwall displacement and maximum heave, though not enough information is available to make a definite conclusion.

Though the governing failure mechanism does appear to dictate the location of maximum heave, the magnitude of maximum heave appears to be somewhat independent of the failure mechanism.

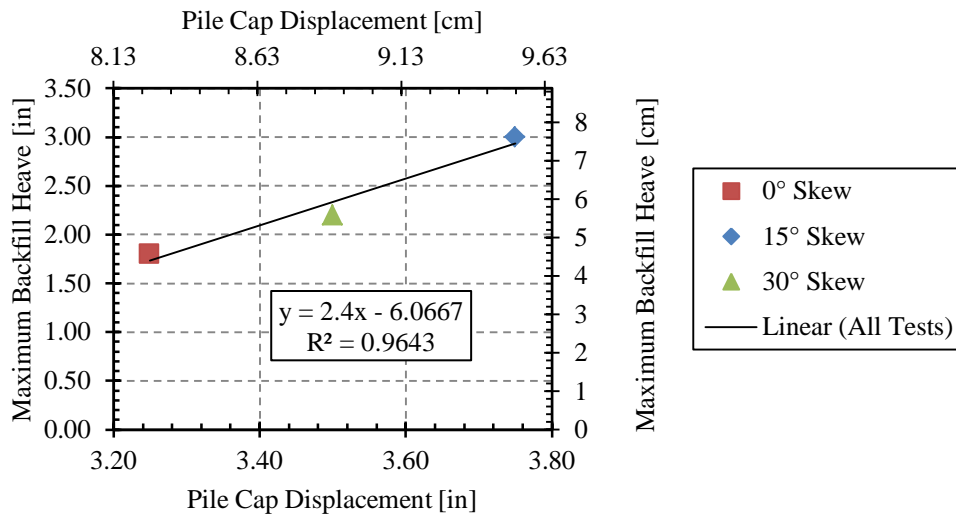


Figure 7-4: Maximum heave with respect to maximum pile cap displacement

7.2 Internal Failure Surfaces

Figure 7-5, Figure 7-6, and Figure 7-8 show the location of the internal failure surfaces for the 0°, 15°, and 30° tests, respectively, as obtained from the red dyed soil columns described in Section 3.3.6.6.

Unfortunately, for the 0° test only four sand columns were installed in the backfill and as such the failure wedge was not visible. However, as the complete failure wedge was not observed beyond the 9-foot (2.74-m) soil column for the 15° test, the lack of soil columns beyond 8 feet (2.44 m) for the 0° test may not have prevented the acquisition of internal failure surface data. Because the complete lower shear plane for both the 0° and 15° tests did not daylight the observation made in Section 7.1 that the surface cracks surrounding the failure bulb appeared at heave values between 0.30 inches (0.76 cm) and 0.5 inches (1.27 cm) was used to estimate the length of the failure wedge. The estimated failure surface shown in Figure 7-5 for the 0° test assumes that the failure surface daylighted at 0.40 inches (1.02 cm) of heave. The

estimated failure surface shown in Figure 7-6 for the 15° test assumes that the failure surface daylighted at 0.30 inches (0.76 cm) of heave.

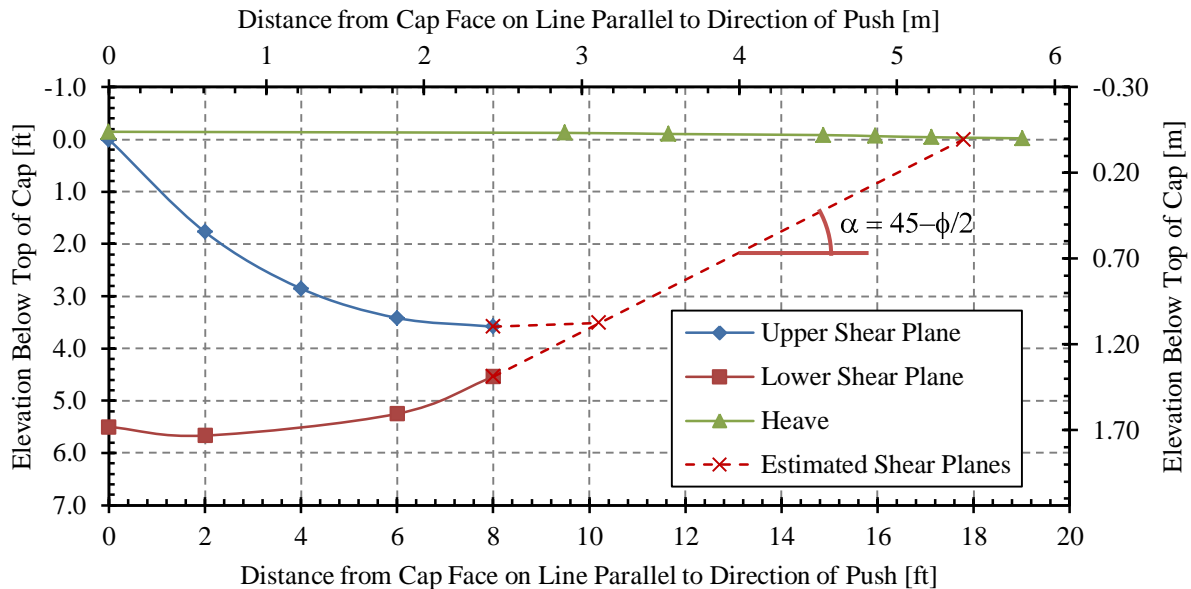


Figure 7-5: Internal failure surfaces for the 0° test

As noted in Section 3.3.6.6, two rows of red-dyed sand columns were installed 2, 6, 9, 12, and 15 feet (0.61, 1.83, 2.74, 3.66, and 4.57 m) from the face of the backwall along lines perpendicular to the face. However, as shown in Figure 7-6 below, neither the lower or upper failure plane was observed in the 12 or 15-foot (3.66 or 4.57-m) sand columns. This is not surprising when considering the change in column offset that occurred between the 6 and 9-foot (1.83 and 2.74-m) sand columns shown in Figure 7-7. This subsurface differential movement suggests that this internal failure wedge did not move as a non-compressing block, but rather experienced significant lateral compression. Specifically, the offset in the 6-foot (1.83-m) column was nearly 1 inch (2.54 cm) whereas the offset in the 9-foot (2.74-m) column was only about 0.25 inch (0.64 cm). This observation suggests that not only did the bulk of the backfill

strain occur subsurface, but that the internal failure wedge appeared to develop progressively, beginning at the face of the backwall, before the entire failure wedge (both internal and external) slid up the linear portion of the lower shear plane.

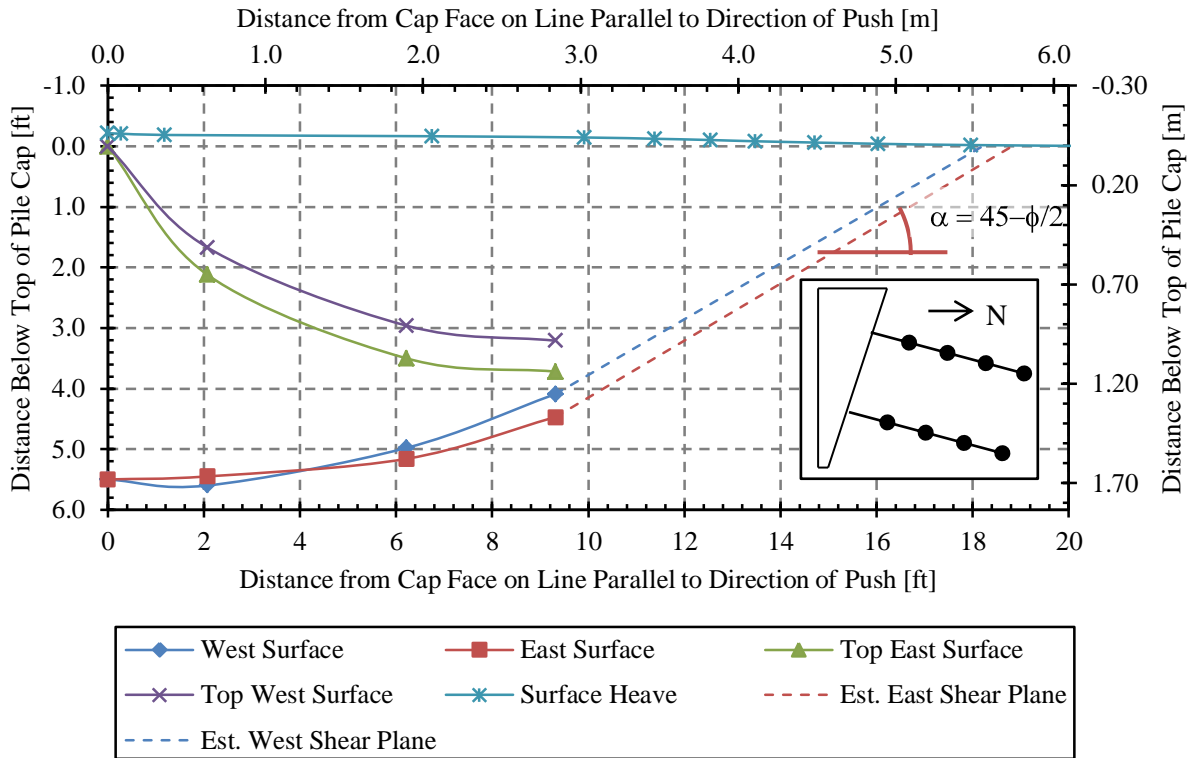


Figure 7-6: Internal failure surfaces for the 15° test (inset shows locations sand columns)

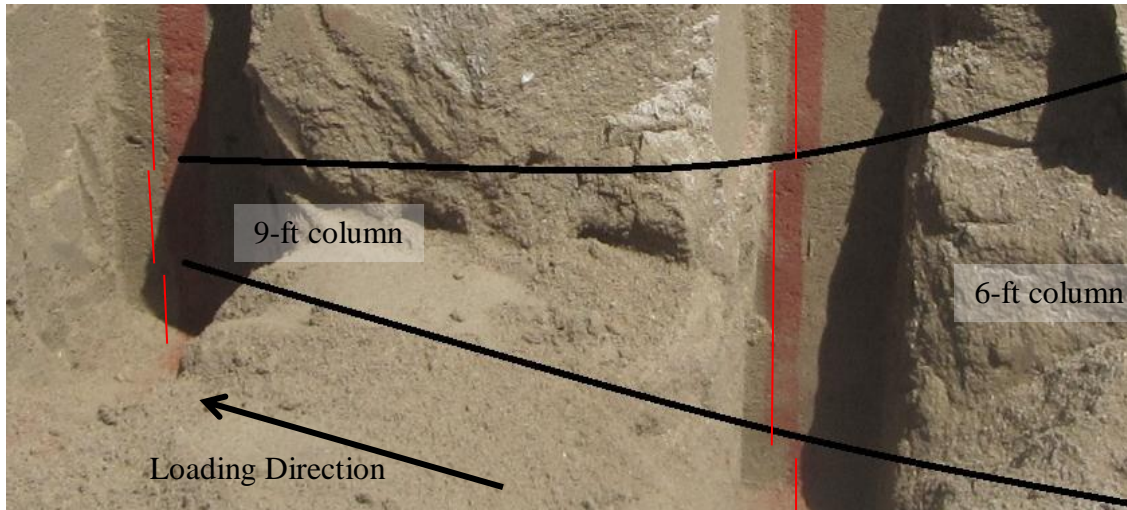


Figure 7-7: Offsets in columns located 6 and 9 feet (1.83 and 2.74 m) back from the backwall face on the east side of the backfill

As noted in Section 3.3.6.6, two rows of red-dyed sand columns were installed 2 feet (0.61 m) to each side of the longitudinal backfill center line at distances of 2, 6, 10, 14, and 18 feet (0.61, 1.83, 3.05, 4.27, and 5.49 m) from the face of the backwall. Unlike either the 0° or 15° test the complete shear planes were observed for the 30° test; though upper shear planes descending from the top of the backwall to intersect the lower shear planes were not observed, possibly for reasons that will be described at the end of this chapter.

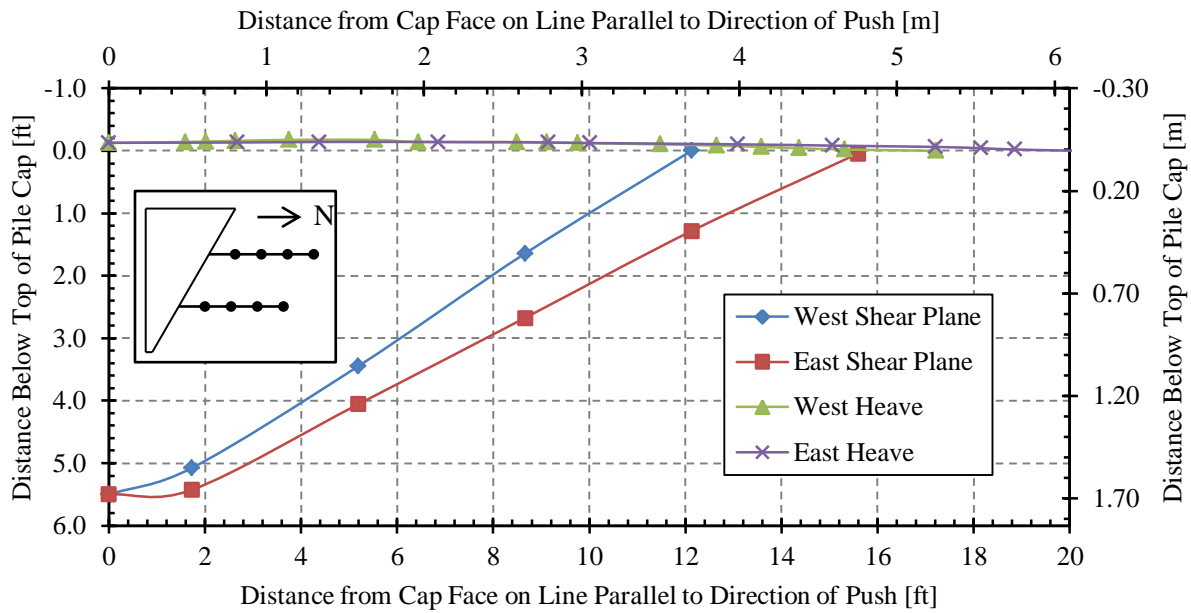


Figure 7-8: Internal failure surfaces for the 30° test (inset shows location of sand columns)

For both the 0° and 15° tests the internal shear planes were remarkably similar to the shear planes that develop during a general bearing capacity failure as described by Terzaghi (1943). Specifically, there was a curved lower shear plane that progresses first downward from the bottom of the backwall and then up to the surface of the backfill at an angle with the horizontal approximately equal to $45^\circ - \phi/2$, and an upper shear plane that descended from the top of the backwall to intersect the rising shear plane at an angle with the horizontal also approximately equal to $45^\circ - \phi/2$. Furthermore, both the upper and lower shear planes shown in Figure 7-5 and Figure 7-6 are consistent with the shear planes observed by Nasr and Rollins (2010) in their finite element analyses as shown in Figure 2-10. However, neither the Rankine failure geometry (see Figure 2-1) nor the Coulomb failure geometry predicts this upper failure surface.

On the other hand, upper shear planes were not observed for the 30° test. Furthermore, the lower shear planes that were observed progressed up from the bottom of the backwall to the backfill surface in a nearly linear fashion. However, the east shear plane did exhibit a slight downward curve before progressing linearly up to the backfill surface. This apparent transition from a curved (possibly log spiral) failure surface at the obtuse corner of the backwall to a linear failure surface (possibly Rankine) at the acute corner of the backwall may suggest, as mentioned in Section 5.3, that the backfill tended to fail in a progressive fashion beginning at the acute corner of the backwall and progressing to the obtuse corner. This also implies that the governing failure mechanism for this test was different than the governing failure mechanism for either the 0° or 15° tests.

If the relationship between the angle of inclination of the linear portion of the failure plane, α , and the soil friction angle, ϕ , is assumed to be $\alpha = 45^\circ - \phi/2$ (Terzaghi 1943), then for the 0° test the back-calculated friction angle is between 44° and 37° if the back of the failure bulb is assumed to develop at 0.30 inches (0.76 cm) and 0.50 inches (1.27 cm) of heave, respectively, as discussed in Section 7.1.

Using the same procedure for the 15° test, the back-calculated average friction angle for both shear planes was between 40° and 27° if the back of the failure bulb was assumed to develop at 0.30 inches (0.76 cm) and 0.50 inches (1.27 cm) of heave, respectively if the distance from the soil column and backwall was measured parallel to the direction of push. However, if the distance between the soil columns and the backwall was measured perpendicular to the face of the backwall then the back-calculated average friction angle for both shear planes was 37° and 22° if the failure bulb was assumed to develop at 0.30 inches (0.76 cm) and 0.50 inches (1.27 cm) of heave, respectively.

Finally, for the 30° test the back-calculated friction angle was 48° and 43° if the distance between the soil columns and the backwall was measured parallel to the direction of backwall movement, and perpendicular to the face of the backwall, respectively. As shown in Figure 7-3 the complete failure bulb was visible at the backfill surface, therefore no extrapolation was needed to determine the location of the back surface crack.

The information presented in the preceding paragraphs indicates that the back-calculated friction angle agrees better with the measured friction angle when the distance between the soil columns and the backwall is measured perpendicular to the face of the wall. Like the observations presented in Section 7.1, this data seems to suggest that the failure wedge appears to develop perpendicular to the face of the backwall and not necessarily parallel to the direction of wall movement.

Particularly with the 0° test, but also to a certain extent with the 15° and 30° tests, the back-calculated friction angle is in reasonable agreement with the measured soil friction angle that between 40.4° and 42.3° as obtained from the direct shear tests (see Table 3-5 for more information).

7.3 Backfill Displacement

As described in Section 3.3.6.4 string pots mounted to the top of the backwall were located in the backfill at various distances from the wall face and data from these instruments was used to determine backfill movement and strain.

As will be seen for the 0° and 30° tests (see Figure 7-9 and Figure 7-12, respectively), occasionally some of the backfill string pots recorded data that did not match the backfill movement trends recorded by nearby string pots. The most likely explanation for these anomalies in the data was that the stake anchoring the offending string pot to the backfill

intersected either a surface crack, or one of the rising/falling internal shear planes described in Section 7.2. When this occurred the differential soil movement on either side of the crack/shear plane caused the top of the stake to rotate to the north or south. If the top of the stake moved to the north than more northward movement of the backfill (less backfill compression) was recorded than actually occurred, but when the top of the stake moved to the south than less northward movement of the backfill was recorded than actually occurred (more backfill compression).

Figure 7-9 shows both corrected and uncorrected backfill string pot displacement data plotted against average pile cap deflection for the 0° test. For this test all string pots recorded similar backfill movement trends. However, the 2-foot (0.61-m) string pot (SP25) recorded some anomalous data when the average pile cap displacement was between 1.39 inches and 2.0 inches (3.53 cm and 5.08 cm). This anomaly in the data shifted the curve for higher pile cap deflections such that the backfill appeared to displace further than what actually occurred. As can be seen in Figure 7-1 SP25 appears to be located directly between two surface cracks running parallel to the face of the backwall. Though Figure 7-10 seems to show that this crack was a compression crack, the fact that the stake was located directly on the crack prevents accurately identifying the direction that the top of the stake moved. Nevertheless, if the 4-foot (1.22-m) and 6-foot (1.83-m) string pots are considered, this excessive movement of the backfill appears to be erroneous, and as such the string pot displacement measurements associated with pile cap deflections greater than 1.39 inches (3.53 cm) were adjusted to follow the general trend exhibited by the 4- and 6-foot (1.22- and 1.83-m) string pots.

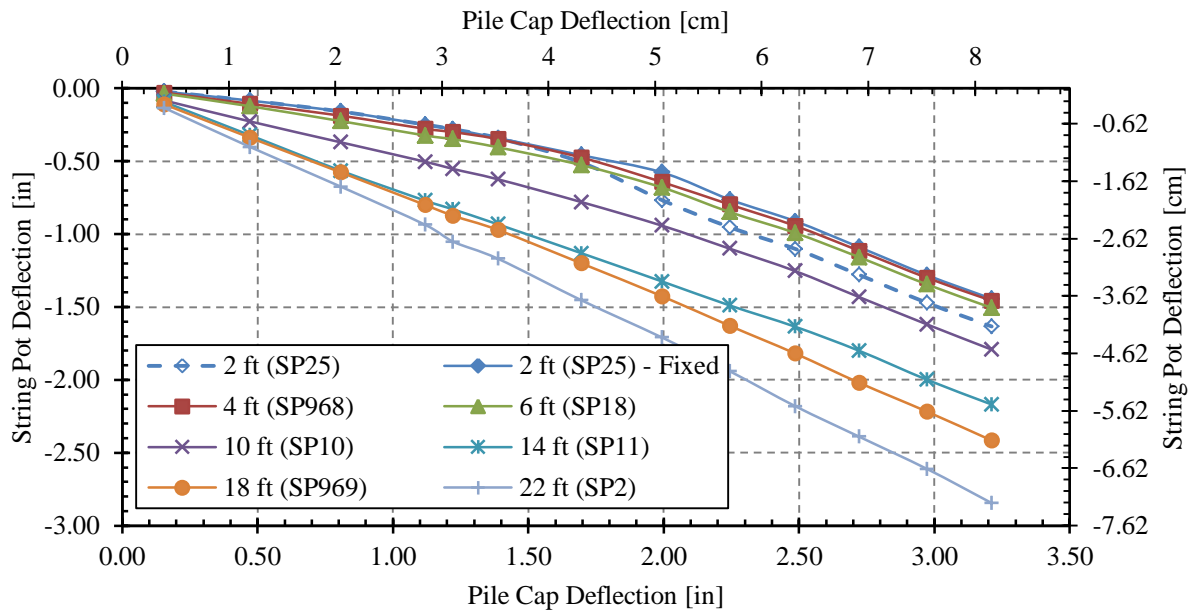


Figure 7-9: Backfill string pot displacement with respect to pile cap displacement for the 0° test



Figure 7-10: Transverse compression cracks at test completion

Figure 7-11 shows backfill string pot displacement data plotted against average pile cap deflection for the 15° test. No inconsistent backfill displacement data was recorded for this test.

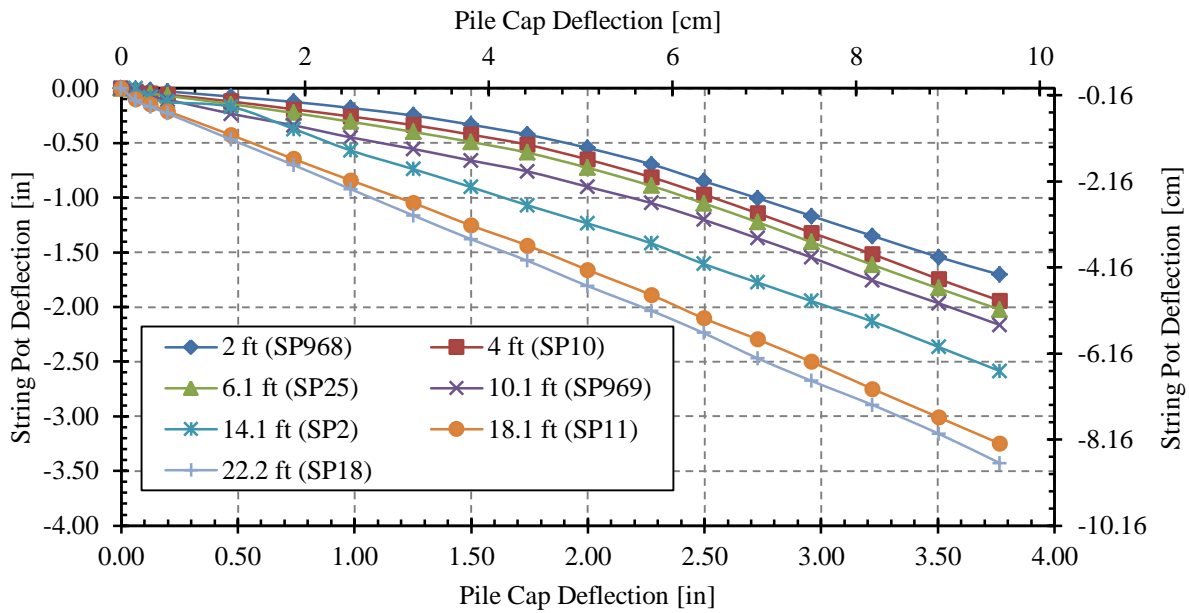


Figure 7-11: Backfill string pot displacement with respect to pile cap deflection for the 15° test

Figure 7-12 shows original and corrected backfill string pot displacement data plotted against average pile cap deflection for the 30° test. Up to a pile cap displacement of about 3 inches (7.62 cm) none of the string pots recorded unusual data. However, at approximately 3.43 inches (8.71 cm) of pile cap displacement the 14-foot (4.27 m) (SP18) string pot showed a slight offset in backfill displacement that likely was not realistic. As shown in Figure 7-3 this string pot stake was at the tail end of a surface crack; however, as this stake was far enough from the back daylighted shear plane and was likely driven sufficiently far into the backfill to prevent excessive rotation the offset in displacement was not overly significant. Nevertheless, the final displacement value recorded by SP18 was extrapolated from the previous displacement values using a linear regression equation.

Additionally, at approximately 3.19 inches and 3.43 inches (8.10 cm and 8.71 cm) of pile cap displacement the 6-foot (1.83-m) (SP25) string pot recorded a fairly significant offset in backfill displacement. Unlike the errors discussed previously this error occurred because of the way SP25 records displacement. Though this string pot is capable of measuring 10 inches (25.40 cm) of deflection the instrument measures 0 to 5 inches (12.70 cm) plus 0 to 5 inches (12.70 cm), rather than 0 to 10 inches (25.40 cm). As such, this offset in displacement was only measured because the string was retracted enough to cross through the instrument's zero point. For simplicity these last two data points were extrapolated from the previous data points using a linear regression equation.

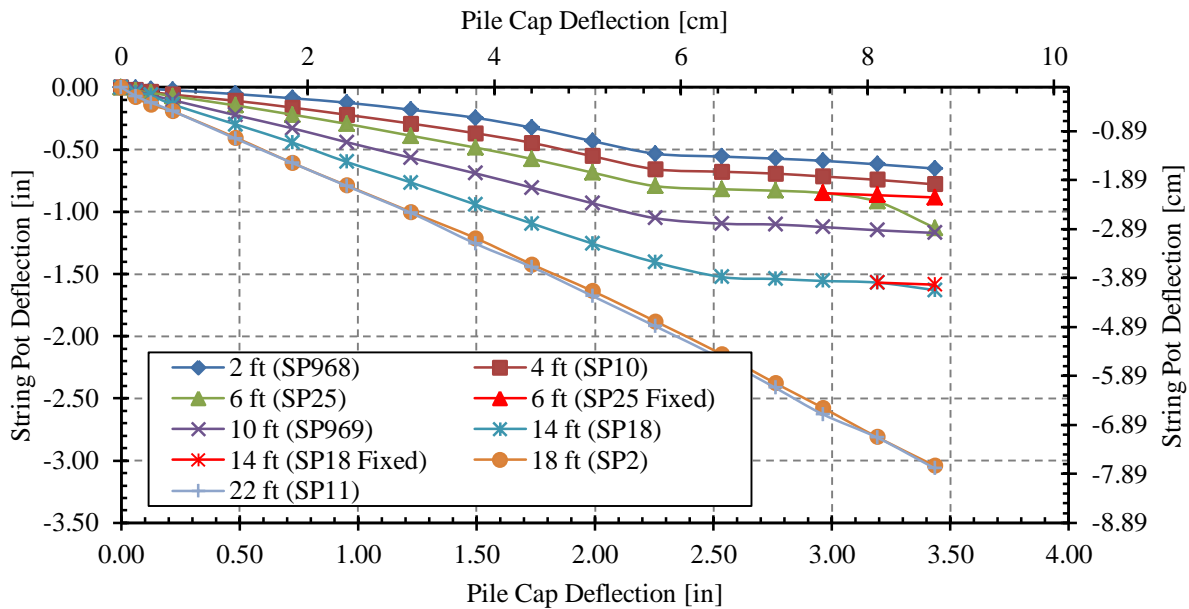


Figure 7-12: Corrected and uncorrected backfill string pot displacement with respect to pile cap displacement for the 30° test

The relatively consistent backfill displacement data observed for the 0° and 15° tests (see Figure 7-9 and Figure 7-11) indicates that backfill materials were compressing fairly linearly with respect to pile cap deflection. As far as these plots are concerned, the steeper the slope of the line, the more the backfill is compressing. Therefore, a horizontal line indicates that the backfill is translating as a block.

For both the 0° and 15° tests the most significant change in backfill movement occurred when the pile cap had been displaced approximately 2 inches (5.0 cm), which displacement essentially corresponds with the peak passive force. A similar trend was observed for the 30° test. However, immediately after backfill failure the soil within the failure bulb boundaries [within about 15 feet (4.5 m) of the backwall face] began translating as an almost perfectly rigid mass. This occurred when the complete failure plane became visible at the backfill surface as shown in Figure 7-13.



Figure 7-13: Completely developed failure wedge for the 30° test

Using this data, relative backfill displacement was calculated with respect to the original distance of the string pot stake from the backwall, and Figure 7-14, Figure 7-15, and Figure 7-16

show these results for the 0°, 15°, and 30° tests, respectively. These figures also show either the estimated or actual distance of the daylighted shear plane from the backwall face [marked as “Surface Crack (Est.)”, or “Surface Crack”, respectively].

All three of these figures show that, as expected, the greatest backfill movement occurred within the first 2 feet (0.61 m) of the backwall face. Beyond this point backfill displacement decreased roughly linearly with respect to the original distance from the face of the backwall for the 0° and 15° tests. For the 0° test (see Figure 7-14) the apparent decrease in backfill movement at the 2-foot (0.61-m) stake relative to the 4-foot (1.62-m) stake after approximately 2 inches (5.0 cm) of pile cap deflection may not be very reliable as the 2-foot (0.61-m) stake intersected a transverse surface crack as discussed previously. As such, the backfill displacement curve associated with 3.21 inches (8.15 cm) may be more appropriately represented as the red dashed line in Figure 7-14.

On the other hand, for the 30° test backfill displacement did not drop off sharply just past the 2-foot (0.61-m) stake, but rather decreased essentially linearly with respect to the original distance from the pile cap face out to a distance of about 16 feet (4.9 m) which corresponds with the location of the daylighted failure wedge. Beyond this point backfill movement decreased to less than 0.5 inches (1.27 cm). This significant difference in the movement of the backfill in comparison to the 0° and 15° tests, like other differences reported in Sections 7.1 and 7.2, suggests that the governing failure mechanism for the 30° test was different than the governing failure mechanism for either the 0° or 15° tests. However, like both the 0° and 15° tests, the small backfill movement at the back of the test pit indicates that the backfill materials beyond the failure wedge were indeed compressing as the failure wedge slid up the shear plane.

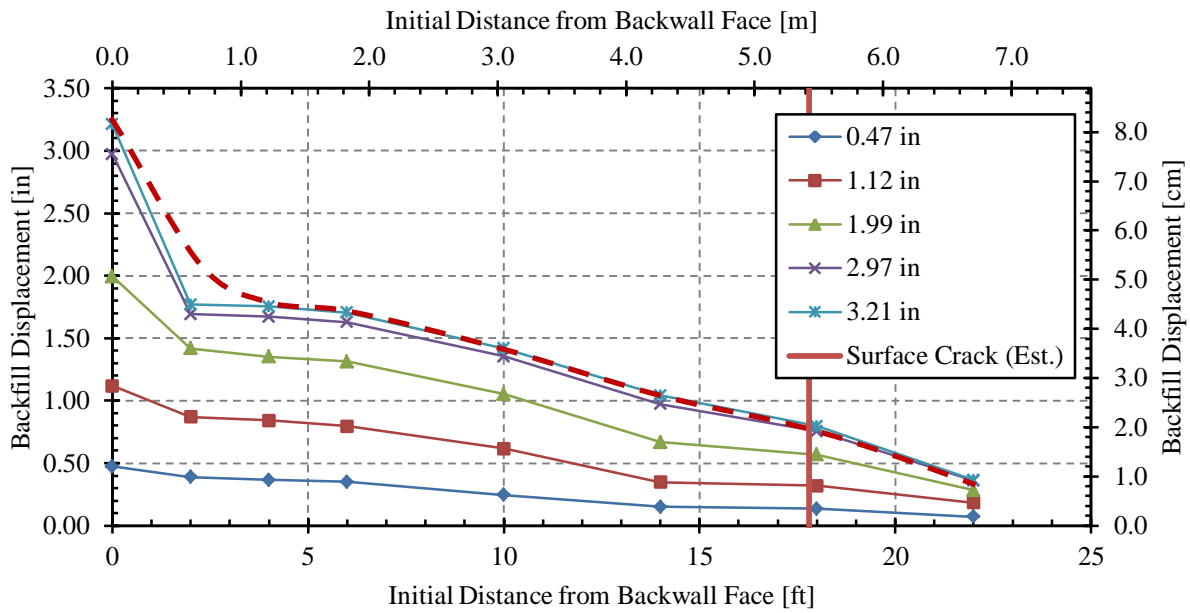


Figure 7-14: Total backfill displacement versus distance from backwall face at selected cap displacement intervals for the 0° test

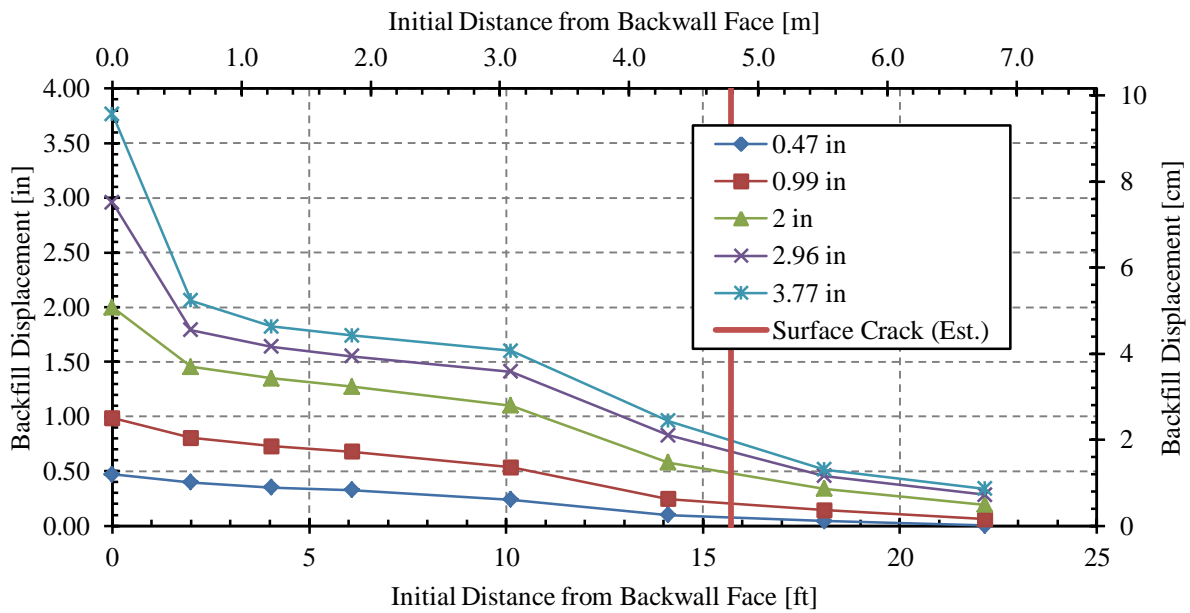


Figure 7-15: Total backfill displacement versus distance from backwall face at selected cap displacement intervals for the 15° test

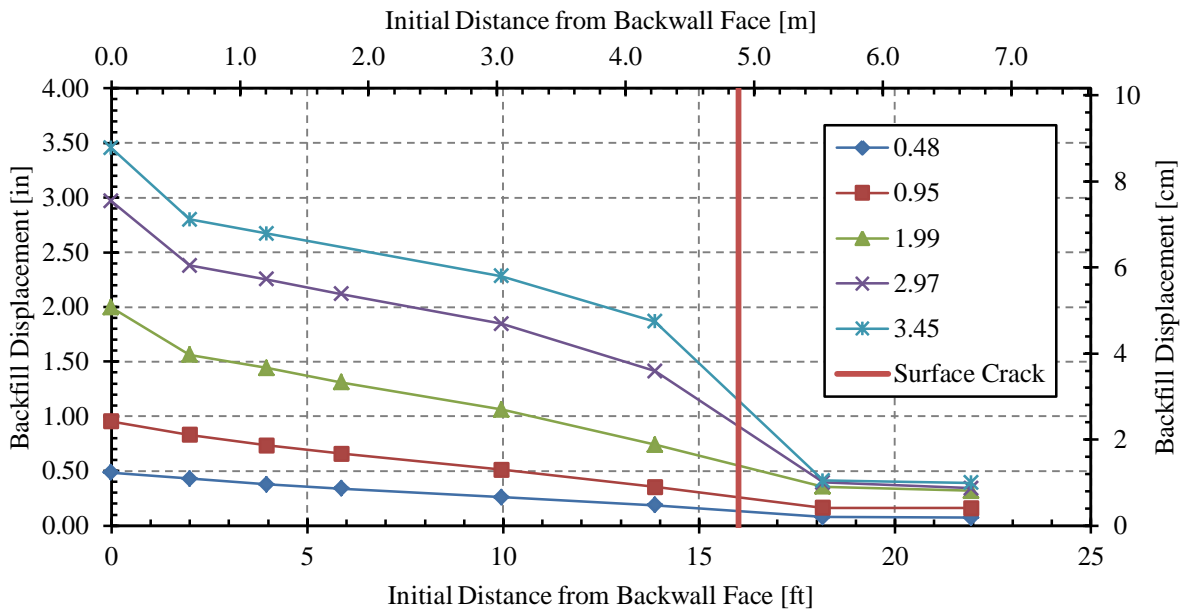


Figure 7-16: Total backfill displacement versus distance from backwall face at selected cap displacement intervals for the 30° test

7.4 Backfill Strain

Using the backfill displacement data described in Section 7.3 backfill strain was calculated using Equation (3-3).

Figure 7-17 shows the calculated backfill strain with respect to distance from the backwall face for the 0° test. Though the very low backfill strains calculated between the 2- and 4-foot (0.61- and 1.22-m) string pots shown in Figure 7-17 are not surprising if the dramatic drop in measured backfill displacement at the 2-foot (0.61-m) string pot (see Figure 7-14) is considered, for the reasons discussed previously, this near-zero strain value should be viewed with some skepticism. All other strain values should be considered realistic. Beyond this point backfill strain was fairly uniform and remained below 1%. However, the slight increase in measured backfill strain at about 20 feet (6.10 m) suggests the backfill zone may not have extended far enough from the face of the cap to insure that the test pit boundaries did not affect

test results. That being said, the measured backfill movement [approximately 0.25 inches (0.64 cm)] was small enough that the measured actuator load was almost certainly not affected. Therefore, the more likely explanation for the backfill movement at this distance is that as the developing failure wedge impinged upon, and then slide up the back failure surface, the underlying soil underwent some compressive strain.

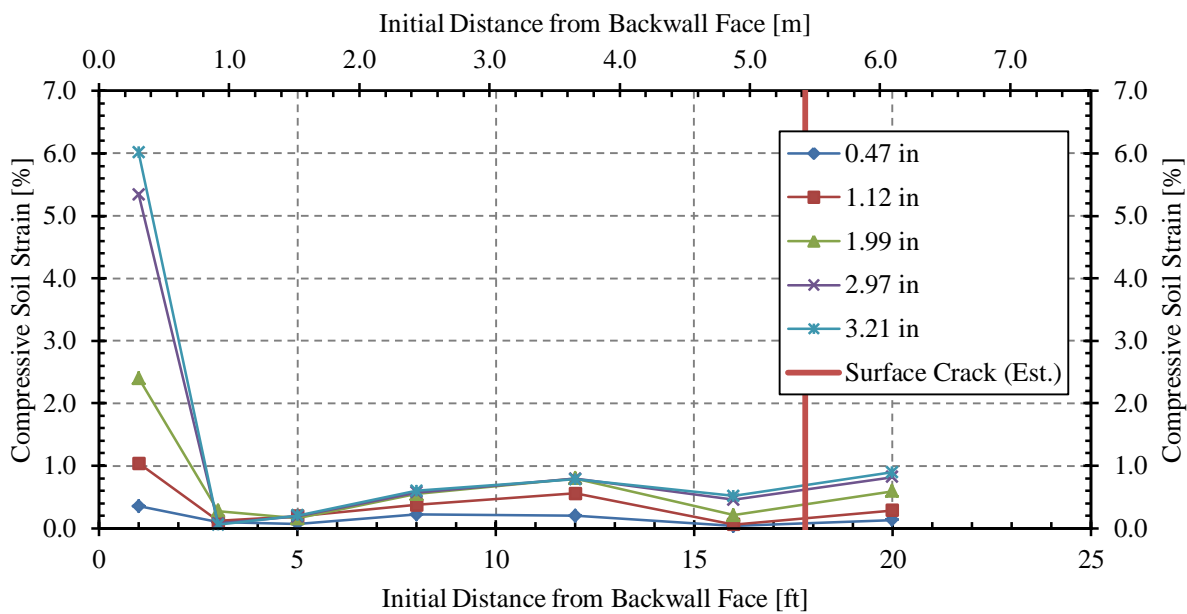


Figure 7-17: Backfill compressive strain versus original distance from backwall face at selected displacement intervals for the 0° test

Figure 7-18 shows backfill strain with respect to the original distance from the backwall face for the 15° test. For this test the backfill behaved very similar to the 0° test with maximum strain occurring immediately adjacent to the backwall face, and all other strain values essentially remaining below 1%. However, as shown in the figure, between the 10-foot and 14-foot (3.05-m and 4.27-m) string pots, compressive strain increased to just above 1% once the pile cap had been displaced approximately 2 inches (5.0 cm). At distances greater than this from the backwall

face the strain decreased to below 1%. This peak in backfill strain likely corresponded with the point at which the shear plane was going to daylight, as shown by the “Surface Crack (Est.)” line in the figure. Like the 0° test, the compressive strain at the back of the failure wedge increased as the failure wedge was forced into and then moved upward over the underlying intact soils.

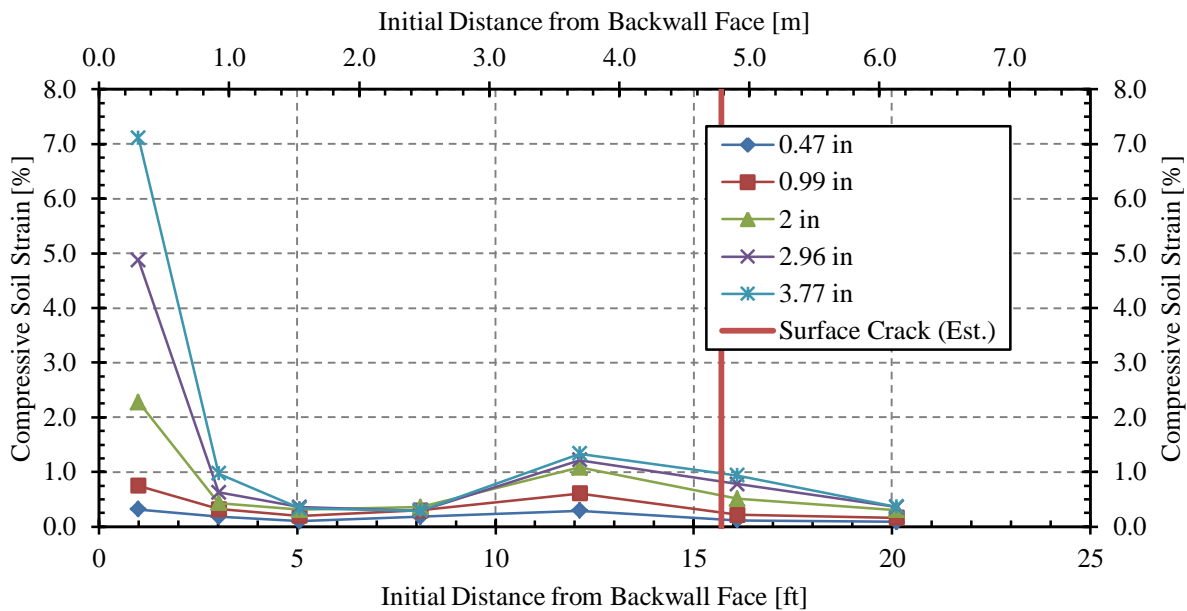


Figure 7-18: Backfill compressive strain versus original distance from backwall face at selected displacement intervals for the 15° test

Figure 7-19 shows backfill strain with respect to the original distance from the backwall face for the 30° test. As observed with the backfill heave patterns, internal failure surfaces, and backfill displacement data (see Sections 7.1, 7.2, and 7.3, respectively) backfill failure behavior for the 30° test was significantly different than the backfill failure behavior for either the 0° or 15° tests. Specifically, backfill strain at the backwall face for the 30° test was much less than either the 0° or 15° test. Additionally, where backfill strain remained essentially below 1% beyond the 4-foot (1.22-m) string pot for the 0° and 15° tests, *maximum* backfill strain occurred

between the 14-foot and 18-foot (4.27-m and 5.49-m) string pots for the 30° test. Unsurprisingly, this peak in strain corresponded exactly with the location of the daylighted failure surface.

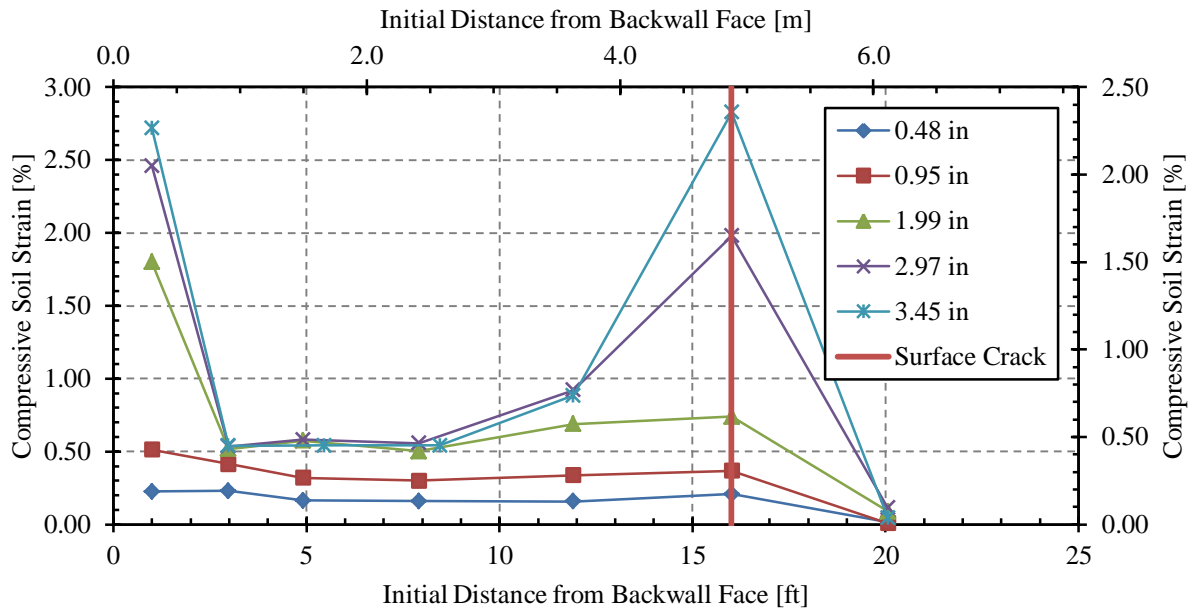


Figure 7-19: Backfill compressive strain versus original distance from backwall face at selected displacement intervals for the 30° test

Figure 7-20 and Figure 7-21 show total backfill movement and backfill compressive strain, respectively, at test completion. These figures highlight the similarities and differences in the longitudinal behavior of the backfill surface. In general, the backfill behaved very similarly for the 0° and 15° tests with the total backfill displacement and strain curves essentially lying right on top of each other. Likely, the fact that the pile cap was pushed about 0.5 inches (1.27 cm) further for the 15° test than the 0° test had a more significant effect on the differences in the displacement and strain curves shown in Figure 7-20 and Figure 7-21, respectively, than did the backwall geometry. Despite this, the peak in backfill strain observed at a distance from the backwall face of approximately 12 feet (3.66 m) could either be the result of higher backwall

displacement or backfill geometry; however, there is not enough information available to identify the cause of this difference with any certainty.

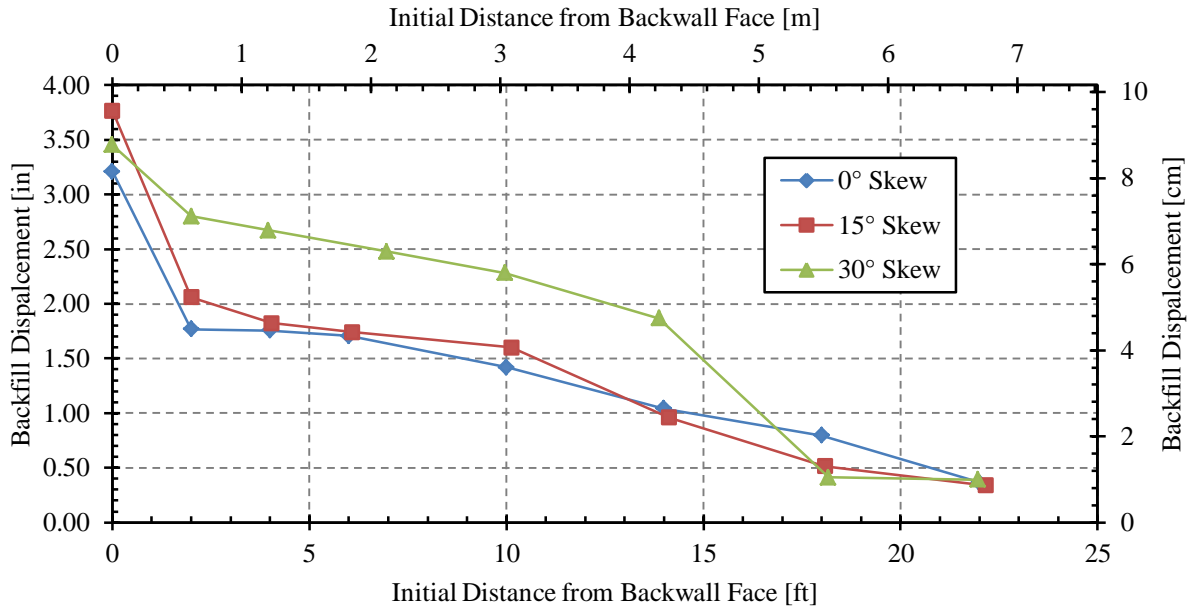


Figure 7-20: Total backfill displacement versus distance from backwall face at test completion for 0°, 15°, and 30° tests

The obvious differences in backfill displacement and strain for the 30° test with respect to the 0° and 15° tests indicate that a different failure mechanism appears to be operative for this test. Specifically, the backfill appears to be translating more as a block for the 30° test than for the 0° or 15° tests as higher average backfill displacement was recorded for the 30° test [2.0 in (5.08 cm)] than for either the 0° or 15° tests [1.51 in and 1.60 in (3.84 cm and 4.06 cm), respectively].

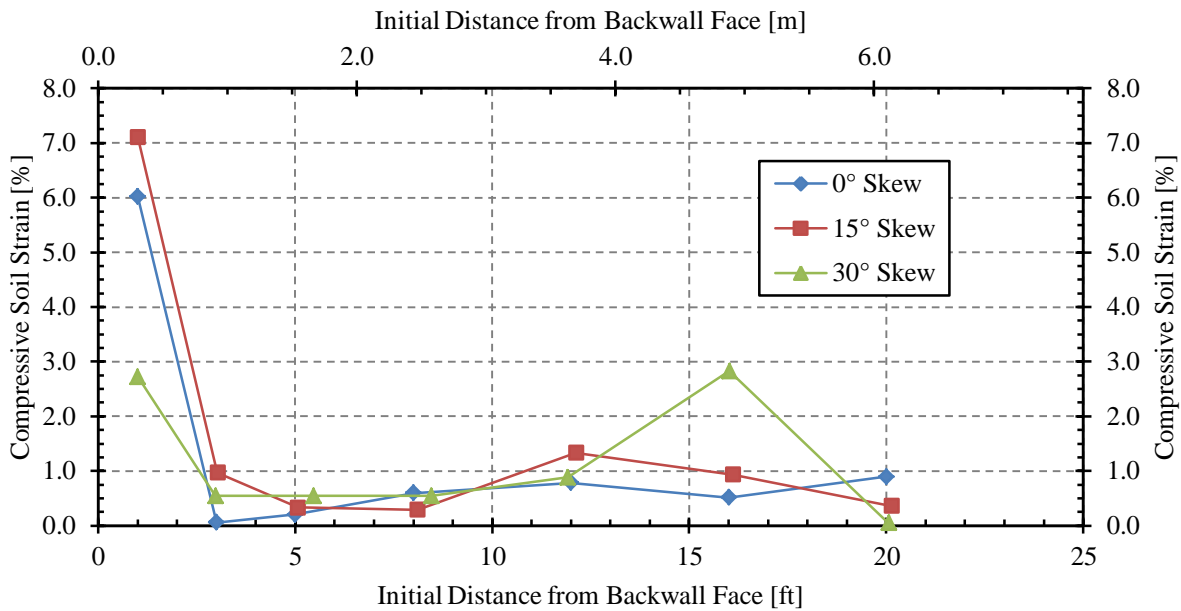


Figure 7-21: Backfill strain with respect to initial distance from the backwall face for the 0°, 15°, and 30° tests at test completion

Backfill strain was approximately proportional to pile cap displacement, as shown in Figure 7-22. However, the lack of a better correlation ($R^2 = 0.543$) between backfill strain and pile cap displacement suggests, among other things, that the backfill was indeed straining beyond the furthest string pot, and/or the backfill was straining perpendicular to the direction of push as expected for a 3D failure geometry. If backfill strain was measured in both the longitudinal and transverse direction an average Poisson's ratio could be developed for the failure wedge. However, as the bulk of the backfill movement appeared to be subsurface for the 0° and 15° tests (see Figure 7-7 in Section 7.2) this Poisson's ratio concept may *only* be viable for backwall geometries that *do not* produce an internal failure wedge.

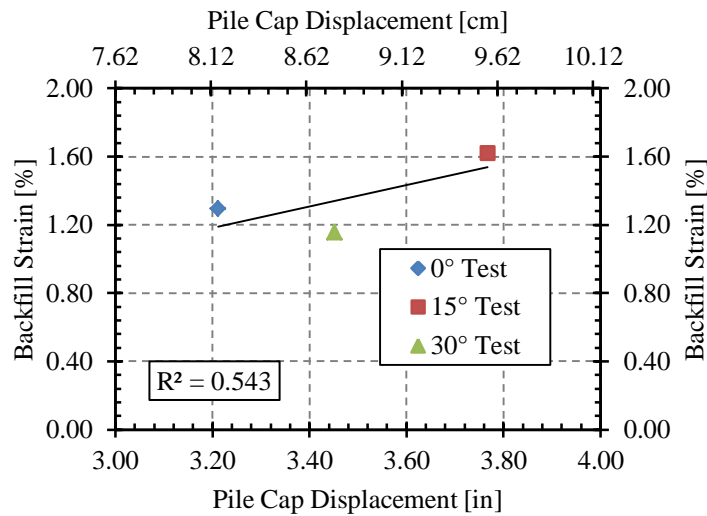


Figure 7-22: Average backfill strain with respect to pile cap deflection for all tests

7.5 Governing Backfill Failure Mechanisms

As noted throughout this chapter, the governing failure mechanism for the 30° test appeared to be significantly different than the governing failure mechanism for either the 0° or 15° test. This section will attempt to identify the differences between the governing failure mechanism for the 0° and 15° tests, and the 30° test.

As noted in Section 7.1 maximum backfill heave for both the 0° and 15° tests occurred immediately adjacent to the pile cap, whereas maximum heave for the 30° test occurred in a zone approximately 4 feet (1.22 m) to the north of the acute corner of the backwall. This difference in heave locations between the 30° test, and the 0° and 15° tests was likely caused because the internal failure wedge did not develop for the 30° test (compare Figure 7-8 with Figure 7-5 and Figure 7-6 in Section 7.2) and force the soil above the wedge to ride up and heave at the face of the backwall. Additionally, for 30° test the component of the backwall/soil interface shear strength acting in the vertical direction was likely significant enough to inhibit the vertical

movement of the material immediately adjacent to the backwall. Together, these two phenomena may have caused the backfill to heave slightly less at the face of the 30° backwall and heave more just to the north of the acute corner of the wedge.

The factor that appears to have the largest effect on the development of an internal failure wedge is the soil/backwall interface shear strength, which is composed of interface friction and adhesion between the soil and backwall [see Equation (2-8)]. As noted in Section 5.3, the peak longitudinal force for the 30° test was 322 kips (1,431 kN), and the back-calculated interface friction ratio, soil friction angle, and cohesion was 0.68, 40.2°, and 137.7 lbf/ft², respectively (Franke 2013). Using this information the peak shear force [see Equation (2-8)] was calculated as 161 kips (716 kN) and the peak shear strength [see Equation (2-9)] was calculated to be 146 kips (649 kN). Using Equation (2-10) the back-calculated factor of safety for the backfill sliding against the wall face was 0.91. This clearly indicates the soil likely slid against the backwall face which would have *significantly* reduced the shear stress acting on a potential shear plane descending from the top of the pile cap. However, for lower skew angles the relatively high factor of safety against the soil sliding horizontally along the face of the wall (2.0 at a skew angle of 15° when using the aforementioned soil strength parameters) would have significantly increased the shear stress acting on the shear plane descending from the top of the pile cap. This higher shear stress, combined with the relatively lower normal stress acting on this shear plane due to the shallow soil depth, would likely cause an internal failure wedge to develop prior to the soil sliding horizontally against the face of the wall.

Figure 7-23 shows the relationship between skew angle and the total longitudinal force, peak passive force, calculated interface shear strength, and calculated applied shear force [for these last two items see Equation (2-9) and Equation (2-8), respectively]. Among other things,

this figure indicates that at a skew angle of 30° the shear strength of the interface is slightly lower than the applied shear force. Furthermore, this figures indicates that while the total longitudinal force my not continue to drop off significantly at higher skew angles the calculated passive force, and therefore the interface shear strength, will continue to decrease, thereby reducing the transverse strength of the abutment.

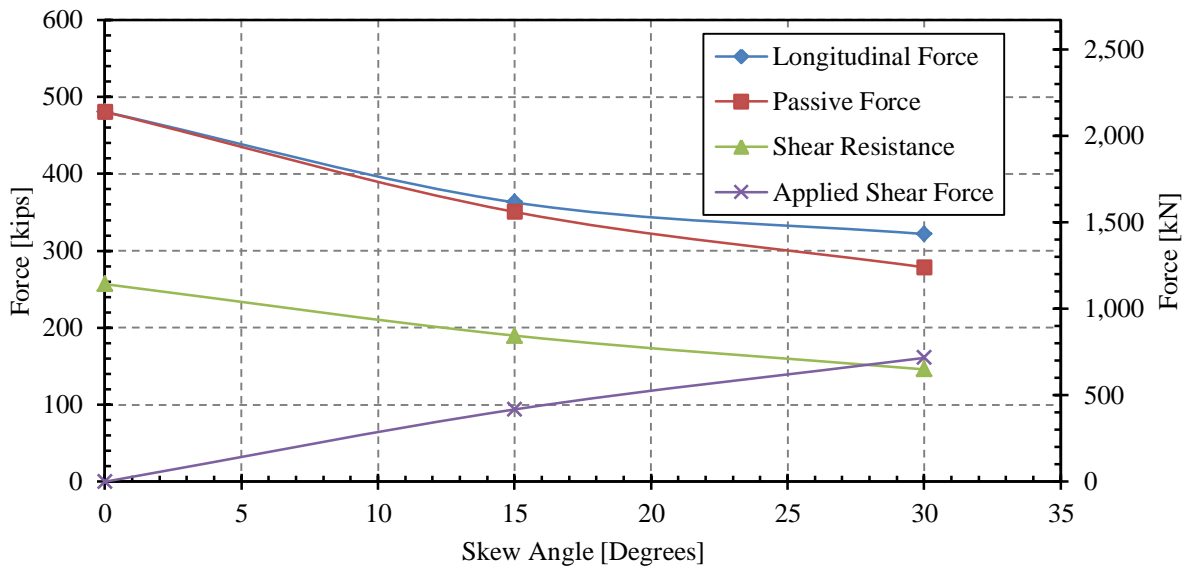


Figure 7-23: Comparison of peak passive force, longitudinal force, shear strength, and applied shear force with respect to skew angle

The development and shape of the internal failure surfaces appear to be highly dependent on the governing failure mechanism. For low skew angle cases, the failure geometry appears to be very similar to the failure geometry predicted by the log spiral method. However, for high skew angles, the failure mechanism appears to transition to a Rankine-type failure geometry, particularly at the acute corner of the backwall. This hypothesis is further substantiated when considering Figure 7-24 which compares the internal failure planes for all tests. This figure shows that the internal failure planes for the 0° and 15° tests were remarkably similar with the

only real difference being that the curved portion of the 0° failure plane dipped a few inches lower than for the 15° test. However, the measured failure planes for the 30° test indeed seem to have developed in a fashion much more similar to what is predicted by the Rankine passive pressure theory. As the Rankine passive pressure theory assumes no interface friction this likely indicates that the vertical component of the mobilized backwall-soil interface shear strength was *significantly* less than for either the 0° or 15° tests. This likely occurs because the shear strength at the soil-structure interface decreases significantly after the interface friction has been fully mobilized in the horizontal direction. The lower resulting interface friction angle in the vertical direction is therefore more in line with the assumptions made by the Rankine method for predicting passive force. However, this hypothesis should be verified by conducting additional tests at higher skew angles.

The difference in curve shape between the acute and obtuse corners of the wedge for the 30° test likely occurred because the soil at the acute corner strained and failed sooner than the soil at the obtuse corner. This progressive backfill failure would have caused the soil-backwall shear strength to mobilized and fail in a progressive fashion as well and thereby significantly reduce the interface friction first at the acute corner, and then at the obtuse corner. The lower wall friction at the acute corner of the wall than the obtuse corner of the wall would lead to a more linear failure surface at the acute corner than the obtuse corner as observed for the 30° test.

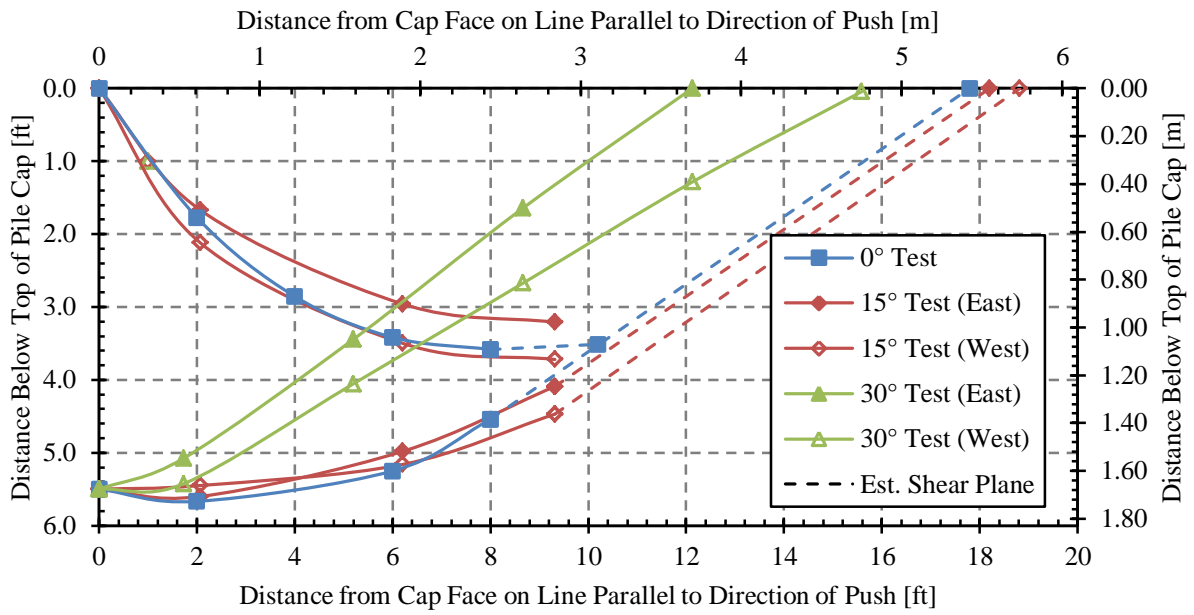


Figure 7-24: Comparison of internal shear planes for 0°, 15°, and 30° tests

8 COMPARISON OF TEST RESULTS TO DESIGN CODE AND ANALYTICAL RESULTS

This chapter will compare the measured passive force versus backwall displacement curves with current design curves (AASHTO 2011; Caltrans 2010), and two currently available methods for approximating the complete passive force versus backwall deflection curve (Duncan and Mokwa 2001; Shamsabadi et al. 2007). Finally, actual backfill failure geometries will be compared against failure geometries predicted by the log spiral, Coulomb, and Rankine methods.

8.1 AASHTO and Caltrans Passive Force versus Backwall Deflection Design Curves

Figure 8-1 compares the passive force versus backwall deflection curve for the 0° skew unconfined backfill test with the Caltrans and AASHTO design curves. As shown in the figure, the Caltrans design curve serves as very reasonable upper bound for the 0° passive force versus backwall deflection curve. However, the AASHTO design curve appears to underestimate the peak passive force, though this is likely the result of limiting the δ/ϕ ratio to 0.5.

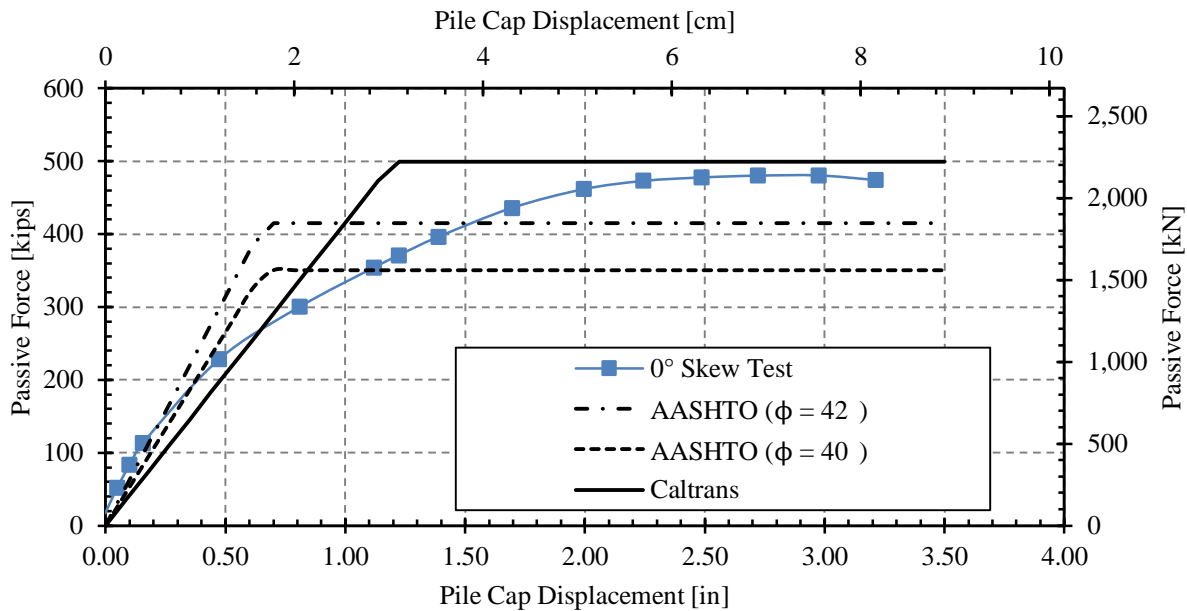


Figure 8-1: Comparison of Caltrans and AASHTO design curves with the passive force versus backwall deflection curve for the 0° skew 5.5-ft (1.68-m) unconfined backfill test

As stated in Section 2.5.2, AASHTO specifications state that a “conservative” estimate for backwall displacement necessary to achieve the peak passive force is 5% of the backwall height. However, if failure was assumed to occur at 5% deflection for this particular test the initial soil backfill stiffness would be significantly underestimated. In order to obtain the best agreement between the design code and test results, “failure” was set to occur at a backwall deflection equal to 1% of the backwall height, or 0.66 inches (1.68 cm) which is consistent with the recommendations made by Clough and Duncan (1991) and reported in the AASHTO design manual (2011). The passive force versus backwall deflection curves shown in Figure 5-9 indicate that the most significant change in slope occurred at approximately 2 inches (5.0 cm) of backwall deflection, or 3% of the backwall height. However, if the AASHTO design curve is assumed to break at a backwall deflection equal to 3% of the backwall height then the initial backfill stiffness is significantly underestimated.

If a soil friction angle of 40° is used, the peak passive force obtained using the AASHTO method [see Equation (2-18)] is 350 kips (1,559 kN). On the other hand, if the friction angle is assumed to be 42° then the calculated peak passive force is 415 kips (1,945 kN). Both of these friction angles produce a peak passive force significantly less than the measured peak passive force of 481 kips (2,138 kN) for the 0° test. All of the soil parameters used for these calculations are shown in Table 8-1 and, where applicable, are based on the soil strength parameters described in Section 3.4.2. The corrected coefficient of passive pressure (K_p) was found using Figure 3.11.5.4-2 in the AASHTO LRFD Bridge Design Specifications manual (2011).

Table 8-1: Soil and Wall Parameters used for Calculating AASHTO Passive Force versus Deflection Design Curve

<i>Parameter</i>	<i>Value</i>	<i>Units</i>
Soil Unit Weight, γ_s	116.5 (18.3)	lb/ft ³ (kN/m ³)
Ovesen-Brinch Hansen 3D Correction Factor	1.65 to 1.74	–
Abutment Width, w_2	11 (3.35)	ft (m)
Effective Width of Failure Wedge, w_1	18.26 (5.57)	ft (m)
Soil Cohesion, c	120 to 75 (5.75 to 3.59)	lb/ft ² (kN/m ²)
Abutment Height, H	5.5 (1.68)	ft (m)
Soil Friction Angle, ϕ	40 to 42	Degrees
Interface Friction Angle, δ	20 to 21	Degrees
Coefficient of Passive Earth Pressure, K_p	10.21 to 12.23	–

NOTE: The first values given in a range corresponds to $\phi = 40^\circ$, and the second to $\phi = 42^\circ$

Based on field test behavior, the Caltrans design curve shown in Figure 8-1 assumed that backfill materials did not meet the Caltrans Standard Specification Requirements (2010) and as such the initial backfill stiffness was taken as 25kip/in per foot of wall width (14.35 kN/mm per meter of wall width) rather than 50 kip/in per foot of wall width (28.70 kN/mm per meter of wall width). Using this value, the abutment stiffness was calculated according to Equation (2-15) and

found to be 275 kip/in (48.16 kN/mm). Using Equation (2-16) the peak passive force was found to be 502 kips (2,233 kN). Though the Caltrans specifications do not specifically suggest accounting for 3D end effects, the relatively low width-to-height ratio for these tests requires that these effects be accounted for if any degree of accuracy is desired when approximating the peak passive force. Other soil and backwall parameters used for calculating the Caltrans passive force versus backwall deflection curve are shown in Table 8-2.

Table 8-2: Soil and Wall Parameters used for Calculating Caltrans Passive Force versus Deflection Design Curve

<i>Parameter</i>	<i>Value</i>	<i>Units</i>
Initial Backfill Stiffness, K_i	25 (14.35)	kip/in/ft (kN/mm/m)
Projected Wall Width, w	11 (3.35)	ft (m)
Effective Wall Width, w_e	18.26 (5.57)	ft (m)
Abutment Stiffness, K_{abut}	275 (48.16)	kip/in (kN/mm)
Wall Height, h	5.5 (1.68)	ft (m)
Ovesen-Brinch Hansen Correction Factor	1.66	–
Effective Backwall Area, A_e	100.4 (9.33)	ft ² (m ²)

8.2 PYCAP and ABUTMENT Passive Force versus Backwall Deflection Curves

Figure 8-2 shows a comparison between the 0° test passive force versus backwall deflection curve with three curves developed using the PYCAP program (Duncan and Mokwa 2001). Soil strength parameters used for each curve are shown in Table 8-3. These three curves indicate that a 1° increase or decrease in friction angle, and a 15 to 35 psf (0.72 to 1.68 kPa) change in cohesion has a very significant effect on the estimated passive force versus backwall deflection relationship.

Table 8-3: PYCAP Soil Strength Parameters

<i>Soil Parameter</i>	<i>Low Range</i>	<i>Best Fit</i>	<i>High Range</i>	<i>Units</i>
Friction Angle, ϕ	39.0	40	41.0	Degrees
Cohesion, c	70.0 (3.35)	85.0 (4.07)	120.0 (5.75)	lbf/ft ² (kN/m ²)
Interface Friction Ratio, δ/ϕ	0.70	0.70	0.70	–
Initial Tangent Modulus, E	415 (19.87)	415 (19.87)	415 (19.87)	kip/ft ² (MN/m ²)
Poisson’s Ratio, ν	0.33	0.33	0.33	–

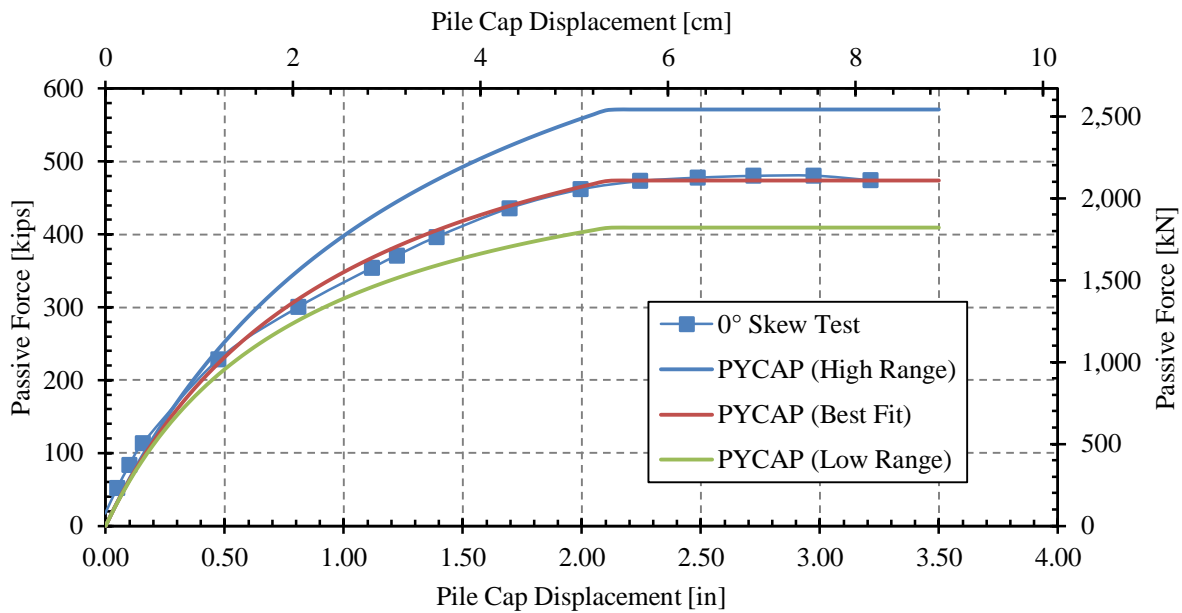


Figure 8-2: Comparison of low bound, best fit, and high bound PYCAP passive force versus backwall deflection curves with the 0° test curve

Figure 8-3 shows a comparison between the 0° skew 5.5-foot (1.68-m) unconfined backfill passive force versus backwall deflection curve with three curves developed using the “Log Spiral Modified Moment” method in the ABUTMENT program (Shamsabadi et al. 2007). Soil strength parameters used for each curve are shown in Table 8-4. With the exception of cohesion, these parameters are very similar to the parameters used in the PYCAP model (see Table 8-3).

Table 8-4: ABUTMENT Soil Strength Parameters

<i>Soil Parameter</i>	<i>Low Range</i>	<i>Best Fit</i>	<i>High Range</i>	<i>Units</i>
Friction Angle, ϕ	39	40	41	Degrees
Interface Friction Angle, δ	27.3	28	28.7	Degrees
Interface Friction Ratio, δ/ϕ	0.70	0.70	0.70	–
Cohesion, c	50.0 (2.39)	50.0 (2.39)	50.0 (2.39)	lbf/ft ² (kN/m ²)
Strain at 50% of Max Load, ϵ_{50}	0.0045	0.0045	0.0045	–
Poisson’s Ratio, ν	0.35	0.35	0.35	–
Failure Ratio, R_f	0.97	0.97	0.97	–

With respect to recommendations made by Shamsabadi et al. (2007), the ϵ_{50} value is somewhat higher than recommended for clean sand (0.002–0.003), though in his paper Shamsabadi et al. uses a “presumptive” ϵ_{50} value of 0.0035 which is also outside the range.

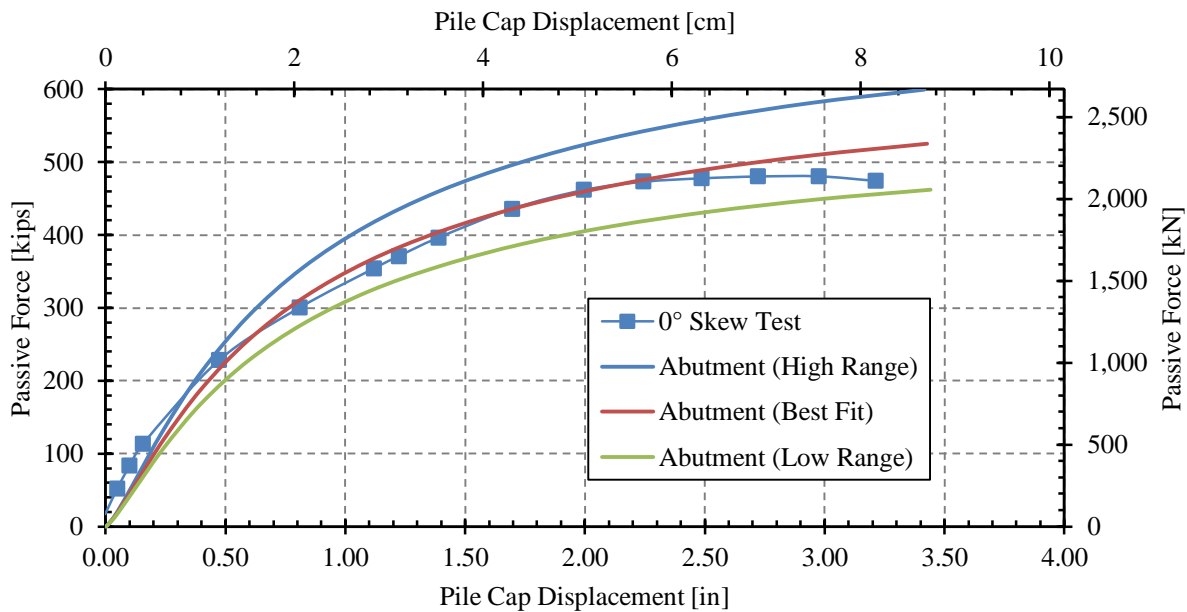


Figure 8-3: Comparison of low bound, best fit, and high bound ABUTMENT passive force versus backwall deflection curves with the 0° test curve

The best-fit soil strength parameters for both the PYCAP and ABUTMENT curves agree reasonably well with the soil strength parameters derived from the direct shear tests as shown in Table 3-5, though cohesion had to be reduced somewhat in order for the ABUTMENT curves to match the rest results.

8.3 Comparison of Calculated Passive Force and Failure Geometry According to the Coulomb, Rankine, and Log Spiral Methods with Test Results

As noted in Chapter 2, researchers have found that the log spiral method provides the most accurate estimate of both passive pressures and soil failure geometry. This section will first compare the calculated passive force according to the several methods with the passive force as measured for the 0° test, then the measured/estimated failure geometry for the 0° test will be compared with the failure geometry as predicted by the log spiral, Coulomb, and Rankine theories.

Table 8-5 shows the calculated and measured passive force per foot of wall width as predicted by the Log Spiral, Coulomb, and Rankine theories, and obtained using PYCAP (Duncan and Mokwa 2001). This table also shows the calculated and measured passive force per foot of wall width, and total passive force, respectively. When calculating the total passive force from the force per width provided by PYCAP a 3D width correction factor (Brinch Hansen 1966) of 1.79 was applied (obtained from PYCAP). The values in this table clearly show that the Rankine and Coulomb theories significantly under and overestimate the total passive force, respectively; whereas the log spiral method provides an exceptionally accurate estimate of the total passive force when coupled with the Brinch Hansen (1966) 3D width correction factor.

Table 8-5: Comparison of Measured Total Passive Force to Values Predicted by Log Spiral, Coulomb, and Rankine Methods

<i>Method</i>	<i>Calculated Passive Force kip/ft (kN/m)</i>	<i>Total Passive Force kips (kN)</i>	<i>Total Passive Force Percent Error</i>
Log Spiral	24.1 (351.7)	474 (2,108)	-1.5%
Coulomb	35.9 (524.1)	706 (3,141)	47%
Rankine	9.73 (141.9)	191 (851)	-60%
Test Results	24.4 (356.7)	481 (2,138)	N/A

Figure 8-4, Figure 8-5, and Figure 8-6 show the measured and predicted internal failure surfaces for the 0°, 15°, and 30° tests, respectively. For these figures the low range, best fit, and high range soil parameters shown in Table 8-3 were used to predict the locations of the shear planes.

As shown in Figure 8-4 and Figure 8-5 the log spiral method appears to provide a very accurate estimate of the location of the internal failure surfaces for the 0° and 15° tests, respectively. On the other hand for both tests, the Rankine and Coulomb theories significantly under and overestimate the length of the failure wedge, respectively.

For the 30° test the Rankine passive pressure theory appears to provide the most accurate estimate of the location of the internal failure wedge, as both the log spiral and Coulomb passive pressure theories significantly overestimate the length of the failure wedge. Despite the relative agreement between the actual and predicted Rankine failure surfaces, the passive force, calculated using the Rankine method still significantly underestimates the peak passive force as the maximum passive force for the 30° test was 279 kips (1,241 kN) but the predicted peak passive force was only 191 kips (851 kN). This is an underestimate of about 32%. Therefore, the Rankine passive pressure theory clearly cannot be used to accurately predict the peak passive force, even for a 30° skewed abutment.

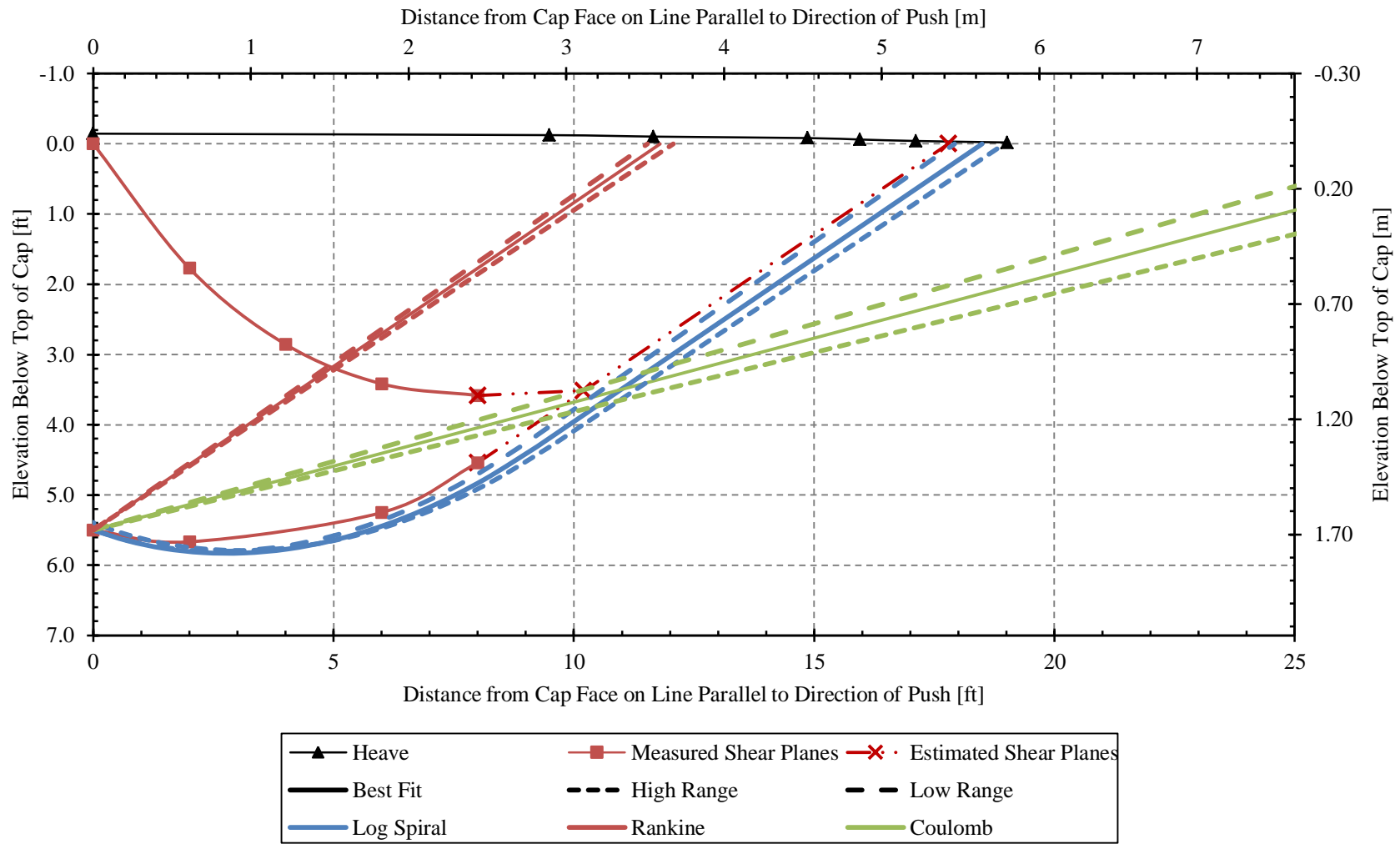


Figure 8-4: Actual and predicted failure surface geometry for the 0° test

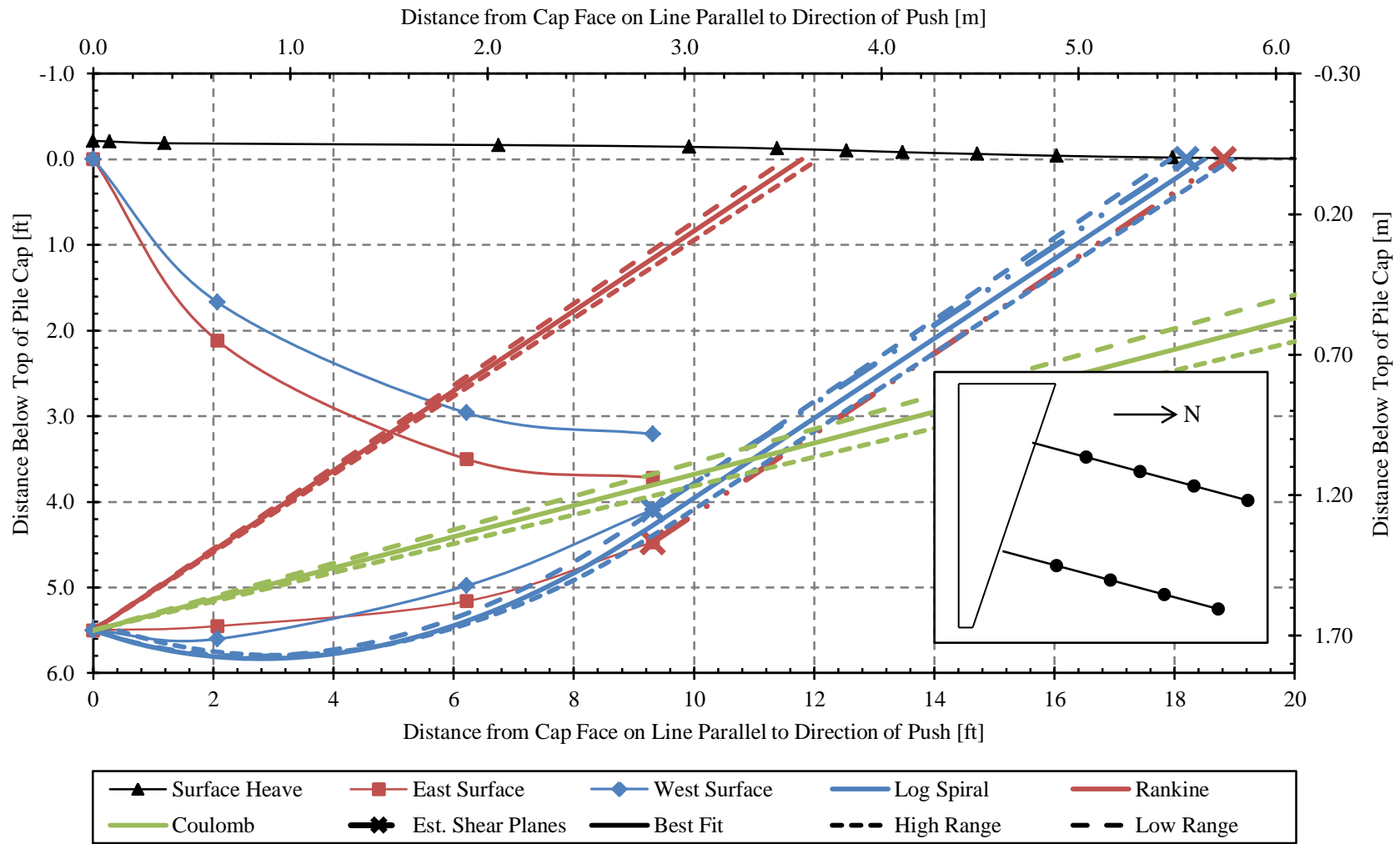


Figure 8-5: Actual and predicted failure surface geometry for the 15° test

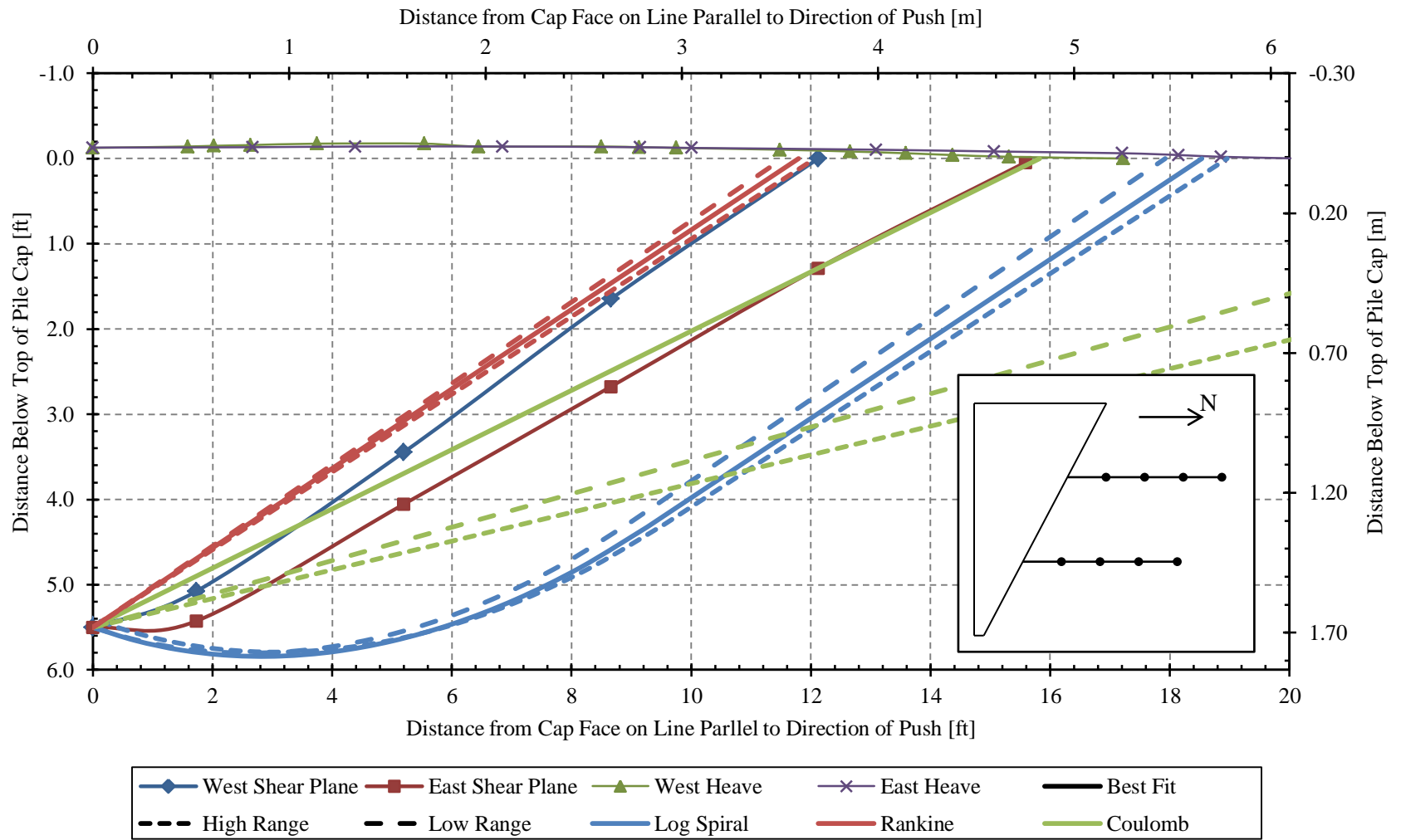


Figure 8-6: Actual and predicted failure surface geometry for the 30° test

9 CONCLUSION AND RECOMMENDATIONS FOR FUTURE TESTING

This thesis presents results from large-scale lateral load tests designed to determine the effect that skew angle has on the ultimate passive force as well as the passive force versus backwall deflection relationship for unconfined backfill geometries. This was accomplished by performing tests at skew angles of 0° , 15° , and 30° at a backfill height of 5.5 feet (1.68 m). Based on this work, the following conclusions are drawn and recommendations made:

1. Skew angle has a significant effect on the developed peak passive force.
2. The deflection necessary to obtain the peak passive force appears to decrease slightly with respect to skew angle; however, normalized deflections necessary to obtain the peak passive force are still within 3% to 5% of the backwall height, which is consistent with values reported in literature.
3. The reduction in peak passive force with respect to time is approximately 7% to 10% after two minutes and appears to be independent of skew angle, but dependent on load.
4. The notion of using an empirically developed equation to relate peak passive force for a skewed abutment to a non-skewed abutment, such as described in Section 2.4.1 and at the end of Section 5.3, appears to be generally applicable, though additional large/small scale tests and/or numerical models should be performed to verify this conclusion (Rollins and Jessee 2012).

5. The governing failure mechanism appears to transition from a type of general shear failure mechanism described by Terzaghi (1943) to a different failure mechanism where the wedge cuts into the backfill and an internal failure wedge does not develop as the skew angle increases from 0° to 30° .
6. The internal failure geometry associated with high skew angles appears to develop such that the failure plane at the acute corner of the backwall develops in a more linear fashion than the failure plane at the obtuse corner of the backwall
7. Skewed bridges significantly underperform in comparison to non-skewed bridges when subjected to lateral forces generated by seismic events or thermal expansion. Current bridge design methods dramatically over-estimate the passive force versus backwall deflection relationship for skewed bridges which has led to skewed bridges not performing as well as non-skewed bridges during seismic events.
8. The Caltrans seismic bridge design manual provides an adequate approximation of the passive force versus backwall deflection relationship for a 5.5-foot (1.68-m) high backwall for which the method was developed. However, additional tests at other fill heights would be desirable to examine the effect of backfill height as classical earth pressure theory suggests that the relationship between developed passive pressures and backwall height is a squared relationship whereas the Caltrans design methods assume a linear relationship.
9. The AASHTO bridge design specifications significantly underestimate the peak passive force for cases where interface friction ratio, δ/ϕ , is much higher than 50%.

10. The log spiral method proved to be the most accurate method for predicting both the internal failure geometry and the peak passive force for the 0° test. Furthermore, at low skew angles (e.g. 15°) the internal failure geometry predicted by the log spiral theory appears to agree quite well with the observed failure geometry. However, the peak passive force predicted by the log spiral theory overestimates the observed peak passive force for skewed bridges.
11. For all skew angles the Coulomb passive pressure theory significantly overestimates both the length of the developed failure wedge and the peak passive force. Therefore, this method should not be used if δ/ϕ is greater than about 0.40 (Duncan and Mokwa 2001).
12. For low skew angles (e.g. 0° or 15°), the Rankine passive pressure theory significantly underestimates the length of the developed failure wedge. However at higher skew angles (e.g. 30°), this theory appears to provide a fairly accurate estimate of the location of the internal failure geometry at the *acute* corner or the backwall.
13. The unaccounted for component of the passive force developed due to thermal expansion that acts perpendicular to the length of the bridge can cause sometimes significant damage to wingwalls as the bridge rotates about a vertical axis.
14. Additional large/small scale tests and/or numerical models should be conducted to verify these conclusions.
15. If possible, for future tests using this test site the backfill zone should be extended at least a couple feet to either side of the existing test pit so that the sides of the pit

don't interfere with a developing failure wedge, particularly for tests with a large skew angle.

16. Red-dyed soil columns should be installed in the backfill in a consistent manner so comparisons between tests can be more easily made.

REFERENCES

- AASHTO. (2011). *LRFD Bridge Design Specifications*, 5th Ed.,
- Apirakyorapinit, P., Mohammadi, J., and Shen, J. (2012). "Analytical Investigation of Potential Seismic Damage to a Skewed Bridge." *Practice Periodical on Structural Design and Construction*, 16(1), 5-12.
- Borowicka, H. (1938). "Distribution of Pressure Under a Uniformly Loaded Elastic Strip Resisting on Elastic-Isotropic Ground." *Proc., 2nd Congress International Association Bridge Structures Engineering*, Vol. 8(3).
- Brinch Hansen, J. (1966). "Resistance of a Rectangular Anchor Slab." *Bulletin No. 21*, Danish Geotechnical Institute, Copenhagen, 12-13.
- Brinkgreve, R. B. J. (2006). *Plaxis 3D Tunnel, Tutorial Manual, Version 2*.
- Burke Jr., M. P. (1994). "Semi-Integral Bridges: Movements and Forces." 1-7 p.
- Caltrans. (2006). *Standard Specifications*, Sacramento, California.
- Caltrans. (2010). *Caltrans Seismic Design Criteria Version 1.6*, California Department of Transportation, Sacramento, California
- Canadian Geotechnical Society. (1992). *Canadian Foundation Engineering Manual*, 3rd Ed., Canadian Geotechnical Society, BiTech, Vancouver, B.C., Canada
- Caquot, A., and Kerisel, J. (1948). *Tables for the Calculation of Passive Pressure, Active Pressure and Bearing Capacity of Foundations*, Gauthier-Villars, Paris.
- Chen, C. S., and Su, J. J. (1994 Published). "A Method for Passive Pressure Earth Computation on Sands." *Paper presented at 8th International Conference on Methods and Advancements in Geomechanics*.
- Christensen, D. S. (2006). "Full Scale Static Lateral Load Test of a 9 Pile Group in Sand." *M.S. Thesis*, Department of Civil and Environmental Engineering, Brigham Young University, Provo, UT.

- Clough, G. W., and Duncan, J. M. (1991). *Foundation Engineering Handbook*, 2nd Ed., H. Y. Fang, ed., Chapman and Hall, New York.
- Cole, R. T., and Rollins, K. M. (2006). "Passive Earth Pressure Mobilization during Cyclic Loading." *Journal of Geotechnical and Geoenvironmental Engineering*, ASCE, 132(9), 1154-1164.
- Coulomb, C. A. (1776). "Essai sur une application des règles de maximis & minimis à quelques problèmes de statique, relatifs à l'architecture." (microform, Microopaque), De l'Imprimerie Royale, Paris.
- Culmann, K. (1875). *Die Graphische Statik*, Meyer and Zeller, Zurich, German.
- Cummins, C. R. (2009). "Behavior of a Full-Scale Pile Cap with Loosely and Densely Compacted Clean Sand Backfill Under Cyclic and Dynamic Loadings." *M.S. Thesis*, Department of Civil and Environmental Engineering, Brigham Young University, Provo, UT.
- Danisch, L. A., Lowery-Simpson, M., and Abdoun, T. (2005). "Shape-acceleration Device and Method." US Patent 7,296,363.
- Das, B. M. (2010). "Principles of Geotechnical Engineering." <>.
- Douglas, D. J., and Davis, E. H. (1964). "The Movement of Buried Footings due to Moment and Horizontal Load and the Movement of Anchor Plates." *Geotechnique*, 14(2), 115-132.
- Duncan, J. M., Byrne, P. M., Wong, K. S., and Mabry, P. (1980). "Strength, Stress-Strain and Bulk Modulus Parameters for Finite Element Analysis of Stresses and Movements in Soil Masses." University of California, Berkeley, California.
- Duncan, J. M., and Chang, C. Y. (1970). "Nonlinear Analysis of Stress and Strain in Soils." *Journal of the Soil Mechanics and Foundations Division*, 96(5), 1629.
- Duncan, J. M., and Mokwa, R. L. (2001). "Passive Earth Pressures: Theories and Tests." *Journal of Geotechnical and Geoenvironmental Engineering*, ASCE, 127(3), 248-257.
- Elnashai, A. S., Gencturk, B., Kwon, O.-S., Hashash, Y., Roesler, J. R., Kim, S. J., Jeong, S.-H., Dukes, J., and Valdivia, A. (2010a). "The Maule (Chile) Earthquake of February 27, 2010: Consequence Assessment and Case Studies." *MAE Center Report No. 10-04*, Mid-America Earthquake (MAE) Center, Department of Civil and Environmental Engineering, University of Illinois at Urbana-Champaign.
- Elnashai, A. S., Gencturk, B., Kwon, O., Al-Qadi, I. L., Hashash, Y., Roesler, J. R., Kim, S. J., Jeong, S., Dukes, J., and Valdivia, A. (2010b). "The Maule (Chile) Earthquake of February 27, 2010: Consequence Assessment and Case Studies." Department of Civil and Environmental Engineering, University of Illinois at Urbana-Champaign, 190 p.

- Franke, B. (2013). "Passive Force on Skewed Abutments with Mechanically Stabilized Earth (MSE) Wingwalls Based on Large-Scale Tests." *M.S. Thesis*, Department of Civil and Environmental Engineering, Brigham Young University, Provo, UT.
- Gerber, T. M., Rollins, K. M., Cummins, C. R., and Pruett, J. M. (2010). "Dynamic Passive Pressure on Abutments and Pile Caps." *Report No. UT-10.18*, Research Division, Utah Department of Transportation, 223 p.
- Johnson, S. R. (2003). "Static Lateral Load Testing of a Full-Scale Pile Group Spaced at 5.65 Pile Diameters." *M.S. Thesis*, Department of Civil and Environmental Engineering, Brigham Young University, Provo, UT.
- Kondner, R. L. (1963). *A Hyperbolic Stress-Strain Formulation for Sands*, Northwestern University, Evanston, IL.
- Kramer, S. L. (1996). *Geotechnical Earthquake Engineering*, Prentice Hall, Upper Saddle River, N.J.
- Kumar, J., and Subba Rao, K. S. (1997). "Passive Pressure Coefficients, Critical Failure Surface and its Kinematic Admissibility." *Geotechnique*, 47(1), 185-192.
- Lee, K. L., and Singh, A. (1971). "Relative Density and Relative Compaction." *Journal of Soil Mechanics and Foundations Design*, 97(7), 1049-1052.
- Lemnitzer, A., Ahlberg, E. R., Nigbor, R. L., Shamsabadi, A., Wallace, J. W., and Stewart, J. P. (2009). "Lateral Performance of Full-Scale Bridge Abutment Wall with Granular Backfill." *Journal of Geotechnical and Geoenvironmental Engineering, ASCE*, 135(4), 506-514.
- Maroney, B. H. (1995). "Large Scale Abutment Tests to Determine Stiffness and Ultimate Strength Under Seismic Loading." *Ph.D. Dissertation*, Civil Engineering Department, University of California, Davis.
- Measurand Inc. (2009). <<http://www.measurandgeotechnical.com/>>. (08/21/12).
- Measurand Inc. (2011). "ShapeAccelArray (SAA) Installation Guide." <http://measurandgeotechnical.com/Installation_Guide_2011.pdf>. (02/08/2013).
- Mitchell, J. K., and Soga, K. (2005). "Chapter 12: Time Effects on Strength and Deformation." *Fundamentals of Soil Behavior*, John Wiley and Sons, Hoboken, New Jersey, p. 489
- Mokwa, R. L., and Duncan, J. M. (2001). "Experimental Evaluation of Lateral-Load Resistance of Pile Caps." *Journal of Geotechnical and Geoenvironmental Engineering, ASCE*, 127(2), 185-192.
- Nasr, M., and Rollins, K. M. (2010 Published). "Numerical Analysis of Limited Width Dense Gravel Backfills for Plane Strain Conditions." *Paper presented at 2011 Pan-Am CGS Geotechnical Conference*.

- Ovesen, N. K. (1964). "Anchor slabs, calculation methods, and model tests." *Bulletin No. 16*, Danish Geotechnical Institute, Copenhagen, 5-39.
- Peterson, K. T. (1996). "Static and Dynamic Lateral Load Testing a Full-Scale Pile Group in Clay." *M.S. Thesis*, Department of Civil and Environmental Engineering, Brigham Young University, Provo, UT.
- PLAXIS. (2004). *Plaxis V8*, R. B. J. Brinkgreve, and W. Broere Eds., Delft, The Netherlands.
- Potyondy, J. G. (1961). "Skin Friction between Various Soils and Construction Materials." *Geotechnique*, 11(4), 339-353.
- Rankine, W. J. M. (1857). "On the Stability of Loose Earth." *Philosophical Transactions of the Royal Society of London*, 147, 9-27.
- Rollins, K. M., and Cole, R. T. (2006). "Cyclic Lateral Load Behavior of a Pile Cap and Backfill." *Journal of Geotechnical and Geoenvironmental Engineering, ASCE*, 132(9), 1143-1153.
- Rollins, K. M., Gerber, T. M., Cummins, C. R., and Herbst, M. "Monitoring Displacement vs. Depth in Lateral Pile Load Tests Using Shape Accelerometer Arrays." *Proc., 17th International Conference on Soil Mechanics and Geotechnical Engineering*, Vol. 5, IOS Press, Alexandria, Egypt, 2016-2019.
- Rollins, K. M., Gerber, T. M., Cummins, C. R., and Pruett, J. M. (2010a). "Dynamic Pressure on Abutments and Pile Caps." *Report No. UT-10.18*, B. Y. University, U. D. o. Transportation, and F. H. Administration, eds., Utah Department of Transportation, 255 p.
- Rollins, K. M., Gerber, T. M., and Heiner, L. (2010b). "Passive Force-Deflection Behavior for Abutments with MSE Confined Approach Fills." *Report No. UT-10.15*, Utah Department of Transportation, Salt Lake City, UT, 83 p.
- Rollins, K. M., and Jessee, S. (2012). "Passive Force-Deflection Curves for Skewed Abutments." *Journal of Bridge Engineering, ASCE*, 17(5).
- Rollins, K. M., King, R., Synder, J. L., and Johnson, S. R. "Full-Scale Lateral Load Tests of Pile Groups and Drilled Shafts in CLay." *Proc., Intl. Conf. on Soil-Structure Interaction, Calculation Methods and Engineering Practice*, ASV Publishers, Moscow, 287-292.
- Rollins, K. M., Nasr, M., and Gerber, T. M. (2010c). "Numerical Analysis of Dense Narrow Backfills for Increased Passive Resistance." *Report No. UT-10.19*, Research Division, Utah Department of Transportation, 192 p.
- Rollins, K. M., and Sparks, A. E. (2002). "Lateral Load Capacity of a Full-Scale Fixed-Head Pile Group." *Journal of Geotechnical and Geoenvironmental Engineering, ASCE*, 128(9), 711-723.

- Rollins, K. M., Synder, J. L., and Broderick, R. D. "Static and Dynamic Lateral Response of a 15 Pile Group." *Proc., 16th Intl. Conf. on Soil Mechanics and Geotechnical Engineering*, Vol. 4, Millpress, Rotterdam, Netherlands, 2035-2040.
- Sandford, T. C., and Elgaaly, M. (1993). "Skew Effects on Backfill Pressures at Frame Bridge Abutments." *Transportation Research Record: Journal of the Transportation Research Board*, 1-11 p.
- Schanz, T., Vermeer, P. A., and Bonnier, P. G. "The Hardening Soil Model: Formulation and Verification." *Proc., Plaxis Symposium "Beyond 2000 in Computational Geotechnics"*, Balkema, Amsterdam, Rotterdam, 281-296.
- Shamsabadi, A. (2007). "Three-Dimensional Nonlinear Seismic Soil-Abutment-Foundation-Structure Interaction Analysis of Skewed Bridges." *Ph.D. Dissertation*, Department of Civil Engineering, University of Southern California, Los Angeles, CA.
- Shamsabadi, A., Ashour, M., and Norris, G. (2005). "Bridge Abutment Nonlinear Force-Displacement-Capacity Prediction for Seismic Design." *Journal of Geotechnical and Geoenvironmental Engineering, ASCE*, 131(2), 151-161.
- Shamsabadi, A., Kapuskar, M., and Zand, A. (2006 Published). "Three-Dimensional Nonlinear Finite-Element Soil-Abutment Structure Interaction Model for Skewed Bridges." *Paper presented at 5th National Seismic Conference On Bridges and Highways*, 1-10.
- Shamsabadi, A., Rollins, K. M., and Kapaskur, M. (2007). "Nonlinear Soil-Abutment-Bridge Structure Interaction for Seismic Performance-Based Design." *Journal of Geotechnical and Geoenvironmental Engineering, ASCE*, 133(6), 707-720.
- Soubra, A. H. (2000). "Static and Seismic Earth Pressure Coefficients on Rigid Retaining Structures." *Canadian Geotechnical Journal*, 37, 463-478.
- Sowers, G. B., and Sowers, G. F. (1961). *Introductory Soil Mechanics and Foundations*, MacMillan, New York.
- Steinberg, E., and Sargand, S. (2010). "Forces in Wingwalls from Thermal Expansion of Skewed Semi-Integral Bridges." *Report No. FHWA/OH-2010/16*, Prepared by Ohio University for Ohio Department of Transportation, Athens, OH, 87 p.
- Steinberg, E., Sargand, S. M., and Bettinger, C. (2004). "Forces in Wingwalls of Skewed Semi-Integral Bridges." *Journal of Bridge Engineering, ASCE*, 9(6), 563-561.
- Stewart, P. S., Taciroglu, E., Wallace, J. W., Ahlberg, E. R., Lemnitzer, A., Rha, C., and Tehrani, P. K. (2007). "Full Scale Testing of Foundation Support Systems for Highway Bridges, Part II: Abutment Backwalls." *Report No. UCLA-SGEL 2007/02 conducted under Caltrans Grant No. 59A0247*, Department of Civil and Environmental Engineering, University of California, Los Angeles, CA.

- Taylor, A. J. (2006). "Full-Scale-Lateral-Load Test of a 1.2 m Diameter Drilled Shaft in Sand." *M.S. Thesis*, Department of Civil and Environmental Engineering, Brigham Young University, Provo, Utah.
- Terzaghi, K. (1943). *Theoretical Soil Mechanics*, J. Wiley & Sons, New York.
- Terzaghi, K., Peck, R. B., and Mesri, G. (1996). *Soil Mechanics in Engineering Practice*, 3rd Ed., John Wiley & Sons, New York.
- Unjoh, S. "Repair and Retrofit of Bridges Damaged by the 2010 Chile, Maule Earthquake." *Proc., International Symposium on Engineering Lessons Learned from the 2011 Great East Japan Earthquake*, Tokyo, Japan.
- Wilson, P., and Elgamal, A. (2010). "Large-Scale Passive Earth Pressure Load-Displacement Tests and Numerical Simulation." *Journal of Geotechnical and Geoenvironmental Engineering*, ASCE, 136(12), 1634-1643.
- Zhu, D.-Y., and Qian, Q. (2000). "Determination of Passive Earth Pressure Coefficient by the Method of Triangular Slices." *Canadian Geotechnical Journal*, 37, 485-491.

APPENDIX A. PROCEDURES FOR CORRECTING SHAPE ARRAY DATA

This Appendix will describe the procedure for aligning the shape array vector with the inclinometer vector.

As noted in Section 6.1 and shown in Figure 6-1, the shape arrays were not installed such that the primary x and y axes of the instrument were aligned with the x and y axes of the pile cap and as such the primary direction vector associated with each shape array had to be aligned with the primary direction vector associated with the adjacent inclinometer reading as no other instrument reading provided the necessary information to correct the shape array data. In order to be the most consistent the uppermost shape array node and inclinometer measurement point was used to obtain the direction vectors used in the following procedures.

The rotation of the shape array data was accomplished through the means of the simple 2D vector rotation equation shown in Equation (A-1).

$$\begin{matrix} x_2 \\ y_2 \end{matrix} = \begin{matrix} x_1 \\ y_1 \end{matrix} * \begin{matrix} \cos\theta & -\sin\theta \\ \sin\theta & \cos\theta \end{matrix} \quad (\text{A-1})$$

where

θ = shortest angle between original vector and desired direction vector

$\begin{matrix} x_1 \\ y_1 \end{matrix}$ = original vector

$\begin{matrix} x_2 \\ y_2 \end{matrix}$ = rotated vector

The formula shown in Equation (A-2) was used to obtain the angle between the original shape array direction vector and the inclinometer direction vector.

$$\theta = \cos^{-1} \frac{a \cdot b}{a} \quad (\text{A-2})$$

where

a = shape array direction vector for top working node

b = unit inclinometer direction vector for highest measurement point

As the linear transformation shown in Equation (A-1) assumes a *counterclockwise* vector rotation, and because the angle between vectors obtained by Equation (A-2) only provides the smallest angle between the two vectors the cross product, as shown in Equation (A-3), of the shape array and inclinometer vectors was used to determine the necessary direction of rotation.

$$c = a \times b = \begin{array}{ccc} i & j & k \\ x_1 & x_2 & x_3 \\ y_1 & y_2 & y_3 \end{array} \quad (\text{A-3})$$

where

$$a = \begin{array}{c} x_1 \\ x_2 \\ x_3 \end{array} \quad \text{and } x_3 = 0 \text{ for this application}$$

$$b = \begin{array}{c} y_1 \\ y_2 \\ y_3 \end{array} \quad \text{and } y_3 = 0 \text{ for this application}$$

A positive sign of the z-component of the cross product indicates that the smallest angle between a and b is in the counterclockwise rotation whereas a negative sign indicates the opposite. For those instances where the smallest angle of rotation between the two vectors was clockwise the complementary, or conjugate, angle was used when performing the linear transformation shown in Equation (A-1). Each nodal shape array node measurement was rotated through the same angle as no information was available to justify a different approach.